AQRP Project 14-022

Use of Satellite Data to Improve Specifications of Land Surface Parameters

Final Report

Prepared for:
Texas Air Quality Research Program (AQRP)

By
Richard T. McNider, Kevin Doty, Yu Ling Wu, and Arastoo Pour Biazar
ESSC
University of Alabama – Huntsville

And

Pius Lee
NOAA Air Resources Laboratory
Min Huang
George Mason University/NOAA Affiliate

To

Vince Torres
AQRP Project Manager

Cyril Durrenberger
Quality Control Manager

August 21, 2015

QA Requirements: Audits of Data Quality: 10% Required

Executive Summary

It is the purpose of this project to evaluate and improve the performance of the land surface models used in the Weather Research and Forecasting model (WRF) by the use of satellite skin temperatures to better specify physical parameters associated with land use classes. Skin temperature, T_S, is the radiating temperature of the surface and thus represents the temperature of an infinitely thin surface that is controlling the outgoing longwave radiation (σT_S^4). Improved temperature performance impacts biogenic emissions, thermal decomposition (chemical chain lengths and slopes of ozone/NOy curves) and thermally driven winds such as sea breezes. Also, land surface parameters control surface deposition which impacts the efficacy of long-range transport.

While considerable work has been done by the national community and especially in Texas to develop improved land use classifications, land use classes themselves are not directly used in models. Rather, physical parameters such as heat capacity, thermal resistance, roughness, surface moisture availability, albedo, etc. associated with a land use class are actually used in the land surface model. Many of the land use class associated parameters such as surface moisture availability are dynamic and ill-observed depending on antecedent precipitation and evaporation, soil moisture diffusion, the phenological state of the vegetation, irrigation applications, etc. Other parameters such as heat capacity, thermal resistance or deep soil temperature are not only difficult to observe they are often unknowable *a priori*. In some sense they are model heuristics with different land surface models having several orders of magnitude difference in parameters such as vegetative thermal resistance. The specification of these physical parameters across grids having mixed land use types is even more problematic. Despite the difficulty in specifying these parameters they are incredibly important to model predictions of turbulence, temperature, boundary layer heights and winds.

The evaluation and use of skin temperature as a model evaluation metric is provided for the period 1-30 September 2015 which was part of the Houston campaign of Deriving Information on Surface Conditions from Column and Vertically Resolved Observations Relevant to Air Quality (DISCOVER-AQ) project. Aircraft measurements of skin temperature and air temperature are also used in this evaluation. The National Oceanic and Atmospheric Administration (NOAA) Comprehensive Large Array Data Stewardship System (CLASS, www.class.ncdc.noaa.gov) was the source of the first skin temperature data we tested. This data was derived from the Geostationary Operational Environmental Satellite (GOES) and is under the CLASS category of GOES Surface and Insolation Products (GSIP). The evaluation of NOAA-GSIP skin temperature product revealed unphysical air temperatures over the western U.S. including parts of Texas when compared to the Moderate Resolution Imaging Spectroradiometer (MODIS) observation. An alternative NOAA skin temperature product used by the Atmosphere-Land Exchange Inverse (ALEXI) group was acquired, evaluated and employed to compare against model skin temperatures. In addition to the cloud clearing used by the ALEXI group, we also carried out additional screening of skin temperatures, which are described in the quality assurance chapter.

Insolation is one of the largest components in the daytime surface energy budget. Insolation largely depends on average solar zenith angle. However, clouds can dramatically alter the solar

energy received at the surface. This produces a potential source of error in air quality simulations since model clouds may be in the wrong place at the wrong time. Thus, on certain days when clouds are present in the model but not in reality the energy difference at the surface can be large. The Weather Research Forecast (WRF) model is run using both the default model insolation and satellite insolation. There are large differences found between model and satellite insolation at the surface largely due the placement of clouds. This in turn leads to large grid point differences in temperatures during the simulations. Because air quality standards such as ozone are based on events rather than long term averages, these large variations on specific times and at specific places can be very important in developing realistic recreations of the physical atmosphere in State Implementation Plan (SIP) modeling. Initial WRF simulations using the GSIP insolation actually had increased bias relative to the WRF control simulation with the National Weather Service (NWS) 2-m temperature as the comparison metric. Because of this, the final set of simulations used the National Aeronautics and Space Administration (NASA) Short-term Prediction Research and Transition Center (SPoRT) Geostationary Operational Environmental Satellite (GOES)-derived insolation product. While the SPoRT satellite derived insolation had better performance statistics against pyranometer data, the model case with satellite insolation showed slightly poorer performance than the run with WRF modeled insolation. This is an area for further investigation. In initial examination it appears that differences between the satellite insolation and modeled insolation cases have a pattern that appears to be related to surface albedo. In past uses of satellite insolation (McNider et al. 1994) the satellite derived insolation cases also used a satellite derived albedo. In the present case the regular WRF landuse albedo was used. This may be the cause of the slightly degraded performance.

The Pleim-Xiu land use model in WRF has used a surface moisture and deep soil nudging technique based on differences between model 2-m air temperatures at NWS observational sites. However, land use, vegetation coverage and convective precipitation can all have variations on spatial scales much smaller than the spatial scale of NWS observations. The major activity under this project was to determine whether satellite observed skin temperature, which has much finer resolution (10 km) than NWS observations (~40 km), can be used to nudge soil moisture and thermal resistance and provide improved model performance.

Using skin temperatures as the performance metric, the results showed that over most of the domain that the bias was improved but there was a slight negative bias increase in the overall bias. This means that the few areas that had an increase in bias were larger causing a slight increase in absolute bias for the domain. An examination of time series from the nudging runs compared to the control showed that the adjustments in moisture appeared to be working as formulated. In some places part of the error may have been due to bad skin temperature data.

Again, using skin temperatures as the performance metric, the root mean square error (RMSE) was calculated for the control run and for the skin temperature moisture nudging case. Here the moisture nudging provided significant improvement over the entire domain. The RMSE was improved by about .7 degrees K over the domain or approximately 20%. For the Texas only domain the decrease in RMSE was even greater with RMSE improving by nearly a full degree.

Comparisons with NWS observations were more mixed in regards to bias for humidity and 2-m temperature. RMSE was unchanged for humidity and decreased slightly for 2-m temperature. For 10-m wind speed and wind direction there was a slight decrease in bias and RMSE for all regions.

The largest areas in RMSE and bias remain in the Western U.S. where even drying the soil using moisture nudging did not give the diurnal range found in skin temperature observations. Here adjustments in other parts of the surface energy budget may be needed. It is felt that implementation of the heat capacity adjustment which was an optional task under this project for which there was not enough time may provide further significant improvement.

In conclusion a comparison of model performance in the WRF model was carried out with and without satellite data. The moisture nudging using satellite skin temperatures within the Pleim-Xiu model was a positive step in improving the model performanceOur findings were that RMSE was reduced by about 20% when satellite observed temperatures were used as a metric. For a special Texas only domain the improvements in performance were even greater for the moisture nudging in that RMSE was decreased by nearly one degree K. In comparison to NWS observations of wind direction and wind speed there was a slight decrease in bias and RMSE across the domain. Similar results were found for the Texas domain in comparison with NWS sites. Thus, it is felt that this supports the overall hypothesis in this research activity that simple land surface models constrained by observations may be path for improved meteorology in air quality simulations.

CONTENTS

Chapter 1 Background and Overview

1. Introduction and Rationale

The land surface is a critical component in local, regional and global modeling. Heat, momentum and scalar fluxes at the surface control temperature, turbulent mixing, winds and dry deposition of chemical species. Because of the importance of the characteristics of the land surface, there has been tremendous investment by the climate, weather forecasting and air quality communities in land surface research. Much of this investment has gone into developing complex land surface models, which include many intricate parameterizations that attempt to capture processes such as plant transpiration rates, leaf water interception, soil moisture and run-off, and parameterizations which control thermal and water transfer through canopies and soils (Sellers 1997, Pitman 2003). Thus, these models require additional parameter specifications to close the model systems.

A second major area of investment has been the development of land-use classification data sets that attempt to define areas which are forested, croplands, urban areas, etc. that can be used with the land surface models. The uses of satellite data (with its observables such as greenness and albedo) have greatly improved the characterization of the surface into classes. However, land surface models such as WRF National Centers for Environmental Prediction (NCEP)–Oregon State University–Air Force–Hydrologic Research Laboratory (Noah) (Chen and Dudhia 2001) do not use land use classifications directly. Rather, they use the physical parameters such as roughness, heat capacity, canopy thermal and water resistances, soil conductivity for water and heat, etc. that are associated with the land use classes. Thus, in the models, such as the WRF – Noah land use model, there are lookup tables that define these land-use associated parameters (Niu et al. 2011).

Unfortunately, the specification of some of these physical parameters is difficult even in homogeneous land use classes (Rosero et al.2009). For example, the rate of temperature change in vegetation is controlled by plant transpiration and evaporation through water resistance parameters and by the canopy thermal resistance. Thermal resistance depends on the heat capacity of the canopy and the thermal conductivity through the canopy (Noilhan and Planton 1989). The water resistance depends on root zone moisture, the phenological state of the plant, leaf area, shaded leaf area, etc. Field campaigns using tower measurements are usually conducted to try to establish these parameters. But, in effect, many of the parameters or processes have to be deduced as residuals in local canopy models, which are tied to specific turbulence and radiative models (Yang and Friedl 2003, Pleim and Gilliam 2009). Thus, the parameters are often model heuristics as opposed to fundamental observables (Wegner and Gupta 2005), which is the reason a parameter such as canopy thermal resistance can vary by three orders of magnitude in different models (Pleim and Gilliam 2009). In inhomogeneous grid boxes, which make up the real world, the situation is even worse (McNider et al 2005). Here, dominant land-use classes are often used in models such as Noah, but they may not well represent the actual mix of urban, crop and forestland uses.

Figure 1-1 illustrates the problem that is faced but also a potential solution. It shows land use classifications and also the satellite observed skin temperature for the Southeast. As can be seen, there is a correlation between land use classes and the skin temperature with urban areas and

crop lands warmer than forested areas. The question facing modelers is, can we ascribe the physical parameters in a land surface model impacting the skin temperature so that the model will reproduce the skin temperature variation seen in the Figure 1-1? In the present project, the assumption is made that two of the most uncertain parameters are surface moisture and thermal resistance. The satellite observed skin temperature is used to improve the specification of these parameters. With these adjusted parameters, will model prediction of skin temperature be closer to that observed by the satellite and will comparison against other observations such as National Weather Service 2-m temperatures, humidity and winds be improved? That is the goal of the present project.

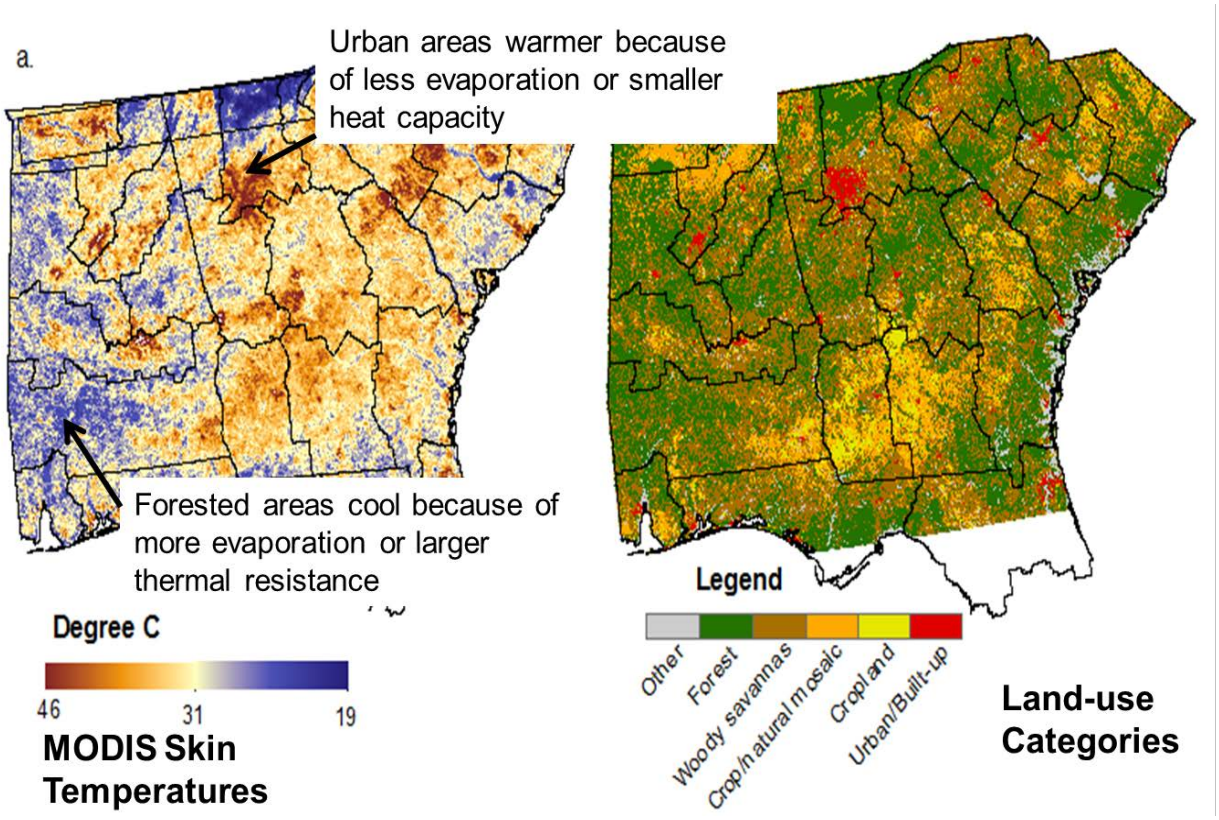

Figure 1-1 Illustration of relation of satellite skin temperature to land use. Left is the MODIS average afternoon temperature for July 2012. The question is can we ascribe the proper physical parameters in the land use classifications so that a model reproduces the observed skin temperature distribution. From Ellenburg et al. (2015).

In this project, we explore two paths to evaluating and improving the land surface model. The first is to use satellite skin temperatures as a model evaluation metric. Satellite skin temperatures have much finer resolution than National Weather Service (NWS) observations and therefore are better able to capture variations in land use and moisture variations. Second, we take an approach that simpler land surface models with fewer unknown parameters but constrained by observations may provide better model performance - especially in the retroactive fashion in which SIP models are utilized.

The development of complex land surface models mentioned above was consistent with the need in the climate modeling community for surface models that could be run for years without being touched by data. Thus, they needed vegetative surface interaction, water balance models, etc. However, Diak (1990), McNider et al. (1994), Anderson et al. (1997) and others argued that for short-term weather forecasting and for retrospective air quality simulations (McNider et al. 1998, Pleim and Xiu 2003) simpler models that could be constrained by observations might be preferred. The simple models avoid setting many uncertain parameters in the complex models. This is the path pursued here, with observational constraints provided by satellite skin temperature data. We employ the Pleim-Xiu assimilation model (Pleim and Xiu 1995, Xiu and Pleim 2001, and Pleim and Xiu 2003) modified to use satellite skin temperature rather than NWS observed 2-m temperatures to adjust soil moisture and to recover the surface thermal resistance following McNider et al. (2005).

Pleim and Xiu (2003) noted that since surface moisture is not a direct observable that use of auxiliary information is needed. They have used observed NWS surface temperatures to nudge moisture. Here they adjust surface layer moisture w_G using the difference between model daytime temperatures (T^F) and analyses of observed temperatures (T^A) and model and observed relative humidity(RH).

$$\Delta w_G = \alpha_1\left(T^A - T^F \right) + \alpha_2\left(RH^A - RH^F \right)_{\text{Daytime}} \quad (1\text{-}1)$$

A similar equation is also used by Pleim and Xiu (2003) to nudge the deep layer soil moisture. The Pleim-Xiu approach has been widely used and in recent California inter-comparisons performed better than the Noah complex land surface model (Fovell 2013). Because observed NWS observations are coarse we replace the NWS observed temperatures with satellite skin temperatures, i.e.

$$\Delta w_G = \beta_1 (T_s^{Sat} - T_s^{Mod})_{Morning} \quad (1\text{-}2)$$

We note that the use of skin temperatures is consistent with the Pleim-Xiu assumption that moisture is related to 2-m temperatures and we make the same assumption for skin temperature. We use the technique proposed by McNider et al. (2005) within the Pleim-Xiu model to nudge thermal resistance, C_T, using afternoon/evening skin temperatures (as opposed to the Pleim and Gilliam 2009 of using afternoon/evening temperatures to nudge deep soil temperature) as illustrated by equation (1-3). Here T_S^{SAT} is the satellite observed skin temperature and T_S^{MOD} is the modeled skin temperature.

$$C_T^{NEW} = C_T^{OLD} \frac{\frac{\partial T_S^{SAT}}{\partial t}}{\frac{\partial T_S^{MOD}}{\partial t}} \quad \text{.....(1-3)}$$

See Mackaro et al. (2011) and McNider et al. (2005) for further details.

2. Road Map of the Report

Chapter 2 provides an overview of the utilization of satellite derived insolation in the WRF framework. Insolation is often the largest term in the surface energy budget. Thus, errors in this term can mask other errors. Here is described the use of satellite insolation products to reduce errors in the placement of clouds which is an endemic problem in models.

Chapter 3 provides a description of the evaluation of satellite skin temperature products which will be used for both model evaluation and assimilation. Three skin temperature products are evaluated - the NOAA GSIP product, the ALEXI product and the MODIS product.

Chapter 4 provides a description of the technique to recover a true skin temperature in the Pleim-Xiu model. It also provides the mathematical description used in the moisture and thermal resistance nudging using satellite skin temperatures within the context of the Pleim-Xiu formulation.

Chapter 5 describes the quality assurance (QA) procedures used to remove erroneous skin temperature data that is used in the skin temperature nudging and model evaluation using skin temperatures. Cloud contamination is a major concern for the quality of the skin temperature from satellite observations. QA procedures are used to minimize erroneous data.

Chapter 6 provides the major output of this study which is an evaluation of the improvement in the model performance when satellite skin temperatures are used to adjust moisture and thermal resistance. A statistical evaluation is provided against satellite observed skin temperatures. A detailed analysis of time series from the model is provided for both those points that show improvement and those that do not. It also provides a comparison of the model results with moisture nudging against standard NWS observations of temperature, winds and humidity.

Chapter 7 provides comparisons against special DISCOVER-AQ observations including aircraft observations of skin temperature. It also provides a final evaluation of whether the skin temperature nudging in the Pleim-Xiu model provides an improvement over the Texas Commission on Environmental Quality (TCEQ) Noah land surface model configuration.

Appendix A contains a list of all the acronyms used in this project.

3. References

Anderson, M.C., Norman, J.M., Diak, G.R., Kustas, W.P., and Mecikalski, J.R., 1997. "A two-source time-integrated model for estimating surface fluxes using thermal infrared remote sensing", Remote Sensing Environ., 60, 195-216.

Chen, F., and J. Dudhia (2001), Coupling an advanced land surface-hydrology model with the Penn State-NCAR MM5 modeling system. Part I: Model implementation and sensitivity, *Mon. Wea. Rev.*, 129, 569-585, doi:10.1175/1520-0493(2001)129<0569:CAALSH>2.0.CO;2

Diak, G. R. ,1990: Evaluation of heat flux, moisture flux and aerodynamic roughness at the land surface from knowledge of the PBL height and satellite-derived skin temperatures, J. Agric. For. Meteorol. 52:181-198.

Ellenburg, W.L., McNider, R.T., Cruise, J.F., 2015: , Towards an Understanding of the 20th Century Cooling Trend in the Southeastern US: Biogeophysical Impacts of Land Use Change" submitted to *Earth Interactions*.

Fovell, R. 2013: WRF Performance Issues in the San Joaquin Valley and Southern California. Traversing New Terrain in Meteorological Modeling for Air Quality and Dispersion. U.California Davis. Sept 9-11,2013.

Mackaro, S., R.T. McNider and A. Pour-Biazar, 2011: Some physical and computational issues in land surface data assimilation of satellite skin temperatures. *Pure Appl. Geophys*. Springer Basel AG DOI 10.1007/s00024-011-0377-0

McNider, R. T., W.M. Lapenta, A. Biazar, G. Jedlovec, R. Suggs, and J. Pleim, 2005: Retrieval of grid scale heat capacity using geostationary satellite products: Part I: Case-study application, *J. Appl. Meteor., **88**,* 1346-1360

McNider, R. T., W. B. Norris, D. M. Casey, J. E. Pleim, S. J. Roselle, and W. M. Lapenta: Assimilation of satellite data in regional air quality models XII. Edited by Gryning, Chaumerliac, and Plenum Press, pp. 25-35. 1998.

McNider, R.T., A.J. Song, D.M. Casey, P.J. Wetzel, W.L. Crosson, and R.M. Rabin, 1994: Toward a dynamic-thermodynamic assimilation of satellite surface temperature in numerical atmospheric models. *Mon. Wea. Rev.,* **122,** 2784-2803.

Niu, G.-Y., et al. (2011), The community Noah land surface model with multiparameterization options (Noah-MP): 1. Model description and evaluation with local-scale measurements, J. Geophys. Res., 116, D12109

Noilhan, J., S. Planton, 1989: A Simple Parameterization of Land Surface Processes for Meteorological Models. Mon. Wea. Rev., 117, 536–549

Pitman, A. J. (2003), The evolution of, and revolution in, land surface schemes designed for climate models, Int. J. Climatol., 23, 479–510

Pleim, J. E. and A. Xiu, 1995: Development and testing of a surface flux and planetary boundary layer model for application in mesoscale models. *J. Appl. Meteor.,* **34**, 16-32.

Pleim, J. E. and A. Xiu, 2003: Development of a land surface model. Part II: Data assimilation. *J. Appl. Meteor*., **42**, 1811-1812.

Pleim, Jonathan E., Robert Gilliam, 2009: An Indirect Data Assimilation Scheme for Deep Soil Temperature in the Pleim–Xiu Land Surface Model. J. Appl. Meteor. Climatol., 48, 1362–1376

Rosero, E., Z.-L. Yang, L. E. Gulden, G.-Y. Niu, and D. J. Gochis (2009), Evaluating enhanced hydrological representations in Noah-LSM over transition zones: Implications for model development, J. Hydrometeorol., 10, 600–62

Sellers, P. J., et al. (1997), Modeling the exchanges of energy, water, and carbon between continents and the atmosphere, Science, 275(5299), 502–509

Wagener, T., and H. V. Gupta (2005), Model identification for hydrological forecasting under uncertainty, Stochastic Environ. Res. Risk Assess., 19, 378–387.

Xiu, A. and J. E. Pleim, 2001: Development of a land surface model. Part I: Application in a mesoscale meteorological model. *J. Appl. Meteor*., **40**, 192-209.

Yang, R., and M. A. Friedl (2003), Modeling the effects of three-dimensional vegetation structure on surface radiation and energy balance in boreal forests, J. Geophys. Res., 108, 8615

Chapter 2 Insolation Replacement

1. Introduction

As noted above, insolation is often the largest term in the daytime surface energy budget. Models have difficulty in placing clouds at the correct place and time. As described below, we will be altering uncertain components in the energy budget such as moisture and thermal resistance based on skin temperature differences between the model and satellite observations. Thus, it is imperative that other components such as incoming solar insolation are described as well as possible.

2. Data Collection

In the past the University of Alabama in Huntsville (UAH) group has utilized an insolation data set that it produces in conjunction with the NASA SPoRT group (Haines et al. 2003 and McNider et al. 1995). This product is based on the physical retrieval technique developed by George Diak at the University of Wisconsin (Gautier and Diak 1980) and has been produced in real-time by UAH and NASA SPoRT since the late 1990's. As part of other funded activities it was possible to implement upgrades to the retrieval including the addition of variable atmospheric water vapor. The latter data will be processed for the DISCOVER-AQ period under this project. However, while waiting for this reprocessing, in order to begin the WRF model simulations, it was decided to try a new NOAA GSIP insolation product. Thus, this data have been downloaded from the CLASS data archive for the DISCOVER-AQ period and processed for use in the WRF model. The next section provides an evaluation of this GSIP product compared to other insolation products. The modeling section below describes the first use of this insolation product.

3. Insolation Evaluation

There are four insolation products that have been collected and evaluated under this activity:

(1) The NASA SPoRT product (Haines et al. 2003 and McNider et al 1995). Originally based on the Gautier and Diak (1980) physical retrieval but with some differences including the calculation of a clear sky albedo based on a 20 day hourly minimum brightness.

(2) The NOAA GSIP product. The GSIP product is also a physical retrieval. The products contain upwelling and downwelling shortwave (0.2-4.0 micrometers) and visible (0.4-0.7 micrometers) radiative fluxes at the top of the atmosphere and at the surface, cloud fraction and skin temperature. In addition to these primary products, cloud phase, visible cloud optical depth, outgoing longwave radiation, as well as derived byproducts (composite clear and cloudy reflectances) and ancillary data (total column amounts of water vapor and ozone) are also included. The primary differences in this product and the SPoRT product are believed to be based slightly different assumptions on creating a surface albedo, and column depths of water vapor and ozone.

(3) A new version of the Gautier and Diak (1980) retrieval developed by George Diak at the University of Wisconsin with new improvements such as time varying water vapor as implemented by UAH.

(4) The insolation computed by the WRF model.

Pyranometer data was collected from various points around the U.S. from both the Surface Radiation Budget Network (SURFRAD) and the Soil Climate Analysis Network (SCAN). Figure 2-1 shows scatter plots of the four products against the pyranometer data. The satellite data and model data are pixel/grid averages whereas the pyranometer is a true point measurement. There was some concern with pyranometer data from a Virginia site so it is treated differently.

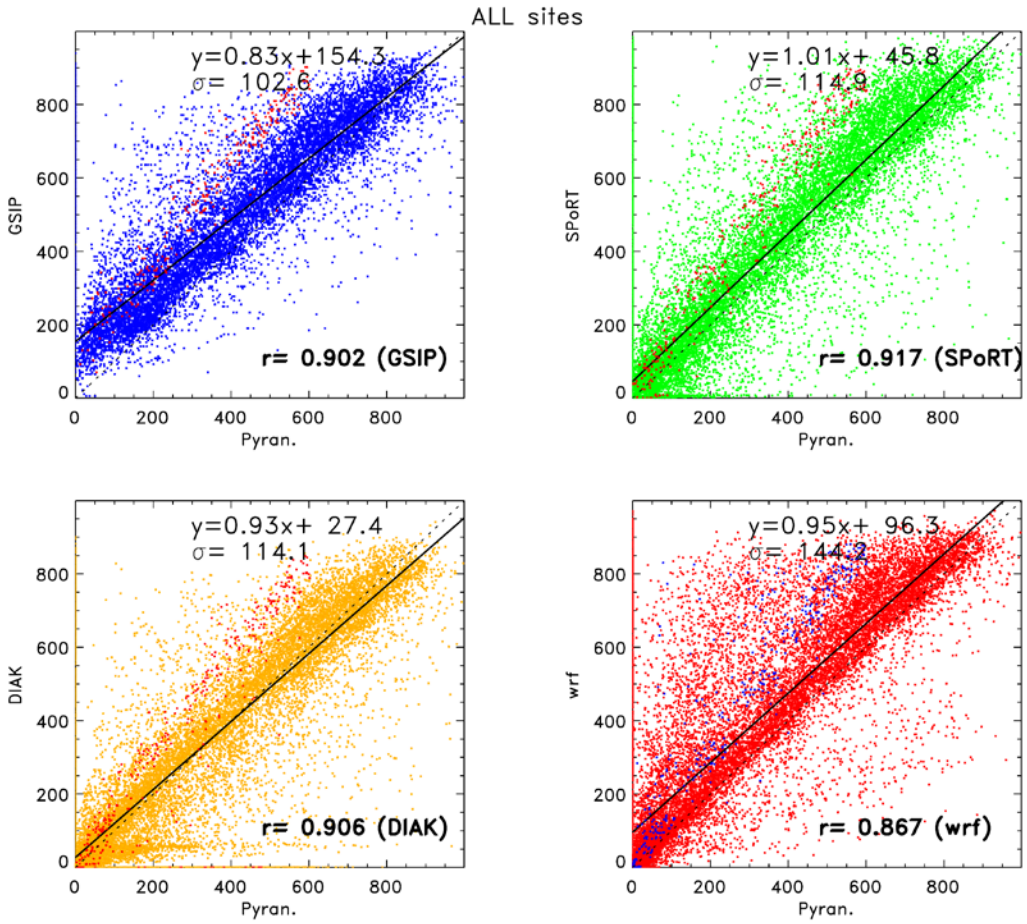

Figure 2-1. Satellite insolation product (and model simulation) versus pyranometer observation. The data points over the Virginia site are plotted in red for GSIP-, SPoRT- and DIAK-pyran. and in blue for WRF-pyran. Dotted line indicates 1:1 ratio. At the top of each plot are the regression equations and the Root Mean Square Errors (RMSE) designated by the "sigma" symbol. The sigma values are in units of W m^{-2}.

There also seemed to be a difference in the satellite data and pyranometer data between the East and West. This is illustrated in Figs. 2-2 and 2-3. In general, satellite products have much less

scatter than the model insolation when compared to pyranometer data in large part because the satellite products have the clouds in the right place.

While the satellite can detect cloud locations there is a need to ensure that clear sky values are consistent with measurements. Figure 2-4 gives a comparison of clear sky values with pyranometer data. It shows very good agreement.

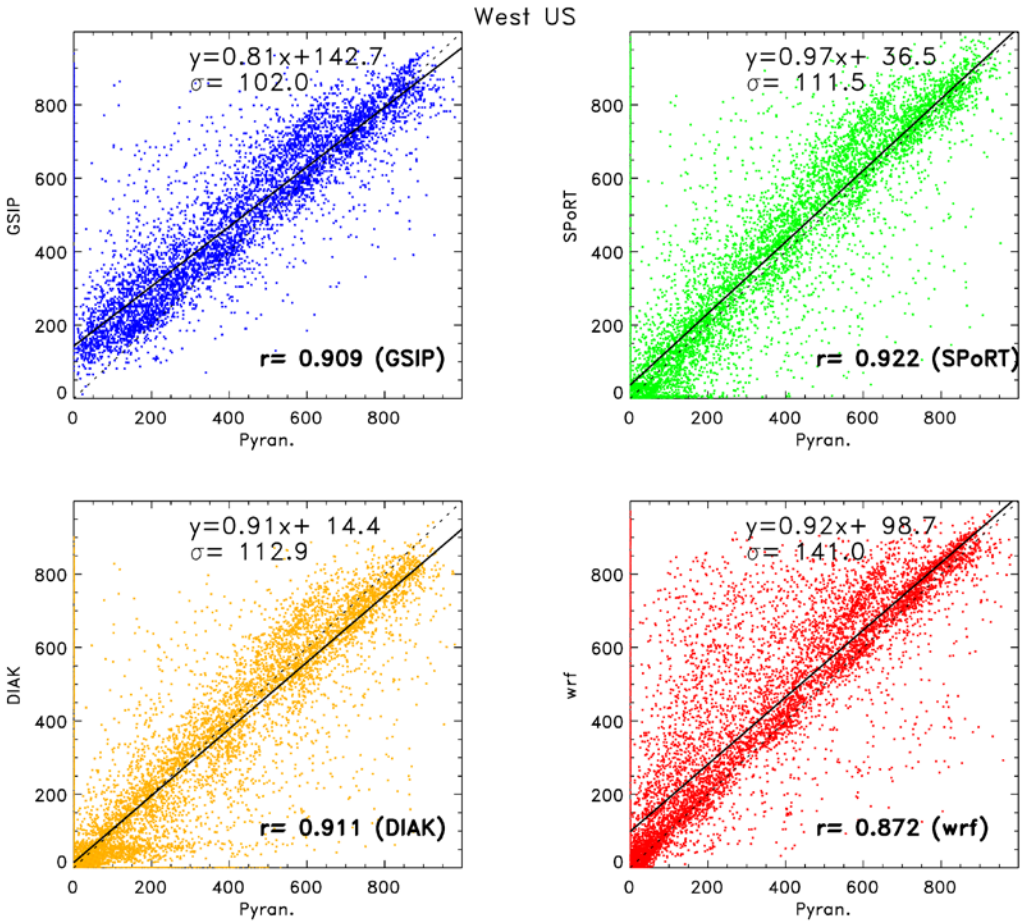

Figure 2-2. Satellite insolation product (and model simulation) versus pyranometer observation for western sites (west of 95^0W). At the top of each plot are the regression equations and the Root Mean Square Errors (RMSE) designated by the "sigma" symbol. The sigma values are in units of W m^{-2}.

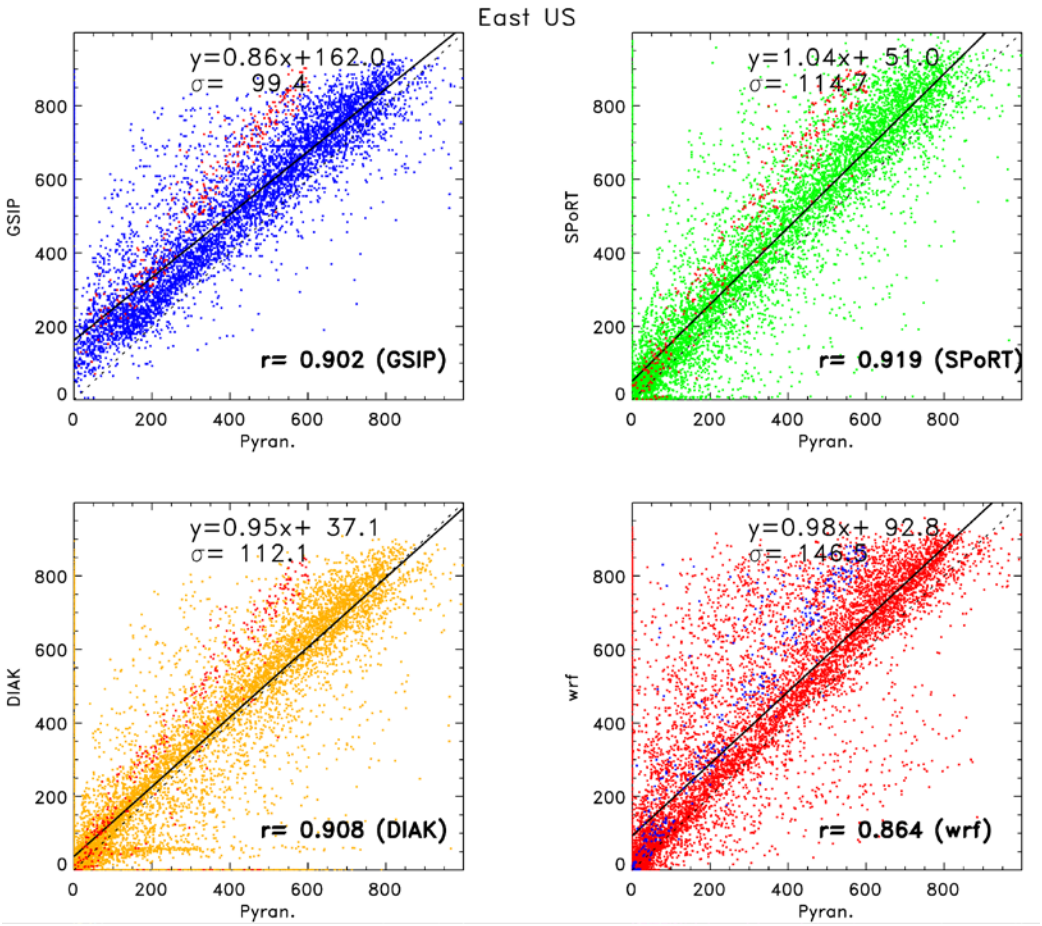

Figure 2-3. Satellite insolation product (and model simulation) versus pyranometer observation for eastern sites (east of 95^0W). At the top of each plot are the regression equations and the Root Mean Square Errors (RMSE) designated by the "sigma" symbol. The sigma values are in units of W m^{-2}.

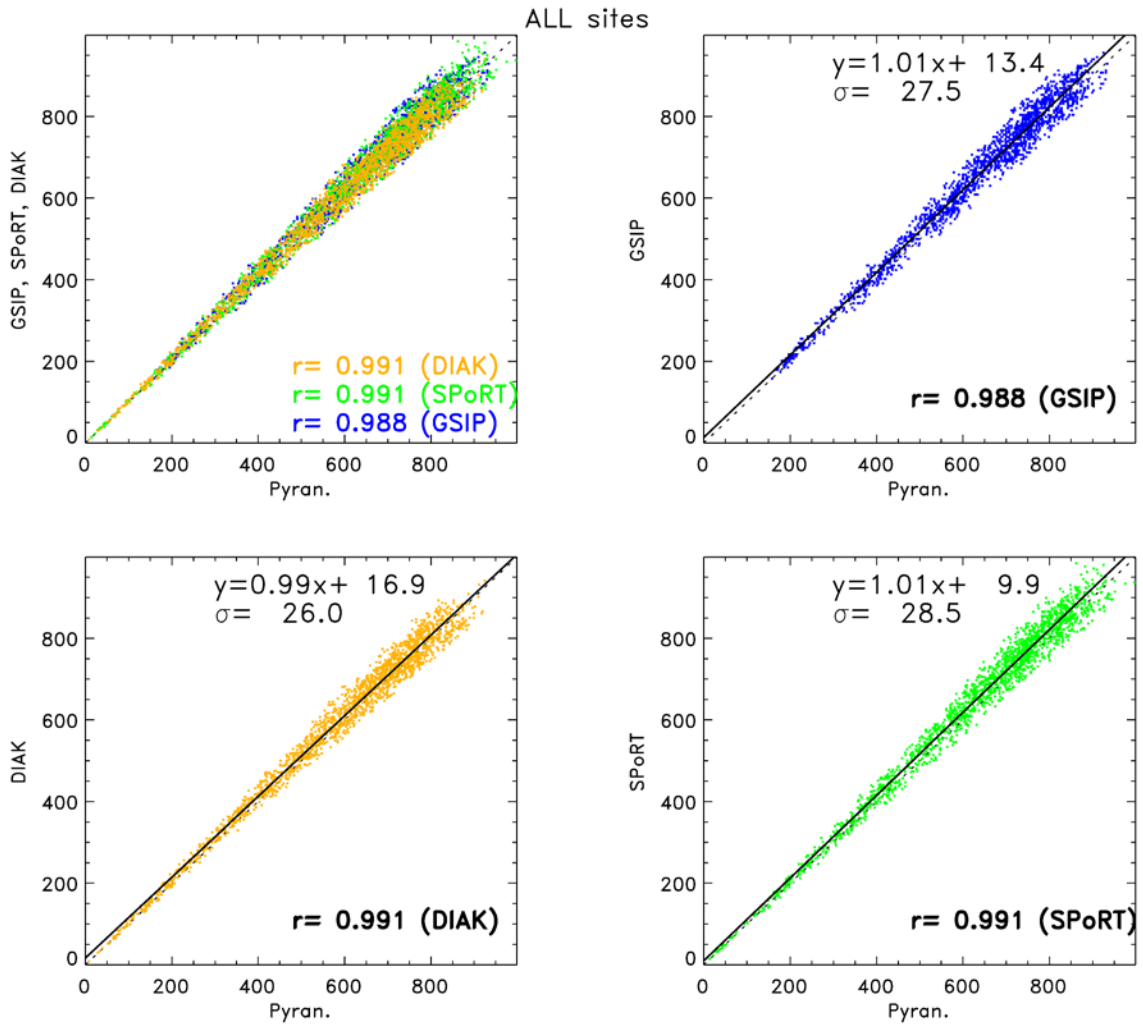

Figure 2-4. Comparison of clear sky satellite insolation with pyranometer data. At the top of each plot are the regression equations and the Root Mean Square Errors (RMSE) designated by the "sigma" symbol. The sigma values are in units of W m^{-2}.

4. Model Insolation Runs

The WRF model was run with and without satellite insolation for the DISCOVER-AQ period (1-30 September 2013). For the results summarized in this section, two consecutive 5.5 day 12-km WRF simulations were performed with a 12-h overlap. The first run covers the period 0000 UTC 1 September 2013 through 1200 UTC 6 September 2013. The second run covers the period 0000 UTC 6 September 2013 through 1200 UTC 11 September 2013. The principal physics choices are summarized in Table 2-1. These runs use a consistent choice of the "Pleim-Xiu" package for the surface layer, land surface, and boundary layer choices. Three-dimensional nudging is performed with a corresponding time scale of about 55 min for temperature and wind but with a smaller water vapor nudging impact with a corresponding time scale of about 28 h. The nudging of soil moisture within the Pleim-Xiu land surface model is activated which uses the 2-m National Weather Service (NWS) observations in an analysis produced by the WRF Preprocessing System (WPS) program "OBSGRID". Version 3.6.1 of the WPS/WRF package is being used.

Table 2-1. Summary of Principal WRF Model Namelist Parameters

Category	Namelist Variable	Namelist Value	Description
Microphysics	MP_PHYSICS	8	New Thompson model
Longwave Radiation	RA_LW_PHYSICS	4	RRTMG model
Shortwave Radiation	RA_SW_PHYSICS	4	RRTMG model
Surface Layer	SF_SFCLAY_PHYSICS	7	Pleim-Xiu surface layer
Land Surface	SF_SURFACE_PHYSICS	7	Pleim-Xiu Land Surface Model
Planetary Boundary Layer	BL_PBL_PHYSICS	7	ACM2 PBL:
Cumulus Parameterization	CU_PHYSICS	1	Kain-Fritsch model
3D Analysis Nudging	GRID_FDDA	1	turned “on”
Wind Nudging	GUV	3.0×10^{-4} s^{-1}	time scale of about 55 min
Temperature Nudging	GT	3.0×10^{-4} s^{-1}	time scale of about 55 min
Water Vapor Nudging	GQ	1.0×10^{-5} s^{-1}	time scale of about 28 h
Pleim-Xiu Soil Nudging	PXLSM_SOIL_NUDGE	0 or 1	run dependent

The WRF model was run with the NOAA GSIP insolation data replacing the model insolation for the first ten days of the DISCOVER-AQ period using the GSIP insolation product. Figure 2-5 (top) shows the average insolation computed from the model radiation model as input into the Pleim-Xiu land surface model over the 10 day model insolation. Figure 2-5 (bottom) shows the average insolation from the satellite product. While the general pattern is similar there are locations where the average difference exceeds 90 W m^{-2} in Figure 2-6. Part of the difference may be due to the radiative parameterization used in the satellite retrieval compared to the model. But larger differences are likely due to cloud differences where the model may have clouds in the wrong place or at the wrong time.

Figure 2-7 shows a scatter plot depiction of the relationship between the model and satellite insolation which shows a large amount of scatter. However, as shown in the right figure, the number of times that the model and satellite are in close agreement is actually very large. The large disagreements are due to the model having incorrect clouds.

While the average change in insolation may not be large over the domain, there are places and times when the differences are large. Figure 2-8 shows the maximum hourly difference between the model insolation and the satellite derived insolation that occurred during the ten day simulation. The large differences occur where the model has clouds which are different from reality as provided by the satellite observation. As discussed below these insolation differences can impact both skin and air temperatures.

Figure 2-9 shows model insolation time series at several locations where the differences were relatively large. These illustrate there may be places where temperatures will be impacted by correcting the insolation field with the satellite product.

As mentioned above there is no question that the satellite data gives a better representation of where clouds occur, but there is some concern that the clear areas are represented well in the satellite product. Both the WRF model insolation and the satellite retrieval are based on similar models of downward radiation starting with a solar constant and using sun angle information which are common in the models. However, there are differences related to assumptions about atmospheric scattering which are likely different from the satellite retrieval method and the WRF model radiative code. To isolate the model radiation differences not due to clouds, we computed the clear sky radiation from the model and made comparisons to the clear sky satellite insolation. Whether the skies were considered clear was based on a clear sky calculation and when the model or satellite was significantly below this value the skies were considered cloudy. Those not cloudy were considered clear. The differences in clear sky insolation are given in Figure 2-10. Figure 2-10 shows that some part of the insolation differences appear to be related to the albedo differences between the model and satellite (because of the spatial pattern which looks like albedo). While it might seem that albedo would not impact insolation (which is the downwelling shortwave radiation to the surface) there is a component (in both the model and satellite retrieval), in which a portion of the radiation reflected from the surface is backscattered to the surface thus contributing to downwelling radiation. Other reasons for clear sky differences are assumptions about clear sky scattering/absorption, which depend on parameterizations or specification of atmospheric constituents such as water vapor and ozone.

5. Impact on Temperatures

This local large difference in insolation discussed above can have a major impact on surface skin temperatures and near surface air temperature. The skin temperatures then impact surface heat fluxes so that boundary layer heights and turbulence are impacted. However, some of the bigger air quality temperature impacts are on biogenic and anthropogenic evaporative hydrocarbon emissions, which are nonlinearly dependent on temperature. Additionally, thermal decomposition of nitrogen species is highly dependent on temperature and can impact the slopes of Ozone/NO_y relations and the efficiency of NO_x control strategies.

Figure 2-11 shows the average difference in 2-m air temperatures between the model simulations with and without satellite insolation. This illustrates the impact that solar insolation can have on temperatures. Because clouds are variable in space and time the average impact is not large. But on certain days the cloud impact can be large. Figure 2-12 shows the maximum difference in temperatures during the ten day simulations. These are quite large. Because air quality standards such as ozone are based on events rather than long term averages, these large variations on specific times and at specific places can be very important in developing realistic recreations of the physical atmosphere in SIP modeling. Figure 2-13 provides a time series of model skin temperature and air temperature for the places given in where insolation differences were relatively large. It shows that insolation differences can impact air temperatures and skin temperatures.

6. Evaluation against NWS 2- meter temperature observations

Initial comparisons were made to NWS observables such as 2-m temperatures. However, this is difficult since the NWS observations are coarse and cloud scale changes may often be felt in places where observations do not exist. Thus, it is perhaps best to simply view the differences as point representations as in Figs. 2-14 through 2-16.

Figure 2-14 shows the difference between the WRF grid point values of 2-m temperatures minus NWS observations for the control case (WRF insolation). Figure 2-15 shows the same plot except for the insolation case. While there are many places where the model is better with the satellite insolation, there are also places where the model is worse than the control case. Below is the definition in bias used.

$$B_C = \left| \frac{1}{n} \sum_{t=1}^{n} \left(T_{WOI} - T_{OBS} \right) \right| \tag{3-1}$$

$$B_{WI} = \left| \frac{1}{n} \sum_{t=1}^{n} \left(T_{wI} - T_{OBS} \right) \right| \tag{3-2}$$

Here, B_c is the bias in the control case (without satellite insolation) and B_{WI} is the bias with satellite insolation replacement.. T_{WOI} is the model 2-m temperature without satellite insolation and TwI is the model temperature for the case with satellite insolation replacement. T_{OBS} are the NWS 2m observed temperatures. Figure 2-16 synthesizes this by showing the differences in magnitude of the bias between the insolation and control runs. It shows that there are improvements in some places but the majority of points show an increase in bias with the satellite insolation. This is somewhat unexpected given the better performance of the satellite products versus pyranometer data.

7. References

Gautier, C., G.R. Diak, S. Mass, 1980: A simple physical model for estimating incident solar radiation at the surface from GOES satellite data. *J. Appl. Meteor.* , **19**, 1005-1012.

Haines, S. L., G. J. Jedlovec, and R. J. Suggs (2003). The GOES Product Generation System. NASA Technical Memorandum, Marshall Space Flight Center

McNider, R.T., A. Song, and S.Q. Kidder, 1995: Assimilation of GOES-derived solar insolation into a Mesoscale model for studies of cloud shading effects. *Int. J. Remote Sens.,* **16,** 2207-2231.

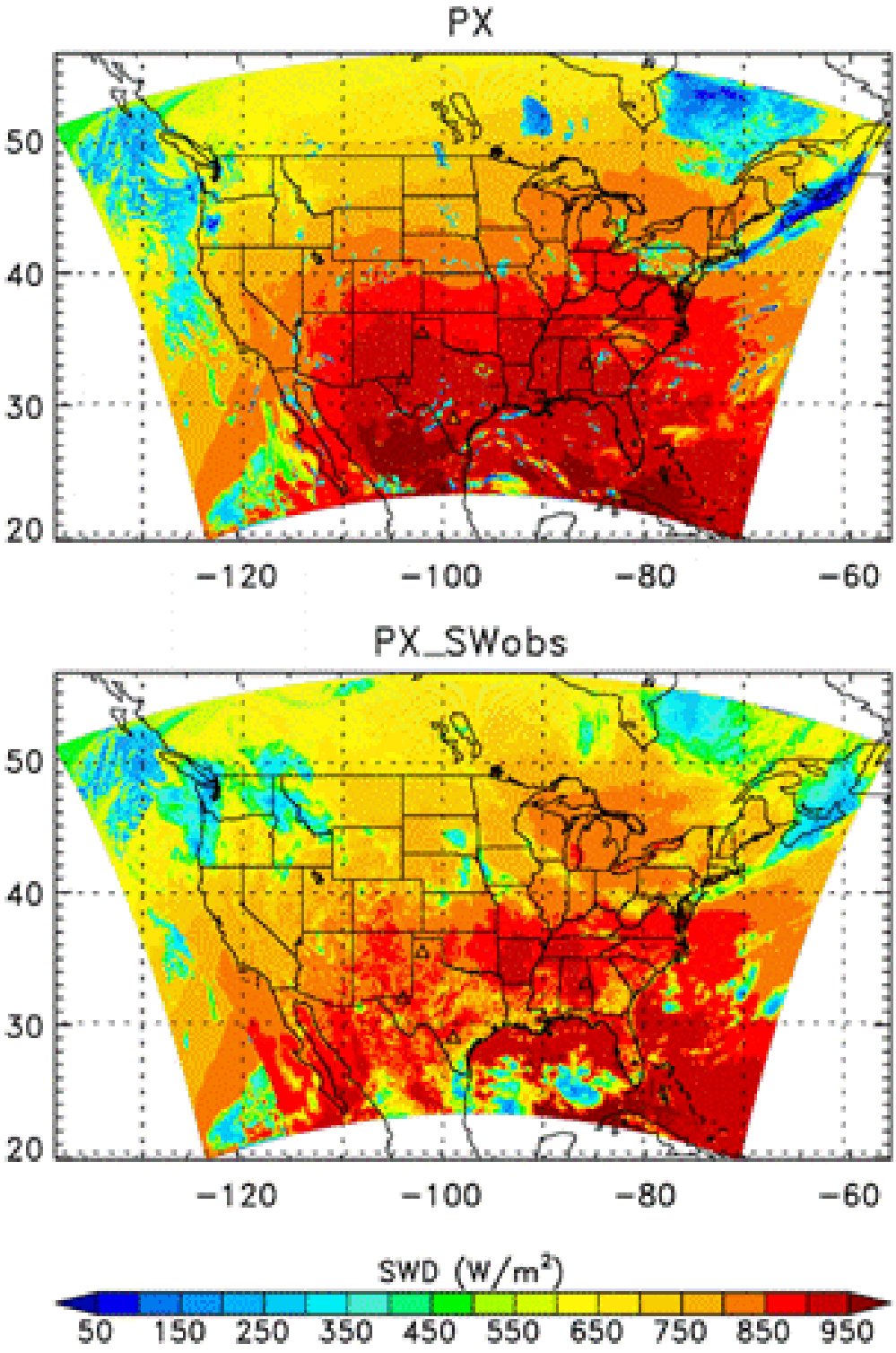

Figure 2-5 (Top) The insolation computed by the WRF model and (bottom) the insolation from the NOAA GSIP data. Note PX refers to the Pleim-Xiu model (or the model insolation) and SWobs refers to satellite derived insolation.

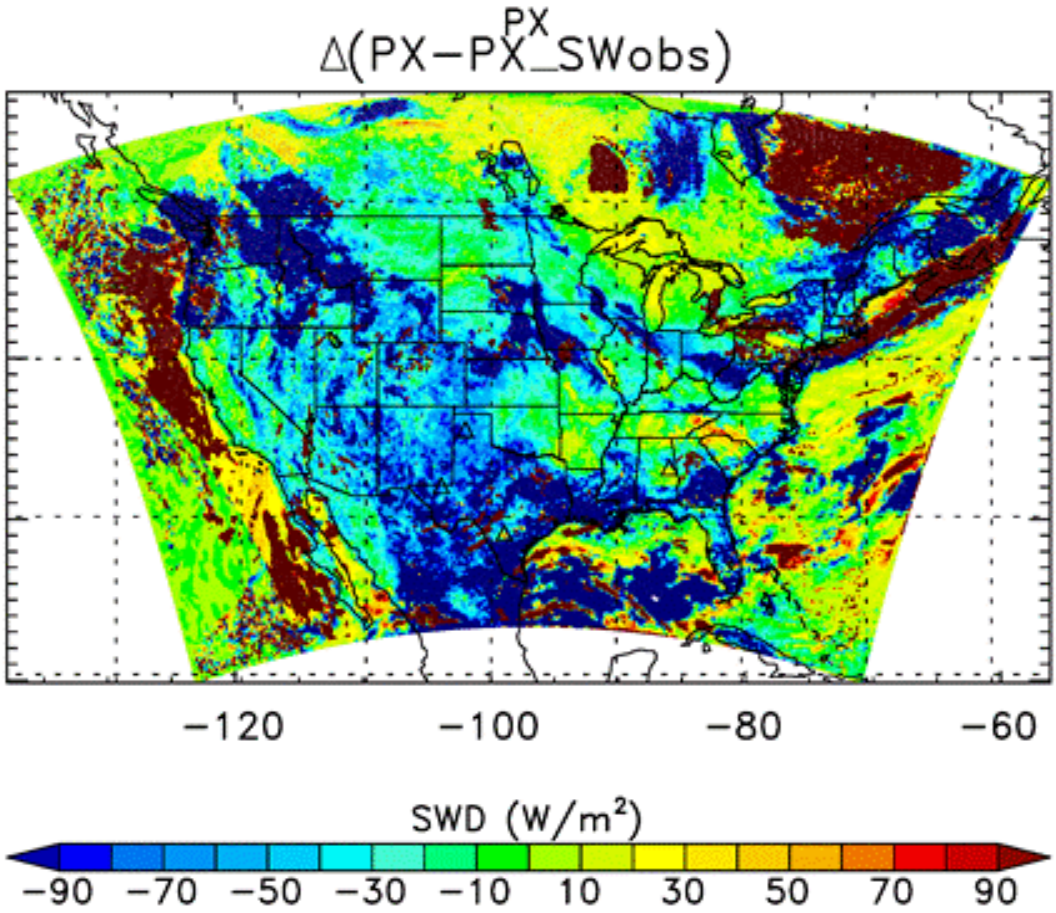

Figure 2-6. *The average difference in insolation between the model and satellite insolation in Figure 2-5 above. Note PX refers to the Pleim-Xiu model (or the model insolation) and SWobs refers to satellite derive insolation.*

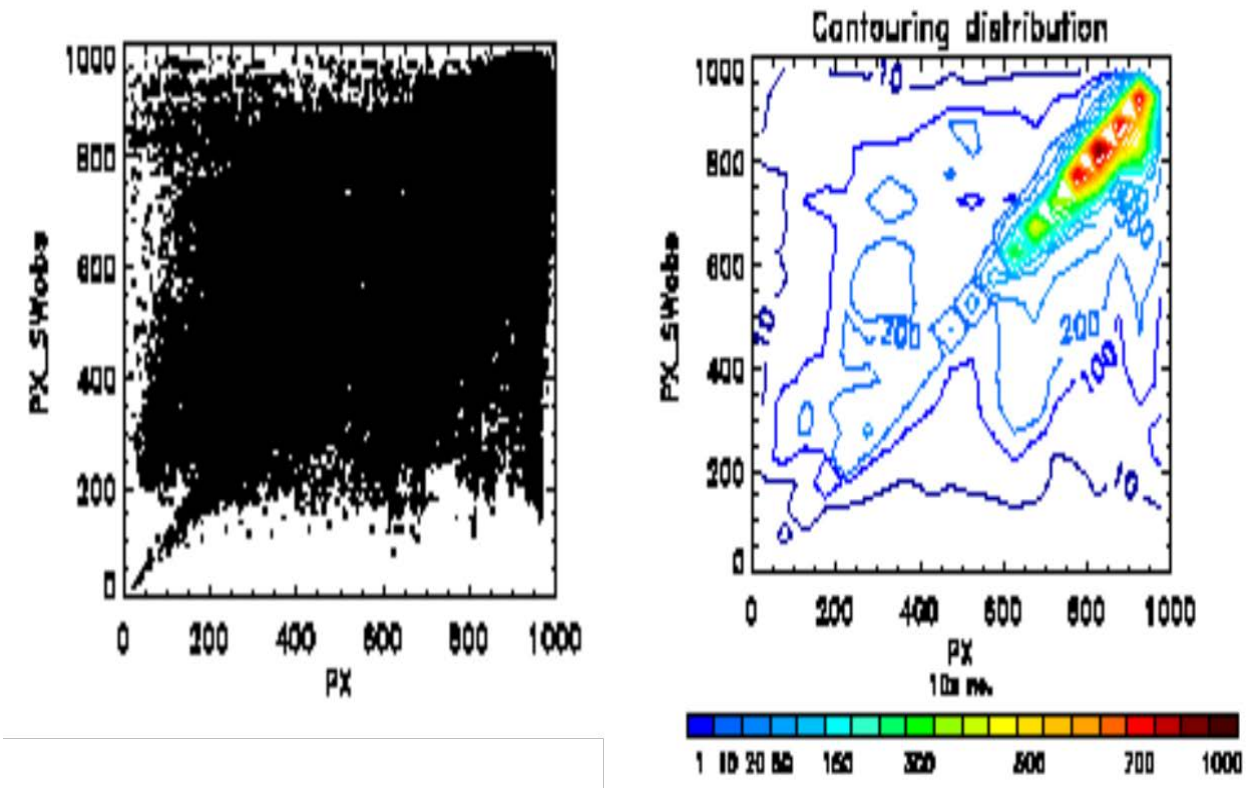

Figure 2-7 (left) scatter plot showing relationships between satellite insolation (px-SWobs) and WRF model insolation for every hour during the ten day simulation. Note the large scatter due to different cloud locations between the model and reality. However, the saturation of points hides the fact that overall (in mostly clear sky conditions) the model and satellite insolation agree. This is shown in the contour plots of the points (right).

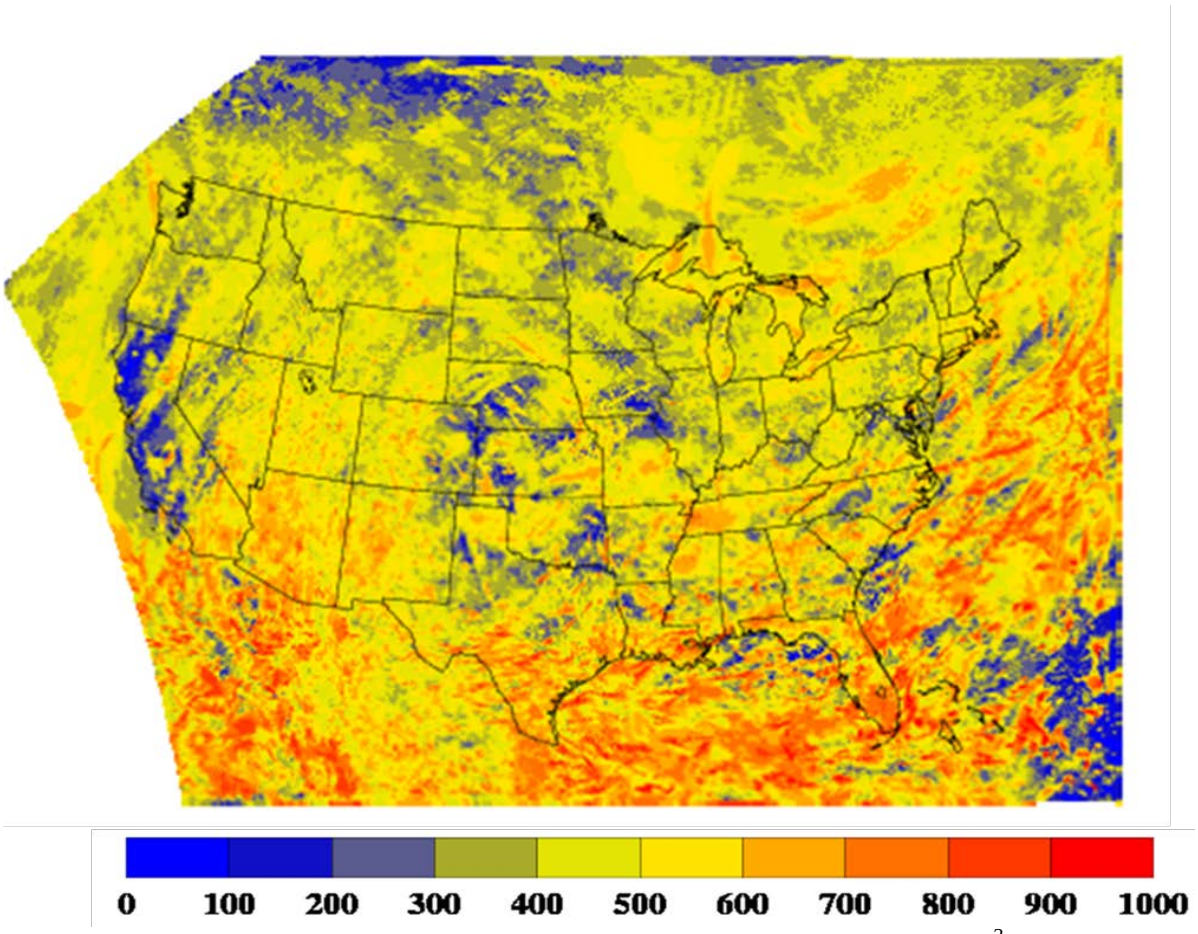

Figure 2-8. Maximum hourly daytime difference (magnitude, in units of W m^{-2}) in downward shortwave radiation between the control WRF simulation and the GSIP insolation for the period 0000 UTC 1 September 2013 through 0000 UTC 11 September 2013.

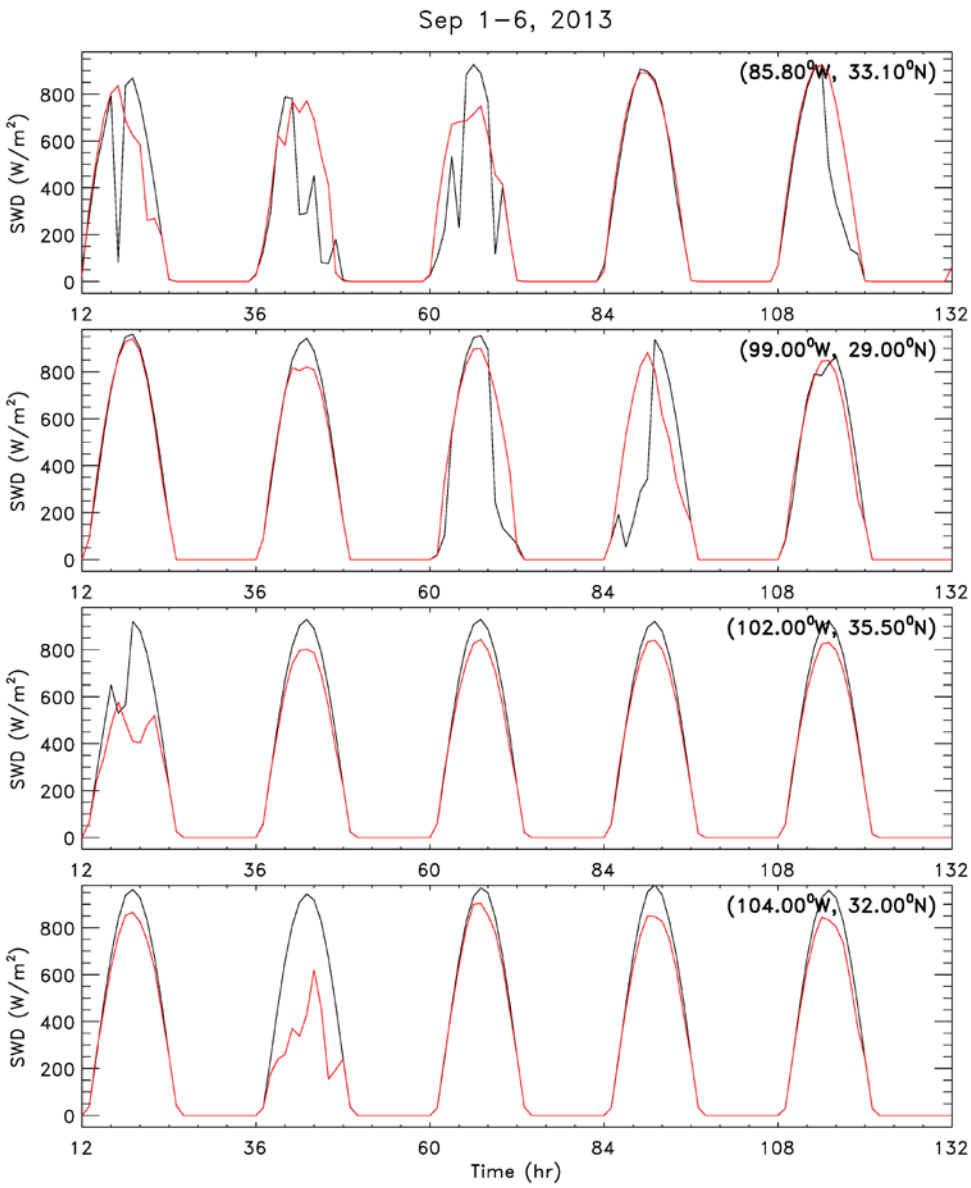

Figure 2-9 Downward shortwave radiation at 4 selected locations. Black line is for the model insolation simulation and red line for the satellite insolation simulation. The 4 locations, in order, are: West of Birmingham Alabama (positive bias), West of Houston (positive bias), Northern Texas (negative bias), Western Texas (negative bias). Bias here is defined as satellite shortwave minus the model shortwave.

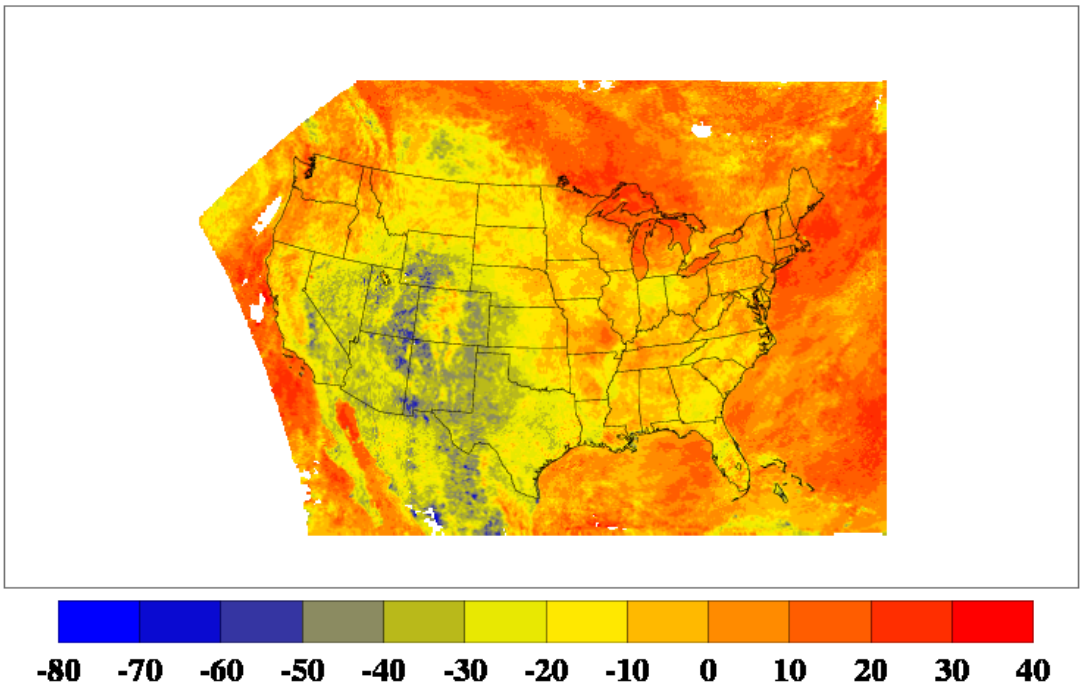

Figure 2-10. Average difference between satellite-observed and model insolation for clear conditions. Units are Watts m^{-2}. Positive numbers indicate observed values higher than the model values.

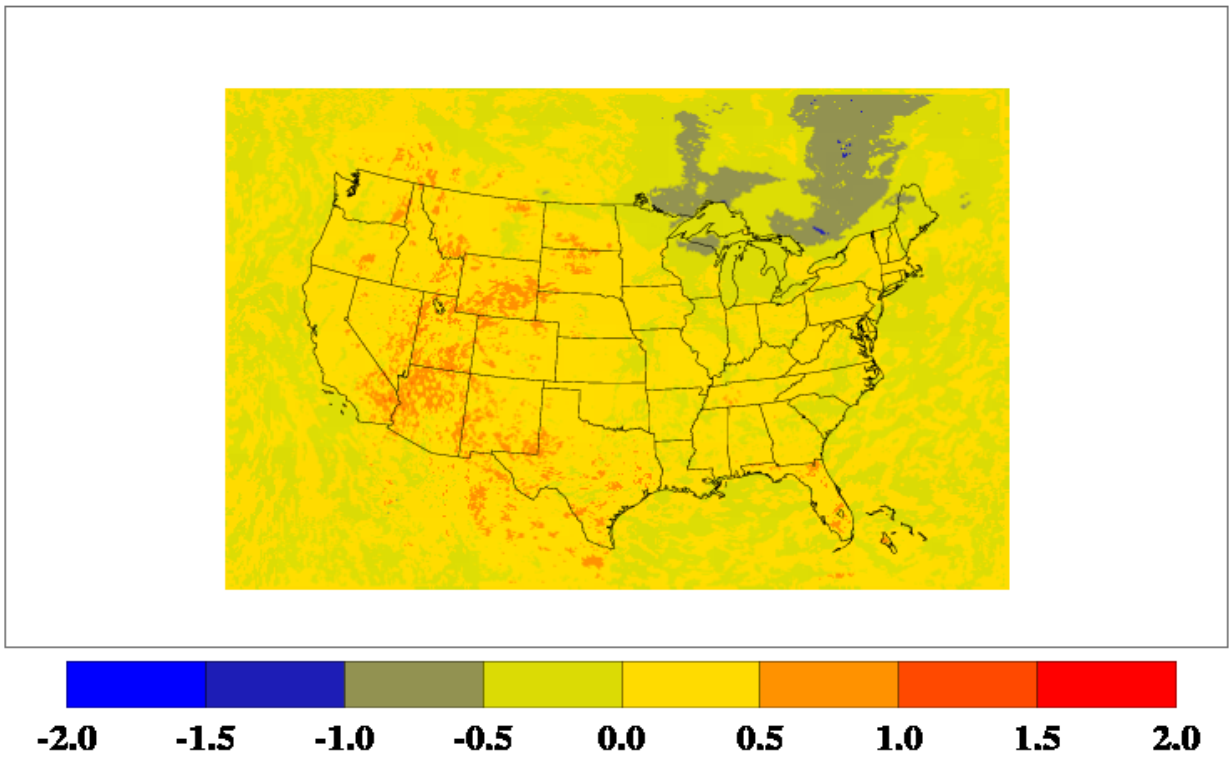

Figure 2-11. Mean hourly daytime difference (model insolation minus satellite insolation runs, in units of K) of 2-m temperature for the period 0000 UTC 1 September 2013 through 0000 UTC 11 September 2013. In general in the eastern U.S. the satellite insolation run is warmer than model insolation run while in the west it is cooler.

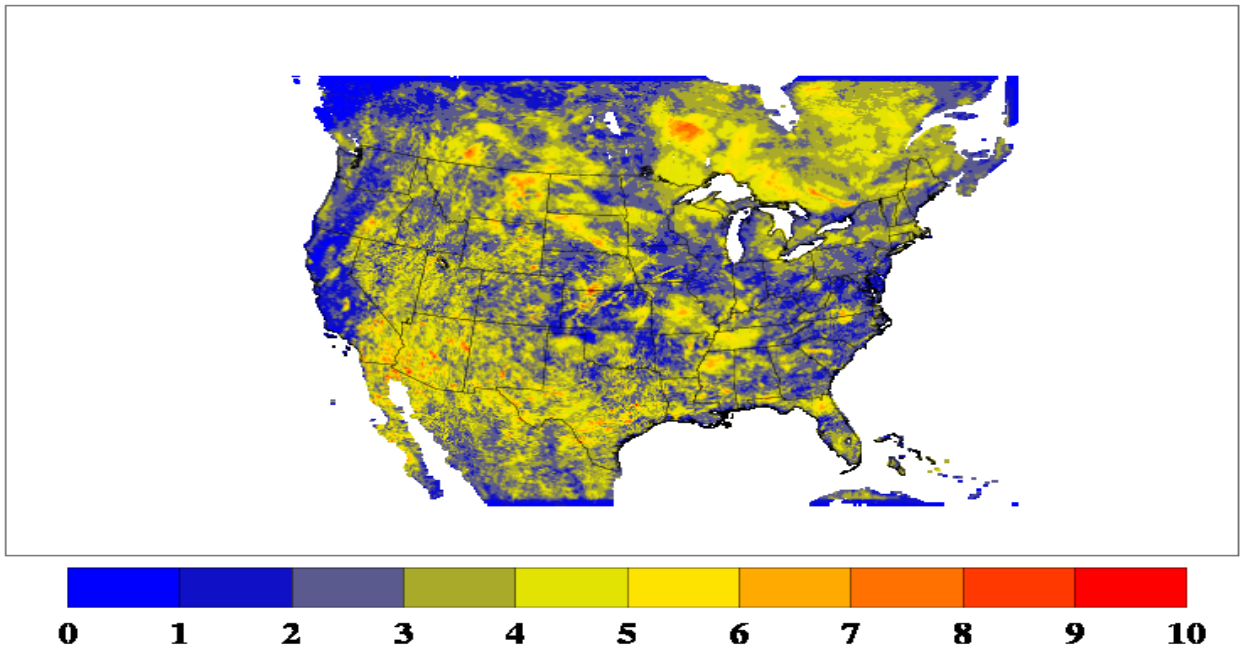

Figure 2-12. Modeled maximum absolute difference in air temperature between the WRF insolation and satellite-derived insolation.

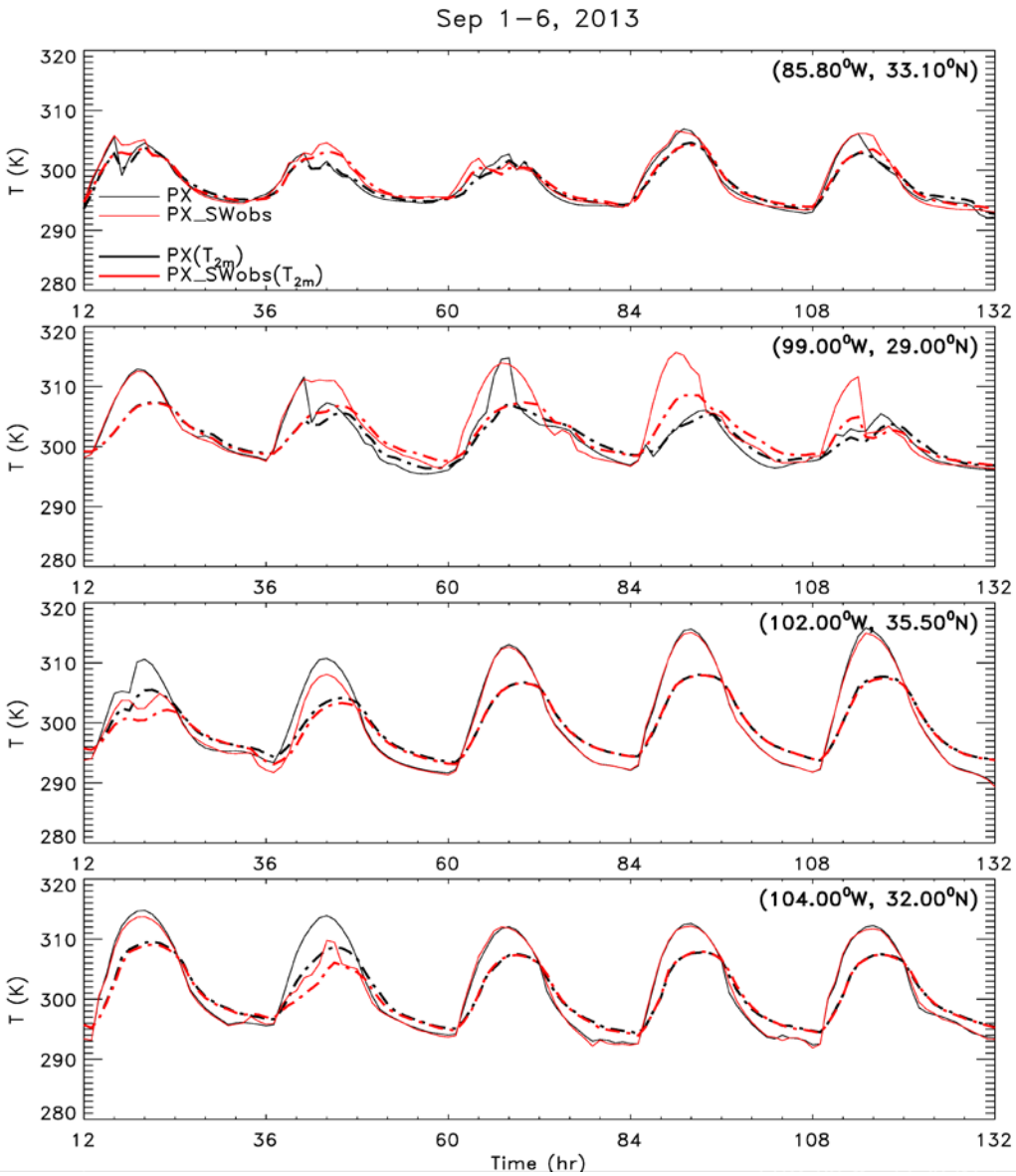

Figure 2-13. Model simulations of skin temperature and air temperature for the locations in Figure 2-9. Solid lines give skin temperature and dashed lines the 2-m air temperature. Black is for the WRF model insolation and red is for the satellite derived insolation.

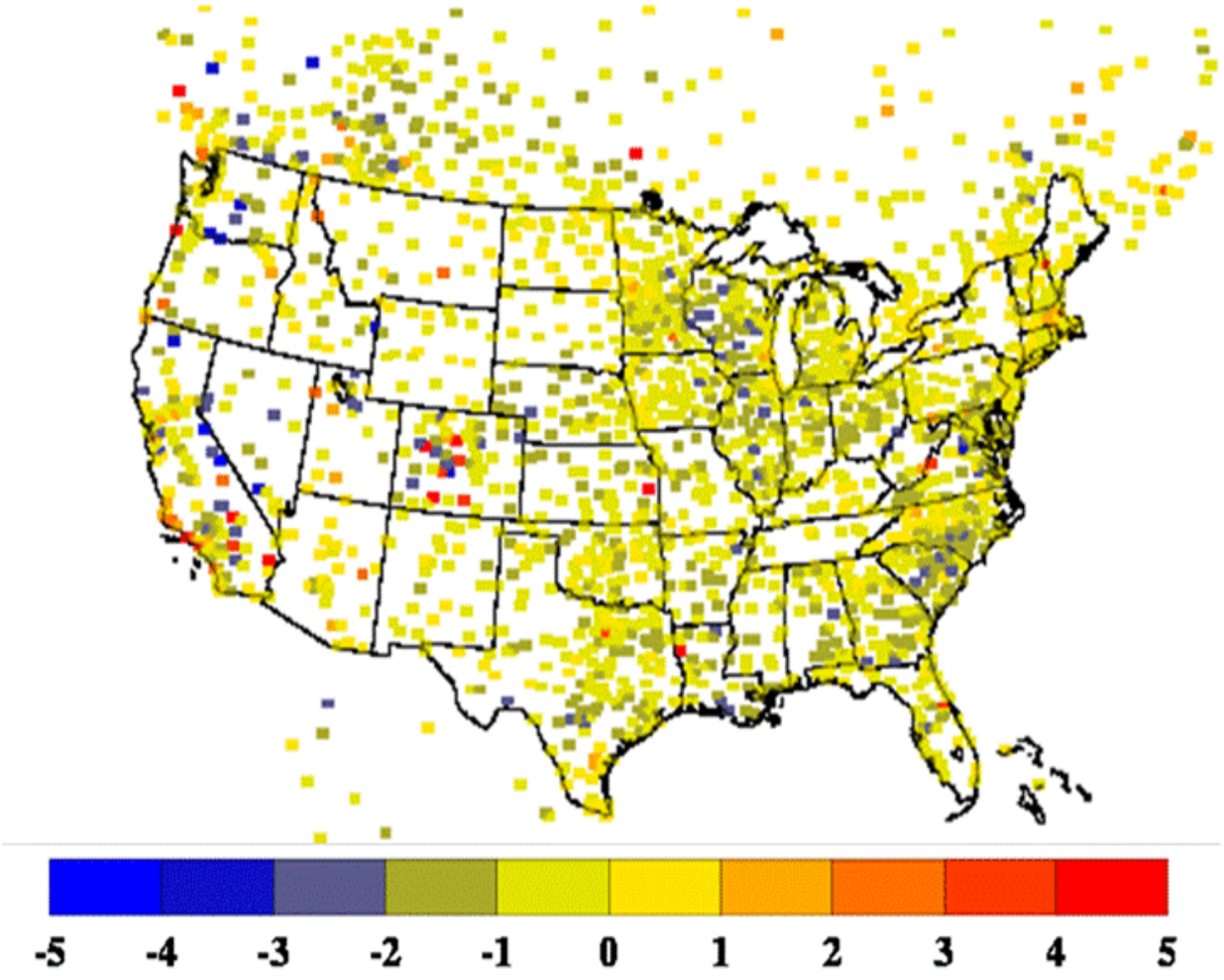

Figure 2-14 Mean daytime bias (model insolation minus satellite observed) of 2-m temperatures at observations locations for the WRF control run for the period 0000 UTC 1 September 2013 through 0000 UTC 11 September 2013

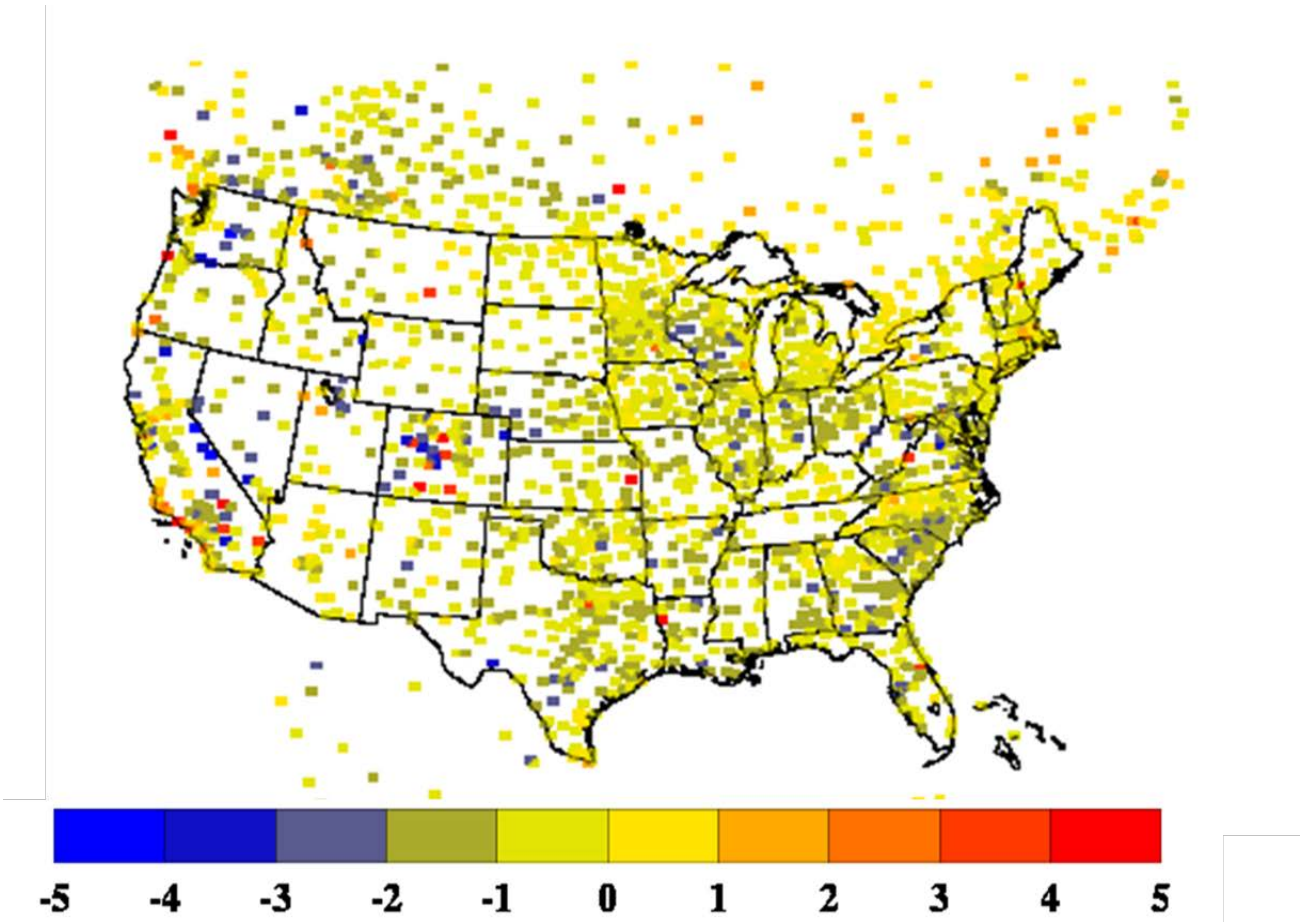

Figure 2-15 Mean daytime bias (model insolation minus satellite insolation) of 2-m temperatures at observations locations for the WRF satellite insolation run for the period 0000 UTC 1 September 2013 through 0000 UTC 11 September 2013.

.

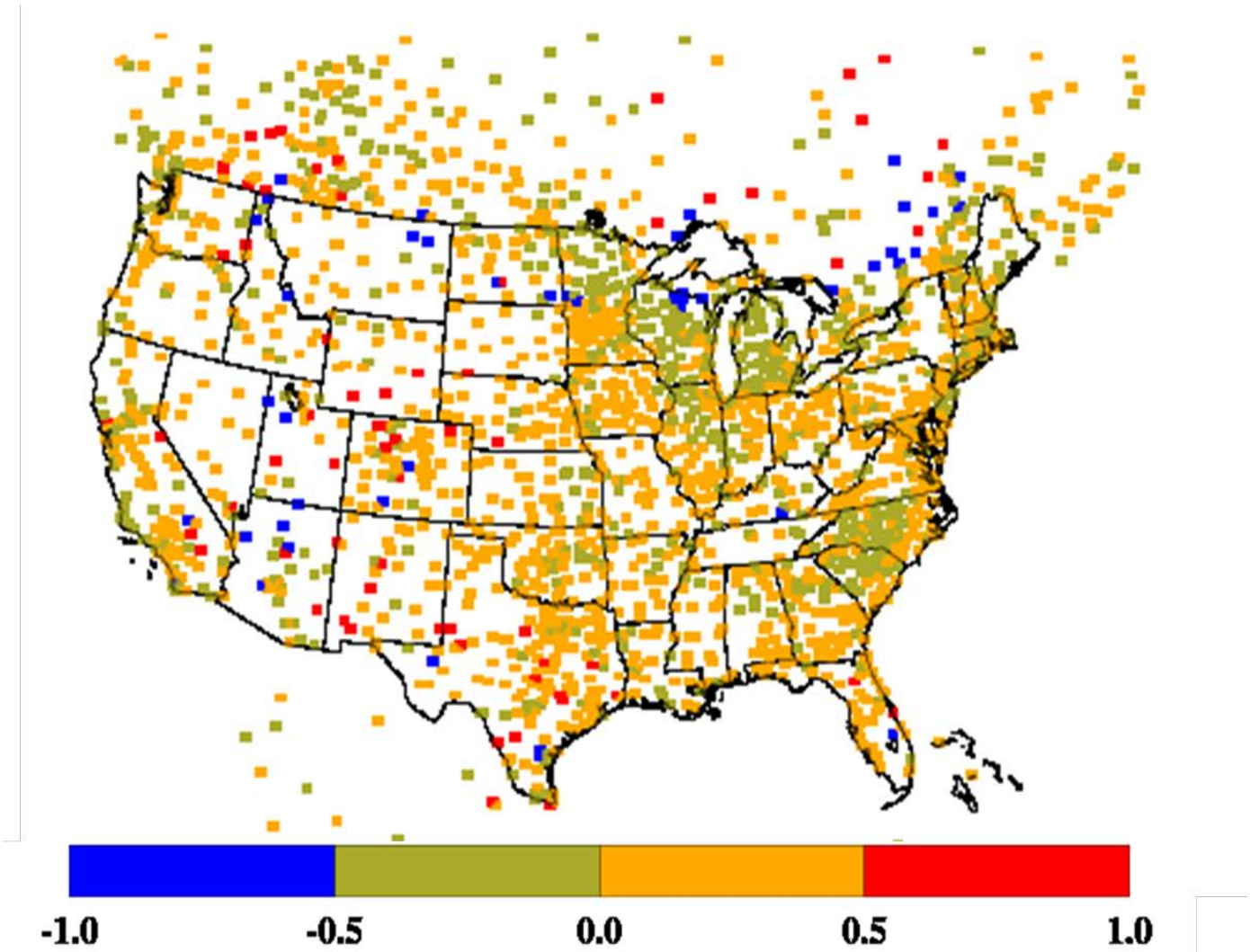

Figure 2-16 Daytime change in bias (| |Bi| – |Bc| |) in units of K at surface observation locations. If |Bi| < |Bc| then the change is given a negative value. Yellow through red colors indicate an increase in bias, whereas green through blue indicate a decrease in bias. Based on the WRF simulations for the period 0000 UTC 1 September 2013 through 0000 UTC 11 September 2013.

.

Chapter 3 Satellite Skin Temperature Evaluation

1. Introduction

As part of this project, it was proposed that satellite skin temperatures might be a better metric for land surface model performance evaluation than standard National Weather Service (NWS) data in large part because of their ability to capture land use variations at fine resolution. Also, satellite skin temperatures are to be used to adjust soil moisture in a revised version of the Pleim-Xiu (PX) model in a similar way that observed 2-m air temperatures are used to adjust moisture in the current PX model. However, skin temperatures as derived from satellite information have potential issues in terms of assumptions about surface emissivity and corrections for intervening atmosphere and cloud contamination. Under this activity the NOAA GSIP product is evaluated for its potential use as a model evaluation metric and as a means to nudge moisture. As seen below the GSIP product has significant issues in the West. In place of the GSIP product another NOAA skin temperature product produced by the ALEXI group is evaluated. This chapter also provides a first comparison to the skin temperatures from the DISCOVER-AQ NASA aircraft.

2. Satellite Skin Temperature Products

Under this activity we provide initial inter-comparisons of three satellite Land Surface Temperature (LST) products – these are the GSIP product (Heidinger et al 2013, see also data links NOAA GSIP Data), a physical split window technique (Haines et al. 2001, Guillory et al. 1993) produced locally at the Marshall Space Flight Center (MSFC) and referred to as the SPoRT product, and the MODIS operational product (see Wan and Dozier 1996 and updates). The GSIP product was initially chosen as the primary data set to be used because it had complete coverage of the Contiguous United States (CONUS) and was an operational product supported by NOAA. The locally produced MSFC product only used GOES- EAST so that western areas beyond the Rockies were not included in the product. The MODIS product also only has 4 times a day coverage between the Terra and Aqua Platforms.

However, as seen in the comparisons below, the GSIP product appeared to have afternoon values in the western U.S. too large to be physically correct. Figures 3-1 and 3-2 show time series of the skin temperatures that gave concern, along with other measures of temperature. They show afternoon temperatures much too large compared to surface air temperatures. Temperatures in the East (Figs. 3-3 and 3-4) show more reasonable values and the expected consistency between the SPoRT product and 2-m air temperatures.

After these differences came to light, the patterns and consistency of these large skin temperatures were further evaluated. There are several in-situ sites in the Eastern U.S. which measure skin temperature by using a downward IR radiometer. As part of the evaluation Figure3-5 shows time series comparisons of the satellite skin temperatures (MODIS and GSIP) and WRF skin temperatures using the skin temperature retrieval in the Pleim-Xiu model (see Chapter 4) against these sites. The GSIP comparison here looks close to the MODIS values (within a degree or so) for these selected points but as noted later has larger differences in the West. For most of the Eastern sites, the GSIP is within a couple of degrees compared to the in-situ observations as does the MODIS LST product. It is noted that the WRF retrieved skin temperature seems consistent except for days such as September 21 and 22 when obviously

clouds are present at the in-situ site but not in WRF (this WRF run did not include the satellite insolation).

3. Spatial Comparisons

While the GSIP and SPoRT Skin temperature data are based on GOES data, the MODIS Land Surface Temperature (LST) also provides an independent measure of skin temperature. Figures 3-6 and 3-7 provide a spatial comparison between the WRF and GSIP skin temperatures for the two day-time passes of the MODIS LST for two days (September 22, 24) when skies were relatively clear over Texas. Consistent with the time series data, the extreme high skin temperatures found (> 330 K) in GSIP are not seen in MODIS. GSIP values are within a few degrees or so over the Eastern U.S. to MODIS, but very different (5-20 degrees) with very high extreme values over portions of Mexico and west Texas. The MODIS cloud mask might have missed some cloudy pixels along the Texas and Louisiana coast on Sep 24. These two days give concern that over the western part (perhaps high altitude) part of the domain that GSIP skin temperatures are problematic.

Figure 3-8 shows the average difference for the month of September between GSIP skin temperatures and WRF derived skin temperatures. They show that the differences in GSIP temperatures and WRF with higher temperaturesin GSIP in the western part of the domain are consistent. Figure 3-9 shows a similar plot using the SPoRT skin temperature, which does not show the consistent high skin temperatures found in the GSIP skin temperatures.

The GSIP high temperatures in the western part of the domain are troubling and will have to be dealt with (see section 4below). However, Figure 3-10 shows that in the East the differences in skin temperature between GSIP and the WRF model correspond to differences tied to land use. This image may indeed show that our proposed path of using differences between model and skin temperatures can be used to adjust moisture. Note that in the agricultural regions of the Mississippi Delta, Iowa, Illinois, and Indiana, GSIP temperatures are higher than WRF. In these areas the crops have stopped transpiring (and in the Delta irrigation has stopped). This may be the case where the nudging technique would decrease soil moisture levels causing model temperatures to increase. The opposite would occur in the heavily forested regions of the Appalachians where WRF may have moisture levels too low.

4. NOAA ALEXI Skin Temperature

The NOAA/U. S. Department of Agriculture (USDA) ALEXI group has employed a skin temperature technique to adjust moisture (Anderson et al. 2007a, Anderson et al. 2007b). Chris Hain of the ALEXI group has kindly provided their single channel retrieval of skin temperature for 1 September to 1 October 2013 and it has been processed for input to the model. A comparison similar to that above for GSIP was performed. Figure 3-11 provides an example of two days of these comparisons. It shows that the ALEXI product does not appear to have the high temperatures in the West seen in the GSIP product and has much greater agreement with the MODIS product. Based on these comparisons, the skin temperature to be used in the moisture nudging and model evaluation will be the NOAA ALEXI product. Chapter 5 provides additional quality assurance techniques for this data set.

5. Statistical Comparisons

In addition to spatial and time series variations, standard statistical comparisons can provide quantitative information. The bias is defined as difference of the means

$$Bias = 1/N \sum (T1\ (i,j) - T2(i,j))$$

and root mean standard error is

$$RMSE = sqrt\ \left(\frac{1}{n}\right) sqrt\ ((\ \sum \left(\left(T1\ (i,j) - T2(i,j)\right) ** 2\right))$$

where T1 and T2 are two skin temperature variables to be compared and the sums are over all i,j grids.

The Root Mean Square Error (RMSE) between the WRF skin temperature and either the MODIS values (see Figure 3-13) or the ALEXI values (see Figure 3-14) are on the order of 4-5 K, whereas the RMSE between the MODIS and ALEXI values (see Figure 3-12) is only on the order of 2 K. This indicates what might be the irreducible error given the uncertainty between two satellite skin temperature data sets. This provides evidence that with additional improvement in land surface parameters (e.g. soil moisture or thermal resistance) that the scatter in model performance can perhaps be further reduced before we reach the limit of irreducible uncertainty.

6. Summary and Conclusions

The GSIP data set, which was initially proposed for use in the present investigation, was shown to have unrealistic skin temperatures in the West. The dual channel skin temperature product by SPoRT/MSFC has a coarser resolution and only uses GOES-East so it does not adequately cover the west coast. For these reasons, under the present project we will use the GOES single channel skin temperature product produced by the NOAA ALEXI group. As shown above, it appears to not suffer from high temperatures in the West like the GSIP product. It also compares well with the independent MODIS polar orbiter skin temperatures. Data for the month of September has been obtained and additional quality assurance procedures are described in Chapter 5.

The Root Mean Square Error (RMSE) between the WRF skin temperature and either the MODIS or the ALEXI are larger than the RMSE between the MODIS and ALEXI values. This provides hope that improvement of the specification of land surface parameters could lead to improvement in model performance. This is the goal of this project and these results are given in Chapter 6.

7. References

Anderson, M.C., Norman, J.M., Mecikalski, J.R., Otkin, J.A. and Kustas, W.P., 2007a. A climatological study of evapotranspiration and moisture stress across the continental United States based on thermal remote sensing: 1. Model formulation. J. Geophys. Res., 112(D10): D10117.

Anderson, M.C., Norman, J.M., Mecikalski, J.R., Otkin, J.A. and Kustas, W.P., 2007b. A climatological study of evapotranspiration and moisture stress across the continental United States based on thermal remote sensing: 2. Surface moisture climatology. J. Geophys. Res., 112(D11): D11112.

Guillory, A. R., G. J. Jedlovec, and H. E. Fuelberg, 1993: A technique for deriving column-integrated water content using VAS split window data. J. Appl. Meteor.,32,1226–1241

Haines, S. L., R. J. Suggs, and G. J. Jedlovec, 2001: Inter-comparison of GOES-8 Imager and Sounder skin temperature retrievals. Preprints, 11th Conf. on Satellite Meteorology and Oceanography, Madison, WI, Amer. Meteor. Soc., 516-519.

Heidinger, A. K., I. Laszlo, C. C. Molling, and D. Tarpley (2013), Using SURFRAD to Verify the NOAA Single-Channel Land Surface Temperature Algorithm, J. Atmos. Oceanic Technol., 30(12), 2868-2884, doi:Doi 10.1175/Jtech-D-13-00051.1.

Wan, Z., and J. Dozier, 1996: A generalized split-window algorithm for retrieving land-surface temperature from space.IEEE Trans. Geosci. Remote Sens.,34,892–905.

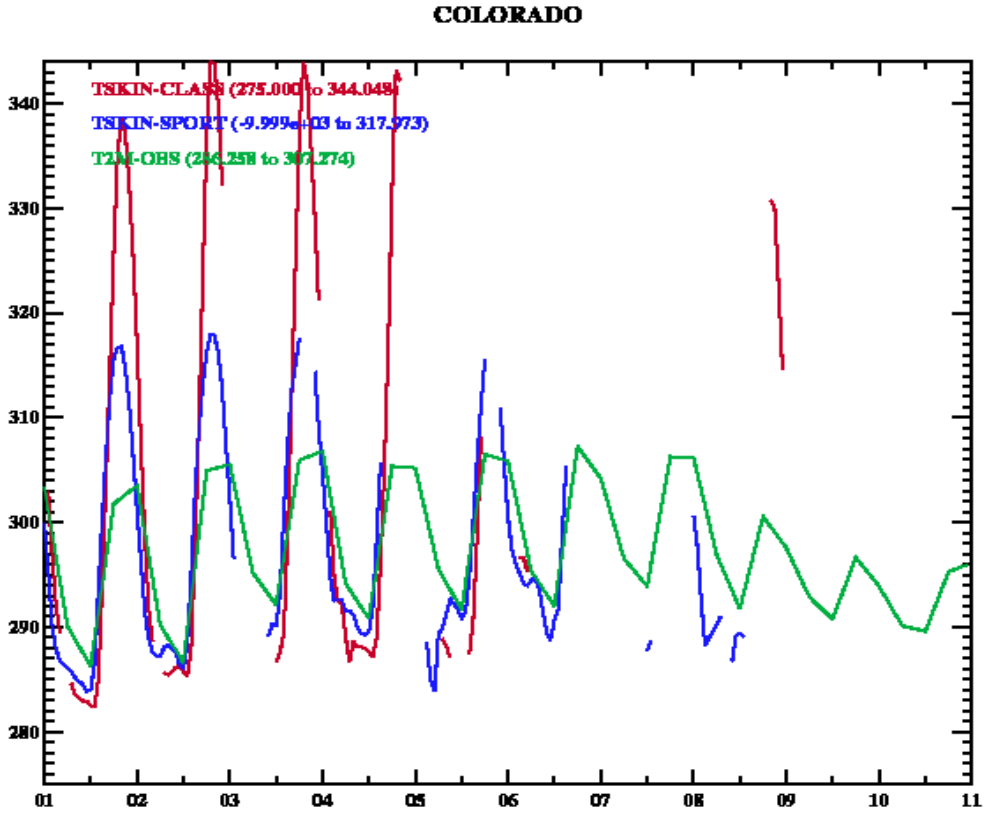

Figure3-1. Time series for the first part of September 2013 showing GSIP skin temperatures (red), SPoRT skin temperatures (blue) and 2m observed temperature (green).

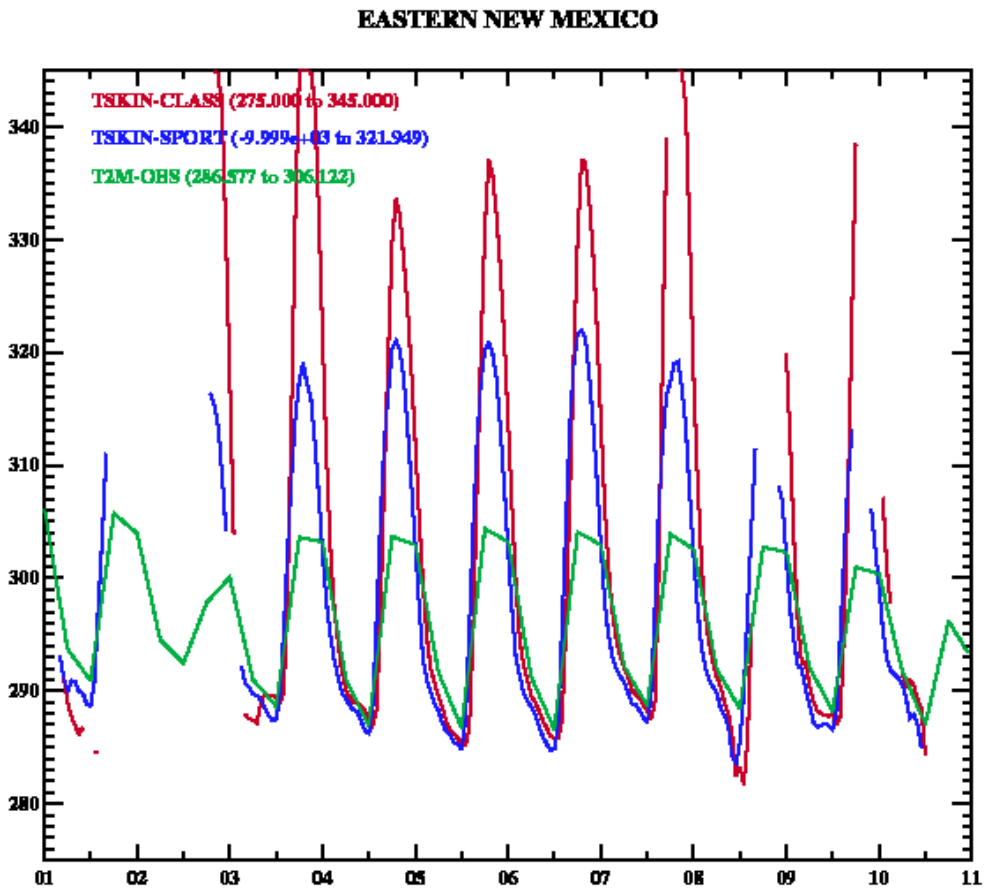

Figure 3-2. Time series for the first part of September 2013 showing GSIP skin temperatures (red), SPoRT skin temperatures (blue) and 2m observed temperature (green).

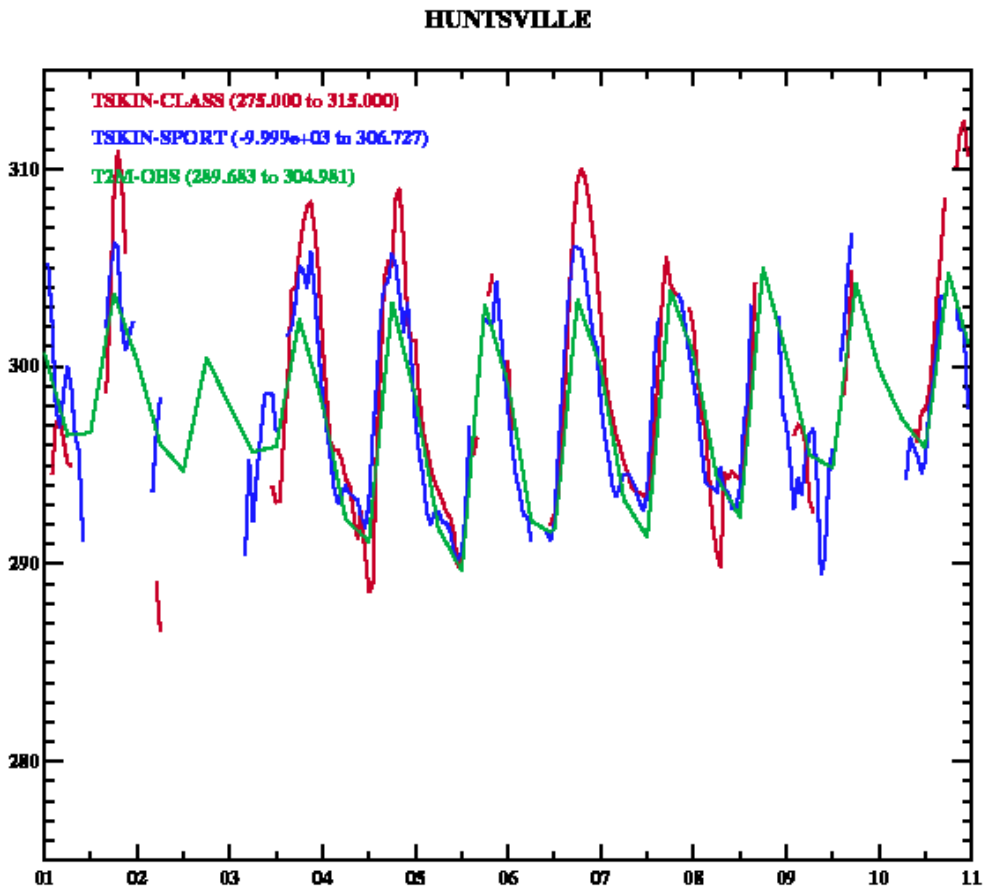

Figure 3-3. Time series for Huntsville, Alabama for the first part of September 2013 showing GSIP skin temperatures (red), SPoRT skin temperatures (blue) and 2m observed temperature (green).

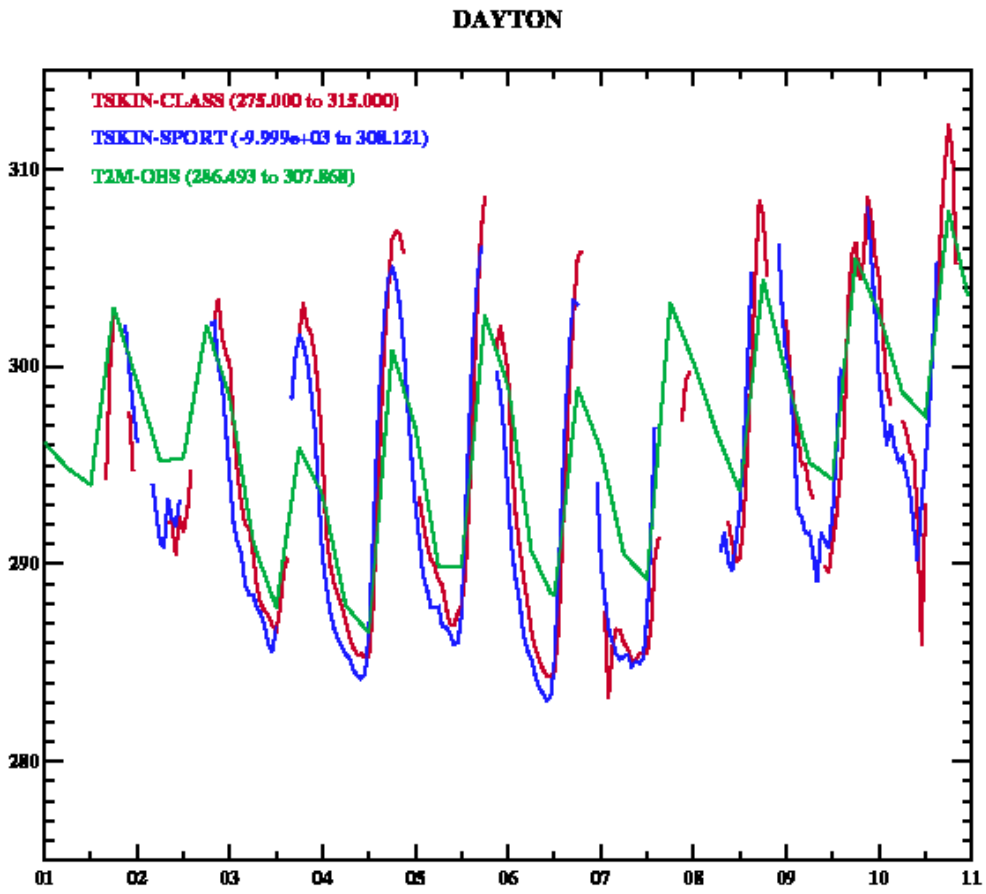

Figure3- 4. Time series for Dayton, Ohio for the first part of September 2013 showing GSIP skin temperatures (red), SPoRT skin temperatures (blue) and 2m observed temperature (green).

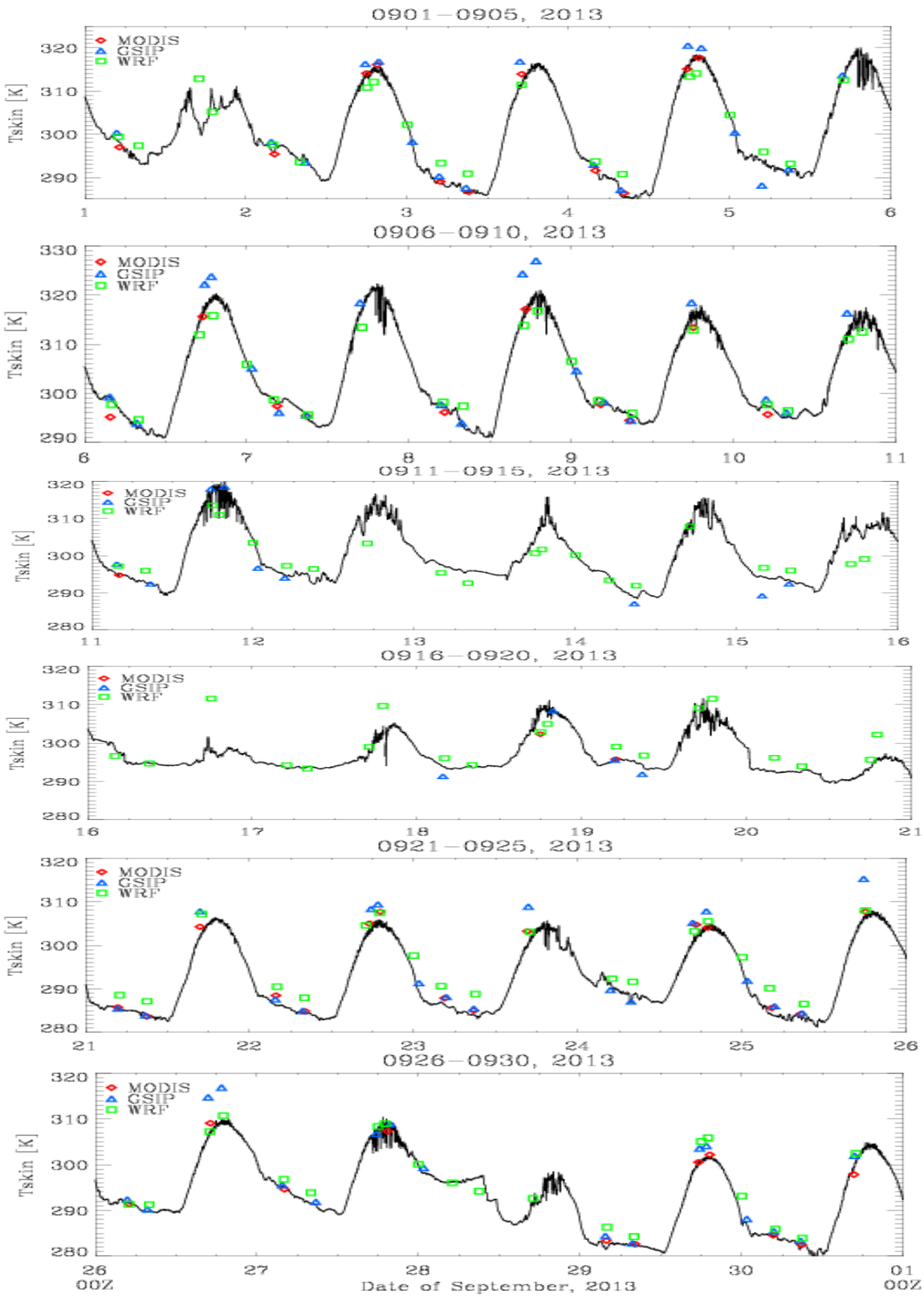

Figure 3-5. Comparison of MODIS, GSIP and WRF skin temperatures compared to in-situ radiometer data for CART-ARM site in central Oklahoma. Different panels show 5 day time series.

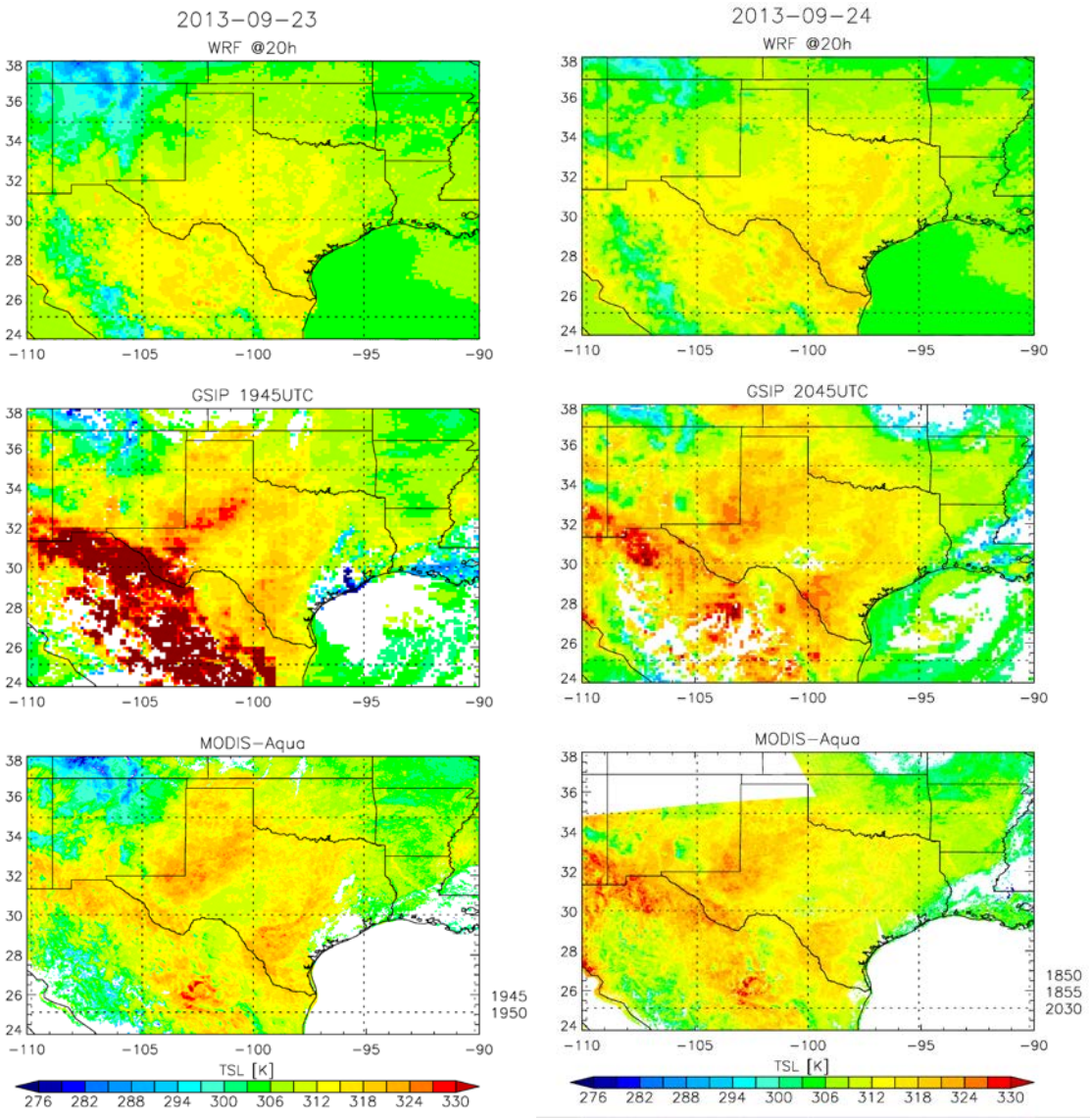

Figure 3-6. Skin Temperature, from top to bottom—WRF, GSIP, and MODIS (Aqua). Left panels are for Sep 23, 2013 (Aqua overpass time was 19:45 and 19:50 UTC), right panels for Sep 24, 2013 (main Aqua overpass time was 20:30 UTC).

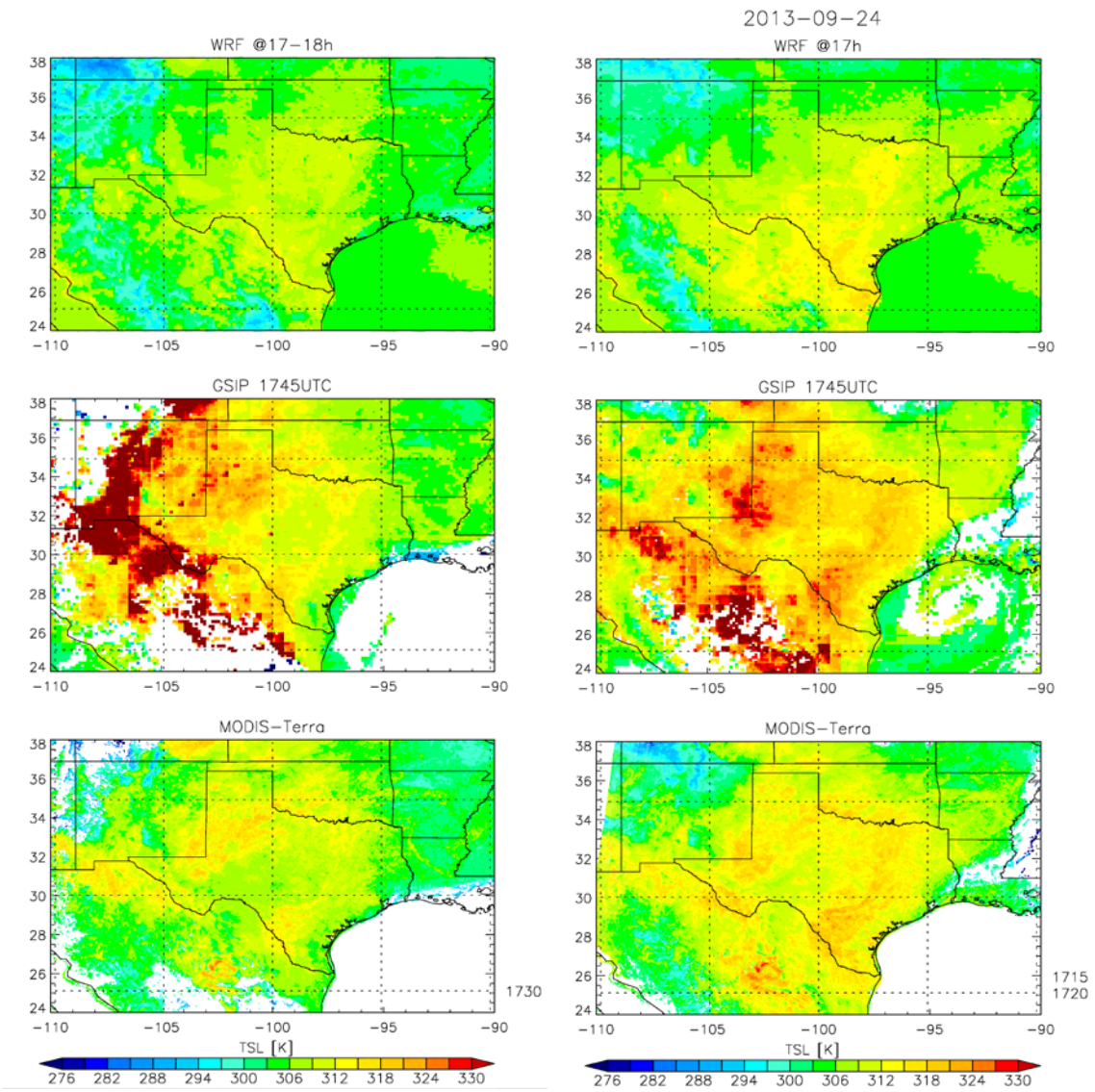

Figure 3-7. Skin temperature from top to bottom—WRF, GSIP, and MODIS(Terra). Left panels are for Sep 22, 2013 (Terra overpass time was 17:30 UTC), right panels for Sep 24, 2013 (Terra overpass time was 17:15 and 17:30 UTC).

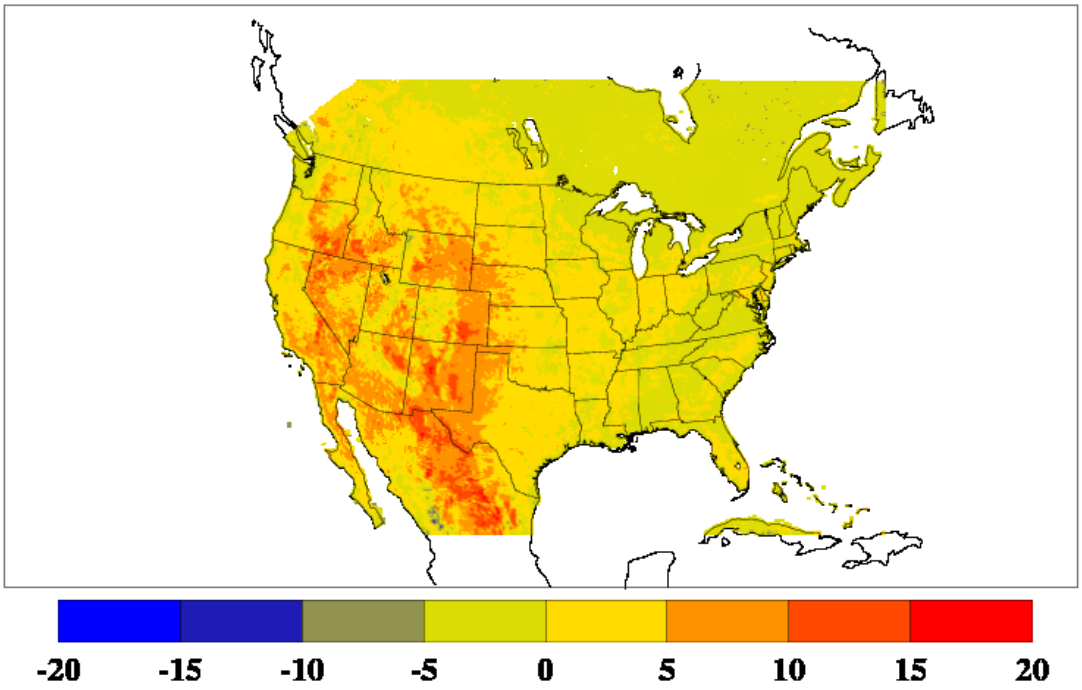

Figure 3-8. Average daytime difference of GSIP observed skin temperature minus the WRF diagnosed skin temperature for the control simulation for the period 0000 UTC 1 September to 2300 UTC 30 September 2013 in units of K. Only land points shown.

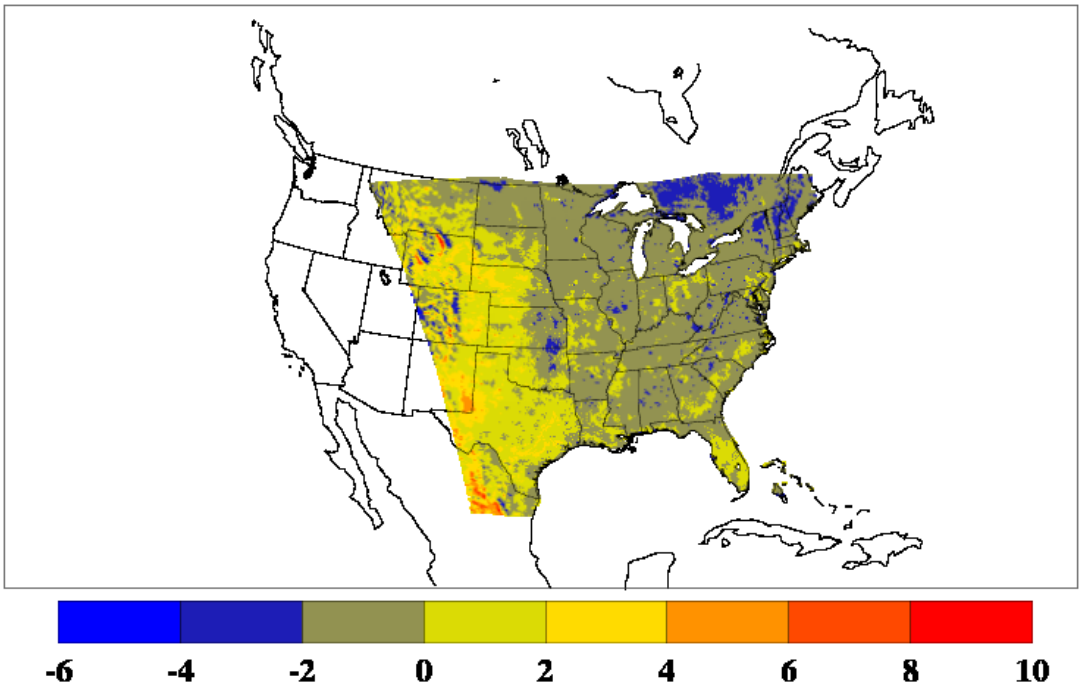

Figure 3-9. Average daytime difference of SPoRT observed skin temperature minus the WRF diagnosed skin temperature for the control simulation for the period 0000 UTC 1 September to 2300 UTC 30 September 2013 in units of K. Only land points shown.

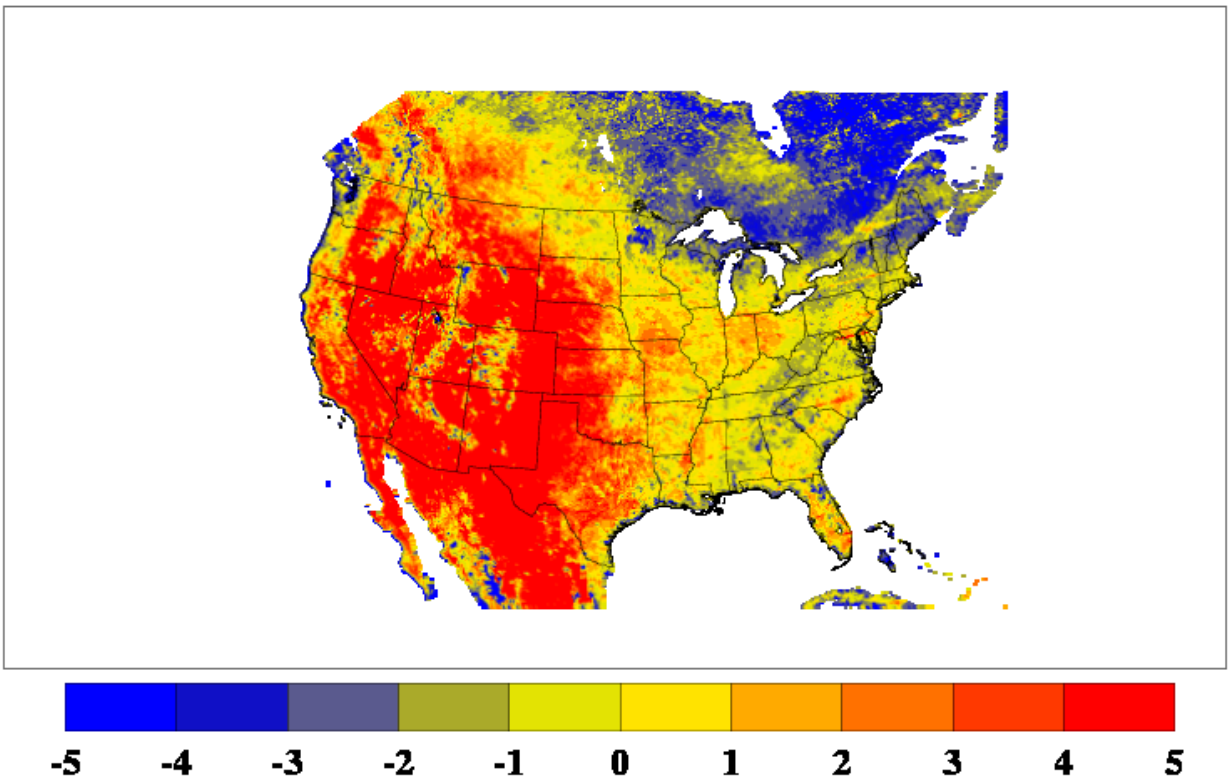

Figure 3-10. Average daytime difference of GSIP observed skin temperature minus the WRF diagnosed skin temperature for the insolation replacement simulation for the period 0000 UTC 1 September to 2300 UTC 30 September 2013 in units of K. Only land points shown. Plotting range truncated to ± 5 K

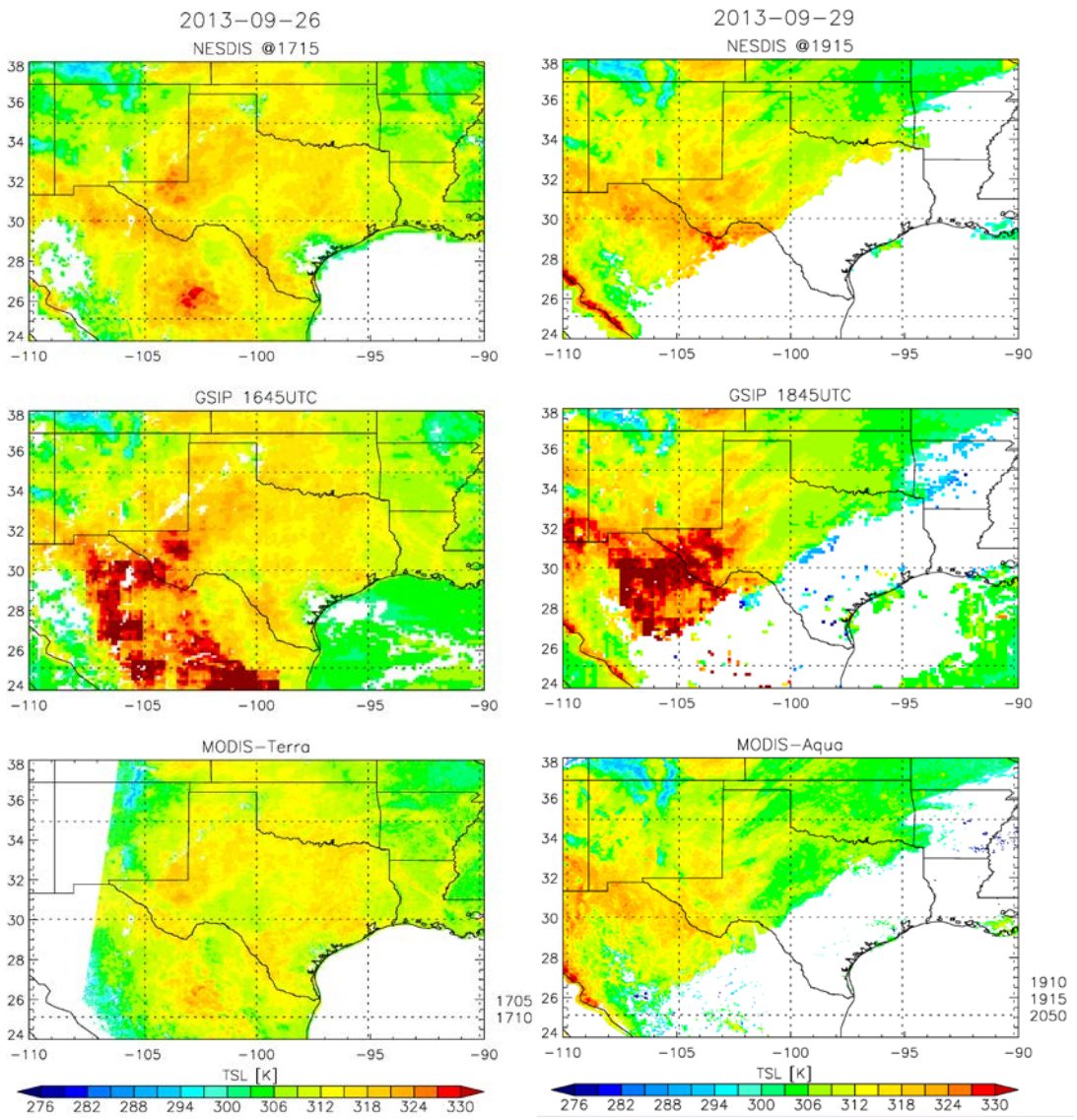

Figure 3-11 Comparison of NOAA ALEXI skin temperature product with GSIP and MODIS for September 26 and September 29. Top panel is the NOAA/ALEXI product. Middle panel is the GSIP product and bottom is the MODIS

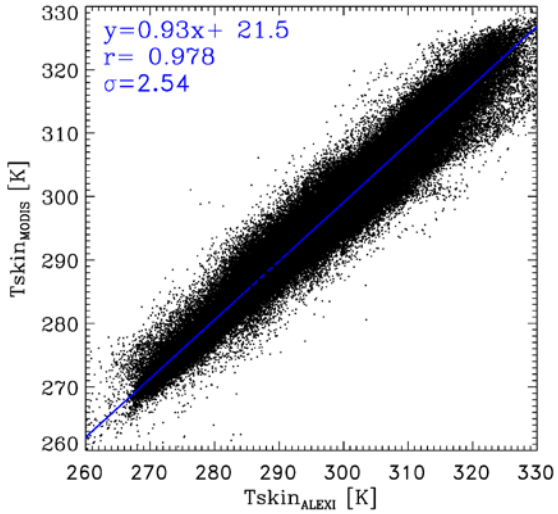

Figure 3-12. Comparison of Tskin from MODIS versus Tskin from the ALEXI product for all hours when data was available for the month of September 2013. This illustrates what may be the irreducible uncertainty in using skin temperatures as a model evaluation metric. At the top of the plot are the regression equation, the correlation coefficient, and the RMSE.

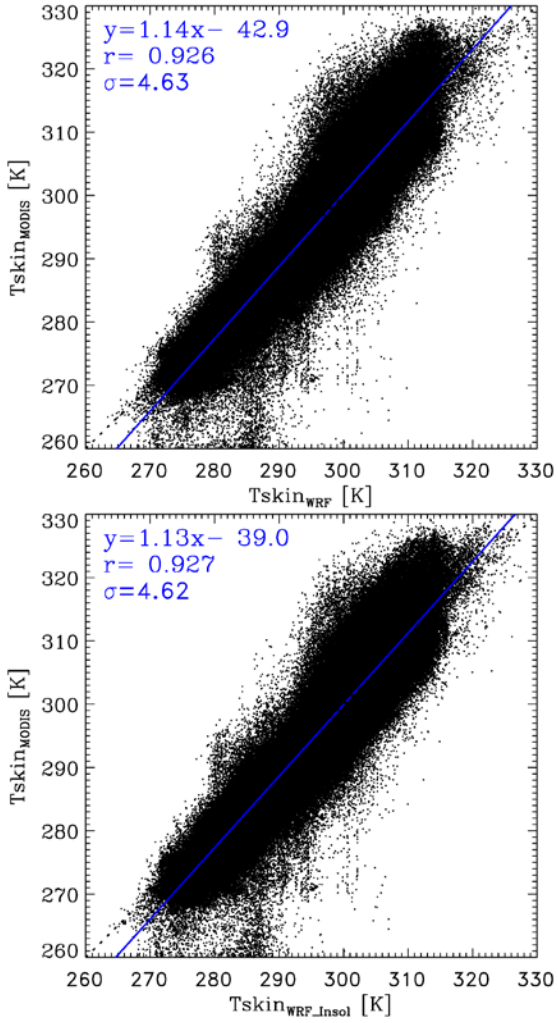

Figure 3-13. Comparison of Tskin of WRF simulation versus ALEXI product against MODIS observation (MODIS on y-axis). The x-axis in the bottom panel is WRF simulation without GOES insolation. This shows that there is room for improvement for a reduction in scatter over the irreducible error see in Figure 3-12 and this is the goal of this project to reduce the scatter. . At the top of each plot are the regression equation, the correlation coefficient, and the RMSE.

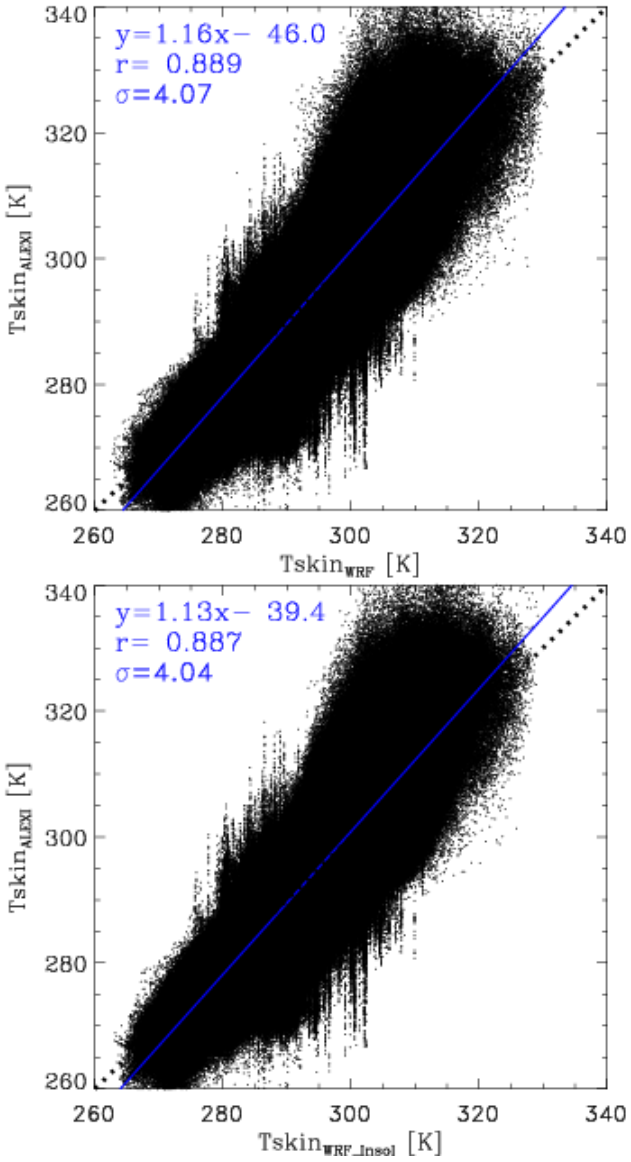

Figure 3-14. Comparison of Tskin of WRF simulation against ALEXI product (ALEXI on y-axis). The x-axis in the top panel is WRF simulation without GOES insolation, in the bottom panel is WRF simulation with GOES insolation. This again shows that there can be a reduction in scatter over the irreducible error see in Figure 3-12 and this is the goal of this project to reduce the scatter. At the top of each plot are the regression equation, the correlation coefficient, and the RMSE

.

Chapter 4 Diagnosis of Skin Temperature in the Pleim-Xiu Model

1. Introduction

As part of this project, it was proposed that satellite skin temperatures might be a better metric for model performance evaluation than standard National Weather Service (NWS) data in large part because of their ability to capture land use variations at fine resolution. Also, the project proposed that these satellite skin temperatures might also provide a better data set to nudge soil moisture than the use of NWS data in the Pleim-Xiu land surface assimilation model. However, the original Pleim-Xiu model did not have a true skin temperature but a ground temperature reflecting a 1-cm layer with a specific heat capacity. This chapter describes a technique to diagnose a skin temperature within the Pleim-Xiu land surface model. This is applied in the WRF model and in examples of skin temperature provided during the DISCOVER-AQ period. Horizontal spatial plots and selected time series plots demonstrate expected behavior.

2. Skin Temperature Diagnosis Technique

The Pleim-Xiu land surface model uses a top soil layer, which has a thickness of 1-cm and an associated temperature tendency as in (4-1).

$$c_g \frac{\partial T_G}{\partial t} = R_L + (1-\alpha_S) R_s - \varepsilon \sigma T_s^4 - H - E - G \quad (4\text{-}1)$$

The variables in (1) and elsewhere in this discussion are defined in Table 4-1. In equation (4-1) the bulk transfer coefficient C_G is dimensionally equivalent to the product of a density, a heat capacity, and a thickness. While the top layer has a small thickness, it still has a finite depth so Tg is in the strict sense not a skin temperature. The formal definition of a skin temperature (T_S) is obtained from (1) by taking the limit as the thickness associated with C_G approaches zero which gives (4-2).

$$R_L + (1-\alpha_S) R_s - \varepsilon \sigma T_s^4 - H - E - S = 0 \quad (4\text{-}2)$$

In (4-1) the ground heat flux term G in the Pleim-Xiu land surface model is modeled in a force-restore fashion and is replaced in (4-2) by S, which will be simply called the surface flux and will be described in detail below. The surface flux is a function of the temperature difference between T_G and T_S. Because of this, (4-2) must be solved by an iteration technique to solve for the skin temperature. After trying and considering several options, we chose Laguerre's method as the iteration technique (e.g., see Ralston and Rabinowitz 1978) because of its speed of convergence. Laguerre's method was compared against an expanded Newton's method described by Ralston and Rabinowitz (1978) and attributed to Madsen (1973) and Madsen and Reid (1975). The FORTRAN subroutines from Madsen and Reid (1975) (available online at www.dtic.mil/cgi-bin/GetTRDoc?AD=ADA278422) were implemented for this comparison. Equation (4-2) was solved by Laguerre's and expanded Newton's method at each WRF horizontal grid point for each hour for the month of September 2013. The results were always in close agreement. Because Laguerre's method was much faster it was adopted for this work.

The replacement of the ground flux with the surface flux was an attempt at a more physically based formulation that would be consistent with our goal of diagnosing a surface skin temperature. The surface flux is a weighted average between bare soil and vegetation flux values. For the soil component, a weighted average dry soil heat capacity is defined by equation (4-3),

$$c_B = f_S c_D + f_C c_C + f_L c_L \tag{4-3}$$

where the sand, clay, and silt fractions are defined by f were already defined within the Pleim-Xiu land surface model and the respective heat capacities are linear functions of T_G based on data in Farouki (1981). A dry soil density, ρ_D, was assigned to the predominant sand/clay/silt category based on the values given by Linsley et al. (1982). The actual and saturated volumetric soil moisture (W and W_{SAT}, respectively) are variables in the Pleim-Xiu land surface model. With these definitions, the weighted soil

$$\rho_S c_S = (1 - W_{SAT})\rho_D c_B + W\ \rho_W c_W \tag{4-4}$$

density times a soil heat capacity is given by (4-4). The soil thermal diffusivity k_S was calculated following the relationship of McCumber and Pielke (1981) (as explained by Smirnova et al. 1997) using the saturated soil moisture potential (or suction) data by the soil texture class found in Clapp and Hornberger (1978). The soil flux coefficient is then defined as in (4-5). The

$$F_S = \rho_S c_S k_S \Big/ \frac{1}{2}\Delta z_S \tag{4-5}$$

corresponding vegetation flux coefficient is given by (4-6), and is a function of air density and specific heat, leaf area index, friction velocity, and the characteristic plant surface dimension. The latter variable is not part of the model and the needed values were taken from Oleson et al (2010). Equation (4-6) was modeled after equation (2) in Zeng et al. (2005) using their value for the turbulent transfer coefficient c_F. The surface flux S is then the weighted average between soil and vegetation fluxes as in (4-7).

$$F_V = \rho_A c_P c_F L_I \sqrt{u_* / D} \tag{4-6}$$

$$S = (1 - V)F_S(T_S - T_G) + V\ F_V(T_S - T_G) \tag{4-7}$$

Table 4-1. Surface energy budget symbols, descriptions, and units.

Symbol	Description	Units
R_L	Downward Longwave Radiation	W m^{-2}
R_S	Downward Shortwave Radiation	W m^{-2}
α_S	Surface Shortwave Albedo	Fraction
ε	Surface Longwave Emissivity	Fraction

σ	Stephan-Boltzmann Constant	$W\ m^{-2}\ K^{-4}$
T_S	Surface Skin Temperature	K
H	Heat Flux	$W\ m^{-2}$
E	Latent Heat Flux	$W\ m^{-2}$
S	Surface Heat Flux	$W\ m^{-2}$
V	Vegetation Fraction	Fraction
F_S	Soil Flux Coefficient	$W\ m^{-2}\ K^{-1}$
F_V	Vegetation Flux Coefficient	$W\ m^{-2}\ K^{-1}$
f_S	Soil Sand Fraction	Fraction
f_C	Soil Clay Fraction	Fraction
f_L	Soil Silt Fraction	Fraction
c_D	Dry Soil Specific Heat for Sand	$J\ kg^{-1}\ K^{-1}$
c_C	Dry Soil Specific Heat for Clay	$J\ kg^{-1}\ K^{-1}$
c_L	Dry Soil Specific Heat for Silt	$J\ kg^{-1}\ K^{-1}$
c_B	Weighted Average Dry Soil Specific Heat	$J\ kg^{-1}\ K^{-1}$
ρ_D	Dry Soil Density (dominant soil category)	$Kg\ m^{-3}$
ρ_S	Weighted Average Soil Density	$Kg\ m^{-3}$
c_S	Weighted Average Soil Specific Heat	$J\ kg^{-1}\ K^{-1}$
ρ_W	Density of Liquid Water	$Kg\ m^{-3}$
c_W	Specific Heat for Liquid Water	$J\ kg^{-1}\ K^{-1}$
W_{SAT}	Volumetric Saturation Soil Moisture	$m^3\ m^{-3}$
W	Volumetric Soil Moisture	$m^3\ m^{-3}$
k_S	Soil Thermal Diffusivity	$m^2\ s^{-1}$
Δz_S	Thickness Top Soil Layer	m
T_G	Top Layer Soil Temperature	K
c_G	Top Layer Bulk Transfer Coefficient	$m^2\ K\ J^{-1}$
ρ_A	Air Density	$Kg\ m^{-3}$
c_P	Specific Heat for Air	$J\ kg^{-1}\ K^{-1}$
c_F	Turbulent Transfer Coefficient	$m\ s^{-1/2}$
L_I	Leaf Area Index	
u_*	Friction Velocity	$m\ s^{-1}$
D	Characteristic Plant Surface Dimension	m

3. Initial One-Dimensional Tests

The First International Satellite Land Surface Climatology Field Experiment (FIFE) provides observations for most of the relevant surface energy budget variables. The diagnosis technique discussed above in section 2 was first tested in a one-dimensional version of the Pleim-Xiu land surface model for a FIFE location for the approximate period 6-22 August 1987 with the results shown in Figure 4-1. A three-dimensional WRF run provided the nudging field that we used above the boundary layer. The diagnosed skin temperatures agreed well with the observed FIFE values on several days, but with considerably higher values than observed during the period 9-11 June. This was likely due to a combination of two factors. The first is that we may not have nudged strongly enough above the boundary layer so that the impact of frontal passages is not being "felt" in the one-dimensional model, especially near the surface. The second is that the one-dimensional model used GOES-derived insolation, which had a fixed

water vapor value that in general overestimates the insolation which would lead to higher temperatures. This is related to the insolation issues we discussed in Chapter 2.

4. Horizontal Plots from WRF Simulation

Figure 4-2 is an example of the diagnosed skin temperature for 1800 UTC 13 September 2013 for the simulation where the WRF internal downward shortwave radiation was replaced by the GOES-derived values from the GSIP archive (described in Chapter 2. as the so-called "insolation" run). Lower values were located mainly in parts of the Rocky Mountains, eastern Canada, and the northeastern United States. The highest values were located in portions of southern California, Arizona, and Texas. Figure 4-3 is the difference in the WRF diagnosed skin temperature (insolation run minus the control run) for the same time. When the pattern in Figure 4-3 is compared with the GOES-13 visible image in Figure 4-4, it is clear, not surprisingly, that cloud features control many of the larger differences. Many details could be discussed, but only two will be mentioned. The first is the northwest to southeast oriented narrow cloud band that extends from southwest Missouri to northern Mississippi in Figure 4-4. This feature is related to a local minimum in skin temperature in Figure4-2 and a narrow band of negative differences in Figure 4-3 indicating that the control run likely missed this feature. The second example is related to a narrow band of convective clouds with broken coverage extending from over Lake Michigan southward to parts of northeastern Illinois and northwestern Indiana (see Figure 4-4). This was the result of cold northerly flow over the relatively warm water leading to instability and the resultant cloud development. In this case, Figure 4-3 indicates large positive differences suggesting that the control run had clouds that were too deep, resulting in less insolation than what the GOES-derived insolation indicated. This is consistent with the observed cloud field having a broken character.

5. Time Series Plots from WRF Simulations

Figure 4-5 shows the vegetation fraction from the WRF model for 0000 UTC 1 September 2013 and also the locations of the time series plots in Figs. 4-6 through 4-11 (Note that in Figure 4-5, this is the U. S. Geological Survey (USGS) vegetation fraction and not the seasonally adjusted vegetation fraction actually used in the PX model). Later in Chapter 6 we will discuss what appears to be a significant problem with the seasonal adjustment. In Figs. 4-6 through 4-11 the WRF diagnosed skin temperature and simulated 2-m temperatures are shown for the first 10 days in September 2013. In general, the skin temperature had a larger amplitude than the 2-m temperature counterparts which was expected. Typical daytime maximum differences between the skin and 2-m temperatures were on the order of 3 K for most locations, but with considerably larger values for the Texas locations where vegetation cover was substantially less.

6. Conclusions and Future Work

From the evidence thus far, it appears that the implementation of a model to diagnose a skin temperature within the structure of the PX model is giving reasonable values. Large differences can occur in the skin temperature field between the control and insolation runs indicating the surface is responding to the GOES-derived estimated insolation. Chapter 6 will focus on comparing the WRF diagnosed skin temperatures with the GOES ALEXI observed skin temperature values.

7. References

Clapp, R. B. and G. M. Hornberger, 1978: Empirical equations for some soil hydraulic properties. *Water Resour. Res.*, **14**(4), 601-604.

Farouki, O. T., 1981: *Thermal properties of soils*, CRREL Monograph 81-1, United States Army Corps of Engineers, Cold Regions Research and Engineering Laboratory, Hanover, New Hampshire, US (available online at http://www.dtic.mil/cgi-bin/GetTRDoc?AD=ADA111734).

Linsley, R. K., Jr., M. A. Kohler, and J. L. H. Paulhus, 1982: Hydrology for Engineers, Third Edition, McGraw-Hill.

Madsen, K., 1973: A root finding algorithm bases on Newton's Method. BIT, 13, 71-75.

Madsen, K. and J. K. Reid, 1975: FORTRAN subroutines for finding polynomial zeros, Harwell Rep. AERE-R 7986 H. M. Stationary Office, London.

McCumber, M. C. and R. A. Pielke, 1981: Simulation of the effects of surface fluxes of heat and moisture in a mesoscale numerical model. *J. Geophys. Res*., **86**(C10), 9929-9938.

Oleson,K. W., D. M. Lawrence, G. B. Bonan, M. G. Flanner, E. Kluzek, P. J. Lawrence, S. Levis, S. C. Swenson, P. E. Thornton, A. Dai, M. Decker, R. Dickinson, J. Feddema, C. L. Heald, F. Hoffman, J.-F. Lamarque, N. Mahowald, G.-Y. Niu, T. Qian, J. Randerson, S. Running, K. Sakaguchi, A. Slater, R. Stöckli, A. Wang, Z.-L. Yang, X. Zeng, X. Zeng, 2010: Technical Description of version 4.0 of the Community Land Model (CLM), NCAR Technical Note NCAR/TN-478+STR.

Ralston, A. and P. Rabinowitz, 1978: *A First Course in Numerical Analysis*, McGraw-Hill.

Smirnova, T. G, J. M. Brown, and S. G. Benjamin, 1997: Performance of different soil model configurations in simulating ground surface temperature and surface fluxes. *Mon. Wea. Rev.*, **125**, 1870-1884.

Zeng, X., M. Barlage, R. E. Dickinson, Y. Dai, G. Wang, K. Oleson, 2005: Treatment of undercanopy turbulence in land models. *J. Climate*, **18**, 5086-5094.

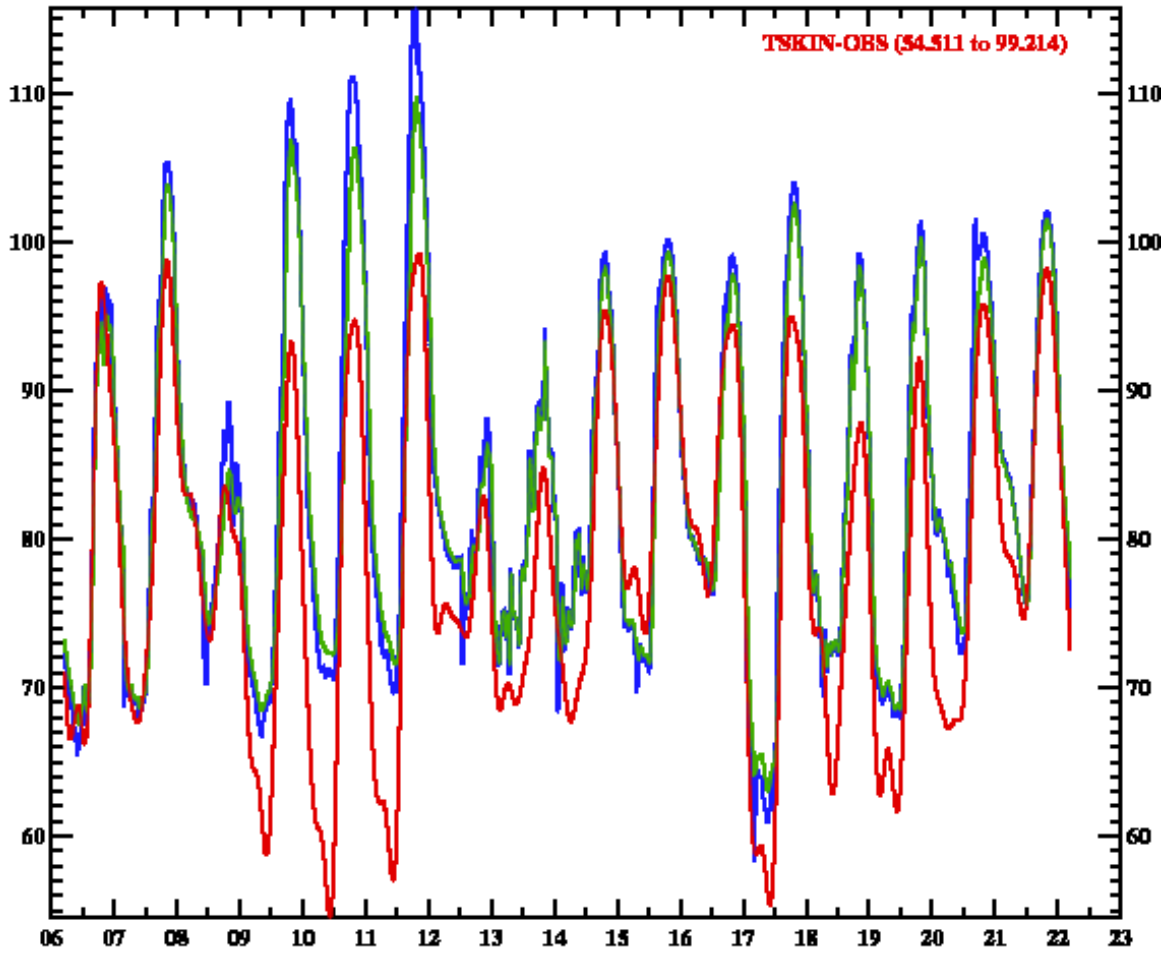

Figure 4-1. Time series of diagnosed skin temperature (blue), top layer PX model temperature (green), and observed skin temperature (red) for the period 0515 UTC 6 August through 0445 UTC 22 August 1987 for FIFE location 1916. Results are from a 1-D model using the same PX model physics as the 3D WRF version. Units are in degrees F.

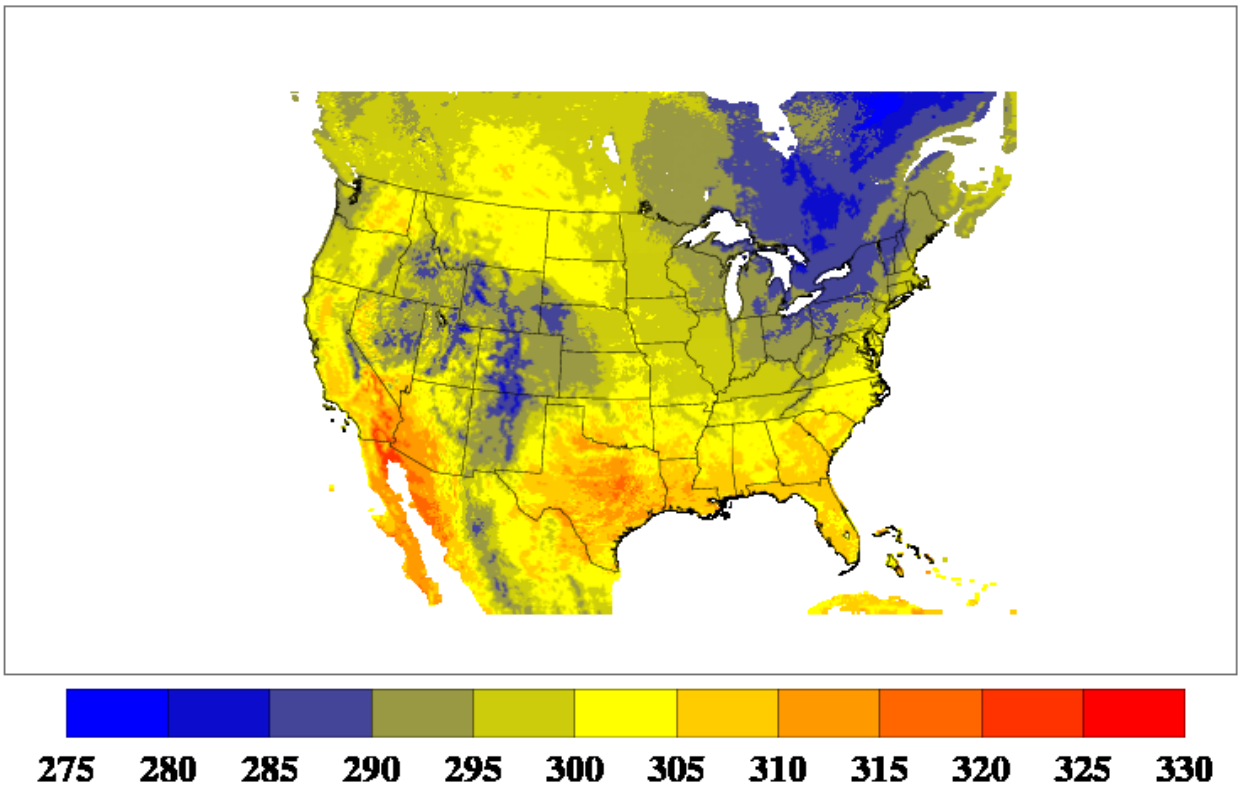

Figure 4-2. WRF diagnosed skin temperature for the insolation simulation for 1800 UTC 13 September 2013 in units of K. Only land points shown.

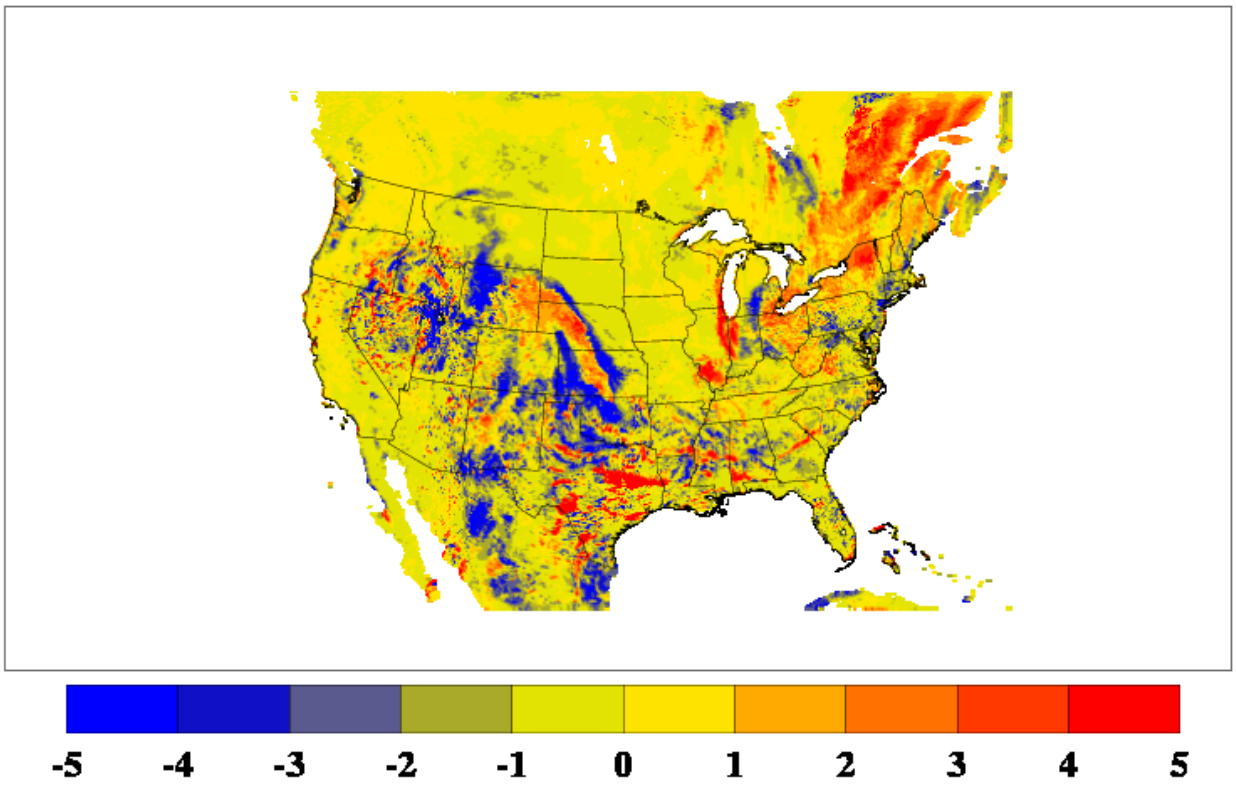

Figure 4-3. Difference of WRF diagnosed skin temperature (insolation run minus control run) for 1800 UTC 13 September 2013 in units of degrees K. Plotted values are truncated for the range ±5 K. Only land points are shown.

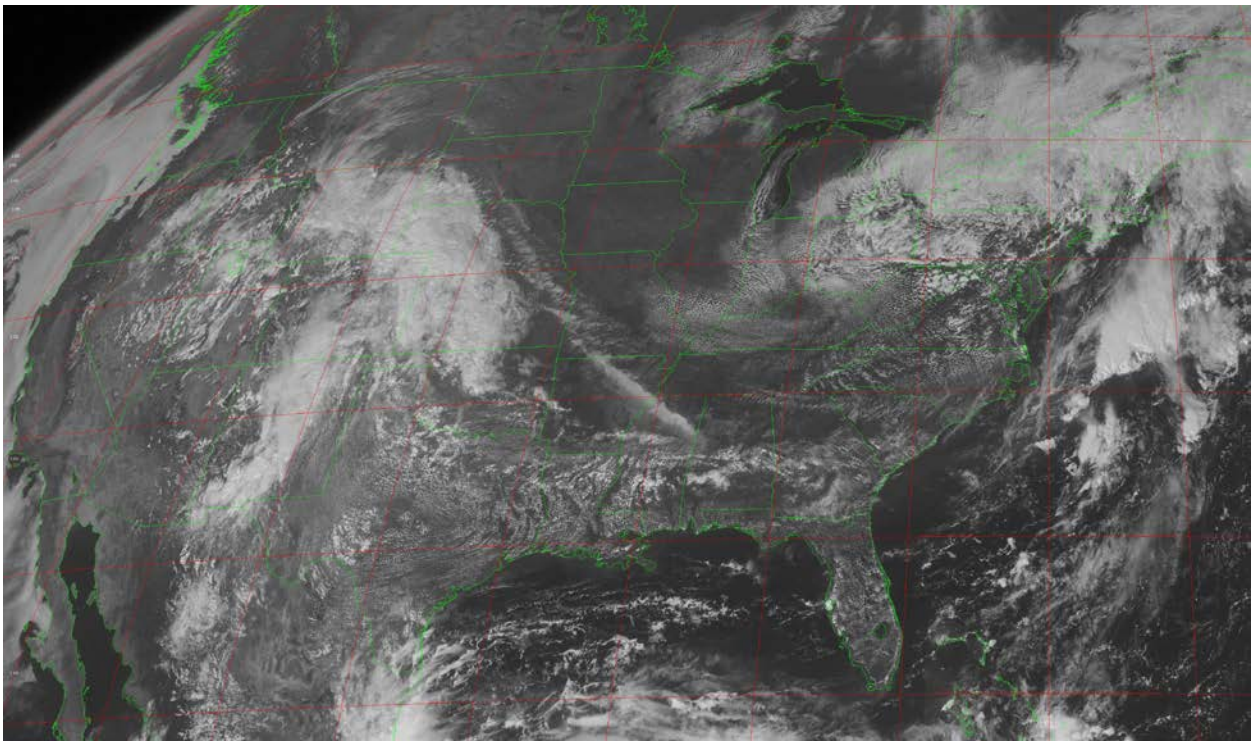

Figure4- 4. GOES-13 visible image for 1825 UTC 13 September 2013.

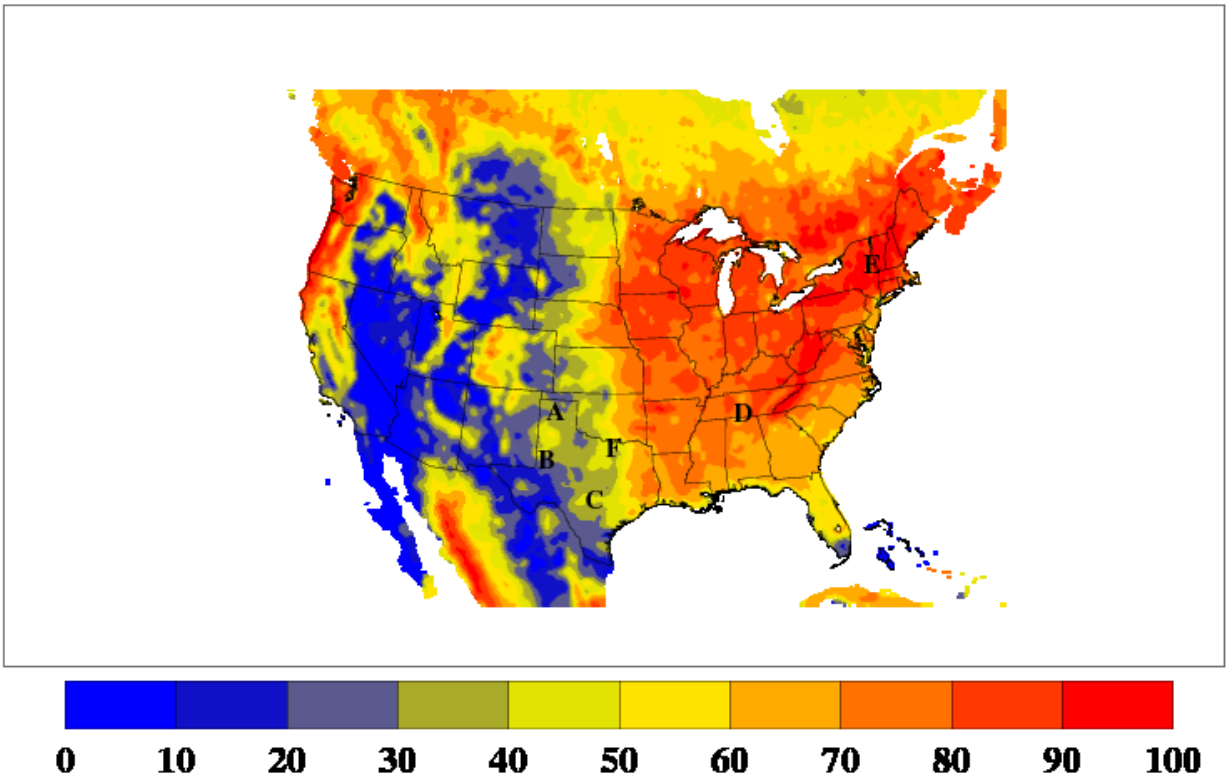

Figure 4-5. WRF vegetative fraction in percent for 0000 UTC 1 September 2013. Time series symbols and locations, respectively, are: (A) Amarillo, Texas; (B) Midland, Texas; (C) San Antonio, Texas; (D) Huntsville, Alabama; (E) Albany, New York; and (F) Dallas/Ft. Worth, Texas.

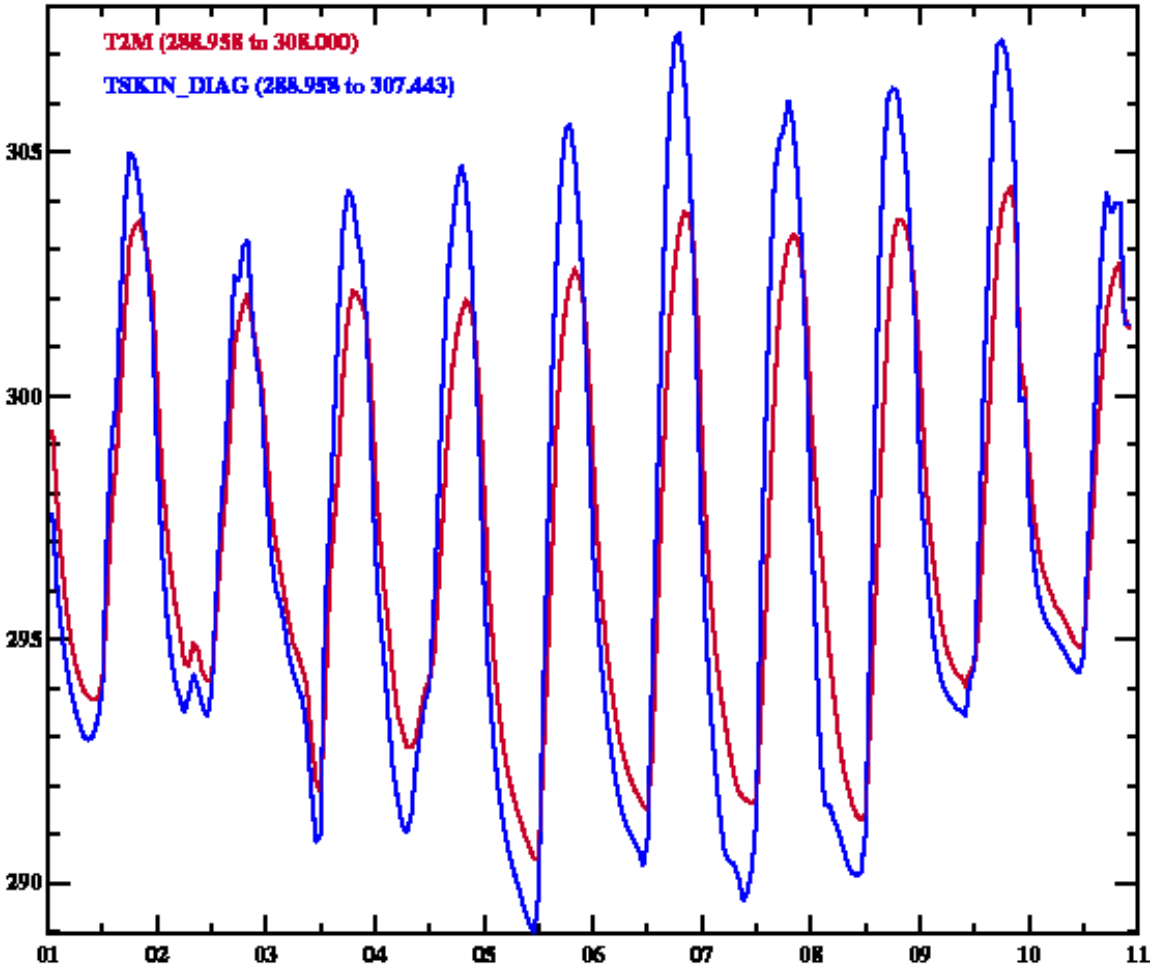

Figure 4-6. Time series of diagnosed skin temperature (blue) and WRF simulated 2-m temperature (red) for the period 1-10 September 2013 for Huntsville, Alabama (site identifier KHSV). Units are degrees K.

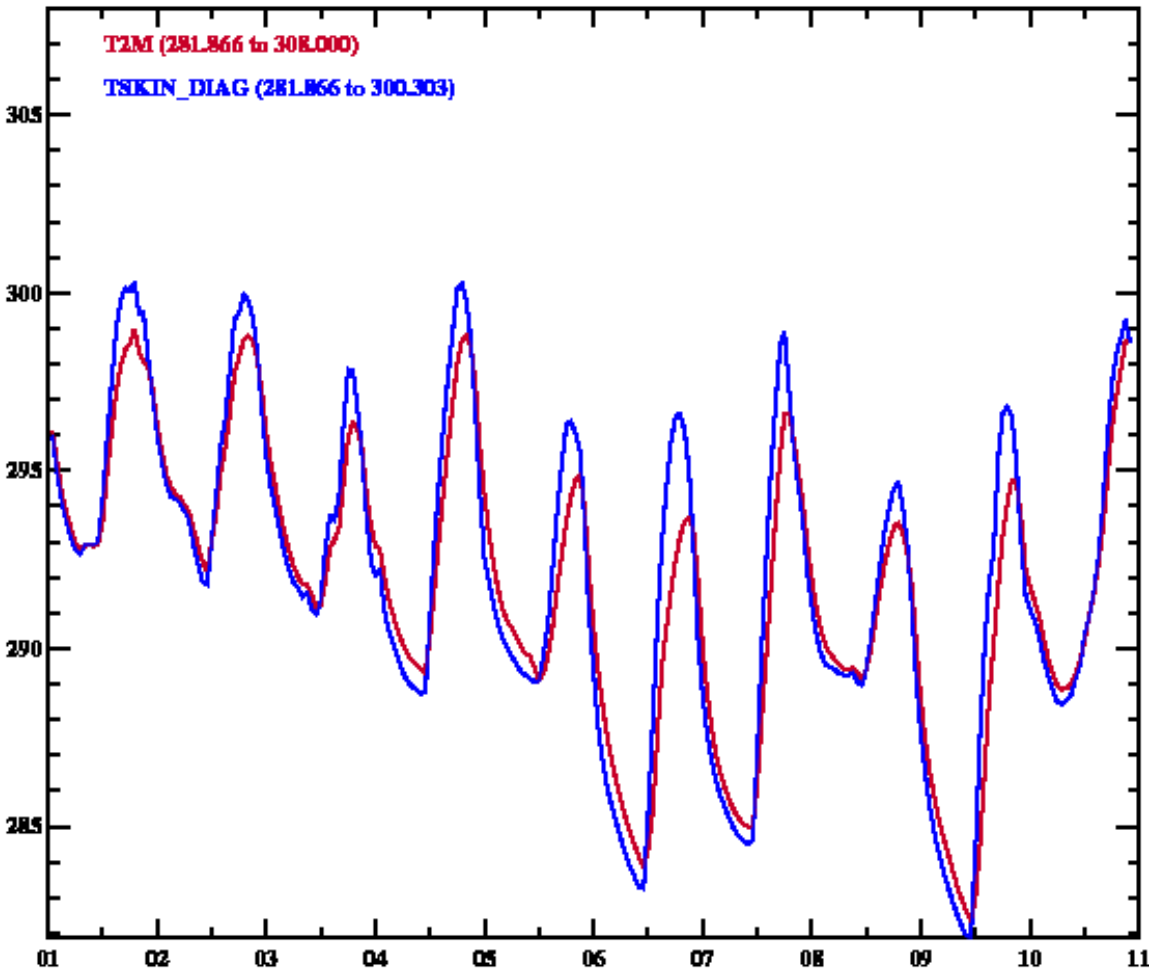

Figure 4-7. Time series of diagnosed skin temperature (blue) and WRF simulated 2-m temperature (red) for the period 1-10 September 2013 for Albany, New York (site identifier KALB). Units are degrees K.

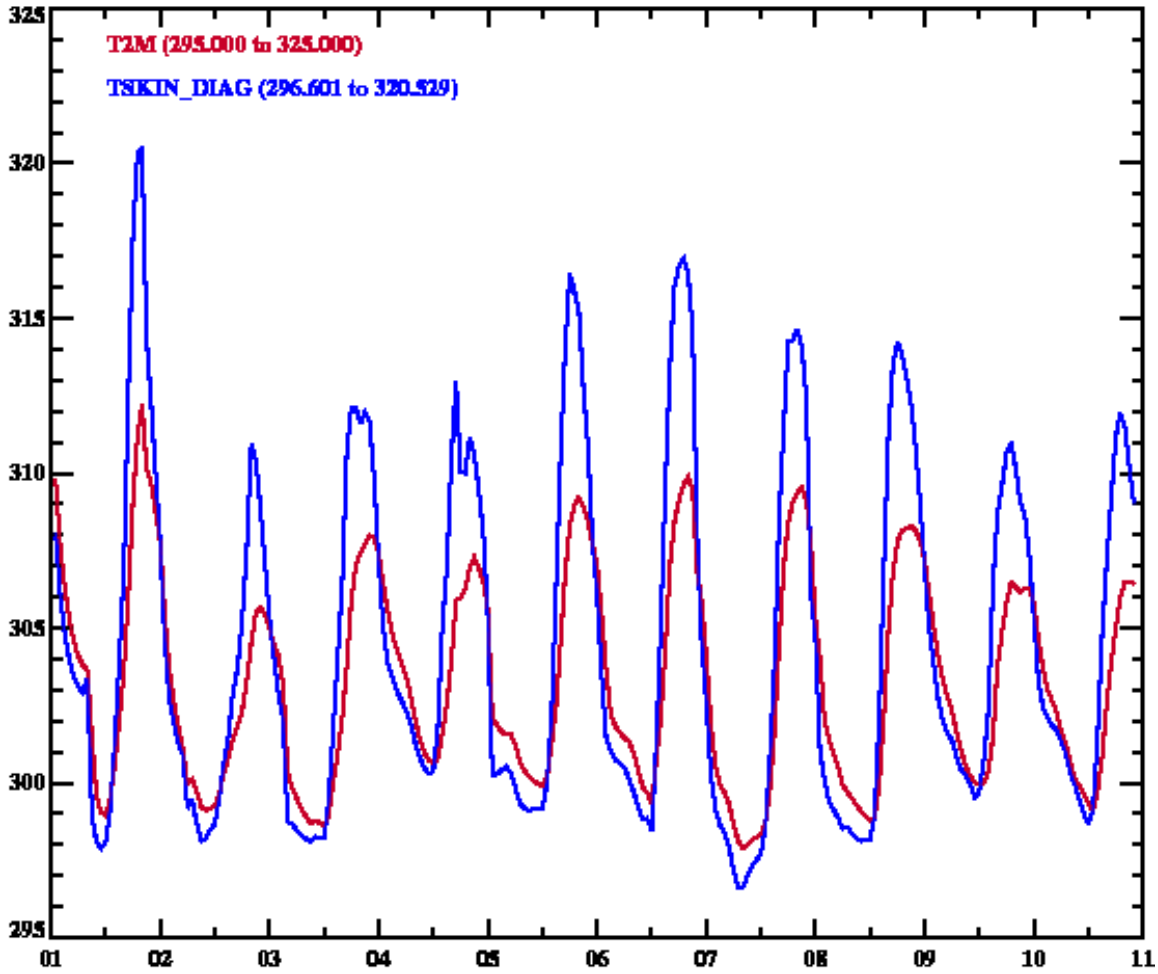

Figure 4-8. Time series of diagnosed skin temperature (blue) and WRF simulated 2-m temperature (red) for the period 1-10 September 2013 for Dallas/Fort Worth, Texas (site identifier KDFW). Units are degrees K.

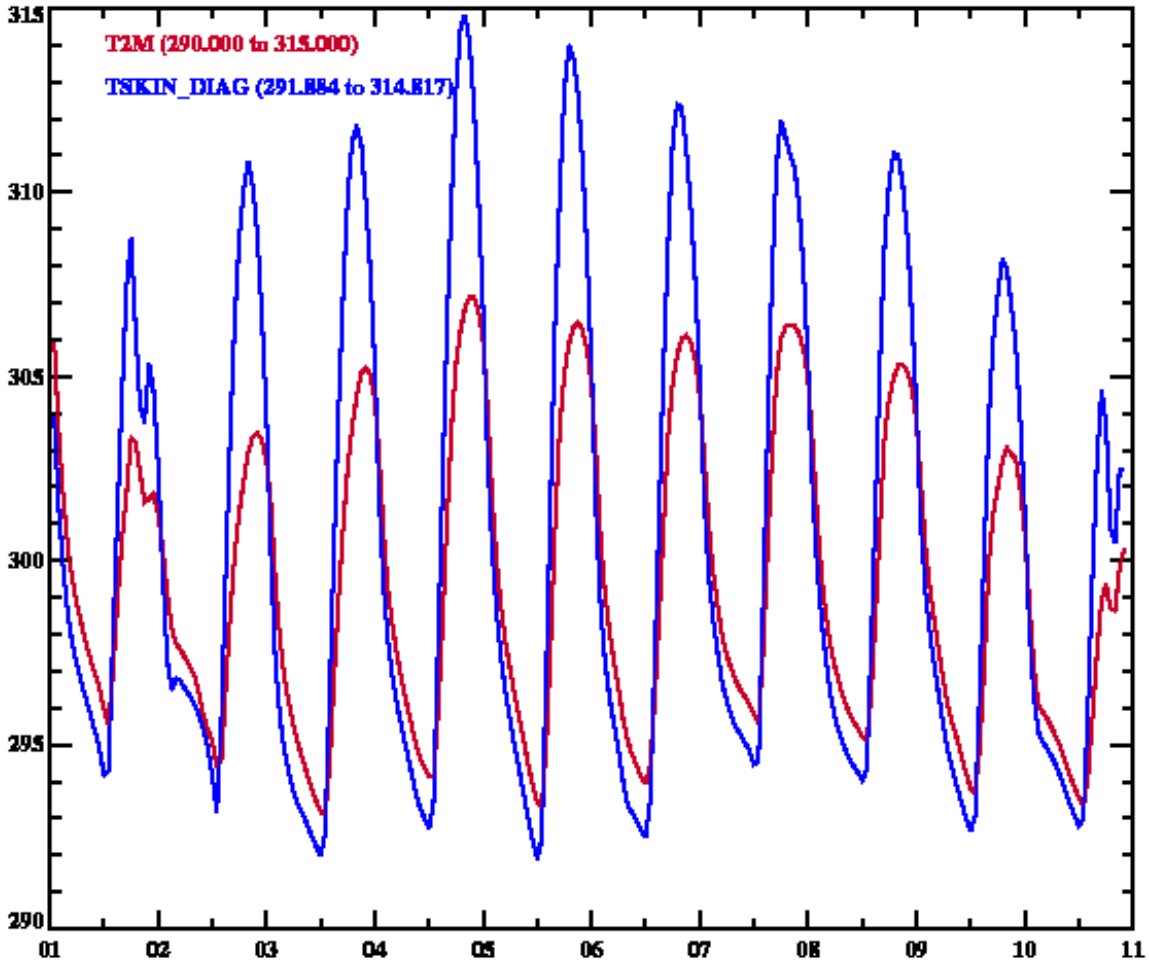

Figure4- 9. Time series of diagnosed skin temperature (blue) and WRF simulated 2-m temperature (red) for the period 1-10 September 2013 for Amarillo, Texas (site identifier KAMA). Units are degrees K.

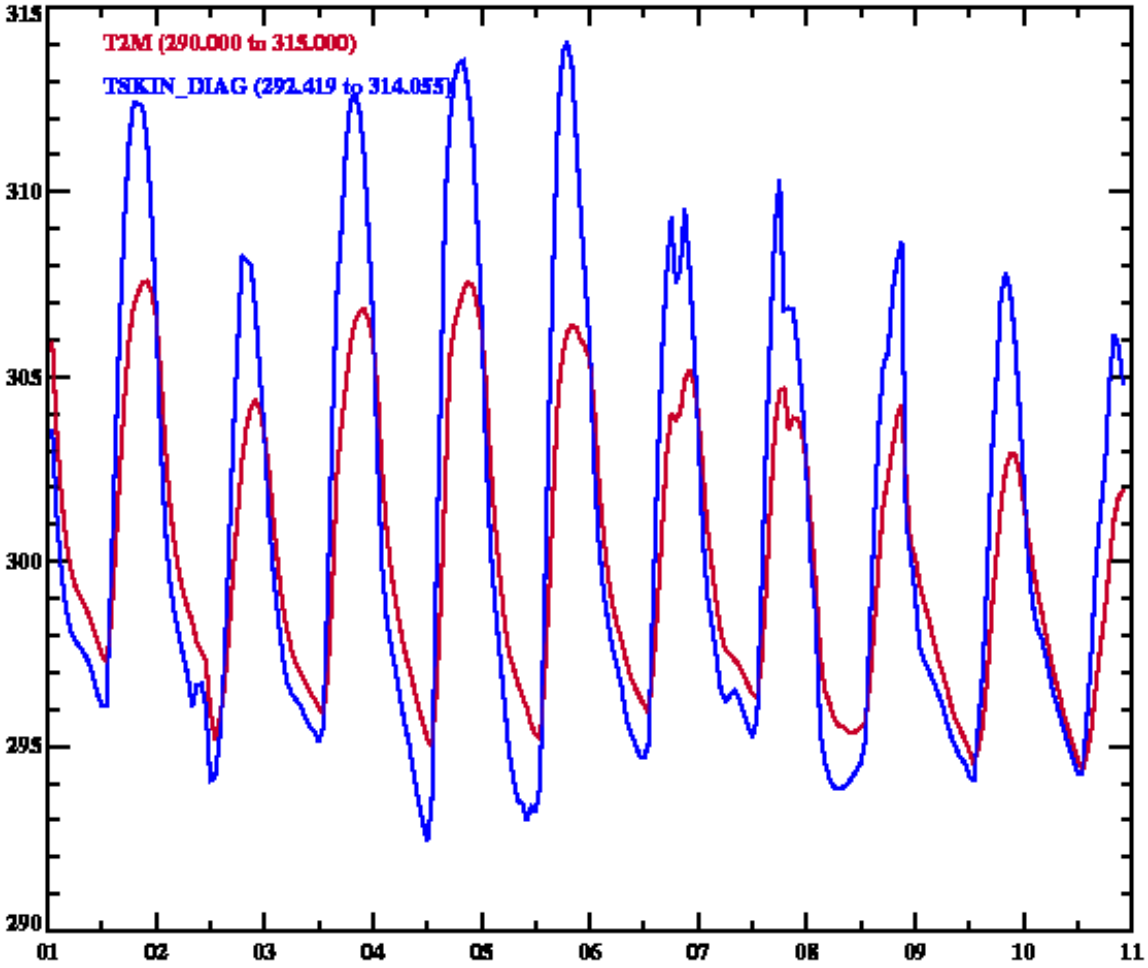

Figure 4-10. Time series of diagnosed skin temperature (blue) and WRF simulated 2-m temperature (red) for the period 1-10 September 2013 for Midland, Texas (site identifier KMAF). Units are degrees K.

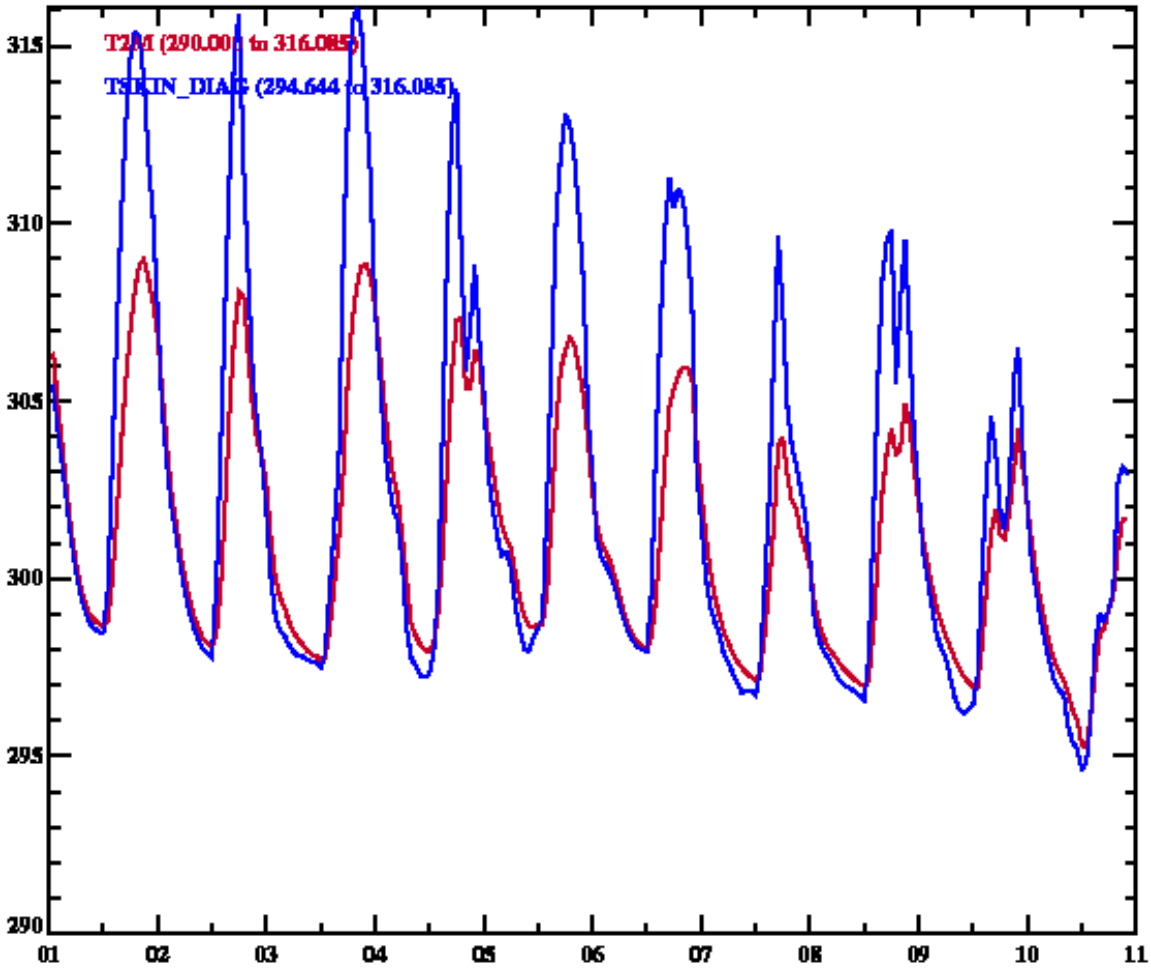

Figure 4-11. Time series of diagnosed skin temperature (blue) and WRF simulated 2-m temperature (red) for the period 1-10 September 2013 for San Antonio, Texas (site identifier KSAT). Units are degrees K.

Chapter 5 Quality Assurance/Quality Control of Satellite Skin Temperature Data and Audits of Data Quality

1. Introduction

Quality Assurance/Quality Control (QA/QC) for models is somewhat different from special or routine observations made by *in situ* instruments. Most of the data used in the model is created and provided by others such as the background meteorological analyses and land use data provided by others. These data are used by multiple groups and as such go through a set of QA/QC procedures overseen primarily by the National Weather Service and the U.S. Geological Survey (USGS) . However, we have used some techniques that should improve the quality of the modeling process. Perhaps the most important is that we employed two independent

modelers in this process and for some products three independent modelers. Thus, issues with making sure the right data sets are used is provided by the independent setup of the models.

The modeling team also spent considerable time on evaluation of the model against observations. This provided checks on model data. For example in evaluating the model it was found that the Pleim-Xiu model when run using the default set up altered the vegetation fraction which was an input from the USGS land use data base. In examining the sensitivity of the model it was found that the altered vegetation fraction was unreasonable especially in the West.

As noted above most of the is used my many organizations and as such multiple layers of review has been given to the data sets, However, there are two data sets used in the present investigation which are not part of the standard model input This is the insolation data and satellite retrieved skin temperature. Thus, this data has been subjected to a QA/QC procedure which is described for skin temperature below. Chapter 2 provides the evaluation/audit of the insolation data versus independent pyranometer data.

As discussed in Chapters 1 and 3, satellite observations of surface skin temperature can have quality issues. These can be related to the algorithm for retrieving a skin temperature from the upward Infrared (IR) radiances where assumptions about the surface emissivity and the impact of the intervening atmosphere affect the derived skin temperature. Additionally, there can also be issues with the calibration of the IR sensor and degradation of the sensor. In Chapter 3 it was shown that the skin temperature product that was finally chosen for this investigation – the NOAA ALEXI single channel retrieval seems to inter-calibrate well with other IR products such as MODIS and with surface in situ data at flux sites around the country. While shown in Chapter 3 that there is an irreducible error that has to be accepted when using the satellite skin temperatures, this appears much smaller than the variation seen in model output. Thus, it is felt that the ALEXI temperature retrieval is a good product to begin the investigation.

However, beyond the actual observation of the skin temperature, there is the concern that the IR temperature is actually representing the surface. Clouds are very good IR emitters. Even the presence of relatively shallow clouds can cause the temperature to be much cooler than that of the surface. This problem referred to as cloud contamination can be a critical factor in the usefulness of the skin temperature data. In the present investigation cloud contamination can produce bad data going into the moisture nudging which would then lead to erroneous soil moisture. In the present investigation skin temperature is also used as a model evaluation metric. Here errors can lead to not only poor assessment of model performance, but can then mask improvements in model performance due to the nudging of moisture.

For these reasons, the present investigation has taken a very aggressive approach to cloud clearing in the surface skin temperature data. This three-tiered approach is provided below. It must be noted that at present only the first two tiers have been implemented in the model results shown in this report. However, future use of skin temperature data for evaluation and assimilation can take advantage of this additional screening.

Percent of data audited: Since the QA/QC procedures here are different than the physical audit of instrumentation data, it is just as easy to QA/QC all the data. In this activity we applied the QA/QC for cloud contamination described below for 100% of the data taken from the satellite.

2. First Pass of Skin Temperature Screening

The ALEXI skin temperature product has used two different cloud screening algorithms. One is the same algorithm used in the GSIP skin temperature and the other involves further screening using established historical skin temperature range to filter out unrealistic values. The second algorithm has only been applied to the data for the 1015-2015 UTC time frames

3. Second Pass of Skin Temperature Screening

A second pass of skin temperature was developed for the purpose of reducing the remaining cloud contaminated data, as well as removing unreasonably high values at the other daytime hours (2115-0315 UTC) in the model domain. This was accomplished by performing historical, spatial and temporal checks. The spatial and temporal checks were not done for grid points which were classified as water or within a distance of 36 km of a water point. The WRF land-water mask was used to determine whether a given point was considered as water from the model perspective.

For the historical check, the first step is to determine the maximum skin temperature for each grid point for September 2013 based on the daily time range of 1015-2015 UTC. This time range of data has already undergone the first pass of screening by the ALEXI group. Any skin temperature which exceeded the latter maximum values for the time range of 2115-0315 UTC was set to missing.

The spatial check is done in two steps where each step is defined by a maximum difference of the skin temperature δT_S and a radius R. When a target cell's skin temperature is more than δT_S lower than any grid cell within a distance of R, then the target cell's skin temperature is set to missing. For the first step, δT_S = 4 degrees K and R = 60 km, and for the second step, δT_S = 10 K and R = 300 km. For the first step an elevation constraint is also utilized. Any grid point within the radius R which has an elevation difference of more than 500 m from the target cell is not considered. The second pass is done only when more than 20% of the cells within a distance of R are defined (i.e., a large percentage of cells are not missing).

The temporal check is done in three steps. In the first step, if a cell's skin temperature decreased more than 6 K from the previous hour it was set to missing. In the second step, if a cell's skin temperature was missing for the previous two hours and was lower than 282 degrees K, then it was set to missing. The third step is a combination of spatial and temporal checks. The second step of the spatial check is repeated (δT_S = 10 degrees K and R = 300 km) but without the 20% check. If this test fails and the skin temperature at the previous hour is missing, then the value at the current time is set to missing.

On average, this second pass of screening (combination of historical, spatial and temporal checks) removes about 6-11% (depending on the hour) of the data for the 2115-0315 UTC time period.

Most of the model results and evaluation in the report used the second screening pass. However, because of some concerns a third screening pass is described below. A separate table for use of the third pass screening is given in Chapter 6.

4. Third Pass of Skin Temperature Screening

In the third pass of skin temperature screening four additional checks were performed. The first check used the ratio of the GOES-derived insolation to an estimate of the clear-sky insolation. Skin temperatures at locations where this ratio was less than 95% were rejected. The clear-sky insolation values were calculated using the approach given by Savijarvi (1990). It involves the usual solar geometry plus simple parameterizations for absorption due to ozone, water vapor, and Rayleigh scattering. This approach is briefly described below.

Defining a time variable A as a function of the day of the year J as in equation (5-1), the time variation of the solar constant at the top of the atmosphere (TOA) is defined as in equation (5-2). The terms inside the square brackets in equation (5-2) are the higher order terms of a longer list given by Pielke (1984) and originally by Paltridge and Platt (1976). The solar irradiance at the TOA is then given by (5-3), where Z is the solar zenith angle.

(5-1) $$A = \frac{2\pi J}{365}$$

(5-2) $$S = 1365\left[(1 + 0.03422\cos(A) + 0.00128\sin(A)\right]$$

(5-3) $$C = S\cos(Z)$$

(5-4) $$E = 90 - Z$$

(5-5) $$O = 0.024\,C\left(\sin(E)\right)^{-\frac{1}{2}}$$

Defining the solar elevation angle E as in equation (5-4), the ozone absorption "O" is given by (5-5) which according to Savijarvi (1990) is his fit to the equation of Lacis and Hansen (1974).

The effective water vapor amount or U is a pressure and temperature weighted integral of water vapor as in equation (5-6), where q is the specific humidity, p is pressure, p_0 is a scale pressure (1013 mb), T_0 is a scale temperature (273 degrees K), g is the acceleration of gravity, and n is a constant set at 0.85 as suggested by Houghton (1984). The water vapor absorption "W" is given by (5-7), which is a fit to the results of Yamamoto (1962), where the constants a=1.20 and b=0.11. The constant "a" is a simplistic factor to account for aerosol enhancement of the water vapor absorption.

(5-6) $$U = \frac{1}{g}\int q\left(\frac{p}{p_0}\right)^{n}\left(\frac{T_0}{T}\right)^{\frac{1}{2}}dp$$

(5-7) $$W = a\,b\,C\left(\frac{U}{\sin(E)}\right)^{\frac{1}{4}}$$

The parameterization of Rayleigh scattering is given by equation (5-8) which follows Lacis and Hansen (1974), where the constants c=1.25 and d=0.28. The constant "c" is once again a simplistic factor to account for aerosol enhancement.

(5-8) $$Y = c\,d\left(1+6.43\sin(E)\right)^{-1}$$

The final term is the estimate of the backscattering of the reflected insolation as in equation (5-9), where the constant e=0.07 and α is the shortwave albedo. The latter albedo is the field used in the WRF model which is a USGS related value. The net downward clear-sky insolation at the surface, R_C, is then given by equation (5-10). The insolation screening statistic δ is then the ratio of the GOES-derived insolation R_S and the clear-sky R_C as in (5-11). Locations where δ was less than 95% were deemed cloud locations and where the GOES-derived skin temperature was set to missing.

(5-9) $$B = C\,c\,e\,\alpha$$

(5-10) $$R_C = C - O - W - Y - B$$

(5-11) $$\delta = \frac{\left(100\,R_S\right)}{R_C}$$

The three remaining checks involve various functions of the GOES-derived skin temperature, $T_{S,OBS}$. Equations (5-12) and (5-13) define the mean and standard deviation, respectively, in the traditional manner for a generic variable V at a given horizontal location and a given UTC hour of the day as described by the triplet (i,j,h) where the index "i" is the west-east dimension, "j" is the north-south dimension, and the index "h" is the hour. The sums in (5-12) and (5-13) are with respect to time at a fixed hour where N is the total number of situations where V(i,j,h) is defined. For example, with respect to the WRF modeling time period of 1-30 September 2013, if V was chosen to be $T_{S,OBS}$, and if h was set to 1800 UTC, then there would be a maximum of N=30 values at 1800 UTC each day. For the mean and standard deviation to be defined a minimum of 10 valid data points was required.

(5-12) $$\overline{V}(i,j,h) = \frac{1}{N}\sum_{t=1}^{t=N} V(i,j,h)$$

(5-13) $$\sigma_V(i,j,h) = \left(\frac{1}{N-1}\sum_{t=1}^{N}\left(V(i,j,h)-\overline{V}(i,j,h)\right)^2\right)^{1/2}$$

The first of the three remaining checks is defined by equation (5-14) and equation (5-15), where the variable "V" in equation (5-12) and equation (5-13) is the difference between the GOES-derived skin temperature ($T_{S,OBS}$) and the WRF diagnosed skin temperature ($T_{S,WRF}$) as in (5-14). The normalized statistic Z_D is then given by (5-15). The model simulation chosen for this was the insolation replacement run with the original Pleim vegetation fraction.

(5-14) $D = T_{S,OBS} - T_{S,WRF}$

(5-15) $Z_D = \dfrac{D - \overline{D}}{\sigma_D}$

The second of the three remaining checks is defined by (5-16) - (5-19) where the variable "V" is the minimum of the horizontal differences in the west-east direction.

(5-16) $G_{XW} = T_{S,OBS}(i, j, h) - T_{S,OBS}(i-1, j, h)$

(5-17) $G_{XE} = T_{S,OBS}(i, j, h) - T_{S,OBS}(i+1, j, h)$

(5-18) $G_X = \min\left(G_{XW}, G_{XE}\right)$

(5-19) $Z_{Gx} = \dfrac{Gx - \overline{G}x}{\sigma_{Gx}}$

The last of the three remaining checks is defined by (5-20) - (5-23) where the variable "V" is the minimum of the horizontal differences in the north-south direction.

(5-20) $G_{YS} = T_{S,OBS}(i, j, h) - T_{S,OBS}(i, j-1, h)$

(5-21) $G_{YN} = T_{S,OBS}(i, j, h) - T_{S,OBS}(i, j+1, h)$

(5-22) $G_Y = \min\left(G_{YS}, G_{YN}\right)$

(5-23) $Z_{Gy} = \dfrac{Gy - \overline{G}y}{\sigma_{Gy}}$

For the metrics Z_D, Z_{GX}, and Z_{GY} the threshold values for rejection were -1.0, -2.0, and -2.0, respectively. These correspond to one-tail normal probabilities of about 15.9%, 2.3%, and 2.3%, respectively. The goal was to identify points which were substantially cooler than their respective climatologies for the month. These metrics were developed by comparing the rejection locations with visible GOES imagery at 1800 UTC for the period 1-5 September 2013. These comparisons indicated that the combined suite of metrics was generally performing as expected. Further refinement of this screening process is outside of the scope of this project. This aggressive screening may be removing good data, but given the potential negative influence on model performance and evaluation it is felt at this stage that this is the prudent path.

For the sake of the following discussion, the metrics given by equations (5-11), (5-15), (5-19), and (5-23) will be referred to as the clear sky, difference, west-east gradient, and north-south gradient tests respectively. Figures 5-1 through 5-4 give the time series of the rejection percentages of the latter tests. The maximum clear sky rejection was about 19%, with most days showing maximum values on the order of 10-15%. The maximum difference rejection was about 29%, with most days showing maximum values on the order of 10-20%. The west-east gradient and north-south gradient tests had lower rejection rates usually less than 5%. Figures 5-5 through 5-9 give horizontal plots of the rejection categories along with visible GOES imagery at 1800 UTC for the period 1-5 September 2013. In general, the areas where the difference test was rejected are adjacent to or close to areas where the first two tiers had rejected data or where the clear sky test had rejected data. The gradient tests usually identified data points in the middle of areas with generally accepted data.

5. References

Houghton, H. G., 1984: *Physical meteorology*. Massachusetts Institute of Technology, 422 pp.

Lacis, A. A., and J. E. Hansen, 1974: A parameterization for the absorption of solar radiation in the earth's atmosphere. *J. Atmos. Sci.*, **31**, 118-133.

Paltridge, G. W., and C. M. R. Platt, 1976: *Radiative Processes in Meteorology and Climatology*, Elsever, 318 pp.

Pielke, R. A., 1984: *Mesoscale Meteorological Modeling*. Academic, 612 pp.

Savijarvi, H., 1990: Fast radiation parameterization schemes for mesoscale and short-range forecast models. *J. Appl. Meteor*., **29**, 437-447.

Yamamoto, G., 1962: Direct absorption of solar radiation by atmospheric water vapor, carbon dioxide and molecular oxygen. *J. Atmos. Sci.*, **19**, 182-188.

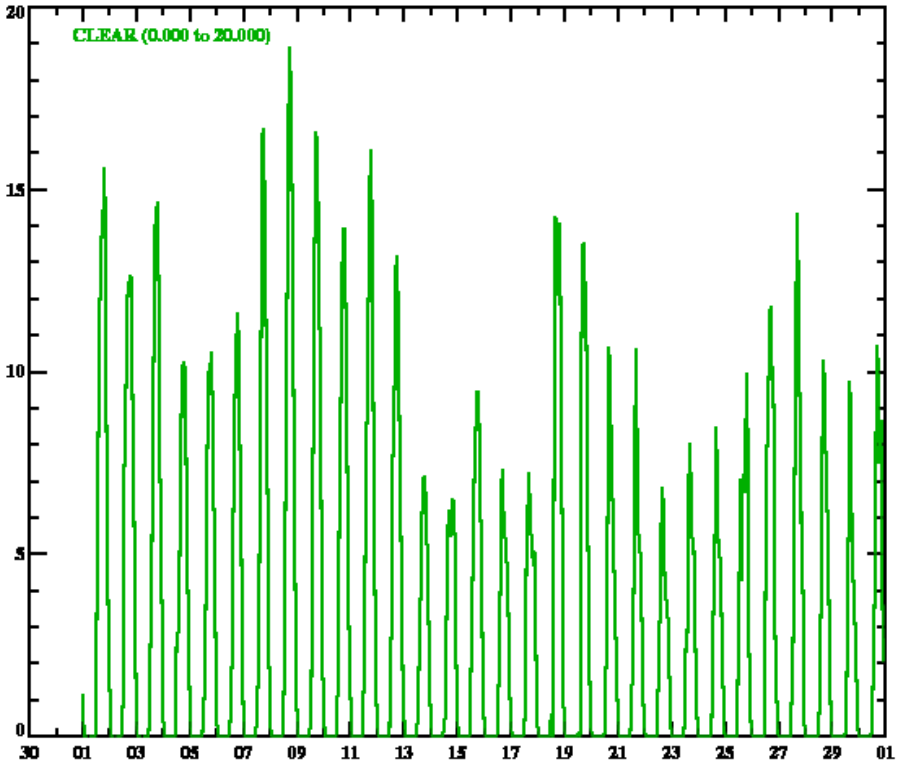

Figure 5-1 Percentage of points rejected by the clear sky test for the month of September 2013.The y axis is percent and x-axis is day of the month.

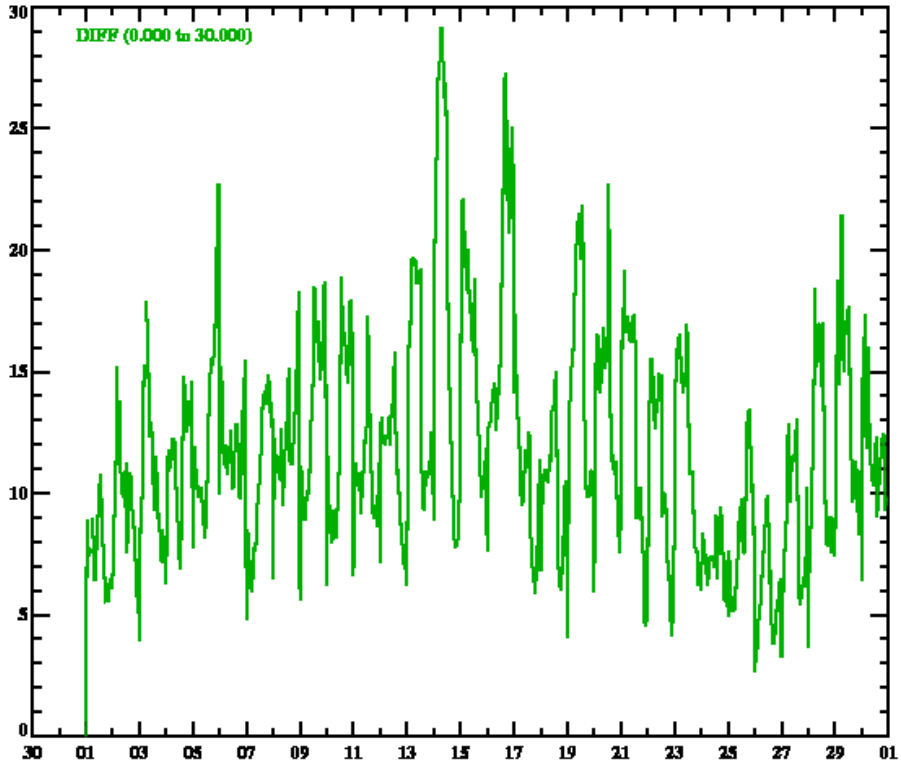

Figure 5-2 Percentage of points rejected by the difference test for the month of September 2013. The y axis is percent and x-axis is day of the month.

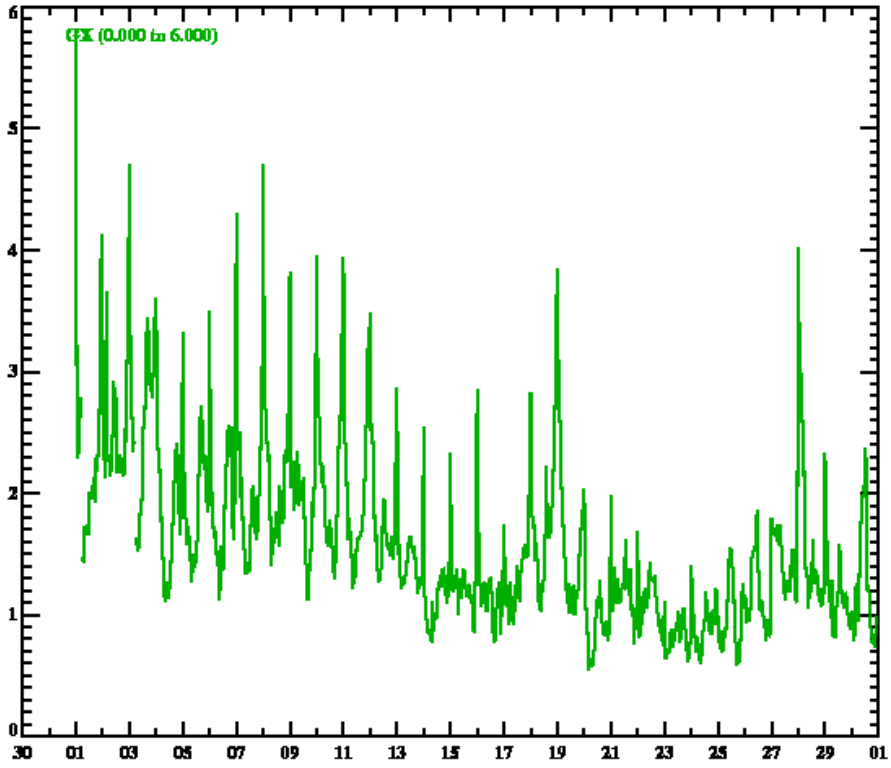

Figure 5-3 Percentage of points rejected by the west-east gradient test for the month of September 2013. The y axis is percent and x-axis is day of the month.

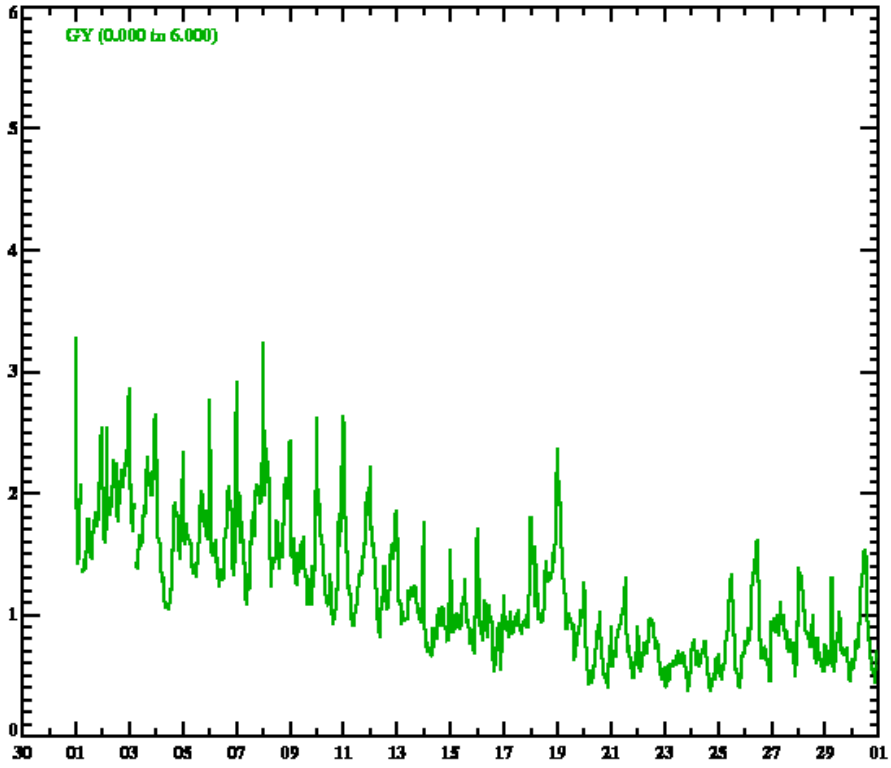

Figure 5-4 Percentage of points rejected by the north-south gradient test for the month of September 2013. The y axis is percent and x-axis is day of the month.

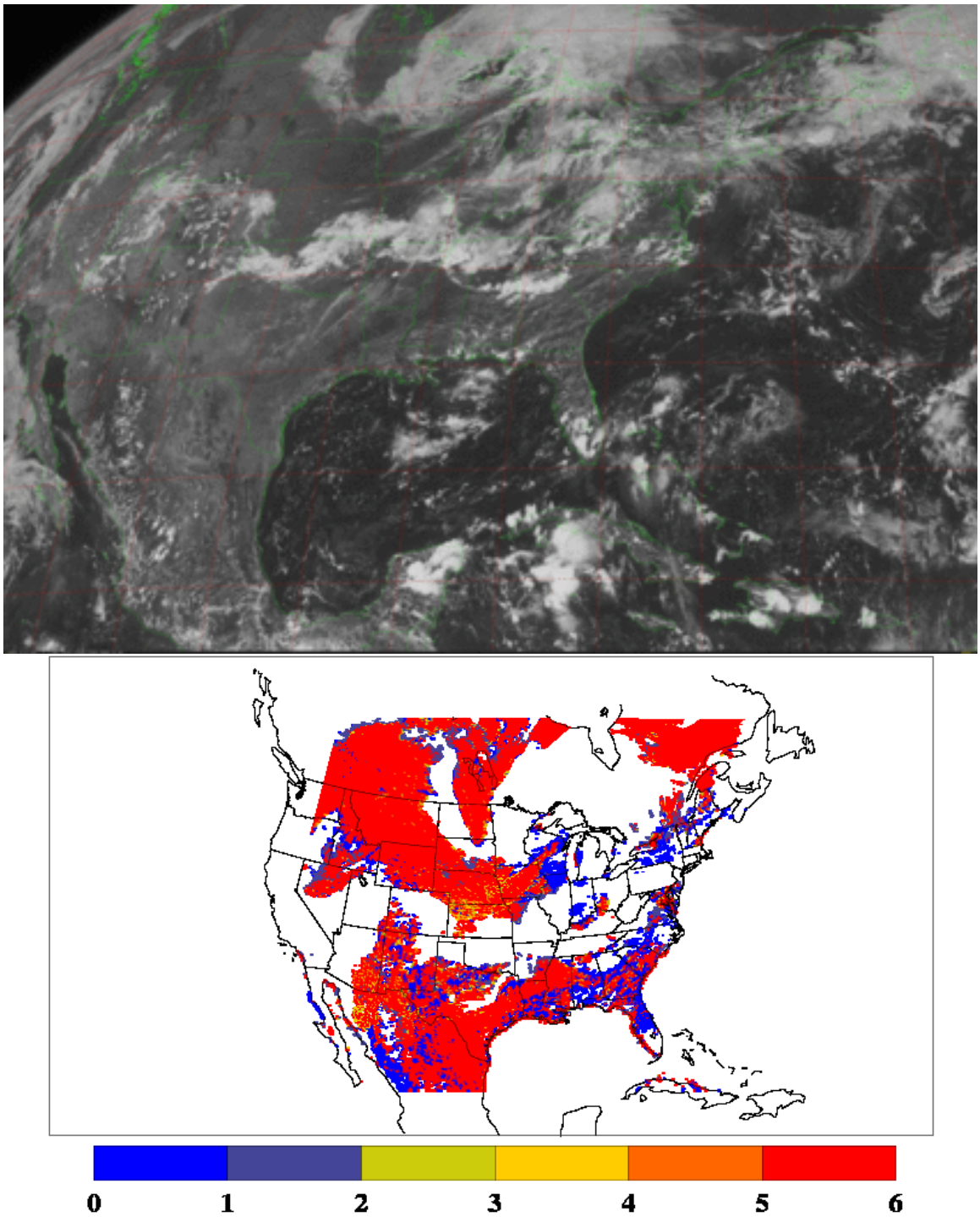

Figure 5-5 (Top) GOES visible image for 1832 UTC 1 September 2013. (Bottom) Rejection categories for the observed GOES NOAA Alexi skin temperature for 1815 UTC 1 September 2013. Colors correspond to the following: 1) blue, failed clear sky insolation test, 2) purple, failed difference test, 3) green, failed west-east gradient test, 4) yellow, failed north-south gradient test, and 5) red, accepted values. White areas mean no change in the accepted values of clouds from the first and second pass screening..

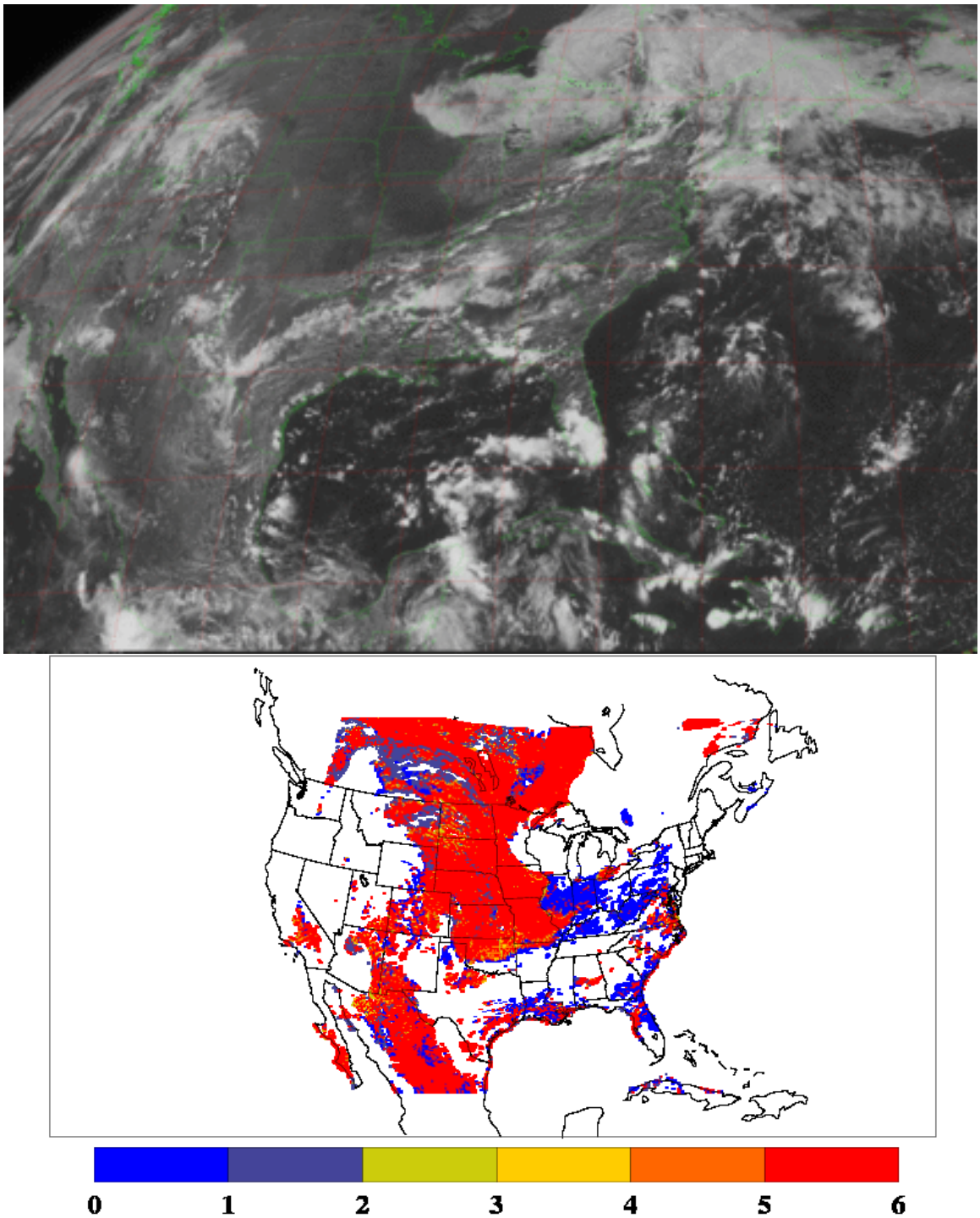

Figure 5- 6 (Top) GOES visible image for 1825 UTC 2 September 2013. (Bottom) Rejection categories for the observed GOES NOAA Alexi skin temperature for 1815 UTC 2 September 2013. Colors correspond to the following: 1) blue, failed clear sky insolation test, 2) purple, failed difference test, 3) green, failed west-east gradient test, 4) yellow, failed north-south gradient test, and 5) red, accepted values. White areas mean no change in the accepted values of clouds from the first and second pass screening..

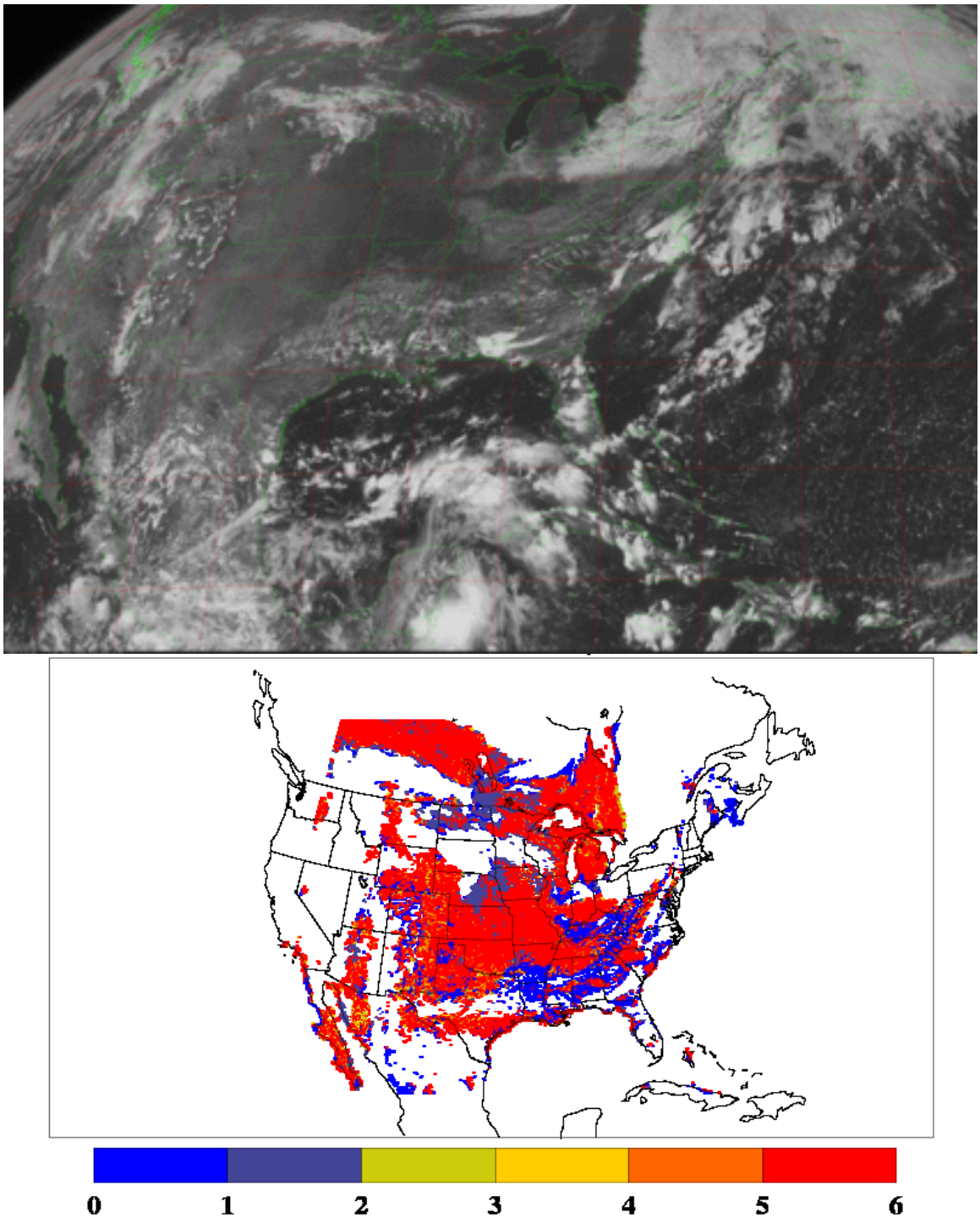

Figure 5-7 (Top) GOES visible image for 1825 UTC 3 September 2013. (Bottom) Rejection categories for the observed GOES NOAA Alexi skin temperature for 1815 UTC 3 September 2013. Colors correspond to the following: 1) blue, failed clear sky insolation test, 2) purple, failed difference test, 3) green, failed west-east gradient test, 4) yellow, failed north-south gradient test, and 5) red, accepted values. White areas mean no change in the accepted values of clouds from the first and second pass screening.

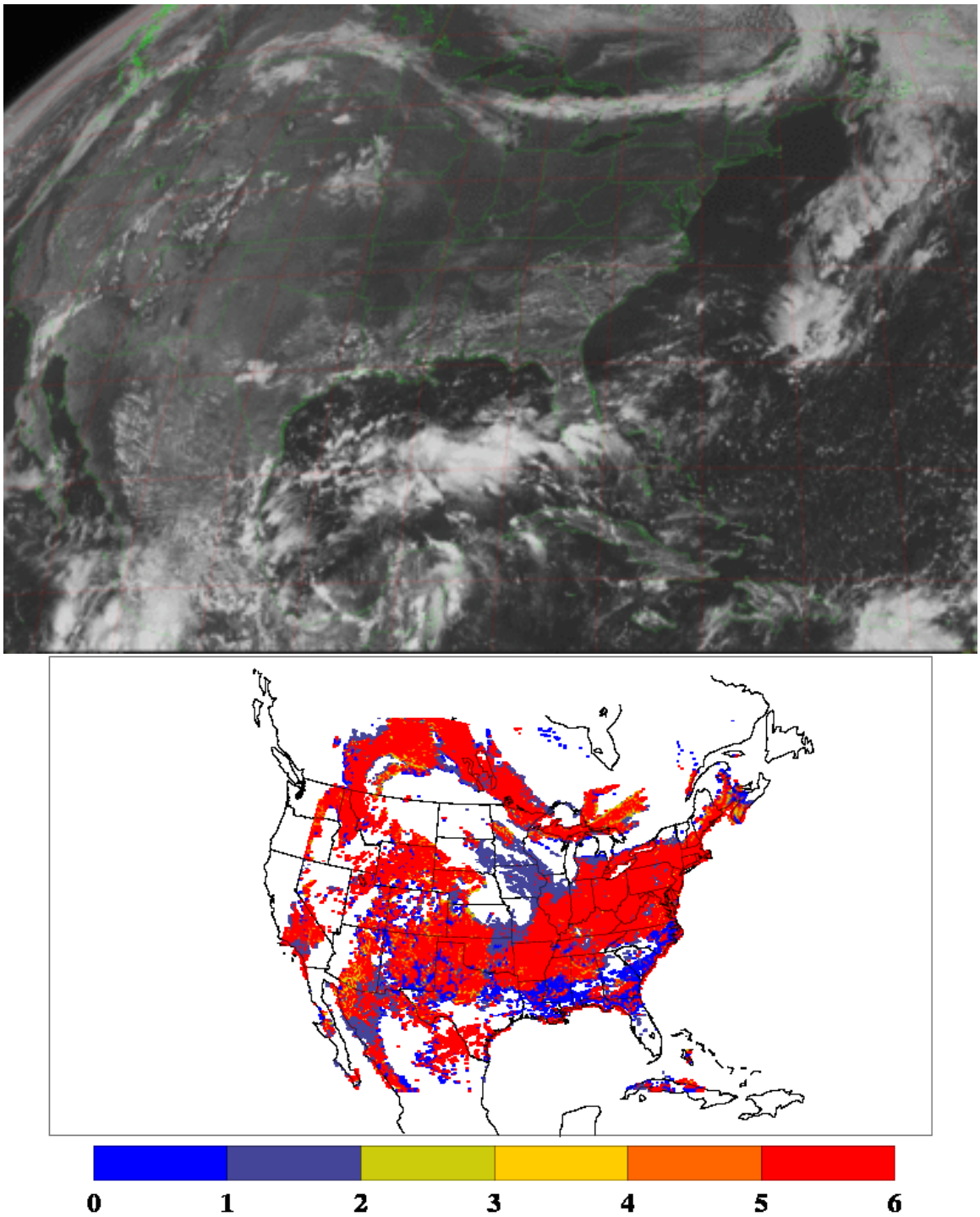

Figure 5-8 (Top) GOES visible image for 1825 UTC 4 September 2013. (Bottom) Rejection categories for the observed GOES NOAA Alexi skin temperature for 1815 UTC 4 September 2013. Colors correspond to the following: 1) blue, failed clear sky insolation test, 2) purple, failed difference test, 3) green, failed west-east gradient test, 4) yellow, failed north-south gradient test, and 5) red, accepted values. *White areas mean no change in the accepted values of clouds from the first and second pass screening.*

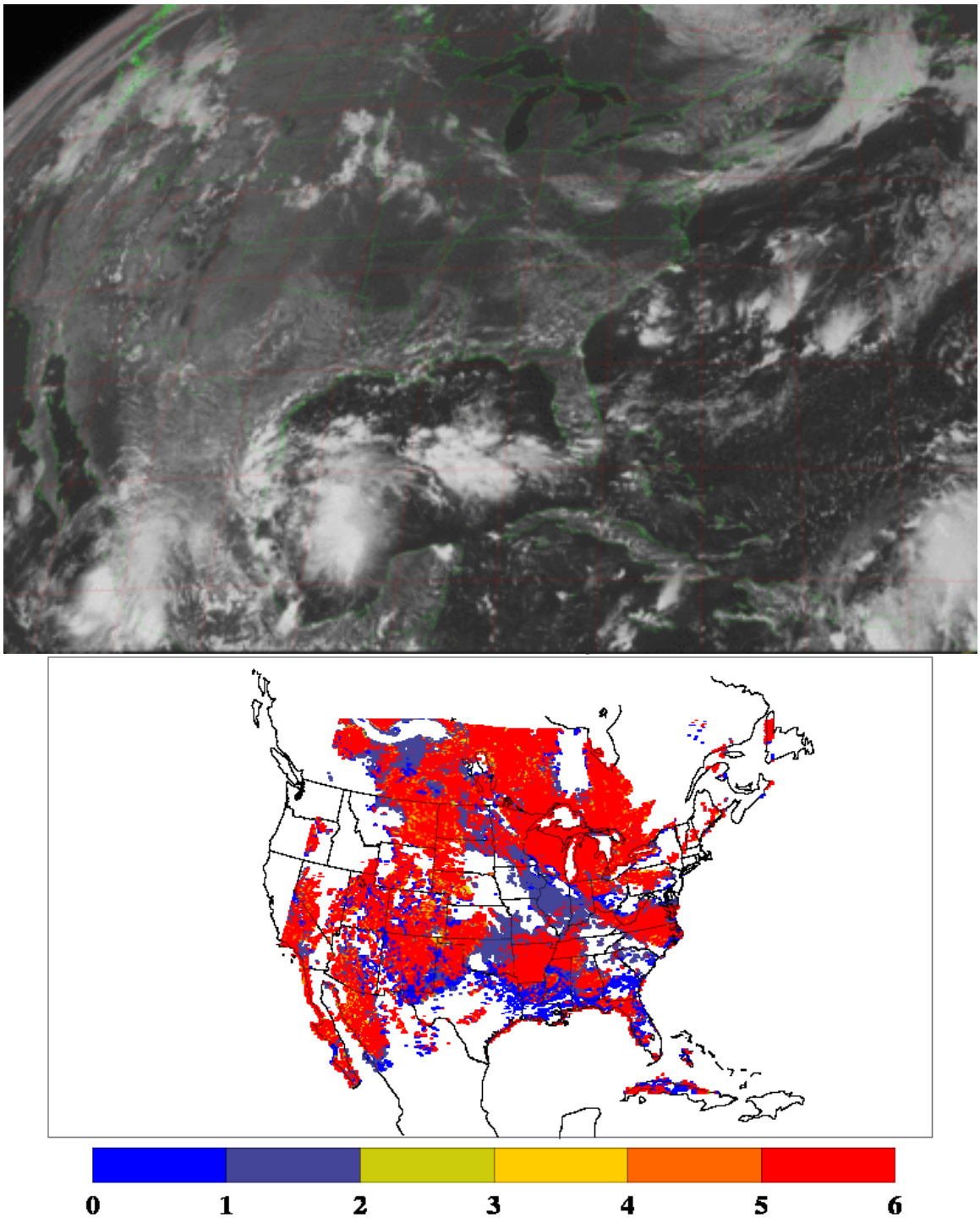

Figure 5-9 (Top) GOES visible image for 1825 UTC 5 September 2013. (Bottom) Rejection categories for the observed GOES NOAA Alexi skin temperature for 1815 UTC 5 September 2013. Colors correspond to the following: 1) blue, failed clear sky insolation test, 2) purple, failed difference test, 3) green, failed west-east gradient test, 4) yellow, failed north-south gradient test, and 5) red, accepted values. White areas mean no change in the accepted values of clouds from the first and second pass screening.

Chapter 6 Tests of Moisture Nudging Using Satellite Skin Temperatures

6. Introduction

In the this project, it was first proposed that satellite skin temperatures might be a better metric for model performance than standard NWS data in large part because of their ability to capture land use variations at fine resolution. Second, that satellite skin temperatures might be used to improve the specification of land surface parameters in land surface models. This chapter describes the second aspect of the project, which is the use of satellite skin temperatures to adjust soil moisture in a new version of the Pleim-Xiu (PX) model in a similar way that observed surface air temperatures are used to adjust moisture in the current PX model. It also explores the use of satellite skin temperatures to adjust the surface thermal resistance, which is another land use parameter which is highly uncertain. This chapter describes the second aspect of the project which is the use of satellite skin temperatures. In section 5 of this chapter the impact of the moisture nudging is described in detail for the first 5 days (September 1-September 6, 2013) including detailed time series at a sequence of selected points. In section 6 of this report the results of the full month simulation is provided including maps and statistical performance.

7. Description of Skin Temperature Nudging Within The Pleim-Xiu Model

Chapter 3 described the skin temperature products and their evaluation. As noted in that chapter, an alternative skin temperature which is a single channel retrieval by NOAA NESDIS that supports the ALEXI suite of products will be used in the land surface adjustment process. Xiu and Pleim (2001) noted that since surface moisture is not a direct observable that use of auxiliary information is needed. They have used observed NWS surface temperatures to nudge moisture. Here they adjust surface layer moisture w_G using the difference between model daytime temperatures (T^F) and analyses of observed temperatures (T^A) and model and observed relative humidity as in equation (6-1).

$$\Delta w_G = \alpha_1\left(T^A - T^F\right) + \alpha_2\left(RH^A - RH^F\right)_{Daytime} \quad (6\text{-}1)$$

The Pleim-Xiu approach has been widely used and in recent California inter-comparisons performed better than the Noah complex land surface model (Fovell 2013). Because observed NWS observations are coarse we proposed to replace the observed temperatures with satellite skin temperatures, i.e.

$$\Delta w_G = \beta_1(T_s^{Sat} - T_s^{Mod})_{Morning} \quad (6\text{-}2)$$

where the nudging will be applied in the morning time frame. While the nudging in the original assimilation in equation (6-2) was applied throughout the day, here we believe it best to only nudge moisture during the morning hours for two reasons. The first is that skin temperature response is most sensitive to moisture in the morning hours (Carlson 1986). Second, because of afternoon cumulus clouds there is also a greater chance that undetected clouds may contaminate the surface skin temperature satellite retrieval.

The observed satellite skin temperatures used in this investigation are described in chapter 3 and is based on a single channel retrieval used by the NOAA/USDA ALEXI group (Anderson et al. 2007a and Anderson et al. 2007b). A summary of the changes required in the WRF system for the revised Pleim-Xiu model is given in Appendix B.

8. Differences Between Satellite and Model Skin Temperatures

The assumption in the skin temperature assimilation process in equation (6-2) is that where model temperatures are cooler than observed temperatures then moisture will be reduced so that more energy will be partitioned into sensible heating rather than evaporation. On the other hand, where model skin temperatures are warmer than observed skin temperatures, then moisture will be increased. This is similar to the original PX moisture nudging by air temperatures. In order to see what differences exist in skin temperatures between model and satellite and the potential for changing surface moisture, Figure6-1 shows the mean difference between model and observed satellite data for the month of September 2013.

In the Eastern and Midwestern U.S. it can be seen that there are subtle differences between the model and satellite skin temperatures in corn growing regions in Iowa, Illinois and Indiana where the model is too cool. This is likely due to the fact that by September corn has senesced - it is has completed its kernel filling stage and leaves have 'browned up' and it is no longer transpiring. Thus, model moisture may be too high causing the model to under predict temperatures. The senescence would also cause an increased albedo over that of actively growing corn which would produce a cooler surface. However, in this case the lack of transpiration is likely overcoming the cooling due to albedo change as McNider et al. (1994) found for winter wheat in Oklahoma. Thus, the differences seen here and which seem physical give hope that the model can be nudged to a drier state and warmer solution more consistent with observations.

In Figure 6-1 the biggest areas of disagreement are in the West. Here the model is greatly underestimating the skin temperatures compared to the satellite observations. Based on the adjustment paradigm, it would be expected that the model may have moisture values that are too high or heat capacity values that are too low.

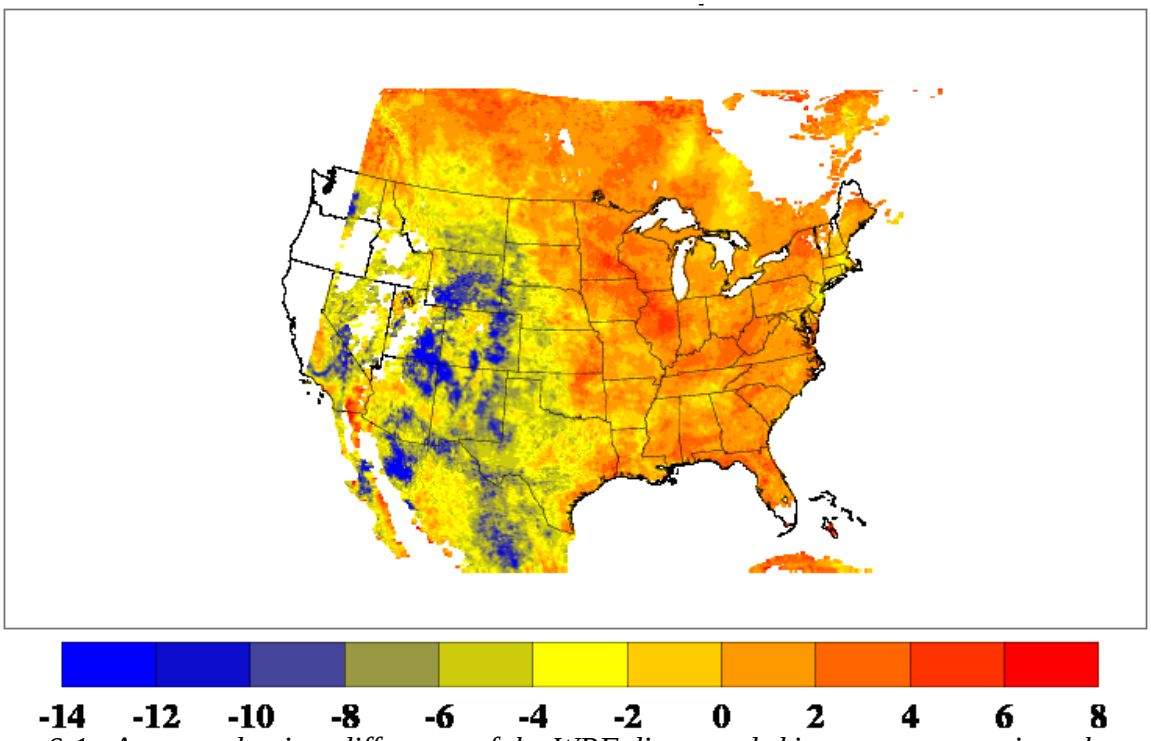

Figure 6-1. Average daytime difference of the WRF diagnosed skin temperature minus the NOAA ALEXI observed skin temperature for the period 0000 UTC 1 September 2013 through 0000 UTC 6 September 2013. The NOAA ALEXI observed skin temperatures are the most recent version with aggressive cloud screening. Simulation is the insolation replacement run with the old (Pleim) vegetation fraction. Values truncated between -14 and +8 degrees K.

In preliminary runs of the assimilation technique one of the disappointing features is that in areas in the West, which showed large differences between model and observed skin temperatures showed little difference after the moisture nudging. In starting our investigation it was found, however, that at least part of the issue was that in those areas where temperature was drastically under-predicted, there were large fractions of vegetation used in the model in contrast with what can be seen in visible images. Figure 6-2 shows the vegetation fraction used in the PX model. It shows that most of the domain has high fractions of vegetation. This is in contrast to the original USGS land use classes (see Figure 6-3). In examining the PX code it was found a seasonal growth algorithm to attempt to correct vegetation fraction in which temperature is used to adjust the vegetation fraction. It appears based on the USGS vegetative fractions and visible images that the seasonal adjustment is producing unrealistic vegetative fractions (at least for September).

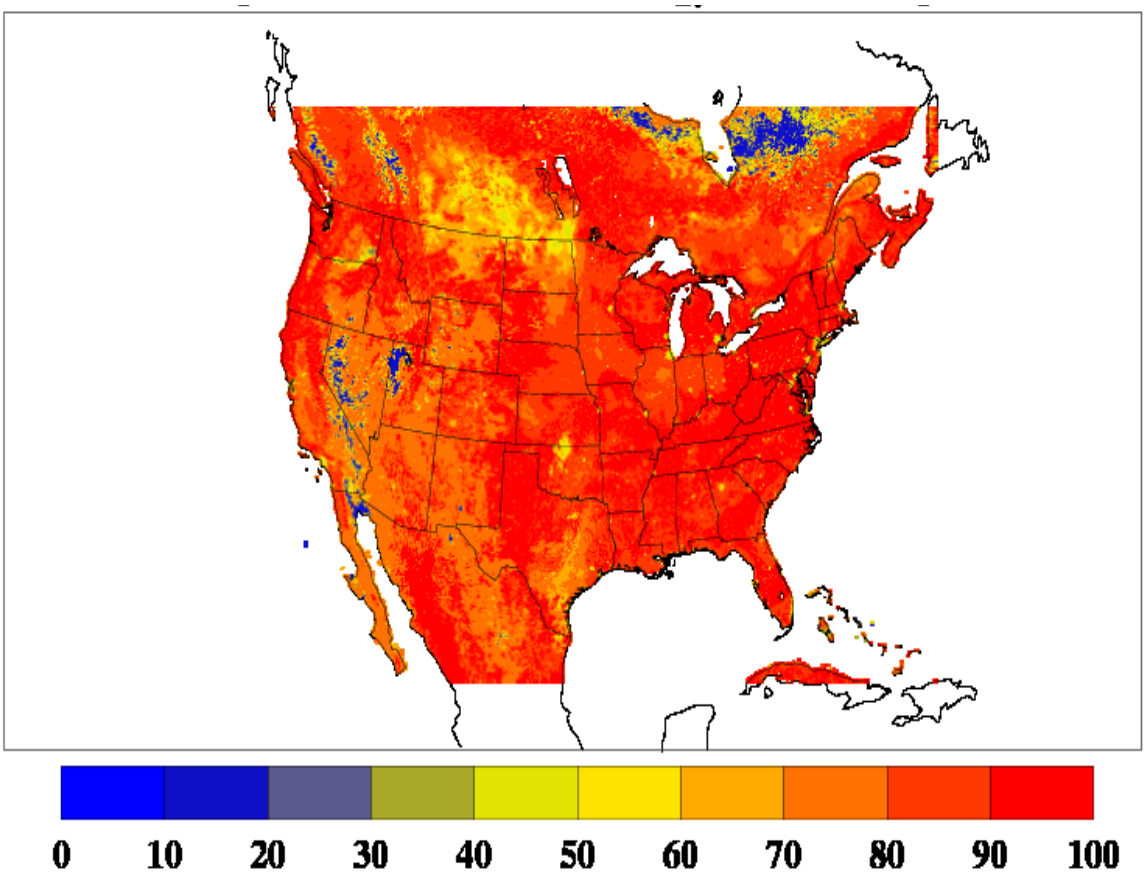

Figure 6-2 Pleim-Xiu vegetation fraction for 1800 UTC 1 September 2013 for the control simulation for September 2013.

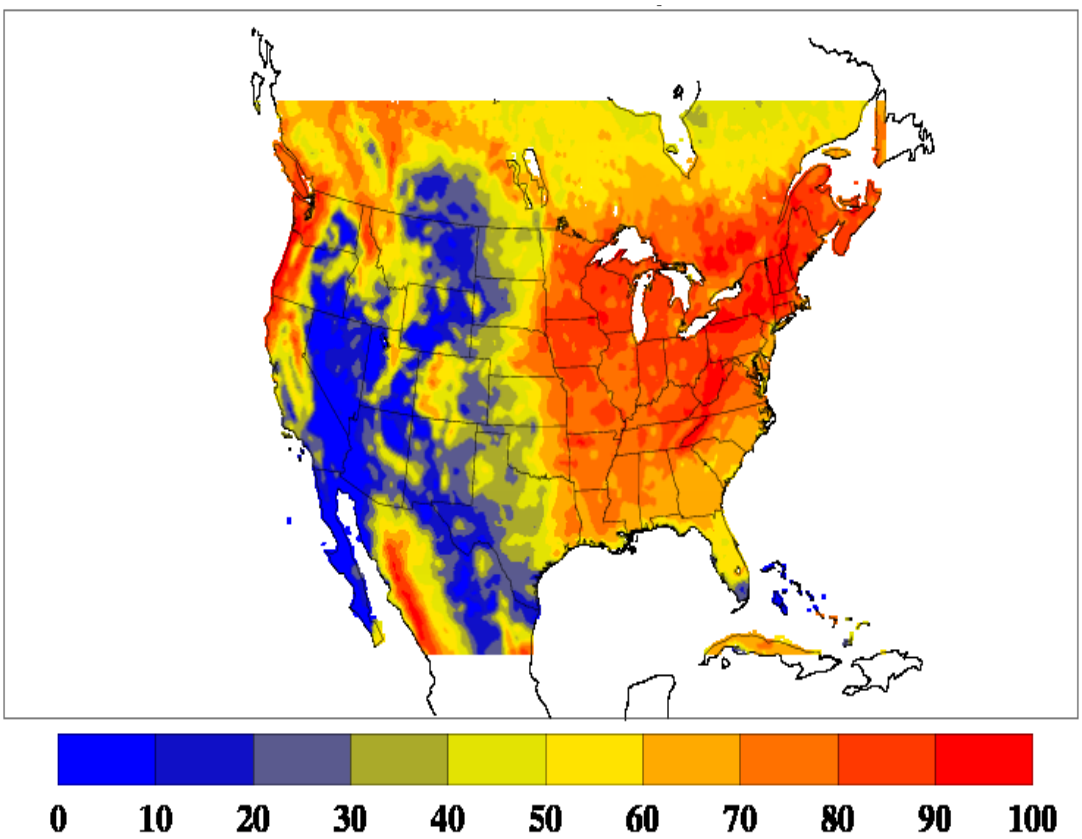

Figure 6-3. WRF USGS vegetation fraction for 1800 UTC 1 September 2013 for the control simulation for September 20

Figure 6-4 provides the difference between the new WRF control simulation and the observed satellite skin temperature. This is the same information as Figure 6-1 except it includes the changes in the control run (USGS vegetation fraction). As can be seen the use of the raw USGS vegetation fraction rather than the default PX seasonally adjusted vegetation fraction has reduced the area and magnitude of the disagreement especially in the western part of the domain. It is noted that in personal communication with Jon Pleim that they also are looking at changing their vegetation fraction calculation and perhaps moving to a MODIS vegetation fraction (Ran et al 2014). Figure 6-4 provides the WRF control simulation to be used in assessing the impact of moisture nudging by skin temperatures.

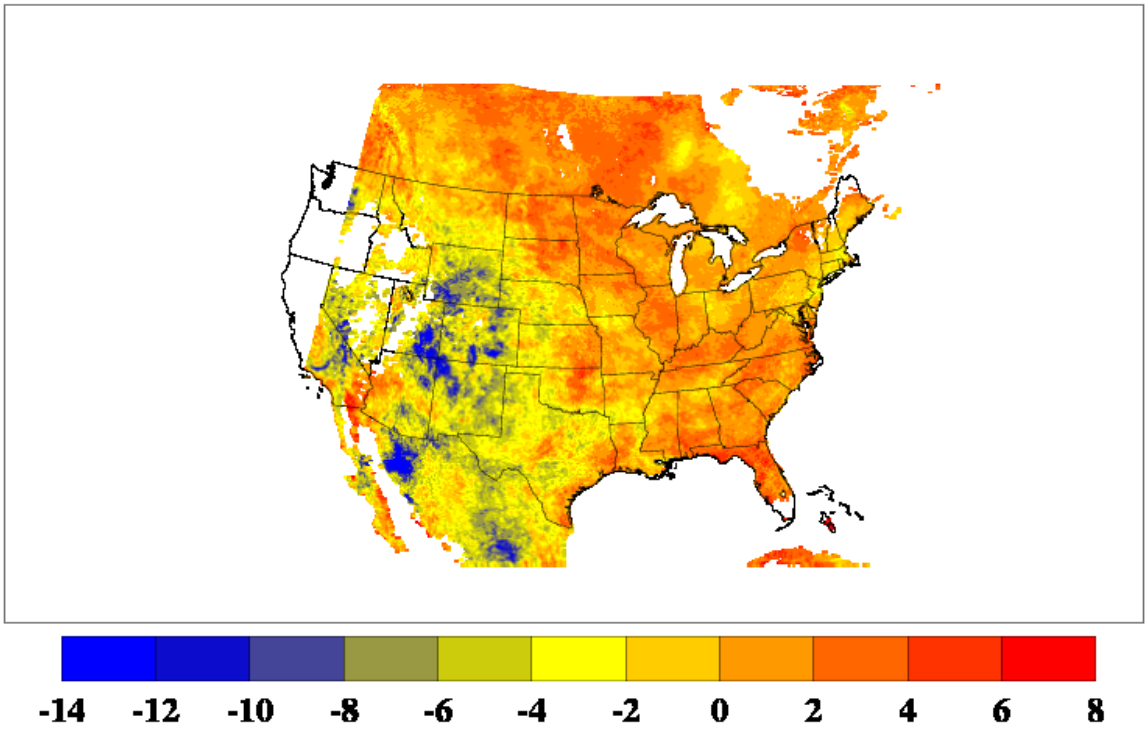

Figure 6-4. Average daytime difference of the WRF diagnosed skin temperature minus the NOAA ALEXI observed skin temperature for the period 0000 UTC 1 September 2013 through 0000 UTC 6 September 2013. The NOAA ALEXI observed skin temperatures are the most recent version with aggressive cloud screening. Simulation is the insolation replacement run with the new (USGS) vegetation fraction and without any nudging. Values truncated between -14 and +8 degrees K. White areas indicate no satellite data

9. Defining Statistical Measures for Assessing Impact of Skin Temperature Nudging

After the first set of runs using the skin temperature it was decided to make some changes in the model and protocols. The nudging coefficient, β_1, was set to a time scale of a few minutes which provides for a fairly fast assimilation. First, it was felt that with the short time available in the morning for assimilation that a stronger nudging coefficient be used than was employed in the original PX form which continuously assimilated the NWS observations.

Second, because in the PX model ET from vegetation is only impacted by deep layer moisture (W_2) it was decided to nudge the deep soil moisture in a similar fashion to the first layer moisture given in (6-2), i.e.

$$\Delta W_2(x,y,t) = \beta_1(T_{SO}\ (x,y,t) - T_{SM}\ (x,y,t))_{morning} \quad . \quad (6\text{-}3)$$

In order to make comparisons of the impact of the assimilation it was felt that the control run that did not include the 2-m NWS nudging was a more appropriate control. With this WRF control run a pure comparison of the impact of the skin temperature can be seen. In the end a comparison with the PX 2-m nudging will be made but to understand the impact of the satellite skin temperature nudging this is a better control. The control run included the satellite insolation forcing. The WRF control will be referred to as WRF-CONTR and seen in Figure 6-4.

The WRF skin temperature nudging run (hereafter referred to as WRF-TS) was run in the same configuration.

Three statistics are used to evaluate whether the case with skin temperature nudging (WRF-TS) was providing an improvement over the control case (WRF-CONTR). These are defined below.

$$B_I = \left| \frac{1}{n} \sum_{t=1}^{n} \left(T_{WI} - T_{OBS} \right) \right| \tag{6-4}$$

$$B_N = \left| \frac{1}{n} \sum_{t=1}^{n} \left(T_{WN} - T_{OBS} \right) \right| \tag{6-5}$$

$$P = \frac{100\left(B_N - B_I \right)}{B_I} \tag{6-6}$$

B_I is the magnitude of the skin temperature bias for the insolation replacement run as in equation (6-4), where n is the total number of comparisons pairs, T_{WI} is the WRF diagnosed skin temperature for the WRF-CONTR, and T_{OBS} is the NOAA-Alexi GOES-derived skin temperature. In a similar manner B_N is the magnitude of the skin temperature bias for the insolation replacement plus soil nudging run as in equation (6-5), where T_{WN} is the WRF-TS diagnosed skin temperature for the run. The comparison statistic is then provided by equation 6-6 which gives the percentage change in bias between the insolation and nudging runs.

10. Model Impact Using Skin Temperature Differences to Nudge Surface Soil Moisture

The soil moisture nudging as given is now tested using the statistical measures discussed above.
Figure 6-5 U.S. map showing average daytime difference between WRF diagnosed skin temperature and the NOAA ALEXI observed skin temperature for 1 Sep 2013 to 6 Sep 2013
Figure 6-6 U.S. map showing percentage change in the magnitude of the soil nudging bias relative to the magnitude of the insolation bias.

Figure 6-7 U.S. map showing difference between the magnitudes of the soil nudging bias relative to the magnitude of the insolation bias.

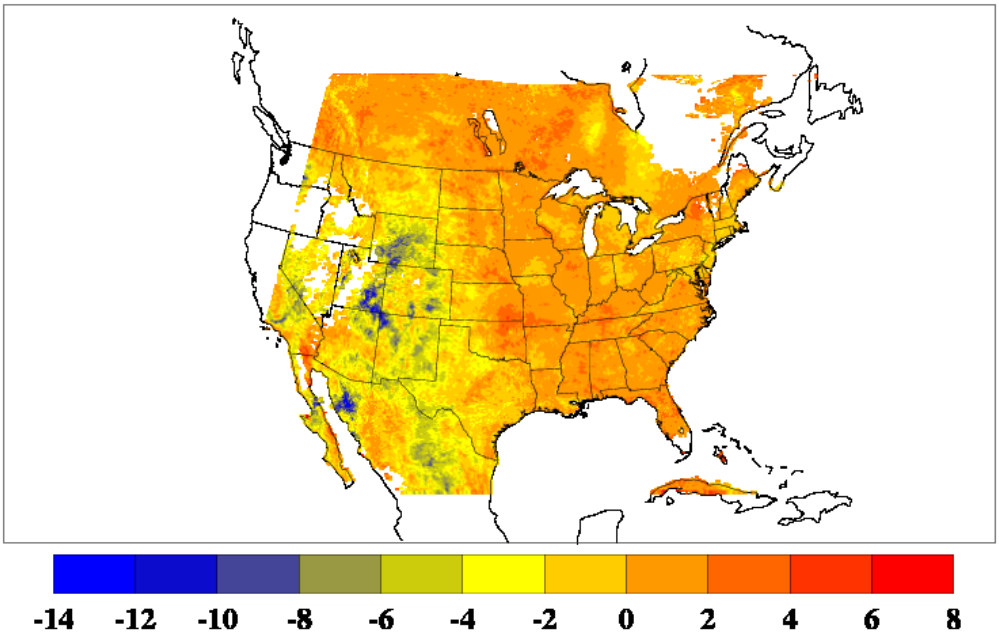

Figure 6-5. Average daytime difference of the WRF diagnosed skin temperature minus the NOAA ALEXI observed skin temperature for the period 0000 UTC 1 September 2013 through 0000 UTC 6 September 2013. The NOAA ALEXI observed skin temperatures are the most recent version with aggressive cloud screening. Simulation is the insolation replacement run with the new (USGS) vegetation fraction with soil nudging (shallow and deep) with a nudging time scale of 600 s. White areas indicate no data. Values are in degrees K.

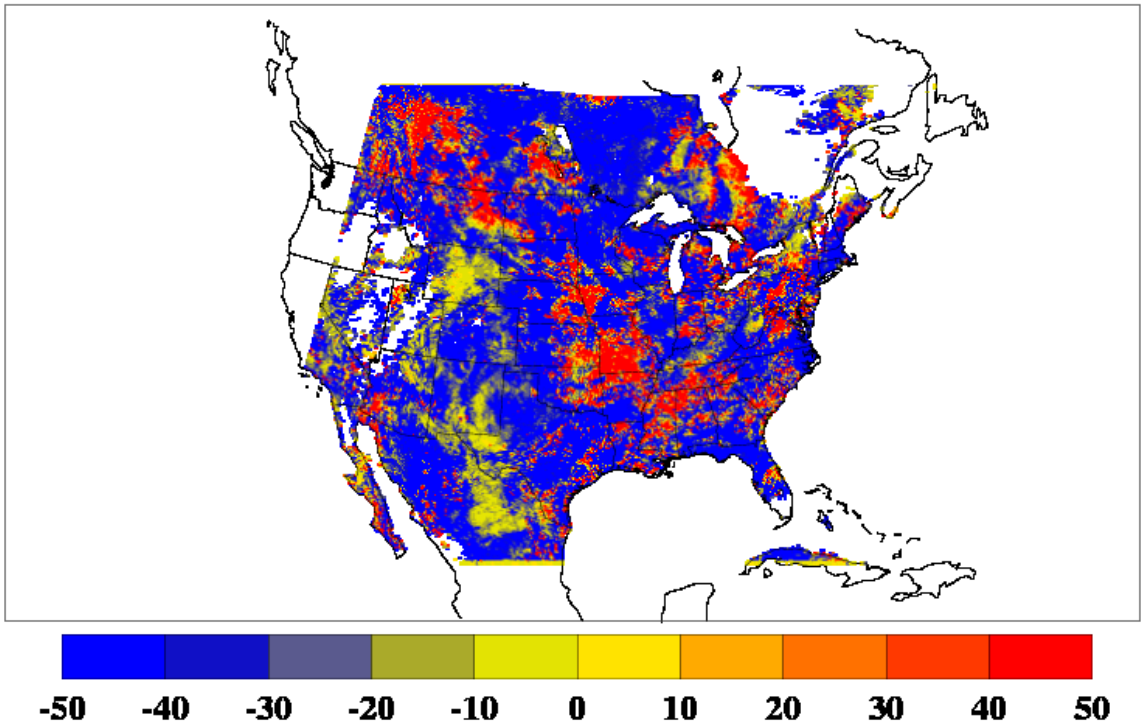

Figure 6-6. Percentage change of the magnitude of the soil nudging bias (BN, absolute value of bias) relative to the magnitude of the insolation bias (BI, absolute value of bias) as given by 100 (BN – BI) / BI. This is the P statistic given by equation (7). Values truncated to ± 50 %. Both simulations used the USGS vegetation fraction. The NOAA ALEXI observed skin temperatures are the most recent version with aggressive cloud screening. Both simulations are for the period 0000 UTC 1 September 2013 through 0000 UTC 6 September 2013. Bias values are daytime only. White areas indicate no satellite data

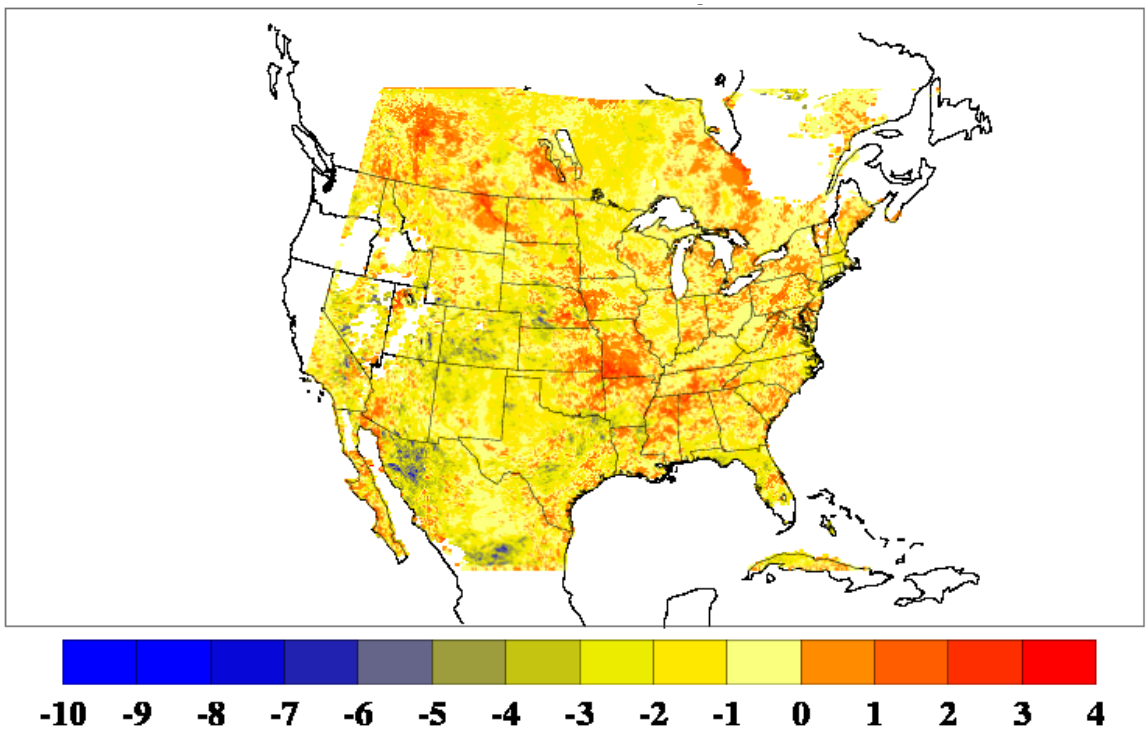

Figure 6-7 Difference between the magnitude of the soil nudging bias (BN, absolute value of bias) and the magnitude of the insolation bias (BI, absolute value of bias) as given by BN – BI in units of K. This is an unscaled version of the P statistic given in (6-6) - i.e. without the division of by $B_{I.}$ The NOAA ALEXI observed skin temperatures are the most recent version with aggressive cloud screening. Both simulations are for the period 0000 UTC 1 September 2013 through 0000 UTC 6 September 2013. Bias values are daytime only because of lack of ability to detect nighttime clouds. Same information as in Figure 6.6 but not normalized with respect to the insolation bias. Negative values (cool colors) correspond to a reduction in the magnitude of the bias, and positive values (warm colors) correspond to an increase in the magnitude of the bia. White areas indicate no satellite data

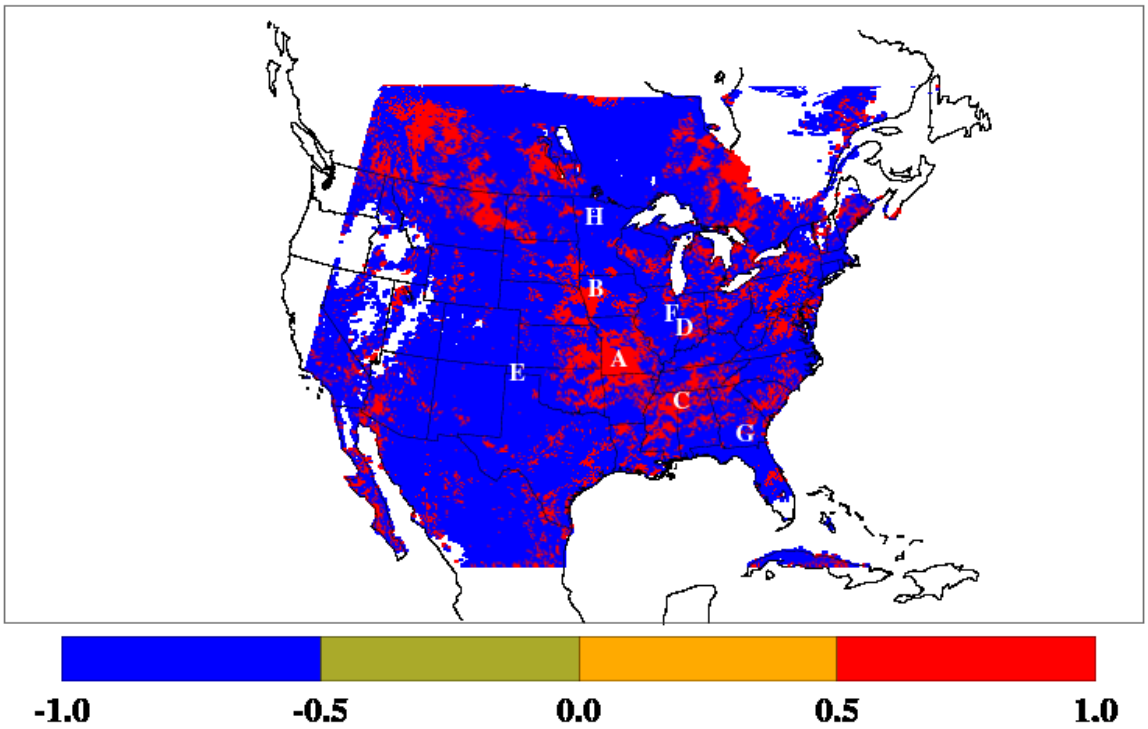

Figure 6-8. Sign of the percentage change in bias from Figure 6-8. Negative areas indicate a reduction in bias whereas positive areas indicate an increase in bias. Key and locations used in the following time series plots are as follow: A- southwestern Missouri, B-western Iowa, C-northwestern Alabama, D-southern Indiana, E- northern Texas, F-eastern Illinois, G-southwestern Georgia, and H-northern Minnesota. Locations A-D correspond to locations with bias degradation, and locations E-H correspond to locations with bias improvement. White areas indicate no satellite data

Next an investigation is made of the behavior of the surface temperatures and soil moisture to try to understand both the improvement and degradation. This is accomplished by examining time series at the points identified in Figure 6-8. The time series are provided in Figs. 6-9 through 6-24. The figures provide model skin temperatures for the control case (WRF-CONTR-green) and for the satellite skin temperature assimilation case (WRF-TS-blue). The satellite skin temperature is also provided in red. Following each of these skin temperature time series is a figure for the same location that provides a time series of soil moisture both for the control case (WRF-CONTR green) and assimilation (WRF-TS-blue) that shows the impact of the moisture nudging.

Figure 6-9 provides the series for one of the places (point A in Missouri) where the average behavior for the point showed degradation. It can be seen, that on the second day when data was available for assimilation, the technique worked as expected and the moisture was reduced (6-11) and brought the temperature closer to the observation. However, on the third day observed skin temperatures were lower and while there was some moistening of the soil it was not enough to lower the skin temperature. This appears to be a case where the morning temperature difference between the model and observations are close so no adjustment would be made. The cooling in the skin temperature later in the day might be due to cold air advection not captured in the model

external analysis or perhaps cloud contamination. A similar situation occurs on the fourth and fifth day in that there is no information that justifies moistening the system. Further investigation using more aggressive cloud removal and adjustment of thermal resistance may give better performance.

Figure 6-11 for point B in Iowa shows a similar pattern with improvement the first day with drying but degradation in the following days. However, the technique is moistening the system (Figure 6-12) and in fact returns back to the control value the last day.

Figure 6-13 shows the time series for point C in northwest Alabama. The differences on the first and fourth day in the afternoon may be due to cloud contamination. There was actually little change in moisture over the period (6-14).

Figure 6-15 for point D in southern Indiana shows excellent results early in the period. However, later in the period the nudging case with the drying is warmer than observations. This may be due to the fact that there was no additional information skin temperature data in the morning to nudge to moister conditions. It also may be cloud contamination.

Figure 6-17 for point E in northern Texas is a case where the nudging technique improved the bias compared to the control runs. However, even with substantial drying over the period it could not match the high observed skin temperatures. Since both minimum and maximum temperatures were lower and higher respectively than the model, this is likely a case where thermal resistance in the model is too high.

Figure 6-19 is for point F in eastern Illinois. In this case the nudging improved performance. This is also a case where the soil is moistened rather than dried by the nudging technique (see 6-20).

Figure 6-21 for point G in southwest Georgia is similar to the Illinois case but shows moistening early in the period and drying later in the period. Figure 6-23, for point H in Minnesota, shows another case where moistening improved the model results.

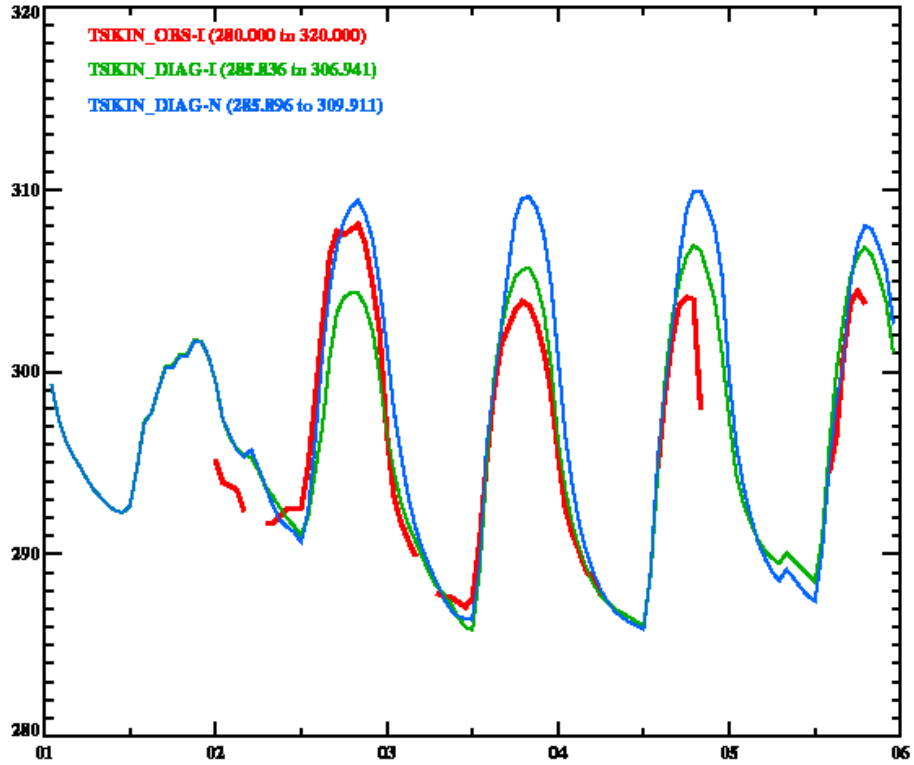

Figure 6-9. Time series for 0000 UTC 1 September 2013 through 0000 UTC 6 September 2013 for southwestern Missouri (location code "A") for the following temperature variables: 1.) observed NOAA-Alexi skin temperature (red, labeled as TSKIN_OBS-I), 2.) WRF diagnosed skin temperature from the insolation simulation (green, labeled as TSKIN_DIAG-I), and 3). WRF diagnosed skin temperature from the insolation plus soil moisture nudging (shallow and deep) simulation (blue, labeled as TSKIN_DIAG-N). This is a location where the magnitude of the bias increased with soil nudging. The y-axis is in degrees K and x-axis is in days.

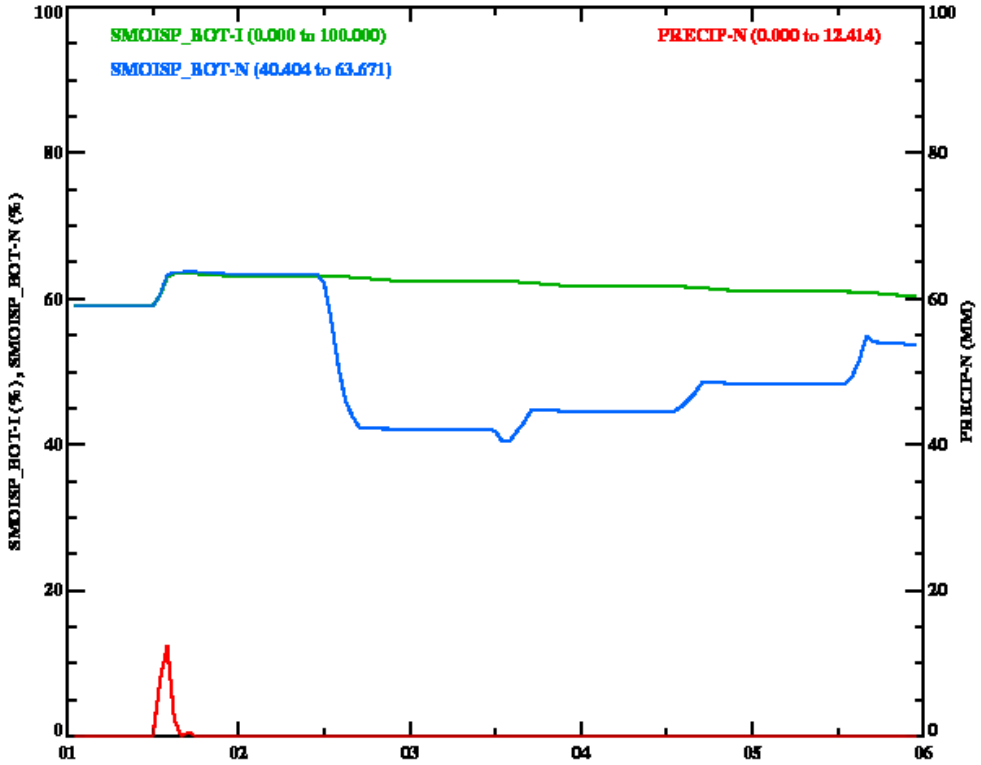

Figure 6-10. Time series for 0000 UTC 1 September 2013 through 0000 UTC 6 September 2013 for southwestern Missouri (location code "A") for the following soil moisture variables: 1.) WRF deep layer soil moisture as a percentage of saturation from the insolation simulation (green, labeled as SMOISP_BOT-I), and 2). WRF deep layer soil moisture as a percentage of saturation from the insolation plus soil moisture nudging (shallow and deep) simulation (blue, labeled as SMOISP_BOT-N). Hourly WRF precipitation (mm) is in red and plotted with respect to the right vertical axis. This is a location where the magnitude of the bias increased with soil nudging. The x-axis is in days.

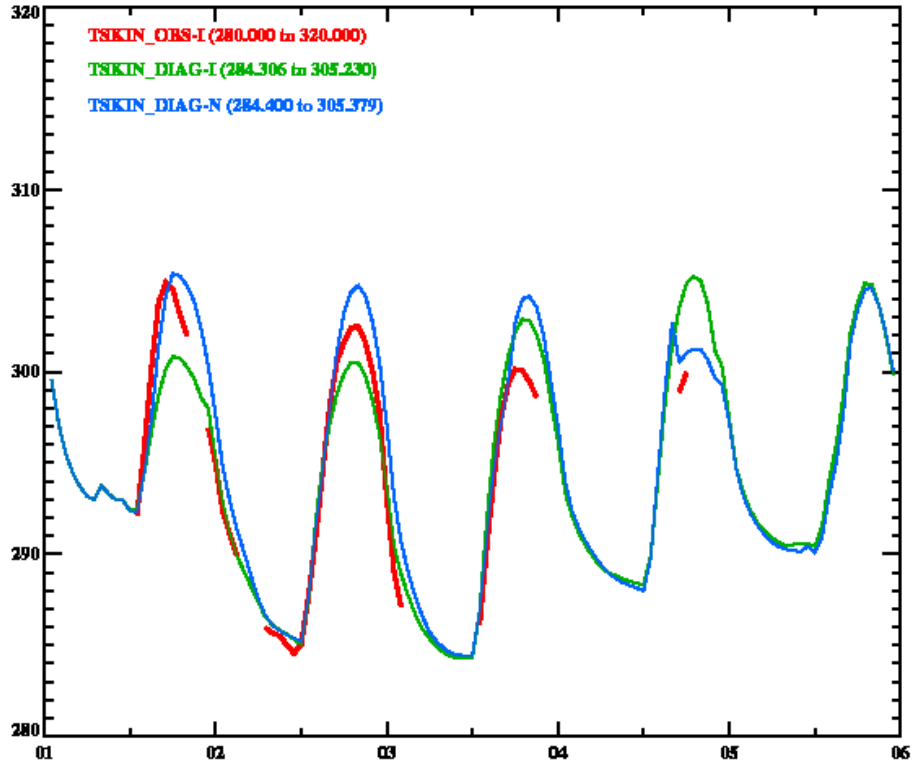

Figure 6-11. Time series for 0000 UTC 1 September 2013 through 0000 UTC 6 September 2013 for western Iowa (location code "B") for the following temperature variables: 1.) observed NOAA-Alexi skin temperature (red, labeled as TSKIN_OBS-I), 2.) WRF diagnosed skin temperature from the insolation simulation (green, labeled as TSKIN_DIAG-I), and 3). WRF diagnosed skin temperature from the insolation plus soil moisture nudging (shallow and deep) simulation (blue, labeled as TSKIN_DIAG-N). This is a location where the magnitude of the bias increased with soil nudging. The y-axis is in degrees K and x-axis is in days.

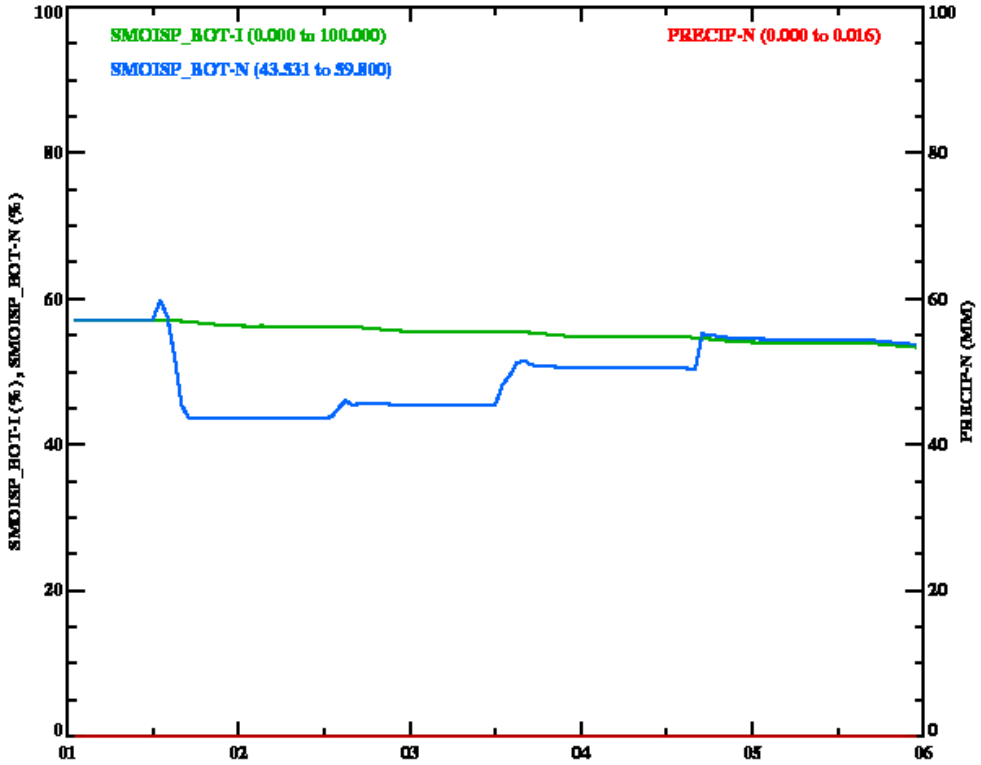

Figure 6-12. Time series for 0000 UTC 1 September 2013 through 0000 UTC 6 September 2013 for western Iowa (location code "B") for the following soil moisture variables: 1.) WRF deep layer soil moisture as a percentage of saturation from the insolation simulation (green, labeled as SMOISP_BOT-I), and 2). WRF deep layer soil moisture as a percentage of saturation from the insolation plus soil moisture nudging (shallow and deep) simulation (blue, labeled as SMOISP_BOT-N). Hourly WRF precipitation (mm) is in red and plotted with respect to the right vertical axis. This is a location where the magnitude of the bias increased with soil nudging.The x-axis is in days.

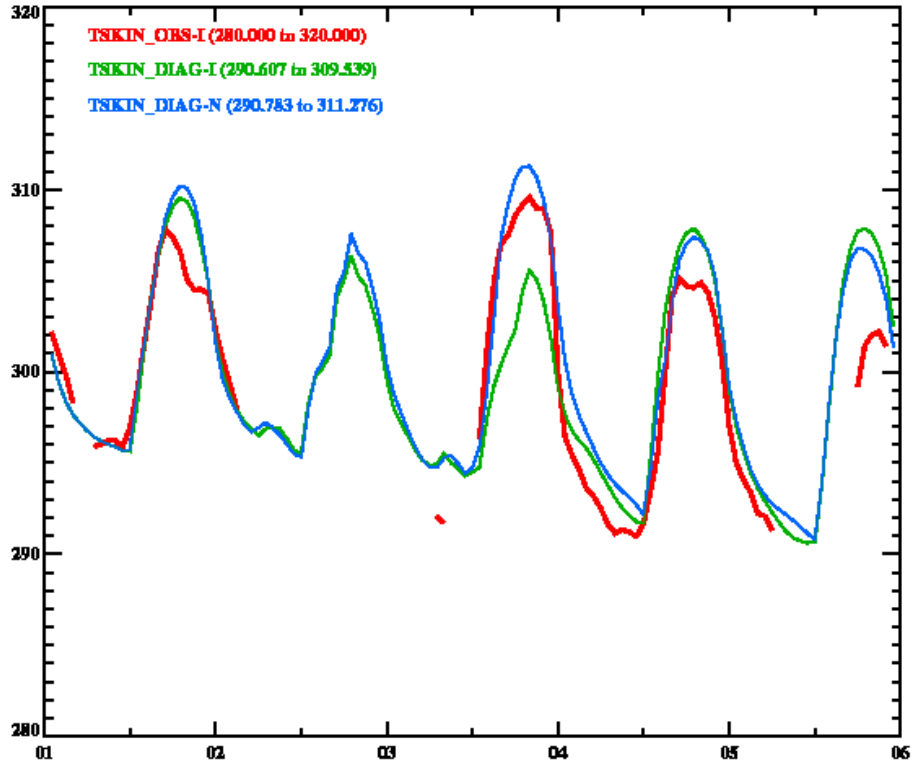

Figure 6-13. Time series for 0000 UTC 1 September 2013 through 0000 UTC 6 September 2013 for northwestern Alabama (location code "C") for the following temperature variables: 1.) observed NOAA-Alexi skin temperature (red, labeled as TSKIN_OBS-I), 2.) WRF diagnosed skin temperature from the insolation simulation (green, labeled as TSKIN_DIAG-I), and 3). WRF diagnosed skin temperature from the insolation plus soil moisture nudging (shallow and deep) simulation (blue, labeled as TSKIN_DIAG-N). This is a location where the magnitude of the bias increased with soil nudging. The y-axis is in degrees K and x-axis is in days.

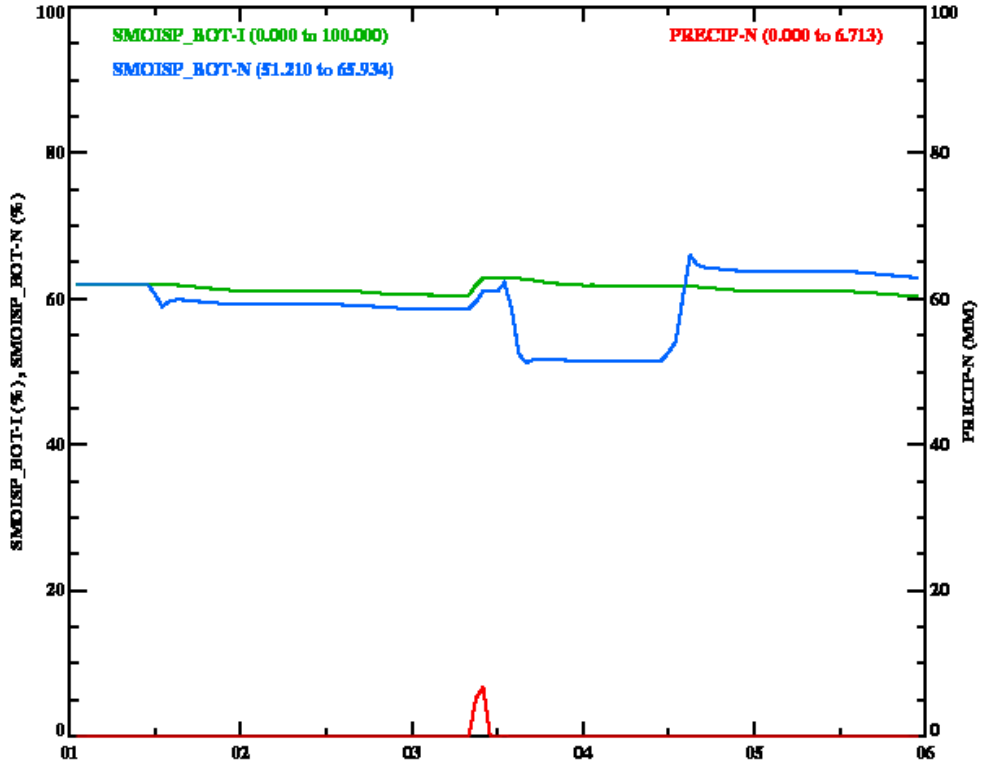

Figure 6-14. Time series for 0000 UTC 1 September 2013 through 0000 UTC 6 September 2013 for northwestern Alabama (location code "C") for the following soil moisture variables: 1.) WRF deep layer soil moisture as a percentage of saturation from the insolation simulation (green, labeled as SMOISP_BOT-I), and 2). WRF deep layer soil moisture as a percentage of saturation from the insolation plus soil moisture nudging (shallow and deep) simulation (blue, labeled as SMOISP_BOT-N). Hourly WRF precipitation (mm) is in red and plotted with respect to the right vertical axis. This is a location where the magnitude of the bias increased with soil nudging. The x-axis is in days.

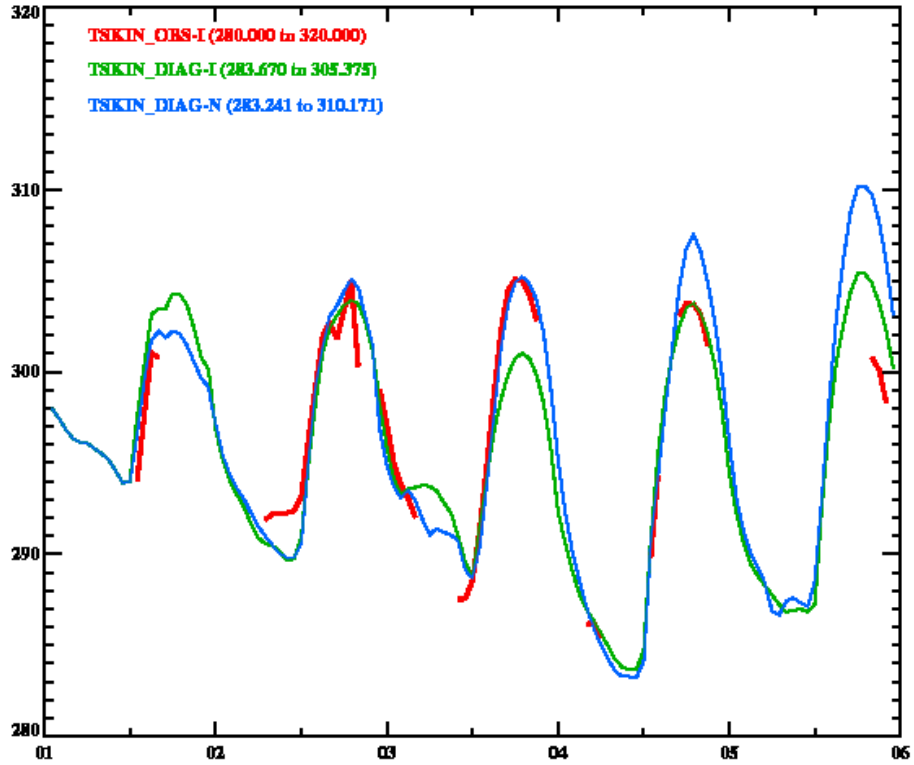

Figure 6-15. Time series for 0000 UTC 1 September 2013 through 0000 UTC 6 September 2013 for southern Indiana (location code "D") for the following temperature variables: 1.) observed NOAA-Alexi skin temperature (red, labeled as TSKIN_OBS-I), 2.) WRF diagnosed skin temperature from the insolation simulation (green, labeled as TSKIN_DIAG-I), and 3). WRF diagnosed skin temperature from the insolation plus soil moisture nudging (shallow and deep) simulation (blue, labeled as TSKIN_DIAG-N). This is a location where the magnitude of the bias increased with soil nudging. The y-axis is in degrees K and x-axis is in days.

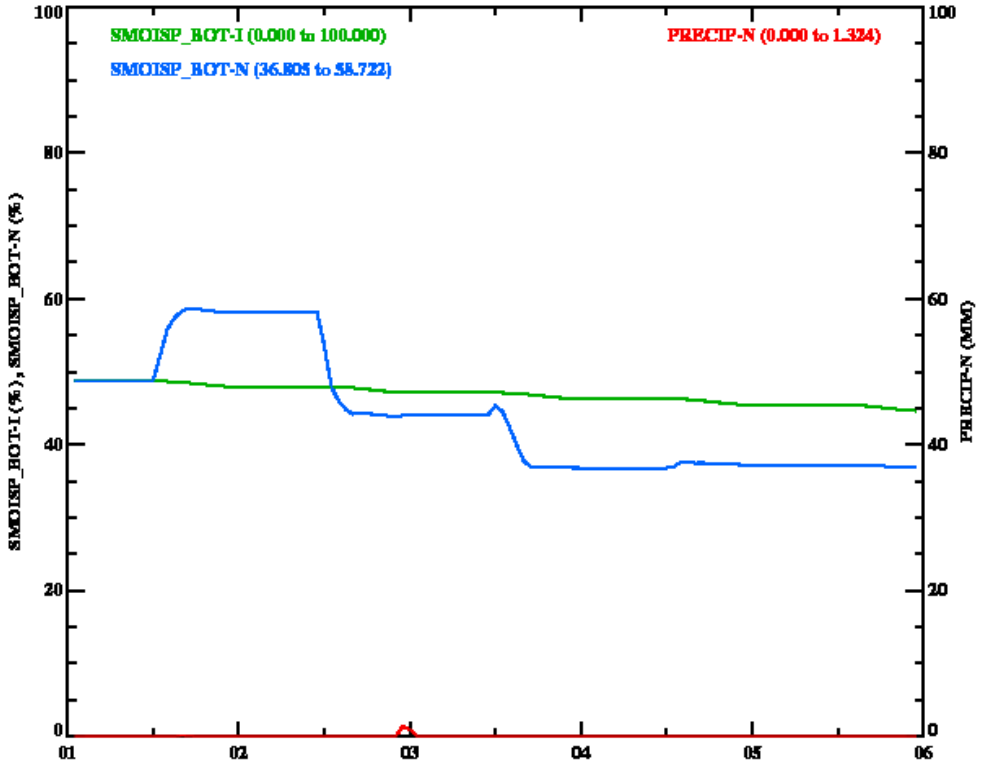

Figure 6-16. Time series for 0000 UTC 1 September 2013 through 0000 UTC 6 September 2013 for southern Indiana (location code "D") for the following soil moisture variables: 1.) WRF deep layer soil moisture as a percentage of saturation from the insolation simulation (green, labeled as SMOISP_BOT-I), and 2). WRF deep layer soil moisture as a percentage of saturation from the insolation plus soil moisture nudging (shallow and deep) simulation (blue, labeled as SMOISP_BOT-N). Hourly WRF precipitation (mm) is in red and plotted with respect to the right vertical axis. This is a location where the magnitude of the bias increased with soil nudging. The x-axis is in days.

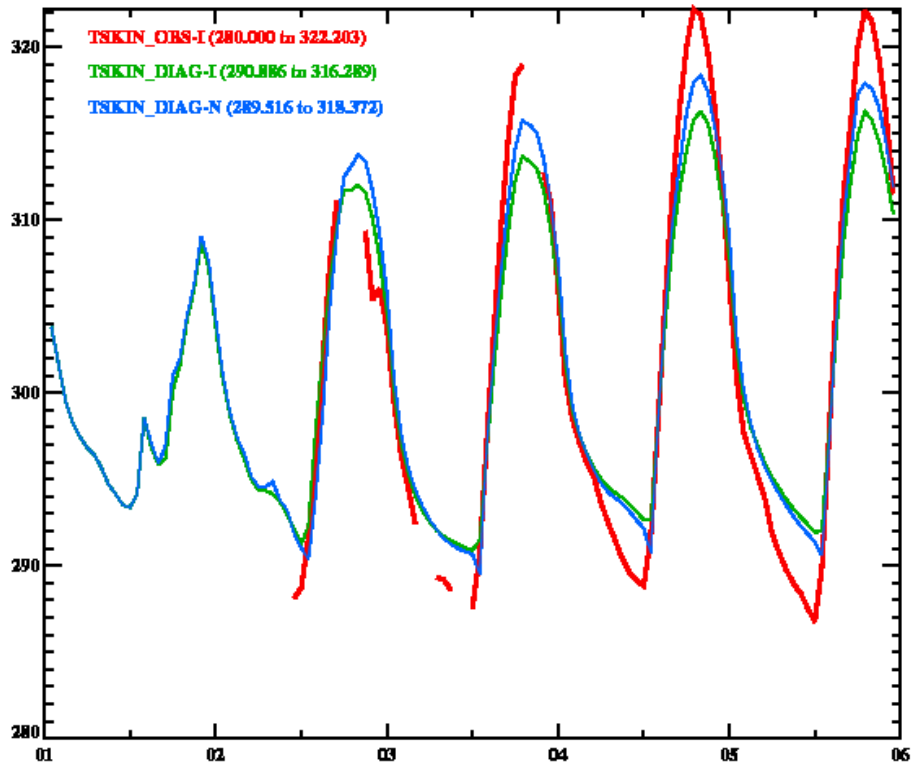

Figure 6-17. Time series for 0000 UTC 1 September 2013 through 0000 UTC 6 September 2013 for northern Texas (location code "E") for the following temperature variables: 1.) observed NOAA-Alexi skin temperature (red, labeled as TSKIN_OBS-I), 2.) WRF diagnosed skin temperature from the insolation simulation (green, labeled as TSKIN_DIAG-I), and 3). WRF diagnosed skin temperature from the insolation plus soil moisture nudging (shallow and deep) simulation (blue, labeled as TSKIN_DIAG-N). This is a location where the magnitude of the bias decreased with soil nudging. The y-axis is in degrees K and x-axis is in days.

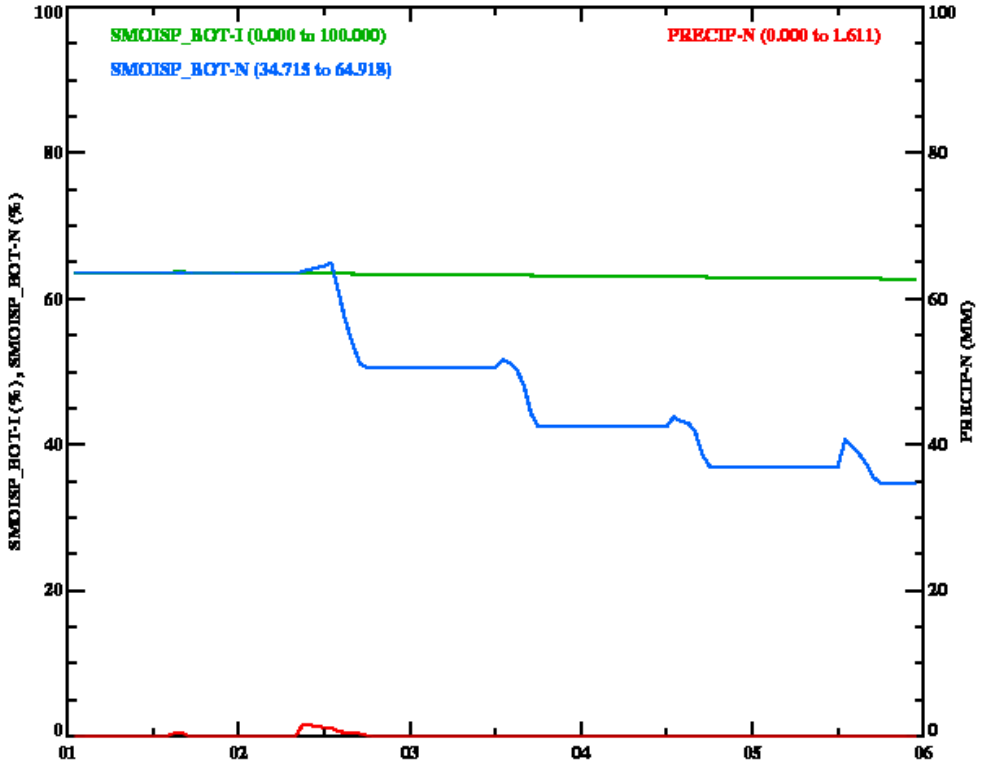

Figure 6-18. Time series for 0000 UTC 1 September 2013 through 0000 UTC 6 September 2013 for northern Texas (location code "E") for the following soil moisture variables: 1.) WRF deep layer soil moisture as a percentage of saturation from the insolation simulation (green, labeled as SMOISP_BOT-I), and 2). WRF deep layer soil moisture as a percentage of saturation from the insolation plus soil moisture nudging (shallow and deep) simulation (blue, labeled as SMOISP_BOT-N). Hourly WRF precipitation (mm) is in red and plotted with respect to the right vertical axis. This is a location where the magnitude of the bias decreased with soil nudging. The x-axis is in days.

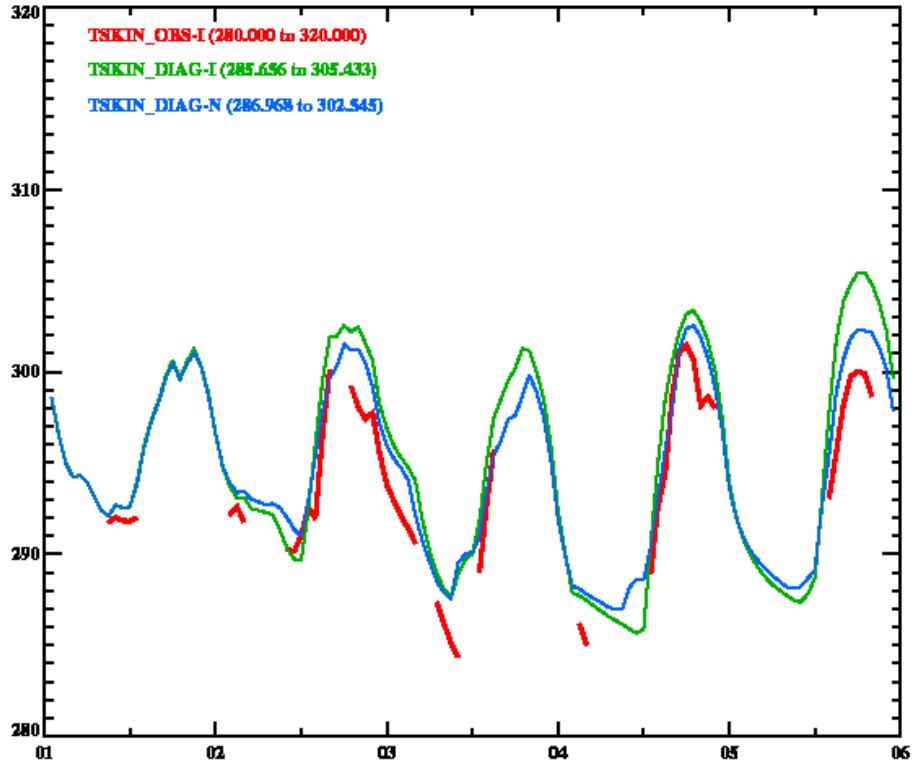

Figure 6-19. Time series for 0000 UTC 1 September 2013 through 0000 UTC 6 September 2013 for eastern Illinois (location code "F") for the following temperature variables: 1.) observed NOAA-Alexi skin temperature (red, labeled as TSKIN_OBS-I), 2.) WRF diagnosed skin temperature from the insolation simulation (green, labeled as TSKIN_DIAG-I), and 3). WRF diagnosed skin temperature from the insolation plus soil moisture nudging (shallow and deep) simulation (blue, labeled as TSKIN_DIAG-N). This is a location where the magnitude of the bias decreased with soil nudging. The y-axis is in degrees K and x-axis is in days.

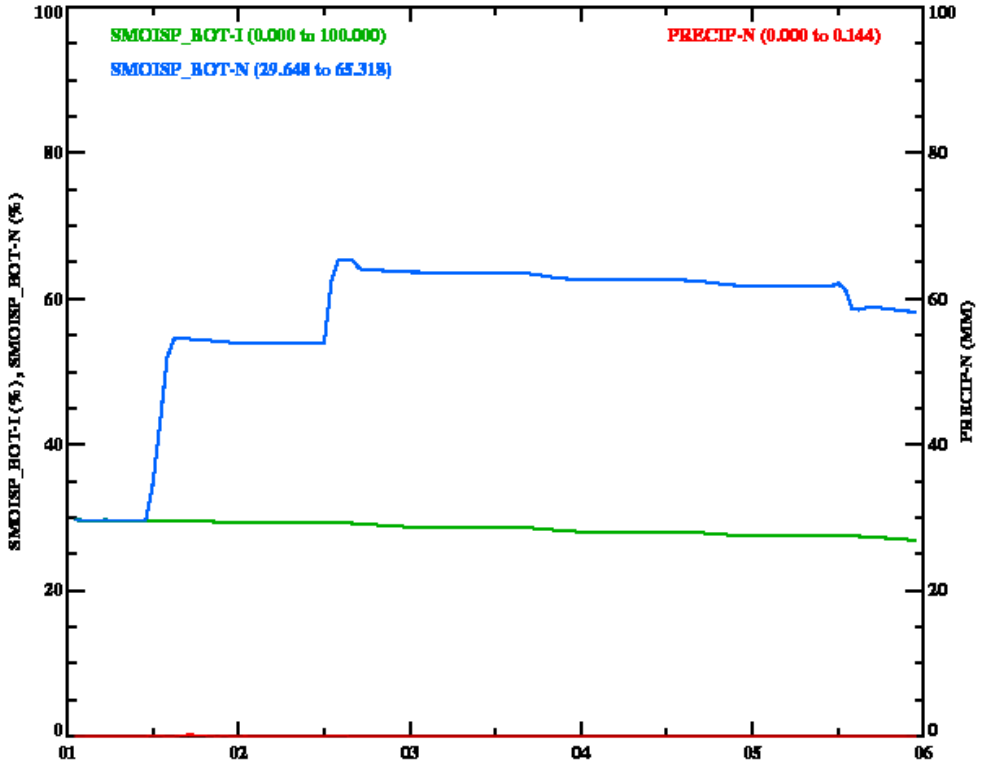

Figure 6-20. Time series for 0000 UTC 1 September 2013 through 0000 UTC 6 September 2013 for eastern Illinois (location code "F") for the following soil moisture variables: 1.) WRF deep layer soil moisture as a percentage of saturation from the insolation simulation (green, labeled as SMOISP_BOT-I), and 2). WRF deep layer soil moisture as a percentage of saturation from the insolation plus soil moisture nudging (shallow and deep) simulation (blue, labeled as SMOISP_BOT-N). Hourly WRF precipitation (mm) is in red and plotted with respect to the right vertical axis. This is a location where the magnitude of the bias decreased with soil nudging. The x-axis is in days.

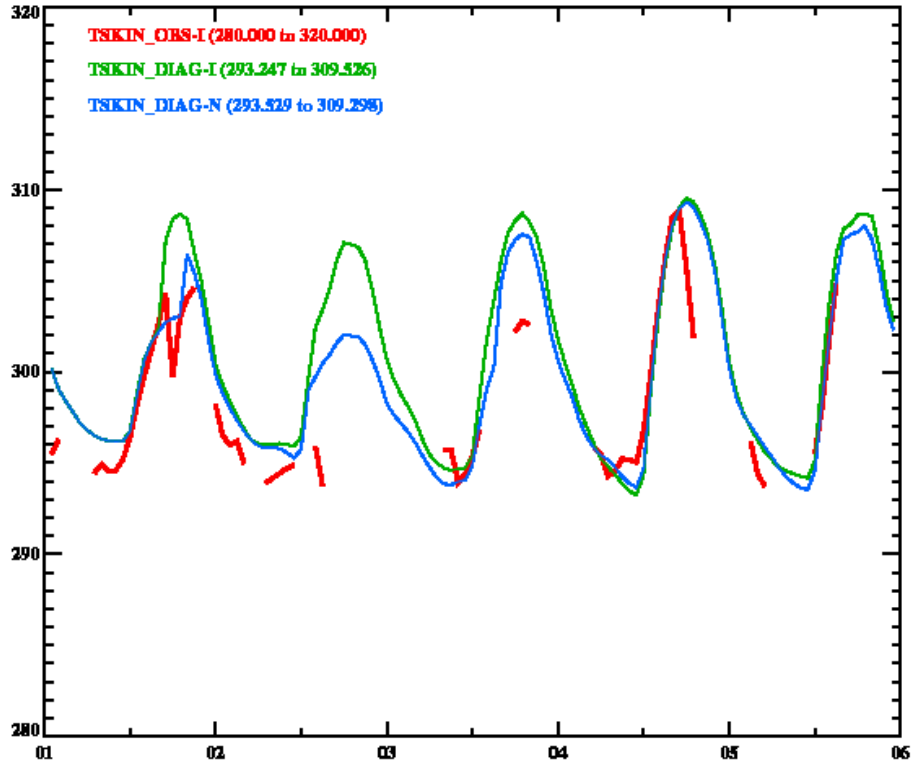

Figure 6-21. Time series for 0000 UTC 1 September 2013 through 0000 UTC 6 September 2013 for southwestern Georgia (location code "G") for the following temperature variables: 1.) observed NOAA-Alexi skin temperature (red, labeled as TSKIN_OBS-I), 2.) WRF diagnosed skin temperature from the insolation simulation (green, labeled as TSKIN_DIAG-I), and 3). WRF diagnosed skin temperature from the insolation plus soil moisture nudging (shallow and deep) simulation (blue, labeled as TSKIN_DIAG-N). This is a location where the magnitude of the bias decreased with soil nudging. The y-axis is in degrees K and x-axis is in days.

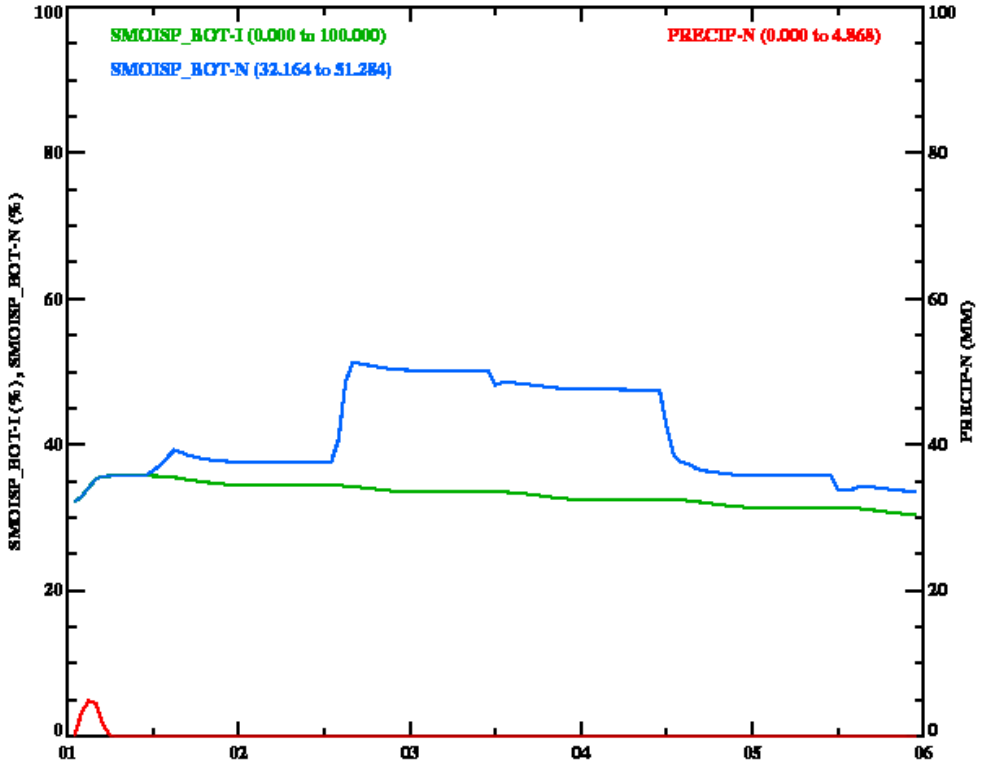

Figure 6-22. Time series for 0000 UTC 1 September 2013 through 0000 UTC 6 September 2013 for southwestern Georgia (location code "G") for the following soil moisture variables: 1.) WRF deep layer soil moisture as a percentage of saturation from the insolation simulation (green, labeled as SMOISP_BOT-I), and 2). WRF deep layer soil moisture as a percentage of saturation from the insolation plus soil moisture nudging (shallow and deep) simulation (blue, labeled as SMOISP_BOT-N). Hourly WRF precipitation (mm) is in red and plotted with respect to the right vertical axis. This is a location where the magnitude of the bias decreased with soil nudging. The x-axis is in days.

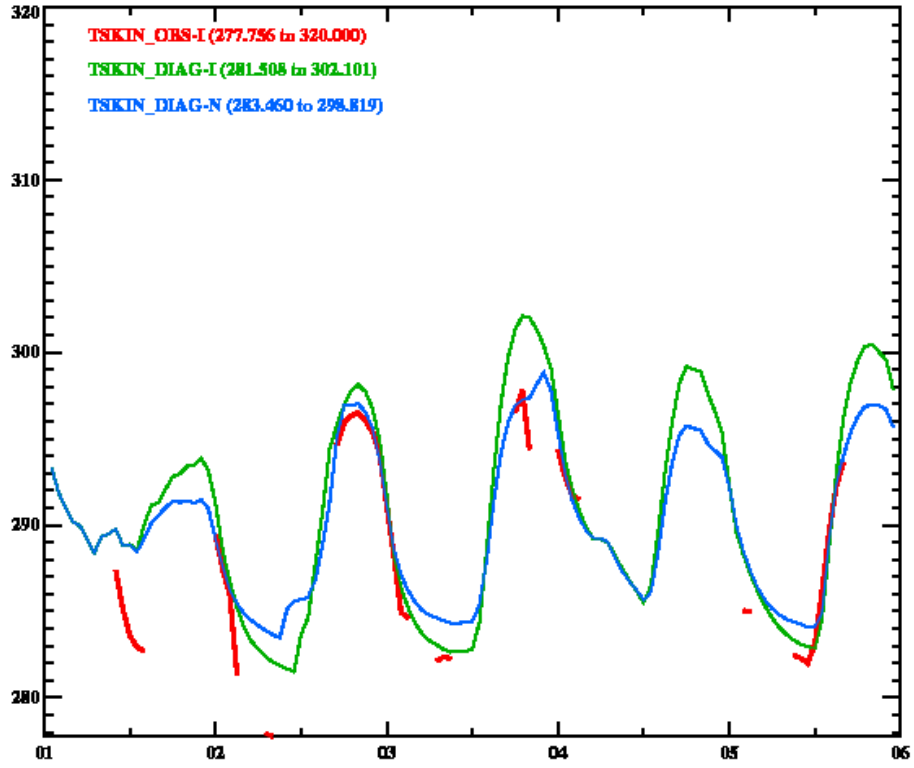

Figure 6-23. Time series for 0000 UTC 1 September 2013 through 0000 UTC 6 September 2013 for northern Minnesota (location code "H") for the following temperature variables: 1.) observed NOAA-Alexi skin temperature (red, labeled as TSKIN_OBS-I), 2.) WRF diagnosed skin temperature from the insolation simulation (green, labeled as TSKIN_DIAG-I), and 3). WRF diagnosed skin temperature from the insolation plus soil moisture nudging (shallow and deep) simulation (blue, labeled as TSKIN_DIAG-N). This is a location where the magnitude of the bias decreased with soil nudging. The y-axis is in degrees K and x-axis is in days.

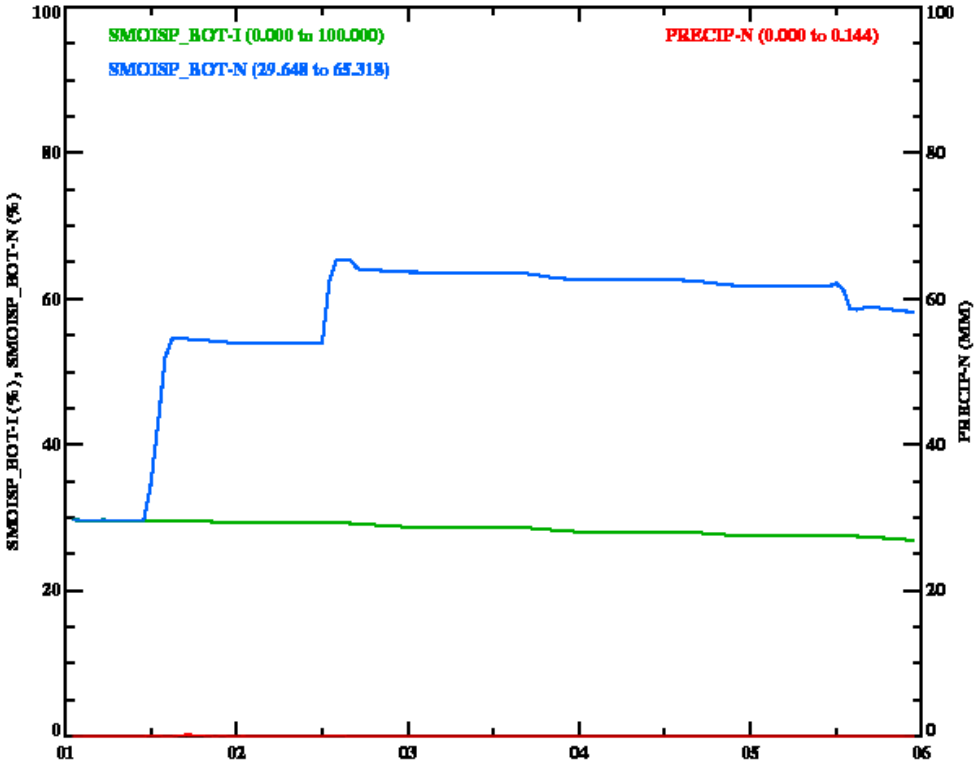

Figure 6-24. Time series for 0000 UTC 1 September 2013 through 0000 UTC 6 September 2013 for northern Minnesota (location code "H") for the following soil moisture variables: 1.) WRF deep layer soil moisture as a percentage of saturation from the insolation simulation (green, labeled as SMOISP_BOT-I), and 2). WRF deep layer soil moisture as a percentage of saturation from the insolation plus soil moisture nudging (shallow and deep) simulation (blue, labeled as SMOISP_BOT-N). Hourly WRF precipitation (mm) is in red and plotted with respect to the right vertical axis. This is a location where the magnitude of the bias decreased with soil nudging. The x-axis is in days.

11. Full Month Results for Moisture Nudging

The WRF model was run in the WRF-CONTR mode and WRF-TS as described above except for the period of 1-30 September 2013. For these runs it was decided to use the SPoRT insolation product (see Chapter 2) rather than the GSIP insolation product. This was based on the first five day simulation which appeared to show the insolation product deteriorated the statistical performance despite the GSIP product performing better than the WRF model in comparison to pyranometer data in Chapter 2. Also, the SPoRT insolation product performed better against pyranometer data than the GSIP product.

Figures 6-25 through 6-26 show the spatial depictions of bias of the WRF-CONTR (with satellite insolation without moisture nudging) and WRF-TS (with moisture nudging) and Figure 6-28

show the differences in bias between the WRF-TS and WRF-CONTR. As can be seen in Figure 6-28 the moisture nudging improves the bias over most areas in the domain.

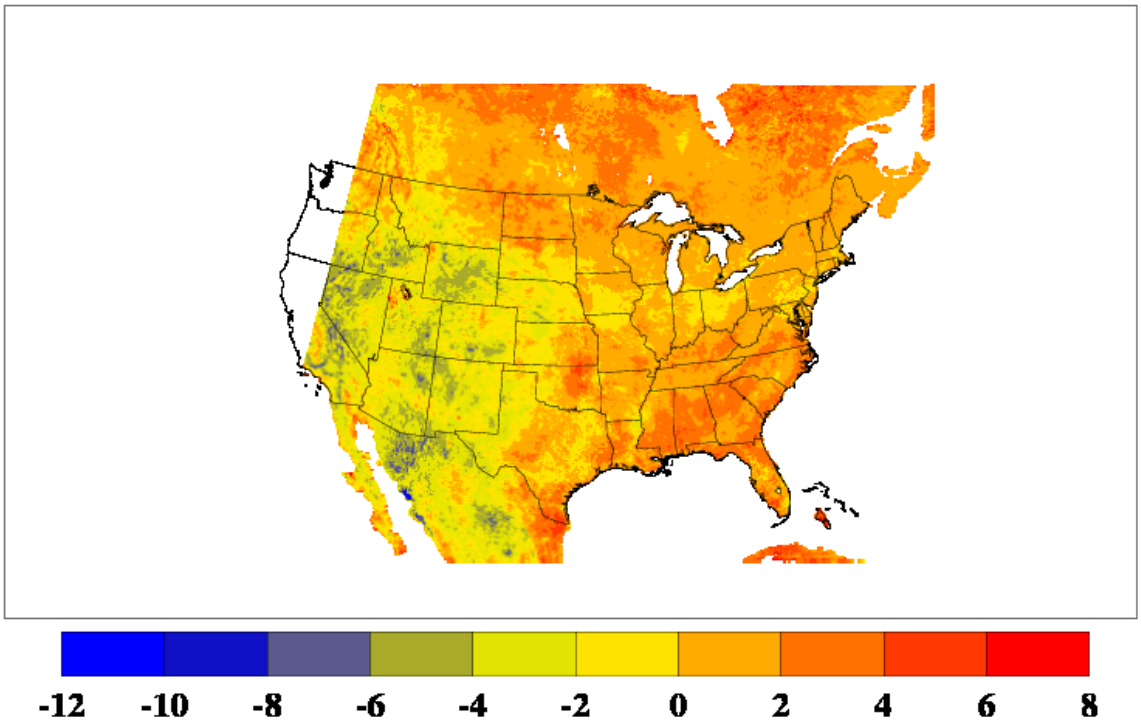

Figure 6-25. Average bias (units of degrees K) (WRF-CONTR minus observed) of skin temperatures for the period 0000 UTC 1 September 2013 through 2300 UTC 30 September 2013 for daytime conditions.

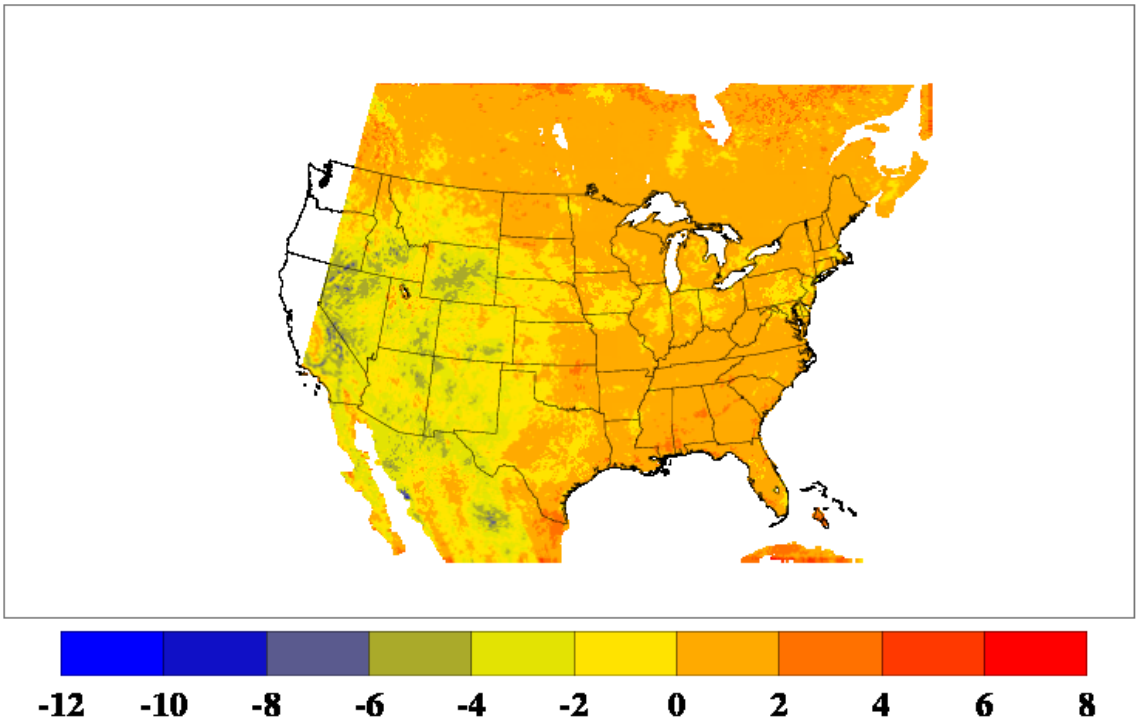

Figure 6-26. Average bias (units of degrees K) (soil moisture nudging (WRF-TS) run minus observed) of skin temperatures for the period 0000 UTC 1 September 2013 through 2300 UTC 30 September 2013 for daytime conditions.

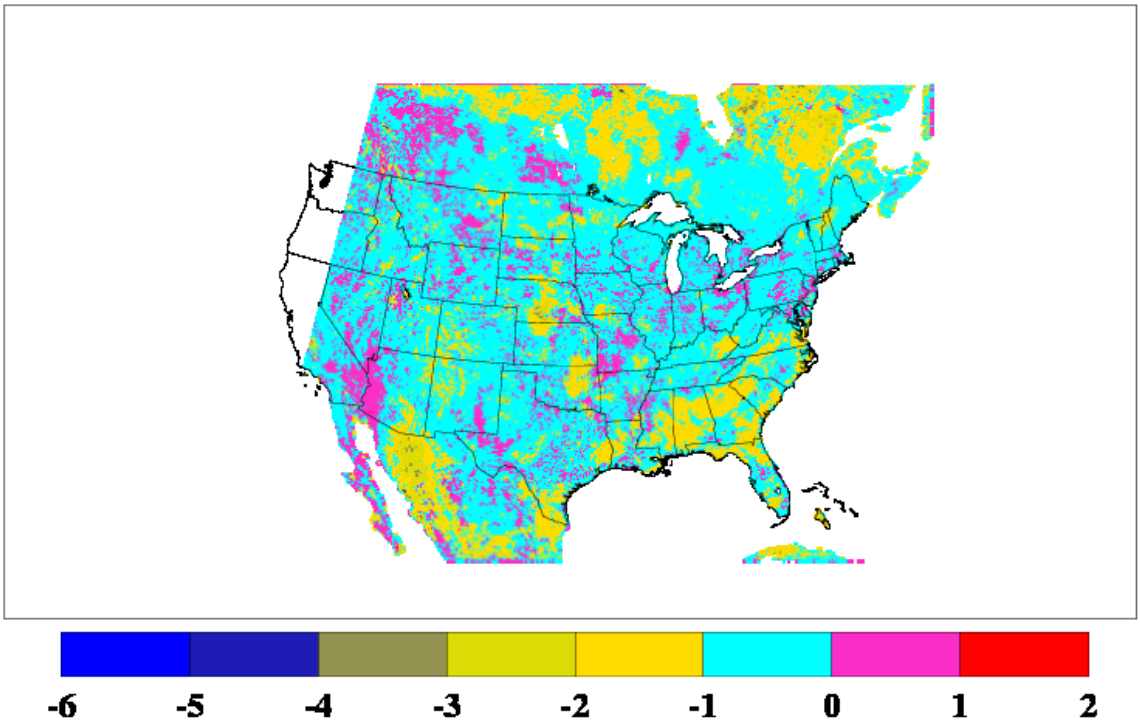

Figure 6-27. Difference in the magnitude of the respective bias values (units of degrees K) soil moisture nudging run (WRF-TS) minus WRF-CONTR) of skin temperatures for the period 0000 UTC 1 September 2013 through 2300 UTC September 30 2013 for daytime conditions. This field is equivalent to the absolute value of Figure 6-26 minus the absolute value of Figure 6-25. Negative values indicate a decrease in the magnitude of the bias, and vice versa.

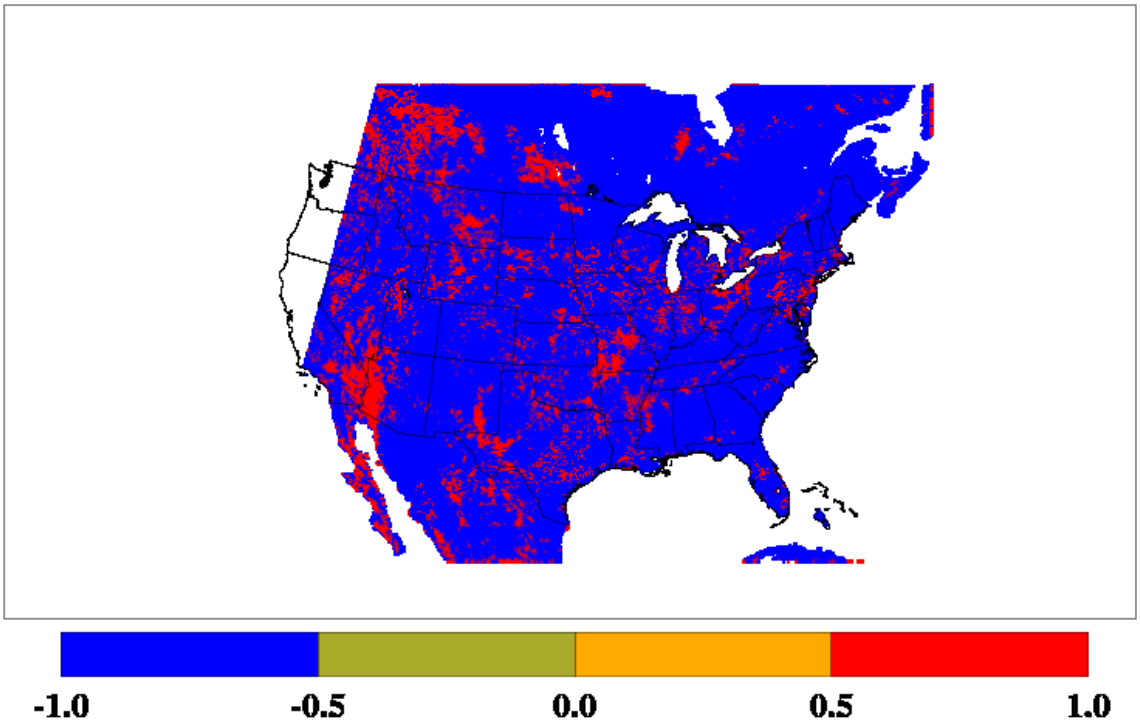

Figure 6-28. Same as Figure 6-27, except only the sign is plotted. Blue areas denote a decrease in the magnitude of the bias, and red areas denote an increase in the magnitude of the bias in degrees K.

The root mean square error (RMSE) is another measure of model performance. Figures 6-29 through 6-32 show the spatial depiction of the RMSE for the domain. As can be seen in Figs. 6-31 and 6-32 the RMSE is reduced over most of the domain.

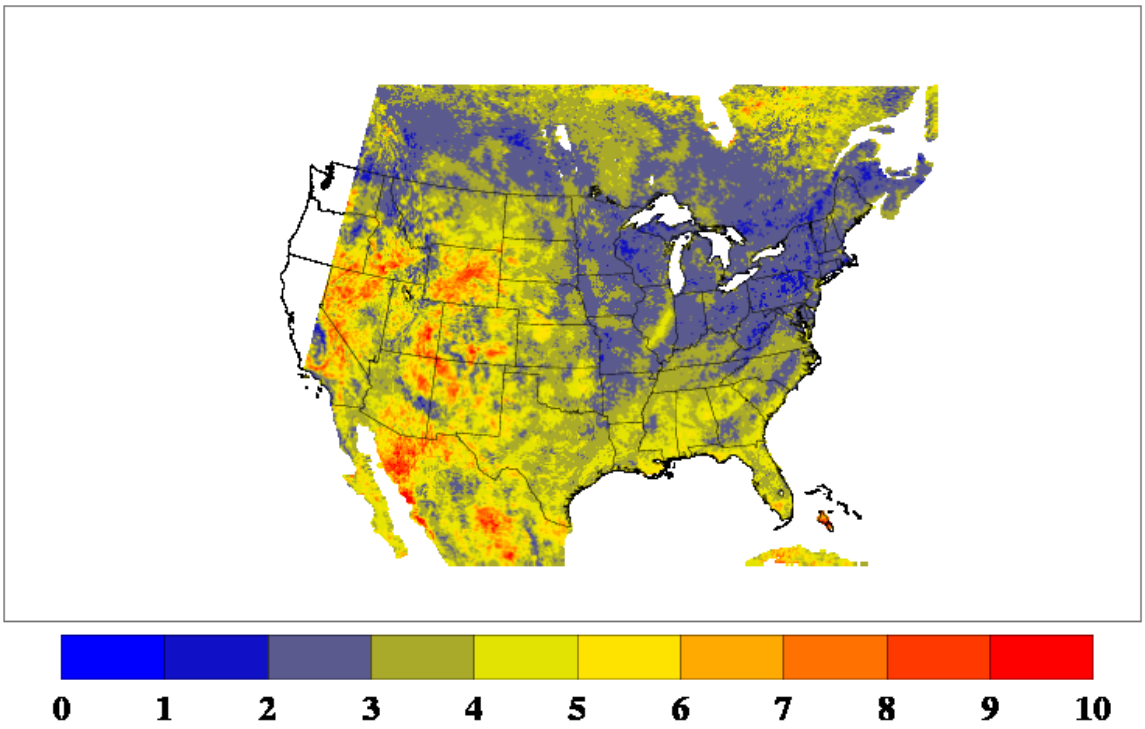

Figure 6-29. Root mean square error (units of degrees K) (WRF-CONTR minus observed) of skin temperatures for the period 0000 UTC 1 September 2013 through 2300 UTC September 30 2013 for daytime conditions. Values truncated to 10 K.

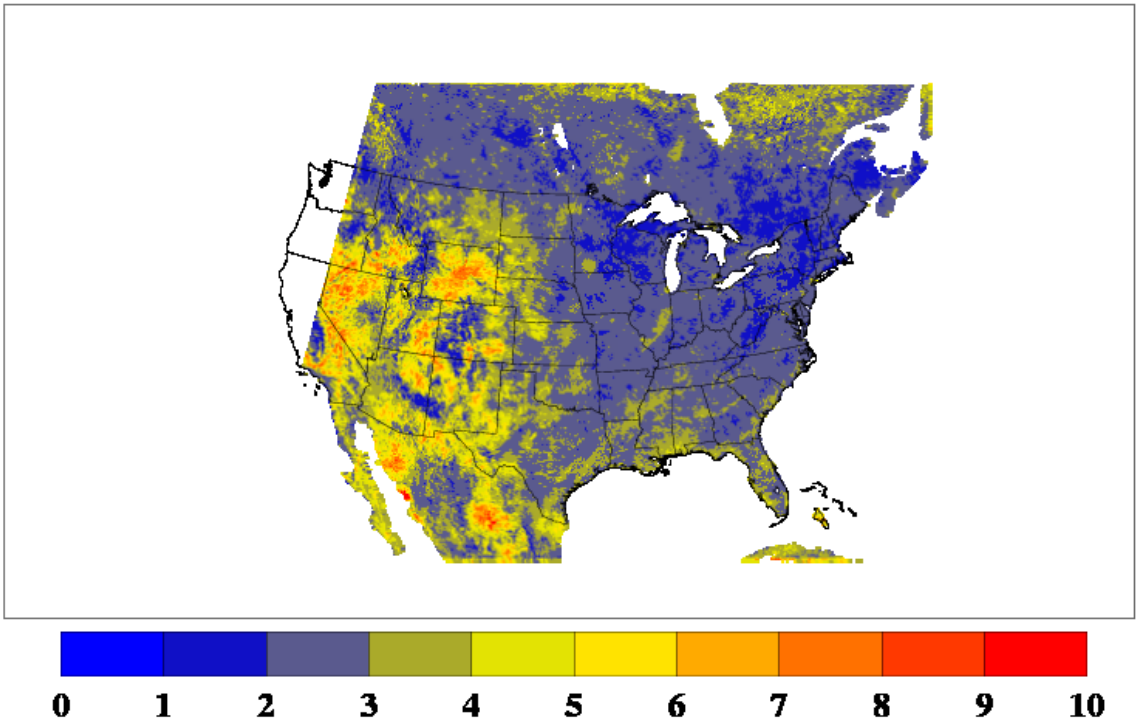

Figure 6-30. Root mean square error (RMSE, units of degrees K) (WRF-TS minus observed) of skin temperatures for the period 0000 UTC 1 September 2013 through 2300 UTC 30 September 2013 for daytime conditions. Values truncated to 10 K.

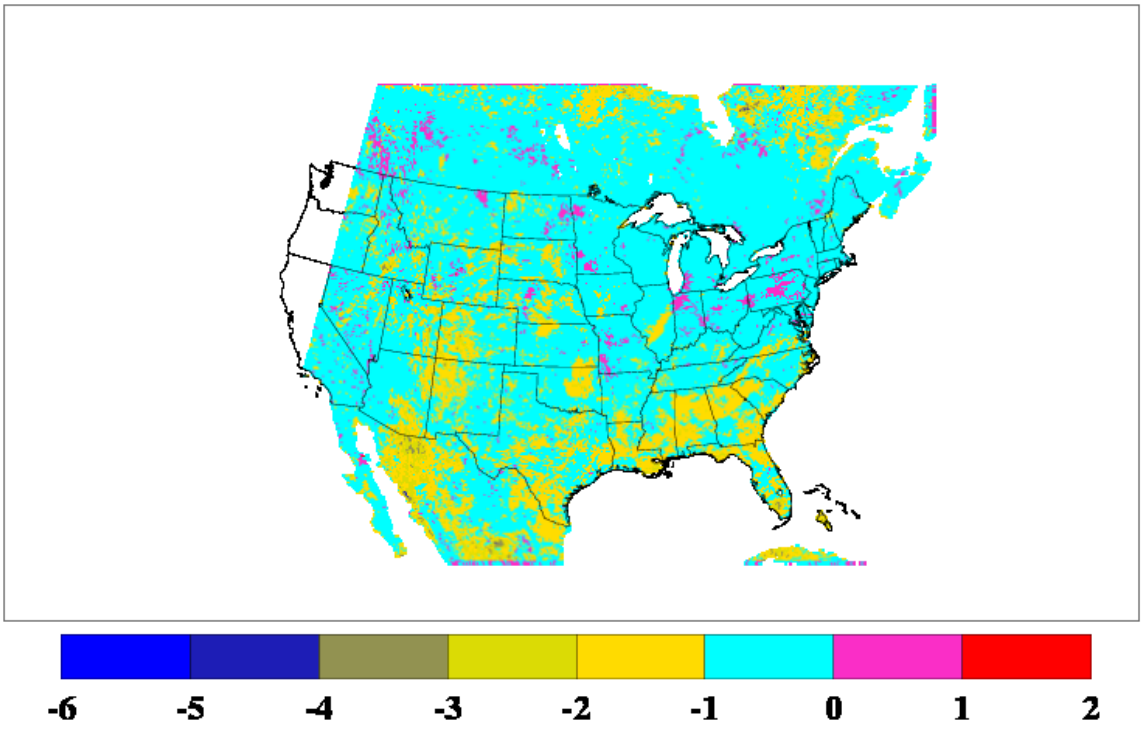

Figure 6-31. Difference in the respective RMSE values (units of degrees K) (WRF-TS minus WRF-CONTR) of skin temperatures for the period 0000 UTC 1 September 2013 through 2300 UTC September 2013 for daytime conditions. This field is equivalent to Figure 6-30 minus the value of Figure 6-29. Negative values indicate a decrease in the magnitude of the RMSE, and vice versa.

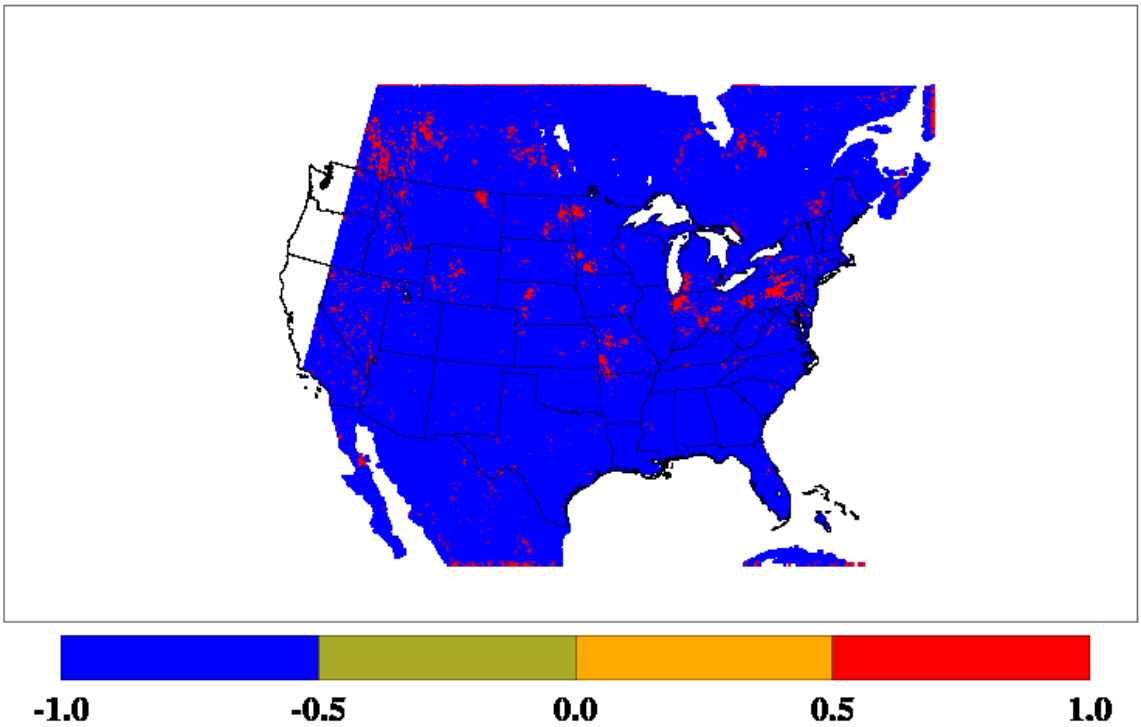

Figure 6-32. Same as Figure 6-30 except only the sign is plotted. Blue areas denote a decrease in the RMSE, and red areas denote an increase in the RMSE (unitless).

Table 6-1 below gives the total statistics for the entire domain relative to skin temperatures for various WRF simulations.

SIMULATION	BIAS ALL	BIAS WEST	BIAS EAST	RMSE ALL	RMSE WEST	RMSE EAST
WRF-BASE	**0.06**	**-1.08**	**1.31**	**3.68**	**4.11**	**3.21**
WRF-PLEIM	**0.08**	**-1.08**	**1.35**	**3.64**	**4.05**	**3.18**
WRF-CONTR	**0.09**	**-1.13**	**1.42**	**3.70**	**4.17**	**3.18**
WRF-TS	**-0.13**	**-0.95**	**0.78**	**3.00**	**3.43**	**2.53**

Table 6-1. Overall bias and RMSE statistics for the 1-30 September, 2013. WRF-BASE is the simulation with no Pleim nudging, no satellite insolation, and no skin temperature moisture nudging. WRF-PLEIM is the same as WRF-BASE except the Pleim nudging is activated. WRF-CONTR is the simulation with no Pleim nudging, with satellite insolation, and no skin temperature moisture nudging. WRF-TS is the simulation with no Pleim nudging, with satellite insolation, and with skin temperature moisture nudging.

As can be seen while Figure 6-28 shows that over most of the domain the bias has decreased the absolute value of the bias over the domain has slightly increased.

While the spatial depictions and tables are one tool for model evaluation, scatter plots and fitted regression lines between models and observations is another method for model evaluation. Figures 6-33 through 6-34 provide this depiction of the WRF simulations made under this activity. Figure 6-33 shows that the spread in the original WRF using its insolation and the

WRF-CONTR (with satellite insolation) have approximately the same correlation (r) and standard error (σ) with a slight deterioration with the satellite insolation.

In Chapter 7 a WRF run is described which employs the Noah land surface model. The Noah Land Surface Model has been employed Texas and is used operationally in the NWS operational WRF system. For a description see *Chen and Dudhia* (2001) and also the present configuration given in Chapter 7.

Daytime only

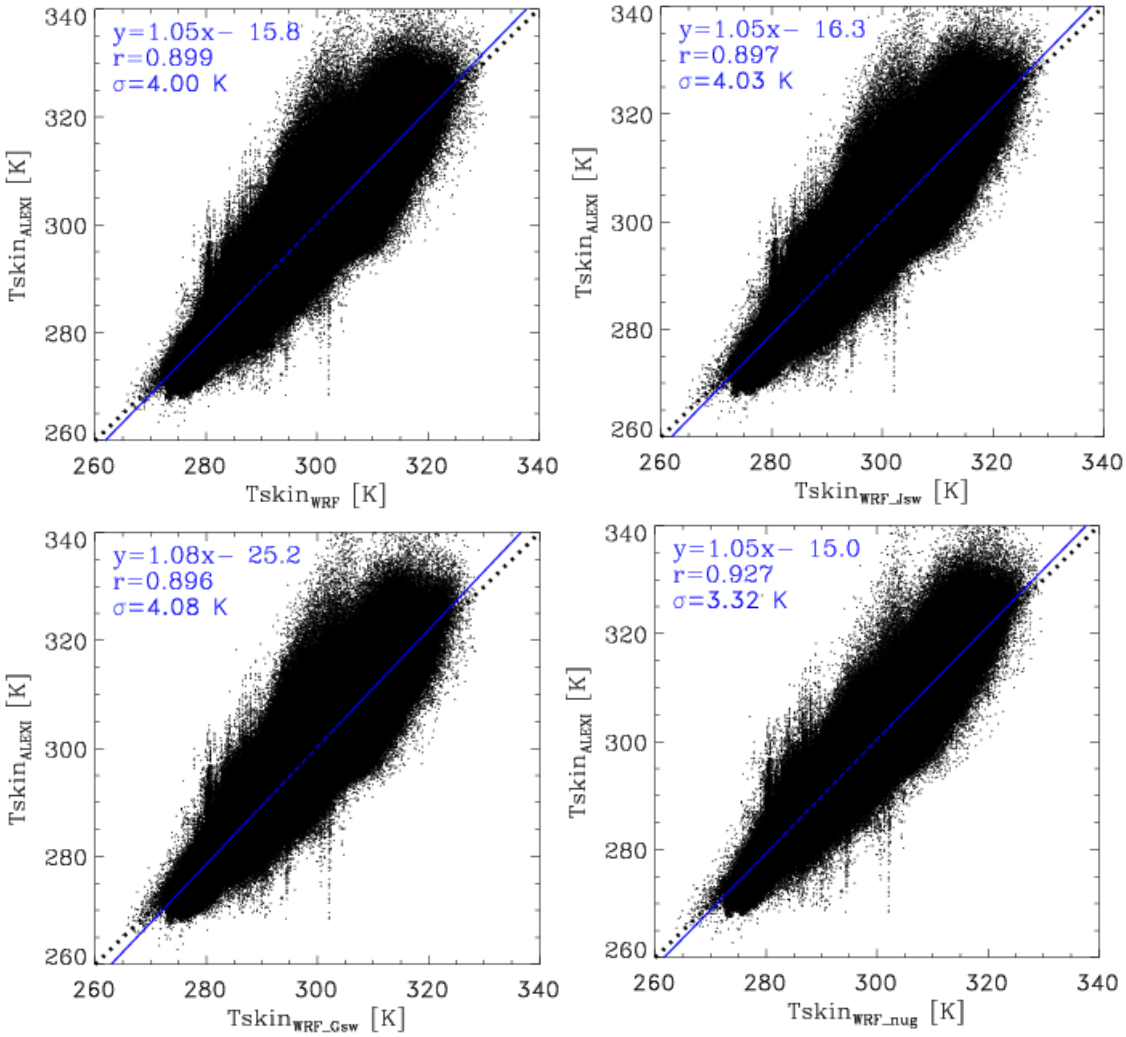

Figure 6-33. Comparison of Tskin–WRF simulation against ALEXI product (ALEXI on y-axis) for daytime-only for the entire month of Sep., 2013. The x-axis in the top-left panel is WRF simulation without ingestion of observational insolation (WRF); in the top-right panel is WRF simulation with SPoRT insolation (WRF-CONTR_Jsw); in the bottom-left panel is WRF simulation with GSIP insolation (WRF-CONTR_Gsw); in the bottom-right panel is WRF simulation with SPoRT insolation and with soil moisture nudging (WRF-TS). At the top of each plot are the regression equation, the correlation coefficient, and the Root Mean Square Error (RMSE) designated by the "sigma" symbol. The sigma values are in units of degrees K.

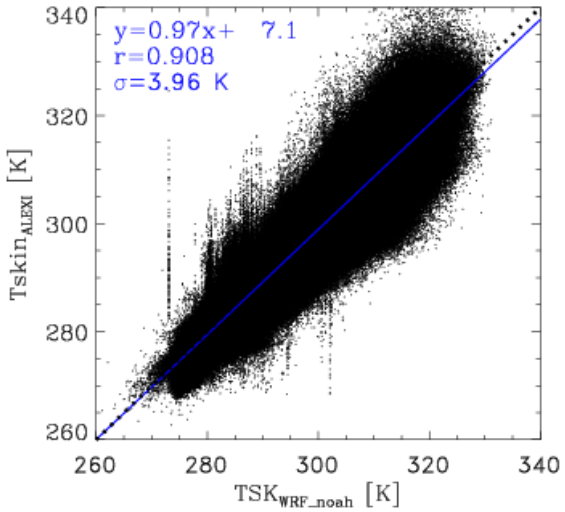

Figure 6-34. Same as Figure 6-33 for daytime only, but the WRF run using the Noah surface-layer model. At the top of the plot are the regression equation, the correlation coefficient, and the Root Mean Square Error (RMSE) designated by the "sigma" symbol. The sigma values are in units of K.

The statistical data presented in the above tables and plots were based on the model output and the ALEXI product skin temperature data based on two levels of data screening for QA/QC described in Chapter 5. Because of concerns with possible cloud contamination a third level of screening described in Chapter 5 was implemented. Figure 6-35 shows similar plots as in figure 6-33 except the evaluation data on the Y-axis is based on the third pass of QA/QC skin temperatscreening. The results show less scatter. The RMSE is 3.32K for the moisture nudging case for the two pass screening but improves to 3.10 using the third pass screening.

The right lower panel in figure 6-35 shows an additional modeling case where the third level of data screening is also applied to the morning skin temperatures used in the moisture nudging. It show a light degradation in RMSE compared to the assimilation case using only the second pass screening seen in the lower left panel of Figure 6-35. This is likely because less data was available for assimilation.

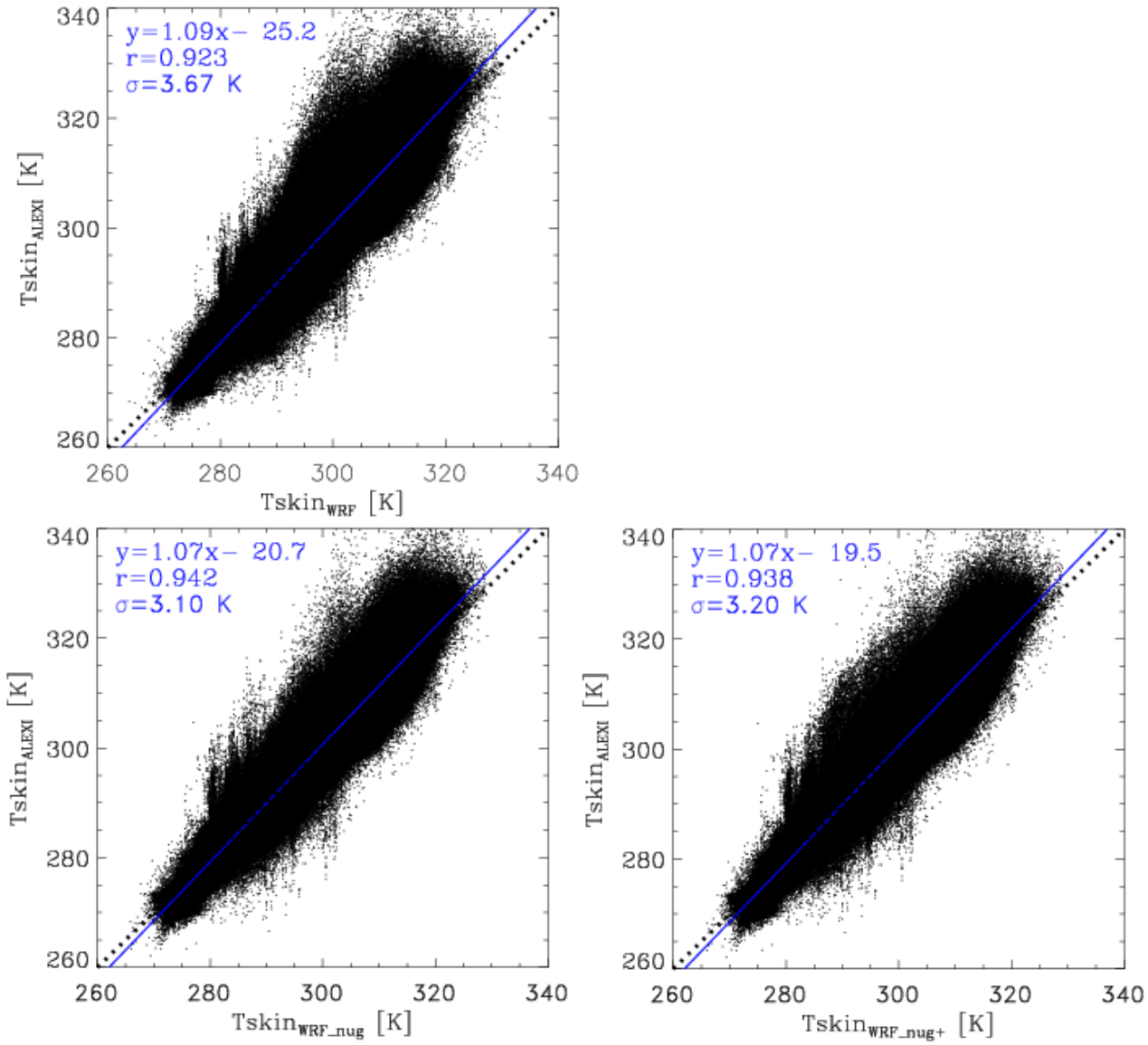

Figure 6-35. Comparison of Tskin–WRF simulation against ALEXI product (ALEXI on y-axis) for daytime-only for the entire month of Sep., 2013. The x-axis in the top panel is WRF simulation without ingestion of observational insolation (WRF); in the middle panel is WRF simulation with SPoRT insolation and with soil moisture nudging (WRF_nug); in the bottom right panel is WRF with insolation and nudging (WRF_nug+), in which the Tskin used is ALEXI with all 3 passes of cloud screening. **r** is correlation and $\boldsymbol{\sigma}$ is the RMSE of scattering. The observational Tskin in Y-axis for all 3 panels is ALEXI Tskin with 3 cloud screening passes.

12. Evaluation against NWS observations

While section 6 above discussed the evaluation of the WRF model in comparison to satellite skin temperature, the more standard model evaluation is against National Weather Service observations. In this section, comparisons are made to National Weather Service (NWS) observables such as 2-m temperatures, 2-m specific humidity and 10-m winds. However,

interpretation is difficult since the NWS observations are point observations while model results are a 12km average for the grid. Land use and cloud scale impacts in the model may not be representative of the point measure. Here the differences at NWS point representations and the closest model grid point are provided as colored boxes representing the NWS observations. An extensive set of observations are included in the plots. These plots are provided in Figs. 6-34 through 6-42.

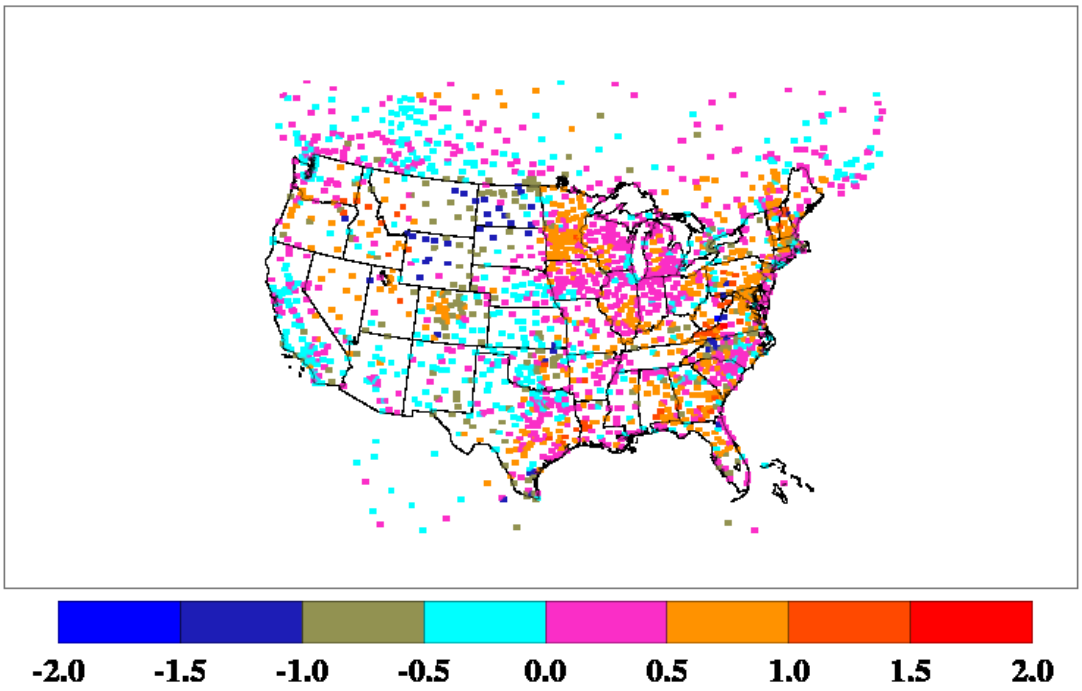

Figure 6-35. Difference in the magnitude of the respective bias values (units of K) (SPoRT insolation plus soil moisture nudging simulation (WRF-TS) minus WRF-CONTR) of 2-m temperature for the period 0000 UTC 1 September 2013 through 2300 UTC September 2013 for daytime conditions. This field is equivalent to the absolute value of the SPoRT insolation plus soil moisture nudging run bias minus the absolute value of the control bias, where bias is defined as the model value minus the observed value. Negative values indicate a decrease in the magnitude of the bias, and vice versa.

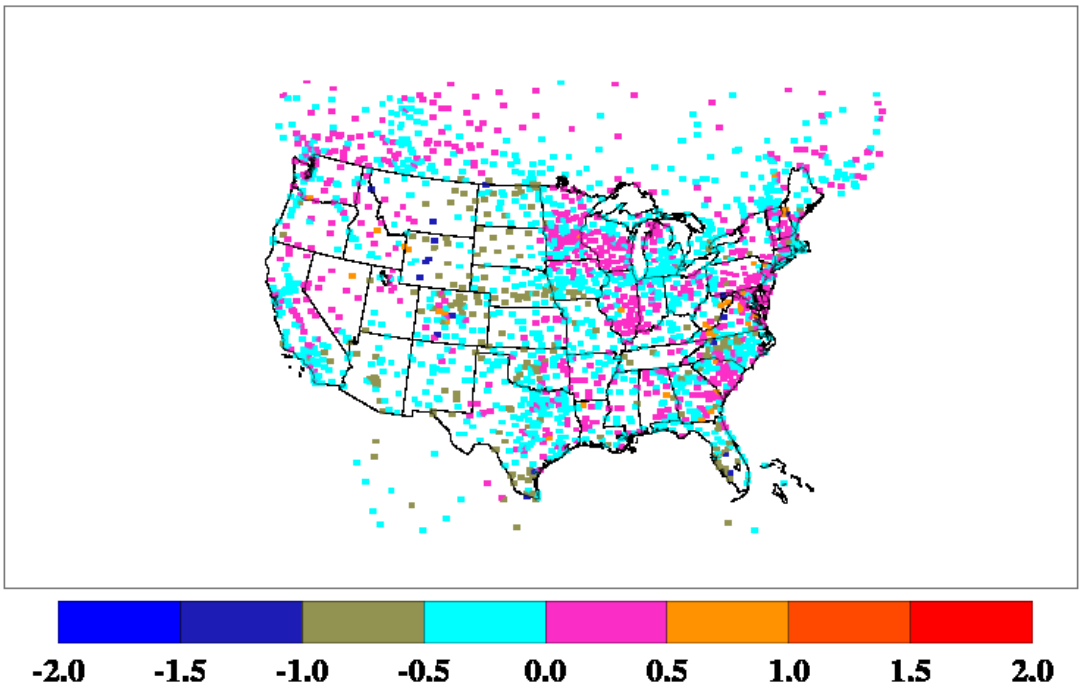

Figure 6-36. Difference in the respective RMSE values (units of K) (SPoRT insolation plus soil moisture nudging simulation (WRF-TS) minus control (WRF-CONTR) of 2-m temperature for the period 0000 UTC 1 September 2013 through 2300 UTC September 2013 for daytime conditions. This field is equivalent to the RMSE of the SPoRT insolation plus soil moisture nudging run minus the RMSE of the control run. Negative values indicate a decrease in the RMSE, and vice versa.

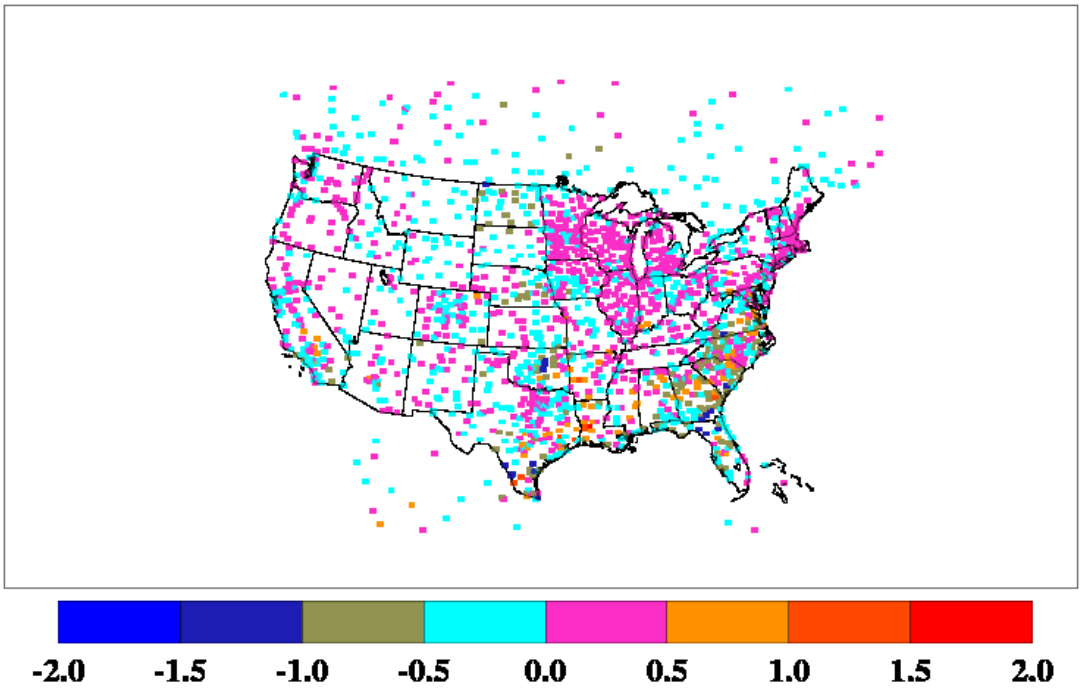

Figure 6-37. Difference in the magnitude of the respective bias values (units of g kg^{-1}) (SPoRT insolation plus soil moisture nudging simulation (WRF-TS) minus control (WRF-CONTR) of 2-m specific humidity for the period 0000 UTC 1 September 2013 through 2300 UTC September 2013 for daytime conditions. This field is equivalent to the absolute value of the SPoRT insolation plus soil moisture nudging run bias minus the absolute value of the control bias, where bias is defined as the model value minus the observed value. Negative values indicate a decrease in the magnitude of the bias, and vice versa.

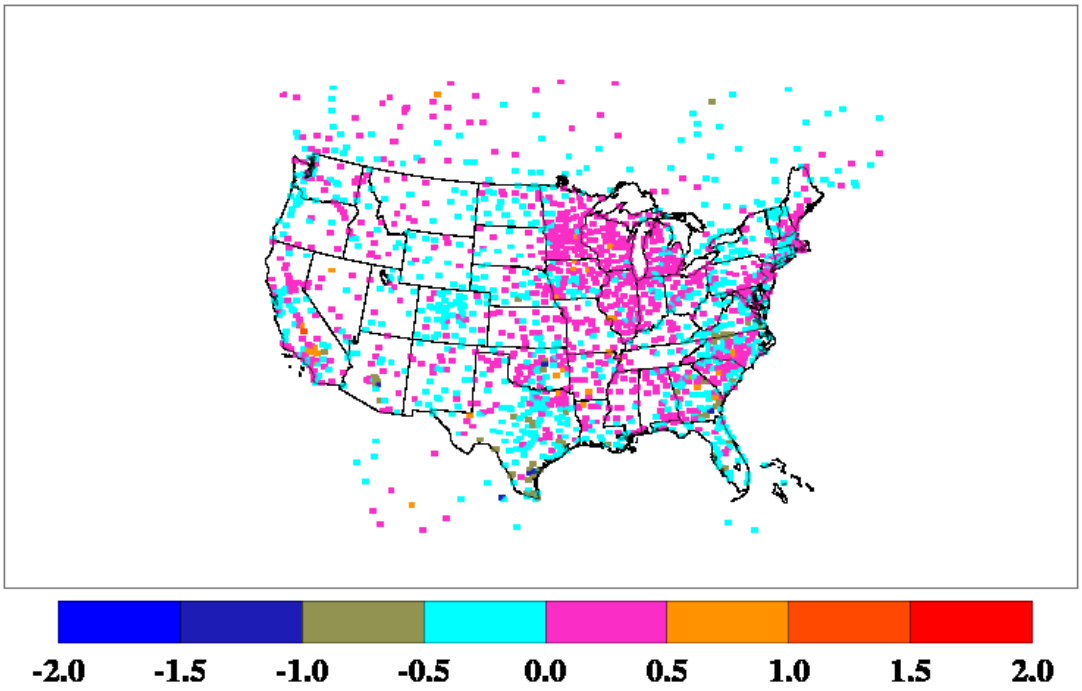

Figure 6-38. Difference of the respective Root Mean Square Error (RMSE) values (units of g kg^{-1}) (SPoRT insolation plus soil moisture nudging simulation (WRF-TS) minus control (WRF-TS)) of 2-m specific humidity for the period 0000 UTC 1 September 2013 through 2300 UTC September 2013 for daytime conditions. This field is equivalent to the RMSE of the SPoRT insolation plus soil moisture nudging run minus the RMSE of the control run. Negative values indicate a decrease in the RMSE, and vice versa.

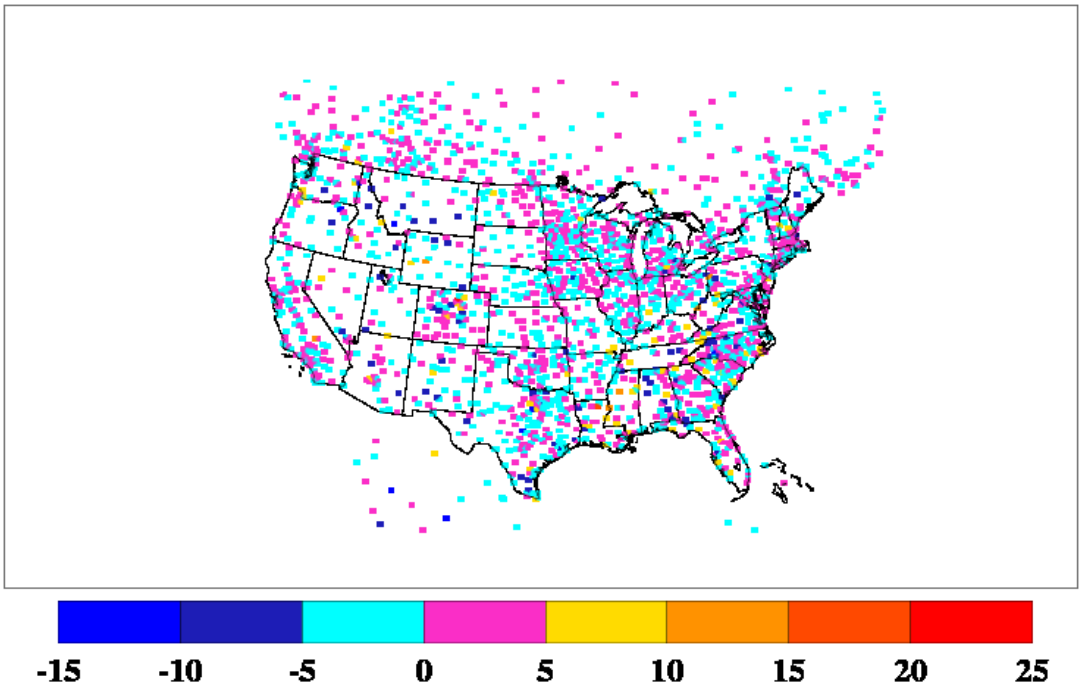

Figure 6-39. Difference in the magnitude of the respective bias values (units of degrees) (SPoRT insolation plus soil moisture nudging simulation (WRF-TS) minus control (WRF-CONTR)) of 10-m wind direction for the period 0000 UTC 1 September 2013 through 2300 UTC September 2013 for daytime conditions. This field is equivalent to the absolute value of the SPoRT insolation plus soil moisture nudging run bias minus the absolute value of the control bias, where bias is defined as the model value minus the observed value. Negative values indicate a decrease in the magnitude of the bias, and vice versa.

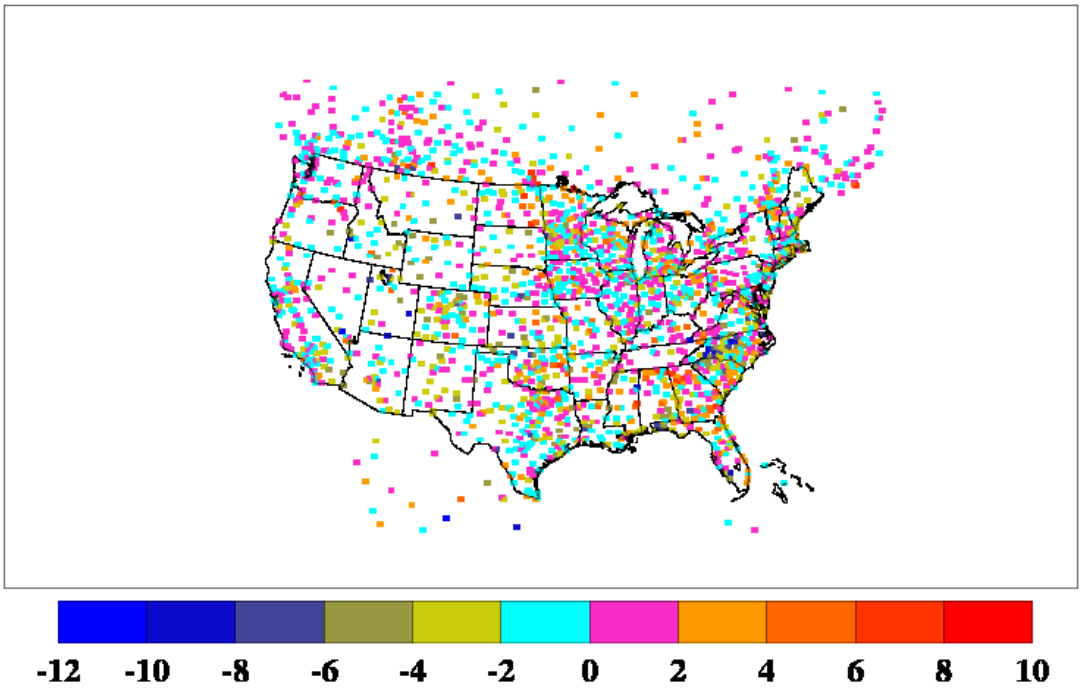

Figure 6-40. Difference of the respective Root Mean Square Error (RMSE) values (units of degrees) (SPoRT insolation plus soil moisture nudging simulation (WRF-TS) minus control (WRF-CONTR) of 10-m wind direction for the period 0000 UTC 1 September 2013 through 2300 UTC September 2013 for daytime conditions. This field is equivalent to the RMSE of the SPoRT insolation plus soil moisture nudging run minus the RMSE of the control run. Negative values indicate a decrease in the RMSE, and vice versa.

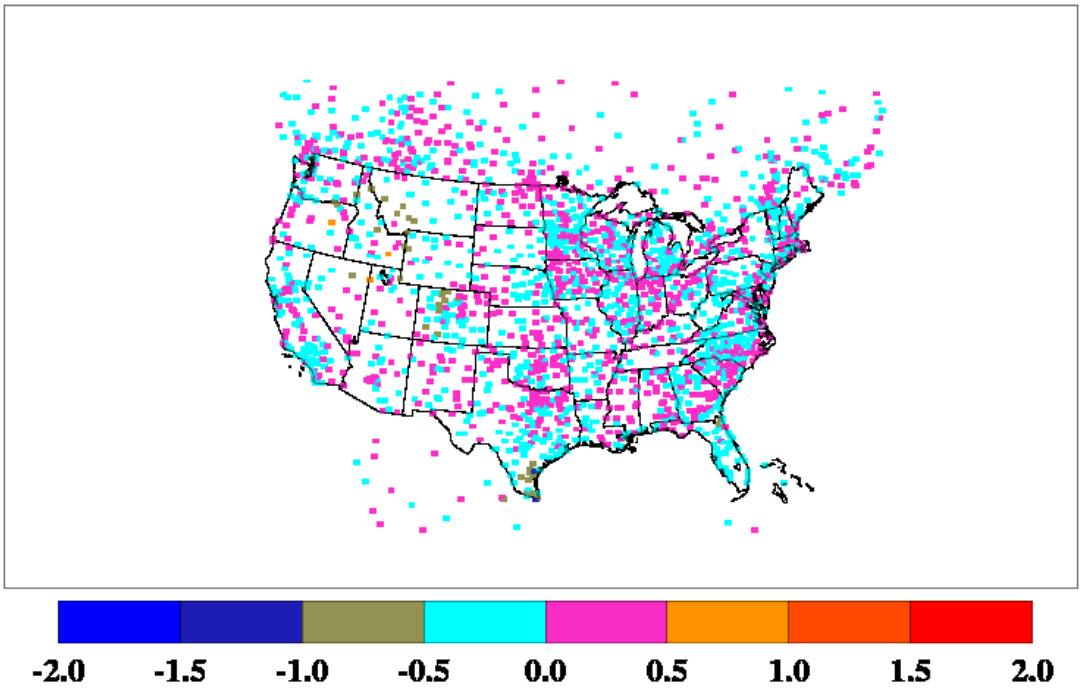

Figure 6-41. Difference in the magnitude of the respective bias values (units of m s^{-1}) (SPoRT insolation plus soil moisture nudging simulation (WRF-TS minus control WRF-CONTR) of 10-m wind speed for the period 0000 UTC 1 September 2013 through 2300 UTC September 2013 for daytime conditions. This field is equivalent to the absolute value of the SPoRT insolation plus soil moisture nudging run bias minus the absolute value of the control bias, where bias is defined as the model value minus the observed value. Negative values indicate a decrease in the magnitude of the bias, and vice versa.

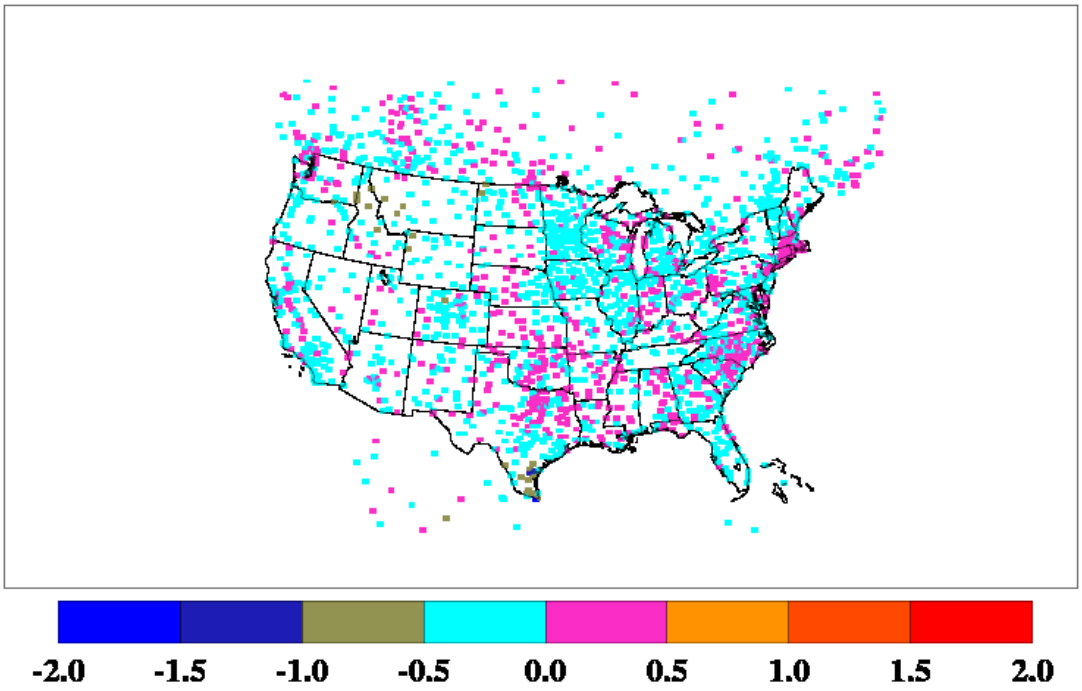

Figure 6-42. Difference of the respective Root Mean Square Error (RMSE) values (units of m s^{-1}) (SPoRT insolation plus soil moisture nudging simulation (WRF-TS) minus control WRF-CONTR) of 10-m wind speed for the period 0000 UTC 1 September 2013 through 2300 UTC September 2013 for daytime conditions. This field is equivalent to the RMSE of the SPoRT insolation plus soil moisture nudging run minus the RMSE of the control run. Negative values indicate a decrease in the RMSE, and vice versa.

The following tables 6-2 through 6-5 provide bias and RMSE for model runs compared to NWS observations for specific humidity, temperature, wind speed and wind direction. In these tables the runs are identified in the following manner. WRF-BASE is the simulation with no Pleim nudging, no satellite insolation, and no skin temperature moisture nudging. WRF-PLEIM is the same as WRF-BASE except the Pleim nudging is activated. WRF-CONTR is the simulation with no Pleim nudging, with satellite insolation, and no skin temperature moisture nudging. WRF-TS is the simulation with no Pleim nudging, with satellite insolation, and with skin temperature moisture nudging. The WRF-TS simulation can be summarized by the following. For specific humidity there was a slight increase in absolute bias but little change in RMSE. For 2-m temperature there was also a slight increase in absolute bias but a slight reduction in RMSE. For 10-m wind direction there was a slight decrease in bias and decrease in RMSE for all regions. This was the same for wind speed which showed a slight decrease in bias and RSME.

Table 6-2. Bias and Root Mean Square Error (RMSE) statistics for 2-m specific humidity (g kg^{-1}) from WRF simulations for the period 1-30 September 2013 for daytime conditions. The west and east domains are divided by – 97^{o} West Longitude meridian.

SIMULATION	BIAS ALL	BIAS WEST	BIAS EAST	RMSE ALL	RMSE WEST	RMSE EAST
WRF-BASE	**0.0**	**-0.2**	**0.0**	**1.8**	**1.9**	**1.8**
WRF-PLEIM	**-0.1**	**-0.1**	**0.0**	**1.8**	**1.9**	**1.7**
WRF-CONTR	**0.0**	**-0.1**	**0.0**	**1.8**	**1.9**	**1.7**
WRF-TS	**0.20**	**0.0**	**0.4**	**1.8**	**1.9**	**1.8**

Table 6-3. Bias and Root Mean Square Error (RMSE) statistics for 2-m temperature (K) from WRF simulations for the period 1-30 September 2013 for daytime conditions. The west and east domains are divided by – 97^{o} West Longitude meridian.

SIMULATION	BIAS ALL	BIAS WEST	BIAS EAST	RMSE ALL	RMSE WEST	RMSE EAST
WRF-BASE	**0.0**	**0.3**	**-0.2**	**2.1**	**2.4**	**2.0**
WRF-PLEIM	**0.0**	**0.2**	**-0.2**	**2.0**	**2.3**	**1.8**
WRF-CONTR	**-0.4**	**-0.1**	**-0.5**	**1.9**	**2.2**	**1.8**
WRF-TS	**-0.5**	**-0.2**	**-0.8**	**2.0**	**2.2**	**1.9**

Table 6-4. Bias and Root Mean Square Error (RMSE) statistics for 10-m wind direction (degrees) from WRF simulations for the period 1-30 September 2013 for daytime conditions. The west and east domains are divided by – 97^{o} West Longitude meridian.

SIMULATION	BIAS ALL	BIAS WEST	BIAS EAST	RMSE ALL	RMSE WEST	RMSE EAST
WRF-BASE	**2.3**	**1.5**	**2.9**	**60.9**	**65.3**	**58.0**
WRF-PLEIM	**2.4**	**1.6**	**2.9**	**60.7**	**65.2**	**57.8**
WRF-CONTR	**2.0**	**1.1**	**2.6**	**60.5**	**65.0**	**57.6**
WRF-TS	**1.8**	**1.0**	**2.3**	**60.6**	**64.8**	**57.8**

Table 6-5. Bias and Root Mean Square Error (RMSE) statistics for 10-m wind speed (m s^{-1}) from WRF simulations for the period 1-30 September 2013 for daytime conditions. The west and east domains are divided by – 97^{o} West Longitude meridian.

SIMULATION	BIAS ALL	BIAS WEST	BIAS EAST	RMSE ALL	RMSE WEST	RMSE EAST
WRF-BASE	**0.2**	**0.1**	**0.3**	**2.6**	**2.9**	**2.4**
WRF-PLEIM	**0.2**	**0.1**	**0.3**	**2.6**	**2.9**	**2.4**
WRF-CONTR	**0.1**	**0.0**	**0.2**	**2.5**	**2.9**	**2.3**
WRF-TS	**0.1**	**0.0**	**0.2**	**2.5**	**2.9**	**2.3**

13. Statistics for Texas Domain

The above analyses described the evaluation and statistics for the skin temperature nudging for the entire domain. Since model performance at one location can be impacted to some degree by model performance at other locations this domain wide approach is useful.Also, this is in keeping with UAH'srole in in the NASA AQAST activity of looking at national performance. However, local model performance is often dominated by model performance at a local or regional scale. Here we provide model evaluation statistics for Texas alone.

A special data mask was created so that for the NWS and satellite skin temperature model evaluations only NWS stations and model grid points in Texas were used. These are described and given below.

Skin Temperature Evaluation Metric: Table 6-6 below gives the total statistics for the state of Texas relative to skin temperatures for various WRF simulations (see Table 6-1 for the comparable full domain statistics). It shows that improvement in performance for the Texas domain for the skin temperature nudging of soil moisture is better than the domain statistics. While the initial WRF-Base case bias was larger the bias has been reduced by the skin temperature nudging (WRF-TS). For the root-mean –square error (RMSE) the initial WRF-Base case and WRF –CONTR (i.e. with insolation replacement) error in the Texas domain is larger than the full domain. However, with the skin temperature nudging the RMSE is reduced by nearly a full degree. Also, note for Texas that the insolation replacement (WRF-CONTR) reduces both the bias and RMSE compared the the WRF run with the modeled insolation (WRF-BASE).

SIMULATION	BIAS	RMSE
WRF-BASE	**-0.34**	**4.10**
WRF-PLEIM	**-0.50**	**3.98**
WRF-CONTR	**-0.13**	**4.02**
WRF-TS	**-0.26**	**3.13**

Table 6-6 Overall bias and RMSE statistics for the 1-30 September, 2013 for the state of Texas. WRF-BASE is the simulation with no Pleim nudging, no satellite insolation, and no skin temperature moisture nudging. WRF-PLEIM is the same as WRF-BASE except the Pleim nudging is activated. WRF-CONTR is the simulation with no Pleim nudging, with satellite insolation, and no skin temperature moisture nudging. WRF-TS is the simulation with no Pleim nudging, with satellite insolation, and with skin temperature moisture nudging.

National Weather Service Observations Evaluation Metric: Tables 6-7 through 6-10 give the performance statistics for the Texas domain. This can be compared to tables 6-2 through 6-5 above for the full domain. The skin temperature nudging increased the bias but reduced the RMSE for specific humidity. For 2-m temperature the bias was increased by a nearly one half a degree but reduced the RMSE. The increase in bias for temperature is a bit puzzling. It may be

that air port thermometers are not representative of the land use in the model grid. For wind speed and wind direction both bias and RMSE were reduced with the skin temperature nudging.

Table 6-7. Bias and Root Mean Square Error (RMSE) statistics for 2-m specific humidity (g kg^{-1}) from WRF simulations for the period 1-30 September 2013 for daytime conditions for locations within the state of Texas.

SIMULATION	BIAS	RMSE
WRF-BASE	-0.12	2.83
WRF-PLEIM	-0.11	2.73
WRF-CONTR	-0.02	2.72
WRF-TS	0.26	2.62

Table 6-8 Bias and Root Mean Square Error (RMSE) statistics for 2-m temperature (degrees K) from WRF simulations for the period 1-30 September 2013 for daytime conditions for locations within the state of Texas.

SIMULATION	BIAS	RMSE
WRF-BASE	0.06	2.18
WRF-PLEIM	0.03	2.10
WRF-CONTR	-0.32	1.94
WRF-TS	-0.51	1.98

Table 6-9. Bias and Root Mean Square Error (RMSE) statistics for 10-m wind direction (degrees) from WRF simulations for the period 1-30 September 2013 for daytime conditions for locations within the state of Texas.

SIMULATION	BIAS	RMSE
WRF-BASE	8.12	58.32
WRF-PLEIM	8.09	58.14
WRF-CONTR	7.38	58.10
WRF-TS	6.97	57.79

Table 6-10. Bias and Root Mean Square Error (RMSE) statistics for 10-m wind speed (m s^{-1}) from WRF simulations for the period 1-30 September 2013 for daytime conditions for locations within the state of Texas.

SIMULATION	BIAS	RMSE
WRF-BASE	0.36	2.76
WRF-PLEIM	0.34	2.75
WRF-CONTR	0.21	2.66
WRF-TS	0.20	2.65

In addition to the table data additional scatter plots (as seen in section 7 above) were also generated for the Texas domain. These are shown in 6-43. The results show that the RMSE is reduced even more in Texas than in the entire domain. In fact the visible reduction is scatter can be seen between the control panel (top left) and the panel with moisture nudging (lower right panel).

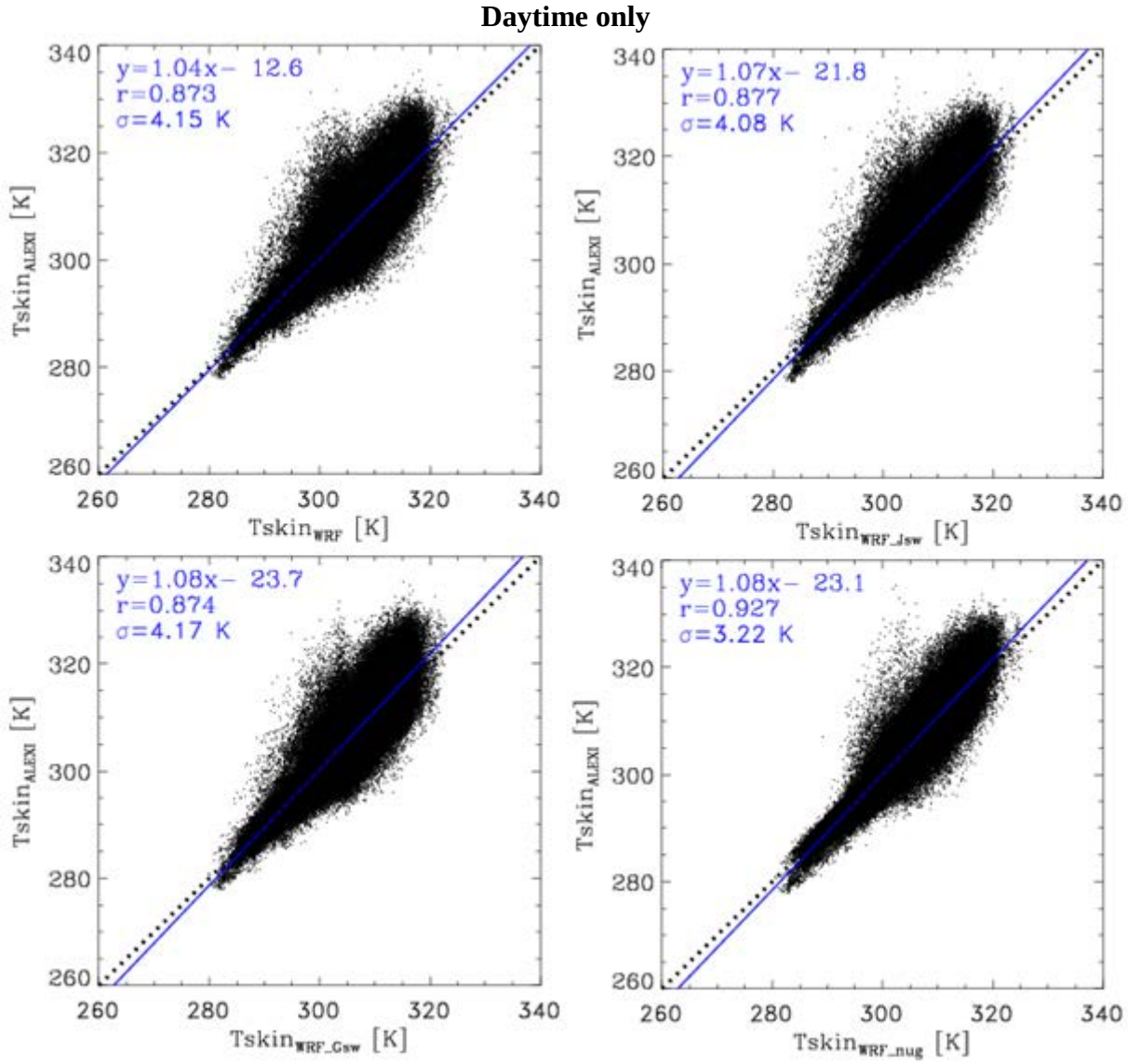

Fig. 6-43. Same as Fig. 6-33, but for Texas only.Comparison of Tskin–WRF simulation against ALEXI product (ALEXI on y-axis) for daytime-only for the entire month of Sep., 2013. The x-axis in the top-left panel is WRF simulation without ingestion of satellite insolation (WRF); in the top-right panel is WRF simulation with SPoRT insolation (WRF-CONTR_Jsw); in the bottom-left panel is WRF simulation with GSIP insolation (WRF-CONTR_Gsw); in the bottom-right panel is

WRF simulation with SPoRT insolation and with soil moisture nudging (WRF-TS). At the top of each plot are the regression equation, the correlation coefficient(r), and the RMSE (σ). The values of σ are in units of K.

14. Summary and Conclusions

Under this activity a technique was developed which diagnoses a skin temperature consistent with the surface fluxes in the PX model. This skin temperature is then used in a technique to nudge soil moisture (see equations (2) and (3)). Fundamentally, if the model temperatures are lower than the observed temperature then soil moisture is decreased. If the model temperatures are greater than the observed temperature then soil moisture is increased. This is consistent with that of Pleim and Xiu in that they argued that soil moisture is ill observed and thus needs an indirect observational adjustment. Techniques have been implemented within the WRF framework which allow the nudging of soil moisture using satellite skin temperatures as opposed to the NWS soil moisture nudging in the original PX model.

A control simulation was carried out (WRF-CONTR) which did not include the skin temperature nudging. Bias statistics were developed for this control. Second, a new WRF run was made using the skin temperature nudging technique. The results showed that over most of the domain that the bias was improved but there was a slight negative bias increase in the overall bias. This means that the few areas that had an increase in bias were larger causing a slight increase in absolute bias for the domain. Results for a smaller Texas domain showed even better improvements than the statistics for the full domain.

Comparisons with NWS observations were more mixed in regards to bias for humidity and 2meter temperature. RMSE was unchanged for humidity and decreased slightly for 2-m temperature. For wind speed and wind direction there was a slight decrease in bias and RMSE for all regions. Similar results were found for the Texas domain.

15. References

Anderson, M.C., Norman, J.M., Mecikalski, J.R., Otkin, J.A. and Kustas, W.P., 2007a. A climatological study of evapotranspiration and moisture stress across the continental United States based on thermal remote sensing: 1. Model formulation. J. Geophys. Res., 112(D10): D10117.

Anderson, M.C., Norman, J.M., Mecikalski, J.R., Otkin, J.A. and Kustas, W.P., 2007b. A climatological study of evapotranspiration and moisture stress across the continental United States based on thermal remote sensing: 2. Surface moisture climatology. J. Geophys. Res., 112(D11): D11112.

Carlson, T. N., 1986: Regional scale estimates of surface moisture availability and thermal inertia using remote thermal measurements. *Remote Sensing Rev.*, **1,** 197-246

Chen, F., and J. Dudhia (2001), Coupling an advanced land surface-hydrology model with the Penn State-NCAR MM5 modeling system. Part I: Model implementation and sensitivity, *Mon. Wea. Rev.*, 129, 569-585, doi:10.1175/1520-0493(2001)129<0569:CAALSH>2.0.CO;2

Fovell, R. 2013: WRF Performance Issues in the San Joaquin Valley and Southern California. Traversing New Terrain in Meteorological Modeling for Air Quality and Dispersion. U.California Davis. Sept 9-11,2013

McNider, R.T., A.J. Song, D.M. Casey, P.J. Wetzel, W.L. Crosson, and R.M. Rabin, 1994: Toward a dynamic-thermodynamic assimilation of satellite surface temperature in numerical atmospheric models. *Mon. Wea. Rev.,* **122,** 2784-2803.

Ran, L., R. Gilliam, F. S. Binkowski, A. Xiu, J. Pleim, and L. Band, 2015: Sensitivity of the Weather Research and Forecast/Community Multiscale Air Quality modeling system to MODIS LAI, FPAR, and albedo, *J. Geophys. Res. Atmos*., **120**, 8491–8511, doi:10.1002/2015JD023424.

Xiu,A. and J. Pleim, 2001: Development of a land surface model. Part II: Data assimilation. *J. Appl. Meteor.*, **42**, 1811-1822.

CHAPTER 7 Noah WRF CONTROL AND DISCOVER-AQ COMPARISONS

16. Introduction

Under this project two activities primarily led by NOAA ARL and George Mason University are carried out. The first is a control run of WRF using the configuration employed by TCEQ in its SIP and research activities including the 4-layer (with thickness of 10, 30, 60, and 100 cm) Noah land surface model. In the present project it was proposed that skin temperature nudging of moisture and thermal resistance in the Pleim-Xiu (PX) land surface model might improve model performance. Chapter 6 above indicates that indeed model performance is improved in the PX model. However, the more practical question for TCEQ is whether the PX model with skin temperature nudging improves the performance over that of the TCEQ protocol using the Noah model. Thus, section 2 below describes the WRF-Noah control run and section 3 compares the performance to the PX skin temperature nudging run and to DISCOVER-AQ aircraft data. The second activity is to make comparisons of the model results against aircraft observations during the DISCOVER-AQ field campaign. Section 4 below describes the special data available and the model comparisons.

17. Noah Control/Baseline Modeling

In order to establish a baseline case to quantify the potential improvement in the WRF model in terms of the surface to air exchange when using a satellite-skin temperature assisted diagnostics for the Pleim-Xiu (PX) Land Surface Model, we followed Texas Commission on Environmental Quality (TCEQ) in the selection of physical options for configuring WRF version 3.6.1 to simulate the meteorology within the continental US domain (Figure 7-1). Table 7-1 lists the customary physics options suggested by TCEQ.

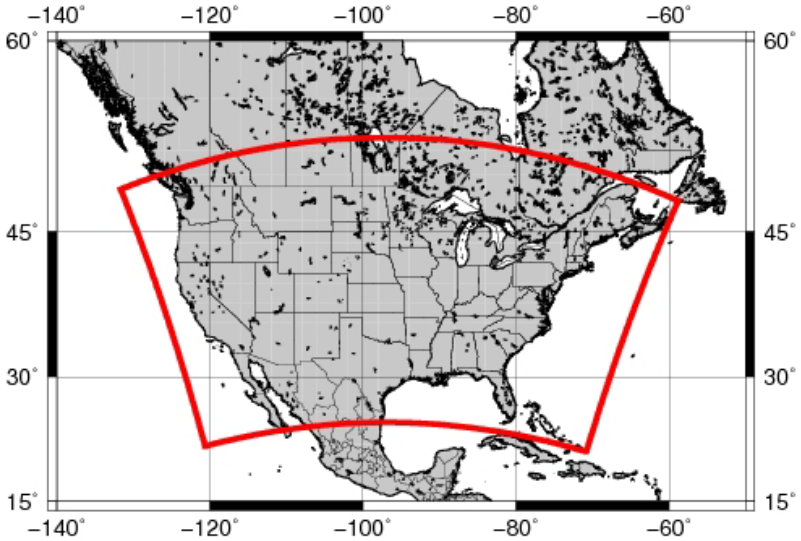

Figure 7-1. 12-km WRF domain used for model simulation (471 (column)×311 (row) grid cells).

*Table 7-1. Configurations of the WRF 3.6.1 simulation using the Noah land surface model and the references. The simulation were conducted between 00 UTC September 1, 2013 and 12 UTC October 1, 2013, and they were restarted every 5 days***.**

WRF Configurations	Descriptions of the Noah case
Domain and resolution	12 km over the continental US (471×311 grids in Figure 7-1): i.e., the domain of NOAA's air quality forecasting system
Initialization	12 km North American Mesoscale Model, which used the NOAH land surface model
Cloud model	Kain and Fritsch model [*Kain*, 2004]
Radiation model	Rapid Radiative Transfer Model model short- and long-wave radiation [*Iacono et al.*, 2008]
Microphysics	New Thompson Model [*Thompson et al.*, 2008]
PBL model	Yonsei University model [*Hong et al.*, 2006]
Surface layer	Monin-Obukhov model [*Monin and Obukhov*, 1954]
Land surface model	Noah [*Chen and Dudhia*, 2001]
Nudging	3 dimensional grid nudging for wind, temperature and moisture. PBL nudging was applied only to the wind (U; V)

While UAH will be using the PX model for testing its assimilation of skin temperature, because Texas has used the Noah model in many of its regulatory activities we feel that the ultimate test for the assimilation is to not just improve the performance of the PX model, but the improved PX model should also be an improvement of the WRF configuration used by TCEQ. Thus, these WRF/Noah simulations will serve as the control against whether or not model performance has been improved.

18. Model Comparisons (Noah case) With DISCOVER-AQ Aircraft Data

During the DISCOVER-AQ (Deriving Information on Surface Conditions from Column and Vertically Resolved Observations Relevant to Air Quality) Houston deployment in Sept 2013, airborne observations of meteorological and chemical species were made on NASA's P-3B aircraft on 9 days at 8 selected locations in the Greater Houston area three times a day (i.e., morning, noon-early afternoon, and late afternoon) to explore their spatial and diurnal variability. The focused 8 locations are denoted in Figure 7-2. The P-3B aircraft sampled over areas of diverse land use types in Houston during DISCOVER-AQ, as indicated by the US Geological Survey (USGS) land use categories used in the WRF simulations (Table 7-2). Some of the observations were taken above the water around Smith Point and Galveston, therefore since we are evaluating land use model in this study we mainly focus on the remaining six inland sites. At each location the aircraft flew circularly around areas within 0.1° latitude/longitude ranges (Table 7-2). Under clear conditions, LST was measured using the Heimann Infrared Radiation Pyrometer Model KT 19.85 (http://airbornescience.nasa.gov/sites/default/files/P-3B%20Experimenter%20Handbook%20548-HDBK-0001.pdf). This pyrometer has a spectral range of 9.6-11.5 μm, a response time of 1s, and a temperature range of -100° to +200°C. The accuracy is ±0.5% plus 0.7% of the difference between target temperature and housing

temperature. The pyrometer has a 2° field of view, and for this campaign its footprints ranged from <10 m to tens of meters in radius varying with the flight altitudes.

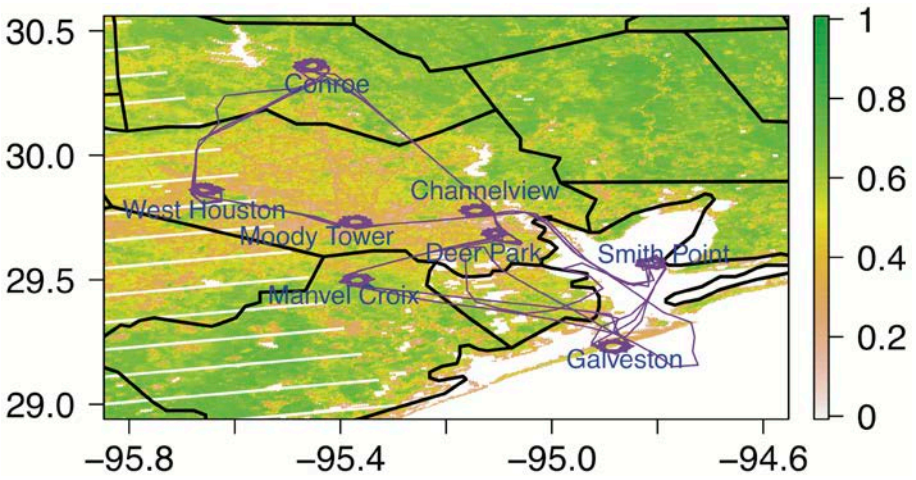

Figure 7-2. The VIIRS Normalized Difference Vegetation Index (TOA NDVI) on September 25, 2013 with the P-3B flight track overlaid in purple line and the focused sites labeled in dark blue. NDVI is the most commonly used vegetation index, calculated using the reflected visible and near-infrared light on vegetation.

Table 7-2. The latitude/longitude ranges at the six inland sites that aircraft sampled and the dominant land use type(s) in corresponding WRF grid box(es).

Location	USGS land use[a]	Aircraft sampled latitude (°N)/longitude (°W) ranges
Manvel Croix	Dryland Cropland and Pasture (2); Cropland/Grassland Mosaic (5)	29.47-29.54 / 95.34-95.40
Deer Park	Dryland Cropland and Pasture (2); Grassland (7)	29.64-29.71 / 95.06-95.13
Moody Tower	Urban and Built-up Land (1)	29.70-29.76 / 95.33-95.41
Channelview	Dryland Cropland and Pasture (2); Grassland (7)	29.75-29.80 / 95.11-95.18
West Houston	Dryland Cropland and Pasture (2)	29.80-29.89 / 95.62-95.69
Conroe	Evergreen Needleleaf (14)	30.31-30.39 / 95.41-95.49

[a]Source of USGS land use categories and descriptions: http://www2.mmm.ucar.edu/wrf/users/docs/user_guide_V3/users_guide_chap3.htm#_Land_Use_and

For the least cloudy day (September 25, 2013) during DISCOVER-AQ Houston, a semi-empirical diurnal temperature cycle model [*Duan et al.*, 2014] and the three sets of aircraft observations) at the six locations were used to formulate daytime land surface temperature (LST as a function of time and location-specific parameters). At each location, the derived function was then used to calculate the LSTs throughout the daytime. The aircraft-derived LSTs at each location enabled their comparisons with model throughout the day on similar scales, which will

be discussed below. The aircraft-derived daytime LSTs (Figure 7-3) show ranges of 11-25 °K varying by location, with the daily maxima occurring near 13-14 local time.

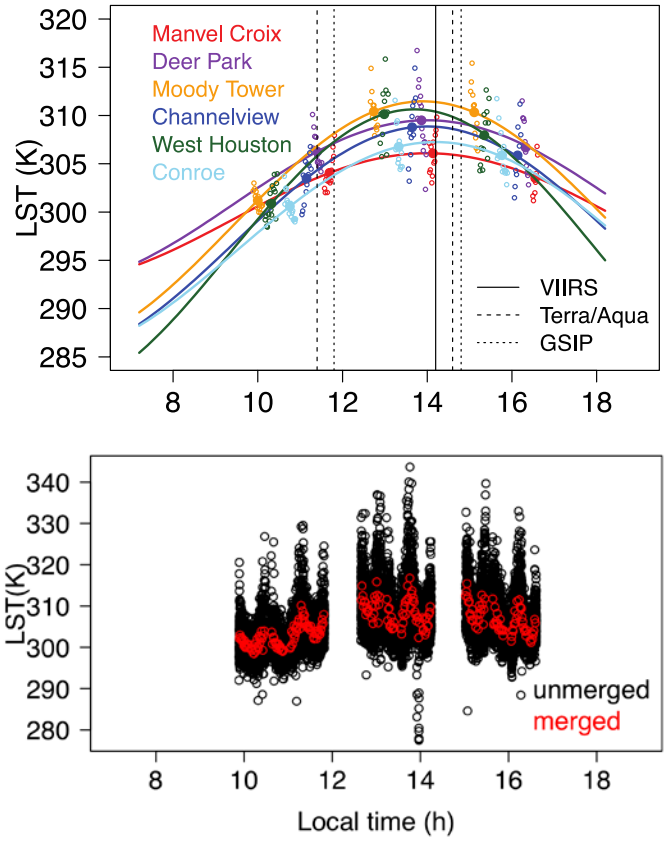

Figure 7-3. (Upper) Time series of LST from P-3B at six inland locations in the Greater Houston area on September 25, 2013. Open circles are 1-minute merged observations (for better readability) and the filled dots indicate the circuit-mean values. LSTs derived by the diurnal temperature cycle model are in solid lines. Satellite overpassing times are indicated in black vertical lines; (Lower) Time series of LST from P-3B at six inland locations in the Greater Houston area on September 25, 2013. Black and red dots represent LSTs from the original (in 1 second resolution) and the merged (in 1-minute resolution) datasets. The mean values of LSTs at each circuit from the merged and the original datasets are almost identical.

The WRF simulation using the Noah land surface model is evaluated against the aircraft-derived LST at the six locations, indicating location- and time-dependent performance. Statistics (Table 7-3) indicated that overall WRF performed best at Deer Park. Better performance is shown at 12-15 local time except at Manvel Croix. The location- and time varying discrepancies were also shown among various satellite instruments and the aircraft-derived LSTs (include in a manuscript under review by JGR-Atmospheres), which indicate that large uncertainties exist for LSTs sampled on these different platforms over smaller temporal and spatial scales. Therefore, great challenges are posed for the evaluation of regional-scale model simulated LSTs, especially in the areas of diverse surface types and lacking surface site observations such as in Houston. These observations are worth further evaluation in order to benefit the WRF model evaluation and improvement.

Table 7-3. Evaluation of WRF modeled LST with the aircraft-derived LST at six sites within different time intervals on September 25, 2013. Root mean square errors (°K) are listed.

Local time (hh:mm)	Manvel Croix	Deer Park	Moody Tower	Channel view	West Houston	Conroe
08:00-11:00	4.34	1.62	6.99	4.00	4.37	4.64
12:00-15:00	6.28	0.64	6.58	0.94	1.70	4.35
16:00-18:00	5.30	0.56	10.45	2.64	6.74	5.03
08:00-18:00	5.37	1.09	7.96	2.83	4.52	4.65

19. Comparison Between PX with Skin Temperature Nudging and DISCOVER-AQ Data

We compared the three WRF simulations (i.e., Noah, PX, and PX nudging) with the aircraft-derived LST time series during the period of 8:00-18:00 local time on September 25, 2013. The root mean square error (RMSE) and the difference between the maximum and minimum LSTs (defined as Diff) for each case at the six inland locations are summarized in Table 7-4.

Table 7-4. Evaluation of WRF modeled LST with the aircraft-derived LST at six sites within different time intervals on September 25, 2013. Root mean square errors (RMSE, °K) and the differences between maximum and minimum LSTs (i.e., Diff) during 8:00-18:00 local time (°K) are listed. Cases with the best and worst performance are colored in green and red, respectively. Whether the PX nudging improved performance of the PX case or not is indicated by the "+/-" signs.

	Case	Manvel Croix	Deer Park	Moody Tower	Channel view	West Houston	Conroe
RMSE	Noah	5.37	1.09	7.96	2.83	4.52	4.65
	PX VF[a]	4.22	4.72	6.34	5.60	4.94	3.77
	PX VF nudging	7.11 (-)	2.70 (+)	4.95 (+)	5.23 (+)	7.39 (-)	5.51 (-)
Max-Min (Diff)	Aircraft-derived	10.01	12.75	18.98	17.82	21.70	16.62
	Noah	18.10	14.44	17.57	15.00	18.79	19.42
	PX VF	15.83	15.13	16.19	16.60	18.11	17.25
	PX VF nudging	20.36 (-)	16.55 (-)	19.13 (+)	18.63 (+)	21.30 (+)	18.88 (-)

[a]Applying to both PX runs: "VF" indicates modified vegetation fraction was used; Diagnostic skin temperature is analyzed.

The PX nudging case reduced the RMSEs related to the PX case at Deer Park, Moody Tower, and Channel View, but only performed better than the Noah case at Moody Tower. At West Houston, the Noah case performed best, and the PX case shows the best performance at Manvel Croix and Conroe among the three cases.

We also examined the WRF performance on the daytime LST range. The PX nudging case enhanced Diff from the case PX at all six locations, best matching the aircraft-derived LST variability at Moody Tower, Channel View and West Houston, where observation-derived Diff

are larger (i.e., ranging from 17.8-21.7 °K). The Noah case performed best only at Deer Park, and the PX case shows the best match with the observation-derived at Conroe and Manvel Croix.

20. Conclusions and Discussions

In this chapter, we explored the usefulness of NASA P-3B aircraft data from the DISCOVER-AQ Houston campaign (in Sept 2013) for evaluating WRF-modeled LSTs over the inland Greater Houston area, where the land use is diverse and rapidly changing but surface sites are lacking. We derived daytime LSTs based on aircraft observations and a diurnal cycle model at six sites in Houston, which enabled their comparisons with WRF throughout the day on similar scales.

RMSEs and the differences between daytime maximum and minimum LSTs were calculated to quantify the discrepancies between the WRF simulations and the aircraft-derived LSTs. No single WRF simulation performed uniformly well at all six locations: e.g., the PX nudging case best matched with the aircraft-derived at Moody Tower, while the Noah case showed least discrepancies from the aircraft-derived at Deer Park, and the PX case showed the best match with the observation-derived at Conroe and Manvel Croix.

In our analysis the model evaluation with aircraft data was limited to one day, and the findings from this evaluation would be more convincing if the comparison was conducted for more days. However, aircraft measurements were more strongly affected by clouds on the rest 8 flight days during this field campaign. Frequent cloudy scenes over this region also limited the use of infrared satellite observations for comparing with the model.

The impact of scale/resolution of the datasets on the comparison should also be accounted for. The aircraft LST footprints are on the scales of 10-100 m varying by the flight altitude, much smaller than the 12 km resolution of the WRF model (as well as some satellite products). As shown in Figure 7-3, at each of the six locations, 1 second aircraft LST ranged by up to >40 °K, with standard deviations of 4-7°K, due to the mixing surface conditions at each location. Therefore, we used the circuit-wide mean values (that covered areas within ~0.1° latitude/longitude ranges) to represent conditions on similar scales to the WRF grid. Further validating and improving this method would be needed, and using finer model resolution for accurately modeling LSTs in urban areas would be helpful. Furthermore, additional aircraft/surface measurements in this region would be beneficial for evaluating the diurnal cycle model and providing nighttime LST information.

21. References

Chen, F., and J. Dudhia (2001), Coupling an advanced land surface-hydrology model with the Penn State-NCAR MM5 modeling system. Part I: Model implementation and sensitivity, *Mon. Wea. Rev.*, 129, 569-585, doi:10.1175/1520-0493(2001)129<0569:CAALSH>2.0.CO;2.

Duan, S.-B., Z.-L. Li, B.-H. Tang, H. Wu, R. Tang, Y. Bi, G. Zhou (2014), Estimation of Diurnal Cycle of Land Surface Temperature at High Temporal and Spatial Resolution from Clear-Sky MODIS Data, *Remote Sens.*, 6, 3247-3262, doi:10.3390/rs6043247.

Hong, S.-Y., Y. Noh, and J. Dudhia (2006), A new vertical diffusion package with an explicit treatment of entrainment processes, *Mon. Wea. Rev.*, 134, 2318–2341, doi: 10.1175/MWR3199.1.

Iacono, M. J., J. S. Delamere, E. J. Mlawer, M. W. Shephard, S. A. Clough, and W. D. Collins (2008), Radiative forcing by long-lived greenhouse gases: Calculations with the AER radiative transfer models, *J. Geophys. Res.*, 113, D13103, doi:10.1029/2008JD009944.

Kain, J. S. (2004), The Kain-Fritsch convective parameterization: An update, *J. Appl. Meteor.*, 43, 170–181, doi: 10.1175/1520-0450(2004)043<0170:TKCPAU>2.0.CO;2.

Monin, A. S., and A. M. Obukhov (1954), Basic laws of turbulent mixing in the surface layer of the atmosphere, *Tr. Akad. Nauk. SSSR Geophiz. Inst.*, 24 (151), 163–187.

Thompson, G., P. R. Field, R. M. Rasmussen, and W. D. Hall (2008), Explicit Forecasts of Winter Precipitation Using an Improved Bulk Microphysics Scheme, Part II: Implementation of a New Snow Parameterization, *Mon. Wea. Rev.*, 136, 5095–5115, doi: 10.1175/2008MWR2387.1.

8. Summary and Conclusions

Under this activity a technique was developed which diagnoses a skin temperature consistent with the surface fluxes in the PX model. This skin temperature is then used in a technique to nudge soil moisture (see equations (6-2) and (6-3)). Fundamentally, if the model temperatures are lower than the observed temperature, then soil moisture is decreased. If the model temperatures are greater than the observed temperature, then soil moisture is increased. This is consistent with that of Pleim -Xiu since they argued that soil moisture is ill-observed and thus needs an indirect observational adjustment. Techniques have been implemented within the WRF framework which allow the nudging of soil moisture using satellite skin temperatures as opposed to the NWS soil moisture nudging in the original PX model.

As part of this activity, a satellite derived insolation was used in place of the WRF modeled insolation for both the control runs and the nudging runs (see Chapter 2). While the satellite derived insolation had better performance statistics against pyranometer data, the model case with satellite insolation showed slightly poorer performance than the run with WRF modeled insolation. This is an area for further investigation. In initial examination it appears that differences between the satellite insolation case and modeled insolation case have a pattern that appears to be related to surface albedo. In past uses of satellite insolation (McNider et al. 1994) the satellite derived insolation cases also used a satellite derived albedo. In the present case the regular WRF land use albedo was used. This may be the cause of the slightly degraded performance. Thus, the moisture nudging experiments are having to overcome this slight deterioration in performance compared to the regular WRF model. It is noted ,however, that for the Texas domain (see Chapter 6) that the satellite insolation replacement in WRF did reduce the bias and RMSE.

Chapter 6 describes the use of skin temperatures to nudge moisture. For the moisture nudging experiment using skin temperatures control simulation was carried out (WRF-CONTR) which did not include the skin temperature nudging. Bias statistics were developed for this control. Second, a new WRF run was made using the skin temperature nudging technique. Using skin temperatures as the performance metric, the results showed that over most of the domain that the bias was improved but there was a slight negative bias increase in the overall bias. This means that the few areas that had an increase in bias were larger causing a slight increase in absolute bias for the domain. An examination of time series from the nudging runs compared to the control showed that the adjustments in moisture appeared to be working as formulated. In some places part of the error may have been due to bad skin temperature data. Note, these statistics did not include the third level of screening discussed in Chapter 5.

Again, using skin temperatures as the performance metric, the root mean square error (RMSE) was calculated for the control run and for the skin temperature moisture nudging case. Here the moisture nudging provided significant improvement over the entire domain. The RMSE was improved by about .7 degrees K over the domain or approximately 20%. For the Texas domain the improvements were even greater with nearly a full degree reduction in RMSE (4.10 to 3.13) or about a 25% improvement in the RMSE. Additionally, the bias was also reduced by about 25% from -.34 to -.26.

Comparisons with NWS observations were more mixed in regards to bias for humidity and 2meter temperature. RMSE was unchanged for humidity and decreased slightly for 2-m temperature. For wind speed and wind direction there was a slight decrease in bias and RMSE for all regions. The results for the Texas domain were similar with RMSE for 2m temperatures decreasing but bias increasing. For wind speed and wind direction both RMSE and bias were reduced across the domain.

The largest areas in RMSE and bias remain in the Western U.S. where even drying the soil using moisture nudging did not give the diurnal range found in skin temperature observations. Here adjustments in other parts of the surface energy budget may be needed. It is felt that implementation of the heat capacity adjustment which was an optional task under this project for which there was not enough time may provide further significant improvement.

In conclusion the moisture nudging within the PX model was a positive step in improving the model performance. Thus, it is felt that this supports the overall hypothesis in this research activity that simple land surface models constrained by observations may be path for improved meteorology in air quality simulations.

Future Work: Two areas need further attention. This is first the implementation of the heat capacity adjustment using skin temperatures described in equation 1-3. The second is an investigation of the cause of the deterioration in model performance when satellite derived insolation was used despite the satellite insolation showing the better performance against pyranometer observed insolation. Finally, because of time constraints, the use of the full third level cloud screening of skin temperature was not available for use in the moisture nudging and model evaluation. It is expected that this will provide further improvement in the RMSE.

This future work will be supported by NASA Air Quality Applied Science Team (AQAST) resources since this was identified as a high priority by the AQAST Physical Atmosphere advisory team. A full report of this additional activity will be proved to AQRP and TCEQ.

9. Acknowledgements and Disclaimer

This research was financed in part by a grant from the Texas Commission on Environmental Quality (TCEQ), administered by The University of Texas through the Air Quality Research Program and in part by NASA Air Quality Applied Sciences Team (AQAST) The contents, findings, opinions, and conclusions are the work of the author(s) and do not necessarily represent the findings, opinions, or conclusions of the TCEQ or NASA.

10. Appendix A: Acronyms

ALEXI	Atmosphere-Land Exchange Inverse
DISCOVER-AQ	Deriving Information on Surface conditions from Column and Vertically Resolved Observations Relevant to Air Quality
CLASS	Comprehensive Large Array-Data Stewardship System

FIFE	First International Satellite Land Surface Climatology Field Experiment
GEWEX	Global Energy and Water Cycle Experiment
GSIP	GOES Surface and Insolation Products
GOES	Geostationary Operational Environmental Satellite
IR	Infrared
LST	Land Surface Temperature
MODIS	The Moderate-resolution Imaging Spectroradiometer
MSFC	Marshall Space Flight Center
NASA	National Aeronautics and Space Administration
NCDC	National Climatic Data Center
NCEP	National Centers for Environmental Prediction
NOAA	National Oceanic and Atmospheric Administration
Noah	NCEP-Oregon State University-Air Force-Hydrologic Research Library
NWS	National Weather Service
PX	Pleim-Xiu
QA	Quality Assurance
RMSE	Root Mean Square Error
SCAN	Soil Climate Analysis Network
SIP	State Implementation Plan
SPoRT	Short-term Prediction Research and Transition Center (http://weather.msfc.nasa.gov/sport/)
SURFRAD	Surface Radiation budget network
TCEQ	Texas Commission on Environmental Quality
TOA	Top Of Atmosphere
UAH	University of Alabama in Huntsville
USDA	United States Department of Agriculture
USGS	United States Geological Survey
UTC	Coordinated Universal Time
WRF	Weather Research and Forecasting Model
WPS	WRF Preprocessing System

11. Appendix B: WRF CHANGES

Logically, the required changes to the WRF code to perform the work in this project are related to these files, respectively: 1) the “namelist.input” file, 2) the “Registry.EM_COMMON” file, 3) the “dyn_em/module_first_rk_step_part1.F” file, 4) the “phys/module_radiation_driver.F” file, 5) the “phys/module_surface_driver.F” file, and 6) the “phys/module_sf_pxlsm.F” file.

Table 11-1 summarizes the changes made to the “namelist.input” file to implement the various runs. If “idebug” and “jdebug” are different from zero then extra debugging statements are output. If “diag_tskin=T” then a WRF skin temperature is diagnosed inside the Pleim model as described in section XX. If “use_goes_insol=T” then the GOES-derived insolation replaces the model calculated value when it is available. If “do_tskin_nudge=T” then either the skin temperature nudging of soil moisture and/or the adjustment of the heat capacity is performed,

depending on the instructions prescribed in the next namelist variable “tskin_nudge_control”. At the time of the submission of this report the adjustment of the heat capacity has not yet been implemented. Relative to the given example in Table 1 of “tskin_nudge_control=’SR++0005E’”, this string instructs the code for soil moisture nudging (chosen by the last character of “E”, shortened nomenclature for soil evaporation) relative to local sunrise (chosen by the substring “SR”), from 0 hours after sunrise (chosen by the first two zeroes or the substring “00”) to 5 hours after sunrise (chosen by the substring “05”). The sign of the hourly interval relative to sunrise is given by the two characters after “SR”. For example the string “SR-+0103E” would instruct the WRF code to perform soil moisture nudging from 1 hour before sunrise to 3 hours after sunrise. If “use_usgs_vegf = T”, then the vegetation fraction used within the Pleim-Xiu model is the USGS fraction and not the seasonally adjusted value in the original code.

Table 11-1 summarizes the necessary changes in the registry “Registry.EM_COMMON” file. The changes are in three basic sections. The first are the addition of several state variables. The second are changes to the “package” statement for the Pleim-Xiu model to make certain variables available to that physics package. The third are “rconfig” changes which enable the changes made to the “namelist.input” file in Table 1 to be made available to the WRF iostream.

Table 11-3 summarizes the changes to the “dyn_em/module_first_rk_step_part1.F” file which passes the new information via calls to “radiation_driver” and “surface_driver”. The changes below this level are best described in a future user manual or the updated code itself.

Table 11-1. Summary of changes required for GOES-insolation and skin temperature nudging in the Pleim-Xu model in the WRF "namelist.input" file. The "px_options" is a new group to the existing "namelist.input" structure.

&px_options
idebug = 199
jdebug = 120
diag_tskin = .true.
use_goes_insol = .false.
do_tskin_nudge = .false.
tskin_nudge_control = 'SR++0005E'
nts_max = 10
use_px_t_wgt_for_wg = .false.
use_px_rh_wgt_for_wg = .false.
use_px_t_wgt_for_w2 = .false.
use_px_rh_wgt_for_w2 = .false.
use_px_t_wgt_for_t2 = .false.
ndg_sec_t_wg = 0.0
ndg_sec_rh_wg = 0.0
ndg_sec_t_w2 = 0.0
ndg_sec_rh_w2 = 0.0
ndg_sec_t_t2 = 0.0
use_usgs_vegf = .true.
/

Table 11-2. Summary of changes required for GOES-insolation and skin temperature nudging in the Pleim-Xu model in the WRF "Registry.EM_COMMON" file. Yellow-highlighted lines indicate lines in the original file for context.

state real soilcat ij misc 1 - i12 "SOILCAT" "SOIL CAT DOMINANT TYPE" ""
state real vegcat ij misc 1 - i12 "VEGCAT" "VEGETATION CAT DOMINANT TYPE" ""
state real tskin_diag ij misc 1 - h "TSKIN_DIAG" "PXLSM Diagnosed Skin Temperature" "K"
state real tskin_qobs ij misc 1 - h "TSKIN_QOBS" "PXLSM Quasi-Observed Skin Temperature" "K"
state real tskin_obs_e ij misc 1 - i7h "TSKIN_OBS_E" "OBSERVED TSKIN EARLY" "K"
state real tskin_obs_m ij misc 1 - i7h "TSKIN_OBS_M" "OBSERVED TSKIN MIDDLE" "K"
state real tskin_obs_l ij misc 1 - i7h "TSKIN_OBS_L" "OBSERVED TSKIN LATE" "K"
state real swd_obs_e ij misc 1 - i7h "SWD_OBS_E" "GOES INSOLATION EARLY" "W m-2"
state real swd_obs_m ij misc 1 - i7h "SWD_OBS_M" "GOES INSOLATION MIDDLE" "W m-2"
state real swd_obs_l ij misc 1 - i7h "SWD_OBS_L" "GOES INSOLATION LATE" "W m-2"
state real sunrise_hr ij misc 1 - h "SUNRISE_HR" "SUNRISE HOUR" "sunrise utc hour 0-24"
state real sunset_hr ij misc 1 - h "SUNSET_HR" "SUNSET HOUR" "sunset utc hour 0-24"
state integer nhts_beg {ntts} misc 1 - - "NHTS_BEG" "TSKIN HOUR BEG" "beg tskin hour 0-24"
state integer nhts_end {ntts} misc 1 - - "NHTS_END" "TSKIN HOUR END" "end tskin hour 0-24"
state integer nsign_beg_sr {ntts} misc 1 - - "NSIGN_BEG_SR" "BEG SR SIGN" "beg sunrise tskin hour sign"
state integer nsign_end_sr {ntts} misc 1 - - "NSIGN_END_SR" "END SR SIGN" "end sunrise tskin hour sign"
state integer nsign_beg_ss {ntts} misc 1 - - "NSIGN_BEG_SS" "BEG SS SIGN" "beg sunset tskin hour sign"
state integer nsign_end_ss {ntts} misc 1 - - "NSIGN_END_SS" "END SS SIGN" "end sunset tskin hour sign"
state integer tskin_mode_local {ntts} misc 1 - - "TSKIN_MODE_LOCAL" "TSKIN_MODE_LOCAL" "tskin mode local"
state integer nts_use - misc 1 - - "NTS_USE" "NTS_USE" "number tskin nudging categories"
package pxlsmmodel sf_surface_physics==7 - state:t2_ndg_new,q2_ndg_new,t2_ndg_old,q2_ndg_old,tskin_diag,tskin_obs_e,tskin_obs_m,tskin_obs_l,sunrise_hr,sunset_hr, nhts_beg, nhts_end, nsign_beg_sr, nsign_end_sr, nsign_beg_ss, nsign_end_ss, tskin_mode_local, nts_use, do_tskin_nudge, tskin_nudge_control, diag_tskin, tskin_qobs
rconFigurefigureinteger sf_lake_physics namelist,physics max_domains 0 - "sf_lake_physics" "activate lake model 0=no, 1=yes" ""
rconFigurefigureinteger idebug namelist,px_options max_domains 0 irh "idebug" "i index debugging location"
rconFigurefigureinteger jdebug namelist,px_options max_domains 0 irh "jdebug" "j index debugging location"
rconFigurefigurelogical diag_tskin namelist,px_options max_domains .false. irh "diag_tskin" "T/F diagnose skin temp"
rconFigurefigurelogical use_goes_insol namelist,px_options max_domains .false. irh "use_goes_insol" "T/F for using GOES insolation"
rconFigurefigurelogical do_tskin_nudge namelist,px_options max_domains .false. irh "do_tskin_nudge" "T/F tskin nudge"
rconFigurefigurecharacter tskin_nudge_control namelist,px_options max_domains " " irh "tskin_nudge_control" "tskin nudge control"
rconFigurefigureinteger nts_max namelist,px_options 1 5 - "nts_max" "max tskin nudging instructions"
rconFigurefigurelogical use_px_t_wgt_for_wg namelist,px_options max_domains .true. - "use_px_t_wgt_for_wg" "T/F for use PX t wgt for wg"
rconFigurefigurelogical use_px_rh_wgt_for_wg namelist,px_options max_domains .true. - "use_px_rh_wgt_for_wg" "T/F for use PX rh wgt for wg"
rconFigurefigurelogical use_px_t_wgt_for_w2 namelist,px_options max_domains .true. - "use_px_t_wgt_for_w2" "T/F for use PX t wgt for w2"
rconFigurefigurelogical use_px_rh_wgt_for_w2 namelist,px_options max_domains .true. - "use_px_rh_wgt_for_w2" "T/F for use PX rh wgt for w2"
rconFigurefigurelogical use_px_t_wgt_for_t2 namelist,px_options max_domains .true. - "use_px_t_wgt_for_t2" "T/F for use PX t wgt for t2"
rconFigurefigurereal ndg_sec_t_wg namelist,px_options max_domains 0.0 - "ndg_sec_t_wg" "nudging sec for t for wg"
rconFigurefigurereal ndg_sec_rh_wg namelist,px_options max_domains 0.0 - "ndg_sec_rh_wg" "nudging sec for rh for wg"

rconFigurefigurereal ndg_sec_t_w2 namelist,px_options max_domains 0.0 - "ndg_sec_t_w2" "nudging sec for t for w2"
rconFigurefigurereal ndg_sec_rh_w2 namelist,px_options max_domains 0.0 - "ndg_sec_rh_w2" "nudging sec for rh for w2"
rconFigurefigurereal ndg_sec_t_t2 namelist,px_options max_domains 0.0 - "ndg_sec_t_t2" "nudging sec for t for t2"
rconFigurefigurelogical use_usgs_vegf namelist,px_options max_domains .false. irh "use_usgs_vegf" "T/F for USGS vegf"

Table 11-3. Summary of changes required for GOES-insolation and skin temperature nudging in the Pleim-Xu model in the WRF "dyn_em/module_first_rk_step_part1.F" file. Yellow-highlighted lines indicate lines in the original file for context. Rows with "SKIPPED LINES" indicate skipped record(s) for sake of brevity.

!WRF:MEDIATION_LAYER:SOLVERZZZZZZZZZZ
#define BENCH_START(A)
#define BENCH_END(A)
MODULE module_first_rk_step_part1
CONTAINS
SUBROUTINE first_rk_step_part1 (grid , config_flags &
, moist , moist_tend &
SKIPPED LINES
CALL radiation_driver(&
& p_top=grid%p_top & !DJW 140312 added p_top for vertical nesting
& ,ACFRCV=grid%acfrcv ,ACFRST=grid%acfrst ,ALBEDO=grid%albedo &
SKIPPED LINES
,gid=grid%id & ! KGD
,idebug=config_flags%idebug & ! KGD
,jdebug=config_flags%jdebug & ! KGD
,use_goes_insol=config_flags%use_goes_insol & ! KGD
,SWD_OBS_E=grid%swd_obs_e & ! KGD
,SWD_OBS_M=grid%swd_obs_m & ! KGD
,SWD_OBS_L=grid%swd_obs_l) ! KGD
SKIPPED LINES
CALL surface_driver(&
& HYDRO_dt=HYDRO_dt, sfcheadrt=grid%sfcheadrt, &
& INFXSRT=grid%INFXSRT, soldrain=grid%soldrain, &
SKIPPED LINES
& ,TS_RUL2D_mosaic=grid%TS_RUL2D_mosaic & !danli mosaic
,gid=grid%id & ! KGD
,idebug=config_flags%idebug & ! KGD
,jdebug=config_flags%jdebug & ! KGD
,diag_tskin=config_flags%diag_tskin & ! KGD
,TSKIN_DIAG=grid%tskin_diag & ! KGD
,TSKIN_OBS_E=grid%tskin_obs_e & ! KGD
,TSKIN_OBS_M=grid%tskin_obs_m & ! KGD
,TSKIN_OBS_L=grid%tskin_obs_l & ! KGD
,TSKIN_QOBS=grid%tskin_qobs & ! KGD
,SUNRISE_HR=grid%sunrise_hr & ! KGD
,SUNSET_HR=grid%sunset_hr & ! KGD
,nts_max=grid%nts_max & ! KGD
,nhts_beg=grid%nhts_beg & ! KGD
,nhts_end=grid%nhts_end & ! KGD
,nsign_beg_sr=grid%nsign_beg_sr & ! KGD
,nsign_end_sr=grid%nsign_end_sr & ! KGD
,nsign_beg_ss=grid%nsign_beg_ss & ! KGD
,nsign_end_ss=grid%nsign_end_ss & ! KGD
,tskin_mode_local=grid%tskin_mode_local & ! KGD
,nts_use=grid%nts_use & ! KGD
,do_tskin_nudge=config_flags%do_tskin_nudge & ! KGD
,tskin_nudge_control=config_flags%tskin_nudge_control & ! KGD
,use_px_t_wgt_for_wg=config_flags%use_px_t_wgt_for_wg & ! KGD
,use_px_rh_wgt_for_wg=config_flags%use_px_rh_wgt_for_wg & ! KGD
,use_px_t_wgt_for_w2=config_flags%use_px_t_wgt_for_w2 & ! KGD

,use_px_rh_wgt_for_w2=config_flags%use_px_rh_wgt_for_w2 & ! KGD
,use_px_t_wgt_for_t2=config_flags%use_px_t_wgt_for_t2 & ! KGD
,ndg_sec_t_wg=config_flags%ndg_sec_t_wg & ! KGD
,ndg_sec_rh_wg=config_flags%ndg_sec_rh_wg & ! KGD
,ndg_sec_t_w2=config_flags%ndg_sec_t_w2 & ! KGD
,ndg_sec_rh_w2=config_flags%ndg_sec_rh_w2 & ! KGD
,ndg_sec_t_t2=config_flags%ndg_sec_t_t2 & ! KGD
,use_usgs_vegf=config_flags%use_usgs_vegf) ! KGD